



University of
Salford
MANCHESTER

A Study of Microwave TDFT Applicator Design for Low Power
Cancer Ablation

EMAN GALAL MAHMOUD IBRAHIM HASSAN

SCHOOL OF COMPUTING, SCIENCE AND ENGINEERING, UNIVERSITY OF
SALFORD, GREATER MANCHESTER, UNITED KINGDOM

SUBMITTED AS A PARTIAL FULFILMENT OF THE REQUIREMENT
OF THE DEGREE OF DOCTOR OF PHILOSOPHY (PH.D)

2019

To the memory of my father..

Table of Contents

Table of Contents	i
List of Figures	iv
List of Tables	xii
Acknowledgement	xiii
Publications	xiv
List of Abbreviations	xv
Abstract	1
Chapter One	2
Introduction and Background of Cancer Treatment Techniques	2
1.1. Background on Cancer Treatment Techniques	2
1.2. Overview on Types of Tumour Ablation Techniques.....	4
1.2.1. Cryo-ablation	4
1.2.2. Focused Ultra Sound (FUS) Ablation	4
1.2.3. Laser Ablation	4
1.2.4. Direct Current (DC) catheter ablation	5
1.2.5. Radio Frequency (RF) Ablation	5
1.2.6. Microwave Ablation	6
1.3. Benefits of Microwave ablation compared to other thermal ablation Techniques	8
1.4. Microwave ablation system.....	9
1.5. Problems and Limitations Found in Microwave Ablation Technology.....	12
1.6. Research Aim and Objectives	13
1.7. Research Contribution.....	14
1.8. Research Process.....	16
1.8.1. Research Process Chart	18
1.9. Thesis outline	19
Chapter Two.....	20

Related Work and Literature Review.....	20
2.1. Introduction.....	20
2.1.1. Linear Element Based Applicator Designs	20
2.1.2. Slot Based Applicator Designs	31
2.1.3. Looped, Helical Based Applicator Designs	37
2.2. Critical Evaluation of Literature	40
2.3. Applicator Design Considerations for Successful Ablation.....	44
Chapter three	46
Semi-analytical Numerical Nearfield Calculation of TDFT Antenna	46
3.1. Introduction and Overview af Opened-Out Coaxial Line Antennas.....	46
3.2. Synthesis of Antenna geometry	51
3.2.1. Geometrical Relations on the Hemisphere.....	52
3.3. Current Distribution on the Antenna Surface.....	55
3.3.1. Current Distribution on Electrically Short Antenna ($\mathcal{L} < \lambda/2$)	56
3.3.2. Current Distribution on Electrically Long Antenna ($\mathcal{L} \geq \lambda/2$).....	56
3.4. Evaluation of the Near Field Distribution.....	57
3.5. Evaluation of Surface Integrals.....	61
3.5.1. Infinitesimal Surface Area in Spherical Coordinates.....	61
3.5.2. Evaluation of Surface Current Divergence on the Hemisphere	63
3.6. Results and Discussions	70
3.6.1. Current Distribution on Electrically Long Antenna ($\mathcal{L} \geq \lambda/2$).....	70
3.6.2. Evaluation of the electric field distribution in the near zone	71
Chapter Four	81
Implementation and numerical modeling of Teardrop Flared Tipped antenna design	81
4.1. Proposed Research Design.....	81
4.1.1. Synthesis of Teardrop Flared Tipped Antenna Structure.....	81
4.1.2. Simulation Results of TDFT antenna in Saline and Healthy Liver	84

4.1.3. Simulation Results of TDFT in Malignant Tissue	93
4.2. Realization of Prototype of TDFT antenna	108
4.2.1. Simulation Results of TDFT in Malignant Tissue	113
4.3. Disparity of Ablated Lesion Size Based on the Applied Microwave Power and the Application Time	128
4.3.1. Ablated Lesion Size Dependence on the Applied Microwave Power	128
4.3.2. Ablated Lesion Size Dependence on the Application time.....	132
4.4. Fabrication of The Proposed TDFT Antenna Design	138
Chapter Five	150
Evaluation of TDFT Design Compared to Previously Proposed Designs	150
5.1. TDFT antenna parameters compared to that attained in MWA therapy	150
5.2. A comparison between TDFT antenna and other MW applicators presented in Literature	152
Chapter Six.....	156
6.1. Conclusion	156
6.2. Future Work	160
References	162

List of Figures

FIGURE 1. COAXIAL CABLE RUNS THE LENGTH OF THE SHAFT, WITH THE RADIATING ELEMENT AT THE DISTAL END OF THE ANTENNA. ENERGY IS PRODUCED AROUND THE RADIATING ELEMENT (BRACE, CHRISTOPHER L, 2010)	11
FIGURE 2. THE RADIATIVE TIP OF THE PROPOSED ANTENNA (PRESTON, ET AL., 2018).	20
FIGURE 3. (A) IMPEDANCE-MATCHED TRANSITION BETWEEN A TEFLON-FILLED AND AN AIR FILLED COAXIAL CABLE. TOPOLOGY OF (B) A MODIFIED CHOKE DIPOLE AND (C) A MODIFIED FLOATING SLEEVE DIPOLE IMPLEMENTED ON THE AIR-FILLED COAX SECTIONS. BLACK REPRESENTS METAL, GREY (LUYEN, HUNG, ET AL., 2017).....	21
FIGURE 4. ILLUSTRATION OF THE (A) ANTENNA TIP AND (B) GEOMETRY EMPLOYED FOR 2D COMPUTATIONAL MODEL (FALLAHI, HOJJATOLLAH, ET AL., 2017).	22
FIGURE 5. TOPOLOGY OF THE THREE STRUCTURES STUDIED IN THIS PAPER. YELLOW, GREY, AND WHITE REPRESENT TEFLON, COPPER, AND AIR, RESPECTIVELY. (A) AXISYMMETRIC MONOPOLE ANTENNA. (B) REFLECTED BACKED MONOPOLE ANTENNA (C) REFLECTOR BACKED SLOT MONOPOLE ANTENNA (MOHTASHAMI, YAHYA, ET AL., 2017).	23
FIGURE 6. TOPOLOGY OF THE INTERSTITIAL ANTENNA DESIGN WITH A SINGLE-SLOT TAPERED BALUN AND TWO ACTIVE SEGMENTS (LUYEN, ET AL., 2017).	24
FIGURE 7. TOPOLOGY OF THE INTERSTITIAL ANTENNA DESIGN WITH A DOUBLE-SLOT TAPERED BALUN AND THREE ACTIVE SEGMENTS (LUYEN, ET AL., 2017).	25
FIGURE 8. PROPOSED MWA ANTENNA CROSS SECTION AREA (TAL & LEVIATAN, 2017).	25
FIGURE 9. ANTENNA TOP AND SIDE SECTION (ALNASSAN, HUSSEIN, ET AL., 2014).	26
FIGURE 10. TOPOLOGY OF THE FLOATING SLEEVE DIPOLE ANTENNA USED IN ABLATION EXPERIMENTS. (A) SIDE VIEW. (B) CROSS-SECTIONAL VIEW (LUYEN, HUNG, ET AL., 2013; 2014).	27
FIGURE 11. SCHEMATIC DIAGRAM OF MULTI-SECTION FLOATING SLEEVE ANTENNA (MAINI, SURITA & MARWAHA, ANUPAMA, 2013).....	28
FIGURE 12. SIMULATED HEATING PATTERNS (TAJ-ELDIN, MOHAMMED & PRAKASH, PUNIT, 2014).	28
FIGURE 13. SCHEMATIC DIAGRAM OF MULTI-SECTION FLOATING SLEEVE ANTENNA (MAINI, 2016)	29
FIGURE 14. SCHEMATIC OF THE COAXIAL DIPOLE ANTENNA (MAINI, SURITA & MARWAHA, ANUPMA, 2012).	30
FIGURE 15. SCHEMATIC OF THE COAXIAL SLOT ANTENNA (MAINI, SURITA & MARWAHA, ANUPMA, 2012).	30

FIGURE 16. CLOSE-UP OF THE DESIGN OF THE RADIATING TIP THAT INCLUDES THE CHANNEL USED TO TRANSPORT BIOLOGICAL TISSUE OR INTRODUCE RADIOACTIVE PELLETS (HANCOCK, CHRIS P, ET AL., 2013).	31
FIGURE 17. 3D REPRESENTATION OF THE PROPOSED STRUCTURE (LIU, ET AL., 2017).....	32
FIGURE 18. GEOMETRY DESCRIPTION OF THE PROPOSED ANTENNAS. A) ONE SLOT ANTENNA, B) ONE SLOT CHOKED ANTENNA, C) TRANSVERSAL DESCRIPTION OF THE ANTENNA BODY, D) MODEL USED TO PREDICT THE OUTCOME WHEN BONE TISSUE IS IRRADIATED, E) MODEL USED TO PREDICT THE OUTCOME WHEN A MULTI-LAYER TISSUE IS IRRADIATED (LUJÁN, ET AL., 2017).....	33
FIGURE 19. GEOMETRIES USED TO MODEL THE MICRO-COAXIAL ANTENNAS. A) 2D AXISYMMETRIC VIEW OF THE 3D DOUBLE SLOT ANTENNA, B) 3D MODEL OF THE ANTENNA INSERTED IN THE BONE SECTION TO BE HEATED, AND AN EXAMPLE OF THE MESH USED FOR THE ANALYSES BASED ON THE FINITE ELEMENT (TRUJILLO-ROMERO, CJ, ET AL., 2017).	34
FIGURE 20. GEOMETRY USED TO MODEL THE MICRO-COAXIAL ANTENNA. A) 2DAXISYMMETRIC VIEW OF THE MICRO-COAXIAL ANTENNA WITH ONE SLOT AND ITS INSERTION IN BONE TISSUE, B) EXAMPLE OF THE MESH USED FOR THE ANALYSES BASED ON THE FINITE ELEMENT METHOD (MARTÍNEZ-VALDEZ, R., ET AL., 2017).....	35
FIGURE 21. (A) STRUCTURE OF COAXIAL ANTENNA (ALL UNITS IN MM), (B). HFSS SIMULATION OF ANTENNA (SAWARBANDHE, MAHESH D., ET AL., 2016).....	35
FIGURE 22. SCHEMATIC DIAGRAM OF A BREAST TISSUE WITH TUMOR (RAZIB, ALIMUL, ET AL., 2016).	36
FIGURE 23. MULTI-SLOT COAXIAL ANTENNA AND ITS MODEL INCLUDING THE ANTENNA DIMENSIONS (GAS & SZYMANIK, 2018).....	37
FIGURE 24. COPPER TUBE SLEEVE COAXIAL SPIRAL ANTENNA (MAINI & SHEKHAWAT, 2018).....	38
FIGURE 25. DETAIL OF A HELIX MODELLED IN SEMCAD X (VOJACKOVA, LUCIE, ET AL., 2014).	38
FIGURE 26. (A)TOPOLOGY OF THE PROPOSED HELICAL ANTENNA AND MATCHING SECTION. DARK GREY REPRESENTS COPPER, LIGHT GREY REPRESENTS TEFLON, AND WHITE REPRESENTS AIR. (B) EQUIVALENT CIRCUIT MODEL OF THE MATCHING SECTION (LUYEN, HUNG, ET AL., 2015; 2014).....	39
FIGURE 27. TOPOLOGY OF A BALANCED DIPOLE A) AND LOOP (B) ANTENNA FED WITH A SHIELDED TWO-WIRE LINE (LUYEN, HUNG T., ET AL., 2015).....	40
FIGURE 28. SCHEMATIC CROSS SECTIONS OF MONOPOLE, DIPOLE, TRI-AXIAL, CAP DISK AND TAPERED CAP ANTENNA DESIGNS FOR MICROWAVE ABLATION.....	41
FIGURE 29. SCHEMATIC CROSS SECTIONS OF CHOKED AND FLOATING SLEEVE COAXIAL SLOT ANTENNAS.....	41

FIGURE 30. SCHEMATIC CROSS SECTION OF SPIRAL AND HELICAL ANTENNA PRESENTED IN THE LITERATURE FOR TUMOUR ABLATION.....	42
FIGURE 31. EVOLUTION FROM (A) BROADBAND GRADUALLY TAPERED VOLCANO SMOKE THROUGH (B) INTERMEDIATE BANDWIDTH CONICAL ANTENNA TO (C) NARROW BANDWIDTH $\lambda/4$ MONOPOLE (JOHN & RONALD , 2002).	48
FIGURE 32. CONICAL MONOPOLE ANTENNA AND ITS RADIATION PATTERN IN BOTH ELEVATION (ON THE LEFT) AND AZIMUTH PLANES (ON THE RIGHT) (YEOH & ROWE, 2015).....	50
FIGURE 33. GEOMETRICAL REPRESENTATION OF PROPOSED TDFT ANTENNA.	52
FIGURE 34. DISTRIBUTION OF THE ELECTRIC CURRENT SHEET ALONG THE CIRCUMFERENTIAL LENGTH OF TDFT ANTENNA WHEN IMMERSSED IN BIOLOGICAL TISSUE.	71
FIGURE 35. DISTRIBUTION OF THE MAGNITUDE OF THE ELECTRIC CURRENT SHEET ALONG THE CIRCUMFERENTIAL LENGTH OF TDFT ANTENNA WHEN IMMERSSED IN BIOLOGICAL TISSUE	71
FIGURE 36. 3D GRID REPRESENTATION OF TDFT ANTENNA STRUCTURE IN MATLAB.	72
FIGURE 37. NEAR-FIELD PATTERNS ON A SPHERE OF RADIUS 4.6 CM CENTERED AT THE LOCATION OF TDFT ANTENNA WHEN IMMERSSED IN EGG-WHITE ($\epsilon_r=56, \sigma=10$) AT 7.3 GHZ IN THE ELEVATION AND AZIMUTH PLANES.	74
FIGURE 38. 3D NEAR FIELD DISTRIBUTION ON A SPHERE OF RADIUS 4.6 CM CENTERED AT THE LOCATION OF TDFT ANTENNA WHEN IMMERSSED IN EGG-WHITE ($\epsilon_r=56, \sigma=10$) AT 7.3 GHZ.....	74
FIGURE 39. NEAR-FIELD PATTERNS ON A SPHERE OF RADIUS 4.6 CM CENTERED AT THE LOCATION OF TDFT ANTENNA WHEN IMMERSSED IN TUMOUR TISSUE ($\epsilon_r = 46, \sigma = 8.16$) AT 7.3 GHZ IN THE ELEVATION AND AZIMUTH PLANES.....	75
FIGURE 40. 3D NEAR FIELD DISTRIBUTION ON A SPHERE OF RADIUS 4.6 CM CENTERED AT THE LOCATION OF TDFT ANTENNA WHEN IMMERSSED IN TUMOUR MODEL ($\epsilon_r = 46, \sigma = 8.16$) AT 7.3 GHZ.	75
FIGURE 41. 3D NEARFIELD DISTRIBUTION ON THE LEFT AND NEARFIELD PATTERNS ON A SPHERE OF RADIUS 4.6 CM CENTERED AT THE LOCATION OF TDFT ANTENNA WHEN IMMERSSED IN KIDNEY TISSUE MODEL ON THE RIGHT ($\epsilon_r = 44.368.5, \sigma = 7.8275$) AT 7.3 GHZ IN THE ELEVATION AND AZIMUTH PLANES.....	77
FIGURE 42. 3D NEARFIELD DISTRIBUTION ON THE LEFT AND NEARFIELD PATTERNS ON A SPHERE OF RADIUS 4.6 CM CENTERED AT THE LOCATION OF TDFT ANTENNA WHEN IMMERSSED IN HEART TISSUE MODEL ON THE RIGHT ($\epsilon_r = 46.5, \sigma = 7.892$) AT 7.3 GHZ IN THE ELEVATION AND AZIMUTH PLANES.	77

FIGURE 43. 3D NEARFIELD DISTRIBUTION ON THE LEFT AND NEARFIELD PATTERNS ON A SPHERE OF RADIUS 4.6 CM CENTERED AT THE LOCATION OF TDFT ANTENNA WHEN IMMERSERD IN GLANDULAR BREAST TISSUE MODEL ON THE RIGHT ($\epsilon_r = 49.6, \sigma = 7.89$) AT 7.3 GHZ IN THE ELEVATION AND AZIMUTH PLANES.	78
FIGURE 44. 3D NEARFIELD DISTRIBUTION ON THE LEFT AND NEARFIELD PATTERNS ON A SPHERE OF RADIUS 4.6 CM CENTERED AT THE LOCATION OF TDFT ANTENNA WHEN IMMERSERD IN CANCELLOUS BONE TISSUE MODEL ON THE RIGHT ($\epsilon_r = 14.294, \sigma = 2.776$) AT 7.3 GHZ IN THE ELEVATION AND AZIMUTH PLANES.	78
FIGURE 45. 3D NEARFIELD DISTRIBUTION ON THE LEFT AND NEARFIELD PATTERNS ON A SPHERE OF RADIUS 4.6 CM CENTERED AT THE LOCATION OF TDFT ANTENNA WHEN IMMERSERD IN CORTICAL BONE TISSUE MODEL ON THE RIGHT ($\epsilon_r = 9.0531, \sigma = 1.515$) AT 7.3 GHZ IN THE ELEVATION AND AZIMUTH PLANES.	79
FIGURE 46. 3D SCHEMATIC REPRESENTATION OF THE PROPOSED TDFT ANTENNA DESIGN.	81
FIGURE 47. SYNTHESIS OF TEARDROP LIKE STRUCTURE BY ETCHING THE OUTER SURFACE OF A SOLID CONE.	84
FIGURE 48. RETURN LOSS CHARACTERISTICS (S_{11}) OF THE TDFT ANTENNA LOADED IN LIVER.	86
FIGURE 49. RETURN LOSS CHARACTERISTICS (S_{11}) OF THE TDFT ANTENNA LOADED IN 0.9% SALINE.	87
FIGURE 50. VOLTAGE STANDING WAVE RATIO (VSWR) OF THE PROPOSED TDFT ANTENNA IN LIVER TISSUE.	87
FIGURE 51. CURRENT DENSITY ALONG TDFT STRUCTURE, INNER AND OUTER CONDUCTOR OF THE ENTIRE ANTENNA.	88
FIGURE 52. COMPARISON BETWEEN CURRENT DISTRIBUTIONS ON THE OUTER CONDUCTOR OF THE COAXIAL FEED OF TEARDROP STRUCTURE WITH AND WITHOUT EMBEDDED CHOKE.	88
FIGURE 53. 3D NEAR FIELD DISTRIBUTION OF TDFT ANTENNA IN LIVER.	89
FIGURE 54. NEAR-FIELD RADIATION PATTERNS OF THE PROPOSED TDFT AT 7.3 GHZ IN BOTH AZIMUTH AND ELEVATION PLANES.	90
FIGURE 55. DISTRIBUTION OF SAR ALONG CENTRAL AXIS OF THE TDFT ANTENNA.	91
FIGURE 56. TRANSVERSE SLICE OF SAR VALUES ACROSS THE TDFT STRUCTURE.	92
FIGURE 57. SAR DISTRIBUTION ALONG THE CENTRAL AXIS OF THE TDFT ANTENNA.	92
FIGURE 58. SAR DISTRIBUTION AT A DISTANCE PERPENDICULAR TO THE CENTRAL AXIS OF THE ANTENNA THROUGH THE MIDPOINT OF TEARDROP STRUCTURE.	93

FIGURE 59. RETURN LOSS OF TDFT ANTENNA INSERTED IN TUMOUR TISSUE SURROUNDED BY HEALTHY LIVER TISSUE.	94
FIGURE 60. VSWR OF TDFT ANTENNA INSERTED IN TUMOUR TISSUE OF LIVER.	95
FIGURE 61. CURRENT DISTRIBUTIONS ALONG TDFT ANTENNA AND OUTER CONDUCTOR OF THE COAXIAL CABLE.	95
FIGURE 62. 3D PLOT OF NEARFIELD PATTERN OF TDFT ANTENNA LOADED IN LIVER TUMOUR.	96
FIGURE 63. NEAR-FIELD RADIATION PATTERNS OF TDFT ANTENNA LOADED IN TUMOUR TISSUE AT 7.3 GHZ IN BOTH AZIMUTH AND ELEVATION PLANES.	96
FIGURE 64. DISTRIBUTION OF SAR ALONG CENTRAL AXIS OF THE TDFT ANTENNA WITHIN TUMOUR MODEL.	97
FIGURE 65. TRANSVERSE SLICE ILLUSTRATING SAR VALUES THROUGH THE MIDPOINT OF TEARDROP STRUCTURE.	98
FIGURE 66. SAR VALUES IN THE VICINITY ALONG THE LENGTH OF THE TEARDROP STRUCTURE.	98
FIGURE 67. SAR VALUES ALONG A DISTANCE THROUGH THE MIDPOINT OF THE TEARDROP STRUCTURE.	99
FIGURE 68. SAR VALUES VERSUS DISTANCE THROUGH THE MIDPOINT OF TDFT STRUCTURE FOR DIFFERENT POWER LEVELS.	100
FIGURE 69. SAR VALUES VERSUS AXIAL DISTANCE THROUGH TDFT ANTENNA LENGTH FOR DIFFERENT POWER LEVELS.	100
FIGURE 70. THE SCHEMATIC OF HFSS - ANSYS WORKBENCH LINK ANALYSIS.	102
FIGURE 71. STEADY-STATE TEMPERATURE LEVELS THROUGH HORIZONTAL AND VERTICAL CUTS WITHIN THE TUMOUR MODEL.	103
FIGURE 72. STEADY-STATE TEMPERATURE LEVELS IN THE SURROUDING HEALTHY LIVER MODEL. .	103
FIGURE 73. TEMPERATURE DISTRIBUTION IN HORIZONTAL CUT FOR DIFFERENT TIME DURATIONS 5, 15, 30 AND 60 SECS.	104
FIGURE 74. TEMPERATURE DISTRIBUTION IN VERTICAL CUT FOR DIFFERENT TIME DURATIONS 5, 15, 30 AND 60 SECS.	104
FIGURE 75. TEMPERATURE DISTRIBUTION IN TRANSVERSE CUT FOR DIFFERENT TIME DURATIONS 5, 15, 30 AND 60 SECS IN THE SURROUNDING LIVER MODEL.	106
FIGURE 76. TEMPERATURE DISTRIBUTION IN LONGITUDINAL CUT FOR DIFFERENT TIME DURATIONS 5, 15, 30 AND 60 SECS IN THE SURROUNDING LIVER MODEL.	107
FIGURE 77. SIDE VIEW OF TDFT ANTENNA.	110

FIGURE 78. STEADY STATE TEMPERATURE DISTRIBUTION OF CONE LENGTHS 10.235, 11.065, 12 AND 14 MM FOR INPUT POWER OF 2W.....	112
FIGURE 79. STRUCTURE OF THE NEW TDFT ANTENNA.....	113
FIGURE 80. RETURN LOSS OF TDFT ANTENNA LOADED IN TUMOUR MODEL.	114
FIGURE 81. VSWR OF TDFT ANTENNA LOADED IN TUMOUR MODEL	114
FIGURE 82. CURRENT DISTRIBUTIONS ALONG THE LENGTH OF TDFT STRUCTURE AND THE OUTER CONDUCTOR OF THE COAXIAL CABLE AT 7.3 GHZ.....	115
FIGURE 83. 3D PLOT OF NEARFIELD OF TDFT ANTENNA.....	115
FIGURE 84. NEAR-FIELD RADIATION PATTERNS OF TDFT ANTENNA LOADED IN TUMOUR TISSUE AT 7.3 GHZ IN BOTH AZIMUTH AND ELEVATION PLANES.	116
FIGURE 85. SAR DISTRIBUTION ALONG THE ANTENNA AXIS.	117
FIGURE 86. SAR VALUES IN TRANSVERSE SLICE CUT THROUGH THE MIDPOINT OF THE TEARDROP STRUCTURE.	117
FIGURE 87. AVERAGE SAR IS ALSO OBSERVED VERSUS THE DISTANCE ALONG THE CENTRAL AXIS OF ANTENNA.	118
FIGURE 88. SAR VERSUS DISTANCE PERPENDICULAR TO ANTENNA AXIS AT THE MIDPOINT OF THE TEARDROP STRUCTURE.....	118
FIGURE 89. TEMPERATURE DISTRIBUTION IN VERTICAL AND HORIZONTAL CUTS THROUGH TUMOUR MODEL.	119
FIGURE 90. TEMPERATURE DISTRIBUTION IN VERTICAL AND HORIZONTAL CUTS THOUGH TUMOUR MODEL	120
FIGURE 91. TEMPERATURE ON THE SURFACE OF THE OUTER CONDUCTOR OF THE COAXIAL CABLE.	121
FIGURE 92. TRANSIENT THERMAL ANALYSIS IN HORIZONTAL CUT THROUGH TUMOUR MODEL AT DIFFERENT TIME INTERVALS 30, 60, 120 AND 180 SECS.....	122
FIGURE 93. TRANSIENT THERMAL ANALYSIS IN VERTICAL CUTS THROUGH TUMOUR MODEL AT DIFFERENT TIME INTERVALS 30, 60, 120, 180 SECS.	123
FIGURE 94. TRANSIENT THERMAL DISTRIBUTION IN HORIZONTAL CUT IN THE SURROUNDING LIVER MODEL AT DIFFERENT TIME INTERVALS 60, 120 AND 180 SECS.	124
FIGURE 95. TRANSIENT THERMAL DISTRIBUTION IN VERTICAL CUT IN THE SURROUNDING LIVER MODEL AT DIFFERENT TIME INTERVALS 60, 120 AND 180 SECS.	124
FIGURE 96. TRANSIENT THERMAL ANALYSIS ON THE OUTER CONDUCTOR OF THE COAXIAL CABLE DURING THE ABLATION PROCESS AT DIFFERENT TIME INTERVALS 30, 60, 120, 180 SECS.....	125

FIGURE 97. S ₁₁ RESULTS OF TDFT ANTENNA IN EGG WHITE.....	127
FIGURE 98. NEARFIELD PATTERN OF TDFT ANTENNA LOADED IN EGG WHITE MODEL.	127
FIGURE 99. STEADY STATE TEMPERATURE WITHIN TUMOUR MODEL FOR 3W INPUT POWER.	129
FIGURE 100. STEADY STATE TEMPERATURE WITHIN TUMOUR MODEL FOR 4W INPUT POWER.	129
FIGURE 101. STEADY STATE TEMPERATURE DISTRIBUTION WITHIN TUMOUR MODEL FOR 5W INPUT POWER.....	129
FIGURE 102. TEMPERATURE DISTRIBUTION IN THE SURROUNDING TISSUES INDICATING SAFETY MARGIN ACHIEVED FOR EACH POWER LEVEL.....	130
FIGURE 103. TOTAL ABLATED VOLUME ATTAINED BASED ON 60°C CONTOUR FOR EACH POWER LEVEL.	131
FIGURE 104. TEMPERATURE DISTRIBUTION ALONG THE OUTER CONDUCTOR OF THE COAXIAL CABLE FOR DIFFERENT INPUT POWER.....	131
FIGURE 105. TRANSIENT THERMAL ANALYSIS AT DIFFERENT TIME INTERVALS (60, 120 AND 180 SECS) FOR INPUT POWER OF 3, 4 AND 5 W THROUGH HORIZONTAL CUT WITHIN TUMOUR MODEL.	133
FIGURE 106. TRANSIENT THERMAL ANALYSIS AT DIFFERENT TIME INTERVALS (60, 120 AND 180 SECS) FOR INPUT POWER OF 3, 4 AND 5 W THROUGH VERTICAL CUT WITHIN TUMOUR MODEL.	134
FIGURE 107. TEMPERATURE GRADIENT WITHIN TUMOUR MODEL FOR EACH INPUT POWER.	135
FIGURE 108. GEOMETRICAL REPRESENTATION OF ABLATED VOLUME.....	136
FIGURE 109. THE ORIGINAL AND MODIFIED COPPER STRUCTURE OF TDFT ANTENNA.....	138
FIGURE 110. THE FABRICATED PROTOTYPE OF TDFT ANTENNA AND ITS DIELECTRIC PFTE SHIELD.	139
FIGURE 111. HOLLOW METALLIC PIN USED TO HOLD BOTH ANTENNA TIP AND THE INNER CONDUCTOR OF THE COAXIAL CABLE.	139
FIGURE 112. FULLY ASSEMBLED PROTOTYPE OF TDFT APPLICATOR CONNECTED TO THE COAXIAL CABLE.	140
FIGURE 113. EXPERIMENTAL SETUP AND VERIFICATION OF REFLECTION FOR TDFT ANTENNA IN BOVINE LIVER SAMPLE.	141
FIGURE 114. EXPERIMENTAL SETUP AND VERIFICATION OF REFLECTION FOR TDFT ANTENNA IN EGG- WHITE SOLUTION.....	141
FIGURE 115. COMPARISON BETWEEN SIMULATED AND MEASURED S ₁₁ OF TDFT ANTENNA IN BOVINE LIVER SAMPLE.	142
FIGURE 116. COMPARISON BETWEEN SIMULATED AND MEASURED S ₁₁ OF TDFT ANTENNA IN EGG- WHITE SOLUTION.....	142

FIGURE 117. MICROWAVE GENERATION EQUIPMENT AND EXPERIMENTAL SETUP OF ABLATION IN EGG-WHITE SOLUTION.	143
FIGURE 118. SNAPSHOTS OF THE ABLATED VOLUME OF TDFT ANTENNA IN EGG-WHITE SOLUTION AT DIFFERENT TIME INTERVALS.	144
FIGURE 119. STEADY-STATE TEMPERATURE DISTRIBUTION OF TDFT ANTENNA IN EGG-WHITE MODEL.	145
FIGURE 120. A CLOSE-UP OF SOLIDIFIED WHITE MASS OF EGG-WHITE SOLUTION DEMONSTRATING A COMPLETE ABLATION.	145
FIGURE 121. MICROWAVE GENERATION EQUIPMENT AND EXPERIMENTAL SETUP OF LIVER ABLATION.	146
FIGURE 122. A CLOSE-UP OF TDFT ANTENNA INSERTED IN LIVER SAMPLE AND A SAMPLE PUNCTURED AFTER 90-MIN ABLATION EXPERIMENT.	147
FIGURE 123. TOTAL ABLATED LESION ACHIEVED FOR 15, 30- AND 90-MIN ABLATION EXPERIMENT.	148
FIGURE 124. TRANSIENT THERMAL PROFILE OF TDFT ANTENNA THROUGH HORIZONTAL AND VERTICAL CUTS WITHIN LIVER MODEL FOR 300 SECS AND 600 SECS AT 1W INPUT POWER.	149

List of Tables

TABLE 1. COMPARISON BETWEEN RF AND MICROWAVE ABLATION TREATMENT ACCORDING TO ORGAN SPECIFIC CONSIDERATION.....	10
TABLE 2. COMPARISON BETWEEN ANTENNA DESIGNS PROPOSED IN LITERATURE.....	43
TABLE 3. DIELECTRIC AND THERMAL PROPERTIES OF BIOLOGICAL TISSUES AT 7.3 GHZ.....	76
TABLE 4. ELECTRICAL PROPERTIES OF LIVER TISSUE AND 0.9% SALINE AT 7.3 GHZ.	85
TABLE 5. PHYSICAL PARAMETERS OF THE TDFT ANTENNA	86
TABLE 6. MATERIAL THERMAL PARAMETERS USED IN NUMERICAL SIMULATION.	91
TABLE 7. DIELECTRIC PROPERTIES OF HEALTHY LIVER TISSUE AND MALIGNANT TUMOUR TISSUE AT 7.3 GHZ	94
TABLE 8. THERMAL CHARACTERISTICS OF HEALTHY AND MALIGNANT OF LIVER	97
TABLE 9. PARAMETRIC STUDY OF DIFFERENT CONE RADIUS AND LENGTHS VERSUS REFLECTION ATTAINED AT 7.3 GHZ	110
TABLE 10. STUDY OF DIFFERENT CONE LENGTHS WITH CORRESPONDING REFLECTION AND MAXIMUM SAR VALUE ATTAINED.....	111
TABLE 11. NEW DIMENSIONS OF TDFT ANTENNA AND COAXIAL CABLE.....	113
TABLE 12. DIELECTRIC AND THERMAL PROPERTIES OF EGG-WHITE IMPORTED IN NUMERICAL SIMULATION.....	126
TABLE 13. RADII OF ABLATED VOLUME AT DIFFERENT TIME INTERVAL FOR EACH INPUT POWER .	136
TABLE 14. VOLUME OF THE ABLATED LESION IN CM ³ FOR DIFFERENT INPUT POWER AT DIFFERENT TIME INTERVALS.....	137
TABLE 15. TDFT ANTENNA PARAMETERS VERSUS MOST COMMONLY USED MICROWAVE APPLICATORS IN CANCER ABLATION.....	151
TABLE 16. ASSESSMENT OF TDFT ANTENNA PERFORMANCE COMPARED TO PREVIOUSLY PROPOSED DESIGNS IN LITERATURE	152

Acknowledgement

I would like to express my deepest appreciation and gratitude to my supervisor Professor Haifa Takruri for her great support, constant guidance and continuous encouragement whom without which this work wouldn't have seen the light.

I am very grateful to Eng. Aiden Dunber at the Maker Space in university of Salford for his interest, priceless recommendations and contribution in managing the fabrication process.

I would like to acknowledge the role of the Arab Academy for Science, Technology and Maritime Transport which supported and sponsored me during my Ph.D. study. Special thanks to Dr. Amira Zaki, my local advisor, for her patience and support during the hardest times of my Ph.D. journey.

I also would like to express my unquestionable gratitude to Prof. Khalid Hussein and Dr. Asmaa El-Sayed in National Institute of Research in Cairo, Egypt for their dedication, guidance, long daunting teaching hours of this work.

Finally, I would like to express my ultimate tribute to my mother, my sister and my brother for their undeniable support, patience, understanding and sacrifice during the many hours of this daunting work.

Sincerely,

Eman Hassan

Publications

Hassan, E., Takruri, H., Zaki , A., and Hope, M. (2018). Investigation of Tear Drop Flared Tipped Antenna for Therapeutic Microwave Ablation. 2018 11th IEEE/ IET International Symposium on Communication Systems & Networks Digital Signal Processing (CSNDSP) (CSNDSP18). Budapest, Hungary.

Hassan, E., Takruri-Rizk, H., and Hope, M. (2016). Applicator design considerations of microwave tumor ablation. 2016 10th IEEE/IET International Symposium on Communication Systems, Networks and Digital Signal Processing (CSNDSP) (pp. 1-6). Prague, Czech Republic.

List of Abbreviations

RF	Radio Frequency
MW	Microwave Frequency
SAR	Specific Absorption Rate
TDFT	Tear Drop Flared Tipped Antenna
CT	Computer Tomography
MRI	Magnetic Resonance Imaging
FUS	Focused Ultra Sound
DC	Direct Current
ISM	Industrial Scientific Medical Frequency Bands
EM	Electromagnetic Waves
nsPEF	Nanosecond Pulsed Electric Fields
CD	Choked Dipole
FSD	Floating Sleeve Dipole
OD:	Outer Diameter
ID	Inner Diameter
VSWR	Voltage Standing Wave Ratio
SWR	Standing Wave Ratio
FEM	Finite Element Method
HIFUS	High Intensity Focused Ultra Sound
LCA	Largest Cell Ablation Zone
HFSS	High Frequency Structural Simulator
UWB	Ultra-Wide Band
VSA	Volcano Smoke Antenna
FBW	Fractional Bandwidth
PEC	Perfect Electric Conductor

Abstract

The development of therapeutic thermal ablative techniques become viable alternative method to treat patients who cannot be treated by surgery because of high surgical risk or unfavourable tumour location. Microwave ablation is the least invasive technique recently developed for cancer treatment because of its low cost, smaller antenna size and shorter recovery time. However, there are shortcomings of microwave ablation therapy needed to be fulfilled. Unsuccessfully ablated tumour and destruction of large portion of surrounding healthy tissues due to usage of exceptionally high input power which yields lack of control over heating encountered with previously proposed applicator designs. This work investigates the efficacy of using low power ultra-wide band (UWB) microwave applicator in cancer ablation. A novel Tear Drop Flared tipped (TDFT) antenna was proposed as microwave applicator for treating focal malignant tumours using low input power by the means of directed axial radiation. TDFT antenna is modelled and analysed in different surroundings such as saline, healthy and malignant tissue models. Semi-analytical numerical model is introduced to calculate current distributions required on antenna and consequent near-field distribution for achieving homogenous heating conformal to the targeted lesion to overcome nonuniform field distribution of omni-directional radiation. Electromagnetic simulations showed that TDFT antenna achieved minimum reflection stability of -25.89 dB over ultra-wide bandwidth. Electromagnetic and thermal simulations proved that directed axial radiation within targeted lesion produce confined uniform heating at significantly low input power. Moreover, 60 °C temperatures were attained for successful ablation and provided more control over heating within the targeted lesion. Highest SAR value attained of 967.3 W/kg for only 3W input power. Thermal analysis revealed that TDFT antenna can achieve a successful ablation of spherical cancerous lesions of diameters of 15.5 mm in 3 minutes for input power of 3W. TDFT antenna was fabricated and tested in egg-white solution and bovine liver. A good agreement between the measured and simulated results were observed where overall efficiency of 99.99% was recorded at the operating frequency. Ablation experiments were conducted in egg-white solution and bovine liver for 1W input power. Feasibility of TDFT antenna as a microwave coagulator was clearly observed in creating confined heating manifested in ablated lesions of 16×19.5×19.5 mm³ for 15-min ablation. Highly-directed End-fire radiation of TDFT antenna noticeably achieves confined heating that facilitates using only 60% of the lowest input power recorded in literature to attain successful ablation in standard radiation exposure time of 15 mins. This reduces power consumption of microwave applicator by almost 40% of the lowest input power used in literature.

Chapter One

Introduction and Background of Cancer Treatment Techniques

1.1. Background on Cancer Treatment Techniques

Cancer is the uncontrolled growth and spread of cells. It can affect almost any part of the body for example lung, liver, kidney, breast and bones. Therefore, it is desirable to remove the cancer from the human body as soon as possible. Cancer causes 1 in 8 deaths worldwide and is rapidly becoming a global pandemic. The global cancer burden is expected to nearly double to 21.4 million cases and 13.5 million deaths by 2030 (Siegel, et al., 2015).

Treatment options for cancer patients include surgical resection, chemotherapy, radiation therapy, transplantation and tumour ablation techniques. Surgical resection is considered the gold standard treatment option for cancer patients. However, it is limited for patients with early stage cancer and ineffective for treating metastasis stage where cancer cells have grown into blood vessels and produce cancer recurrence in other part of the body. Surgical resection is also not an option for patients with too spread cancer cells as it might hinder the functional capability of the organ after the operation (Petrich-Munzinger, et al., 2014). In addition, only small percentage of patients with metastasis tumours are amenable to surgical resection due to high surgical risk or un-favourable tumour location. Eligibility of organ transplant for cancer patients depends on finding the suitable organ donor which is not always possible. Chemotherapy is not suitable for treating selected tumour tissues within the body and it comes at the expense of damaging large portion of healthy tissues (Kassner, 2000). Radiation therapy uses high energy levels to kills the cancer cells by destroying their DNA but on the other hand, it destroys the DNA of healthy tissues surrounding the tumour (Bentzen, 2006). All the treatments mentioned measures prove to be ineffective as the tumour can reoccur in the patients in any part of their body which is called cancer metastasis. (Thongsopa & Thosdeekoraphat, 2013).

Such limitations give rise to the development of thermal ablative techniques to be less invasive more effective in eradicating tumours that cannot be treated using the conventional treatment options. The main purpose of ablative treatments is the ability to treat patients who cannot be treated through surgery, resection or any other means as there is high surgical risk, or un-favourable tumour location. Sometimes, these treatments are also used in patients waiting for organ transplant or during surgery to be sure the treatment aimed at the right place.

Ablation refers to the method of selectively killing a well-defined target tissue by the application of heat based (radiofrequency ablation and microwave ablation), cold (cryotherapy), chemicals

(percutaneous ethanol injection), or laser hyperthermia techniques directly to a tumour causing cell death.

The most common cancers treated by thermal tumour ablation are liver, lung, kidney (renal) and bone cancers. Ablative treatments typically do not require a hospital stay and more than 90% of patients are released from the hospital the day after the procedure. Ablation is an image guided treatment which refers to the method of killing selectively targeted tumour tissues by the application of heat-based therapy such as Radio frequency ablation, microwave ablation, cold based therapy (Cryo-ablation), focused ultrasound ablation and Laser ablation and direct current catheter ablation. Each of these techniques work in different ways in order to eradicate tumour tissues with saving as much surrounding healthy tissues as possible, all while maintaining minimally invasive and relatively less painful procedure to the patient. Ablation can be performed in open surgery using a catheter based applicator or percutaneously by inserting a needle or probe - which is called applicator - into the tumour through the skin. This requires only a tiny hole, usually less than 3 mm via which the probe is introduced (McGahan & Raalte, 2005; Kaur & Maini, Surita, 2014). Ultrasound, Computer Tomography (CT) scanning or Magnetic Resonance Imaging (MRI) are used to guide the needle or the probe into the tumour (Vrba Jr, Jan & Vrba, David, 2014). When the probe is within the cancer, it is connected to a generator which provide the required power to “burn” or “freeze” the cancer. “Burning” refers to increasing the temperature of the tumour to such a level that causes internal coagulation which results in cell death. This is usually achieved by radio or microwave frequency probes, referring to the type of energy used to increase the tissue temperature. “Freezing” refers to Cryo-ablation which decreases the temperature to -75 °C which also kills the cancer cells.

Thermal ablation is not only limited to treat cancer patients, but also has a numerous beneficial clinical effects for example, it is used to provide an efficient means for coagulating vessels to stop bleeding during open surgery or carefully eradicate tissues that may not be cancerous e.g. cardiac arrhythmias, prostatic hypertrophy and varicose veins (Prasantamrongsiri, S, et al., 2012; Suseela, Sreekala, et al., 2013; Rosen, Arye, et al., 2002).

Both RF and microwave-based tumour ablation techniques are used to ablate tissue by heating it to cytotoxic temperatures. Temperatures in excess of 60 °C are known to cause relatively instantaneous cell death, while temperatures from 50-60 °C will induce coagulation and cell death in a matter of minutes, depending upon temperature, previous thermal injury (Brace, 2009).

Despite both RF and microwave energy can heat tissue to cytotoxic levels, the mechanisms of RF and microwave heating are quite different and must be considered for ablation of different tissue types.

1.2. Overview on Types of Tumour Ablation Techniques

1.2.1. Cryo-ablation

It is the oldest method of thermal ablation, utilizes nitrogen or argon gas flowing through a cryo-probe to create extremely cold temperatures as low as -75°C (NG, et al., 2003). Living tissues including both healthy and un-healthy cannot survive in such low temperatures and will cause cell death. The limitations encountered in Cry-ablation are small lesion size and the time required to attain adequate results. The long time required for such operation is due series of repeatedly freezing the targeted tumour tissue to assure the unhealthy tissues are completely destroyed (Rubinsky, 2000).

1.2.2. Focused Ultra Sound (FUS) Ablation

FUS ablation technique utilizes both low and high intensity Ultra-Sound for Imaging and increasing the tumour tissue temperature (i.e. between 60°C to 100°C using frequency ranges from 2 to 20 MHz) (Habash, et al., 2007; Zhou, 2011), respectively. This technique requires no incision and Ultra-Sound energy will travel through the body to the targeted tissue for ablation. The main drawbacks of FUS are the high attenuations found due to the existence of bones within the body in addition sharp focus of energy requires longer ablation time for larger tumour size.

1.2.3. Laser Ablation

Laser ablation utilizes fibre-optic probe as an applicator to deliver Laser energy pulses which heat and evaporate the targeted tissue (McGahan & Raalte, 2005; Pacella, et al., 2016; Schwartzberg, et al., 2016; Leuthardt, et al., 2016). Laser ablation is considered one of the most expensive treatment options for tissue ablation which is one of its major drawbacks. In addition, laser penetration through blood hinders the use of Laser for tissue ablation.

1.2.4. Direct Current (DC) catheter ablation

It utilizes catheter to deliver a direct current from defibrillator to generate an electric shock in the targeted area (McRury & Haines, 1996; Friberg, et al., 2016; Wonnell, et al., 1992). The high levels of applied voltage are very difficult to control and may cause extensive damage to the surrounding healthy tissues. This technique was eventually developed and replaced by radiofrequency ablation to provide more controlled of the amount of energy delivered to the targeted area.

1.2.5. Radio Frequency (RF) Ablation

RF ablation is the most commonly used technique for tissue ablation due to its safety, effectiveness. Its mechanism is similar to DC catheter ablation but with different energy source. The key of RF ablation is electrical conduction through the tissue where a complete electrical circuit is created through the body. The most common frequencies used in RF ablation are 13.56 and 27.12 MHz according to Industrial, Scientific, and Medical (ISM) frequencies. RF current is able to pass through tissue because of the abundance of ionic fluid present; however, tissue is not a perfect conductor and RF current causes resistive heating. The most important tissue properties in RF ablation are electrical and thermal conductivity which describe how quickly heat can be transferred to the surrounding tissues. Tissue impedance is inversely proportional to conductivity and increased rapidly with the increase in tissue temperature during RF ablation procedure which hinders RF current to pass through tissues heated to 100°C because the water needed for ion flow is boiled off (Tacke, et al., 2004; Lee, et al., 2003; Chou, 1995; Pop, Mihaela, et al., 2010; Liu, Zhengjun, et al., 2006; Solazzo, et al., 2005; Lee, et al., 2003; Hancock, et al., 2015). The major disadvantage of RF ablation that it depends on the electrical current passing through the complete circuit formed by RF probe, tissue and ground pads attached to the skin which limits its use of only one probe. In addition, the increase in tissue impedance as the temperature increases hinders the current passing through the targeted tissue and decays the power rate during the procedure. Moreover, the resistive heating of the ground pads due to the increase in the impedance may result in skin burns and discomfort of the patient after the procedure (Gananadha, Sivakumar & Morris, David Lawson, 2004; Goldberg, S Nahum, et al., 1996; Goldberg, SN, et al., 1998; Hines-Peralta, Andrew, et al., 2006).

1.2.6. Microwave Ablation

The limitations and shortcomings of aforementioned tissue ablation techniques necessitate the investigation of an alternative technique to maintain high success rate while reducing the complications and limitations of tissue ablation. Microwave (MW) ablation is a special case of dielectric heating, where the dielectric material is the targeted tissue. Dielectric heating occurs when an alternating electromagnetic (EM) field is applied to an imperfect dielectric material. In tissue, heating occurs because the EM field forces water molecules in the tissue to oscillate out of phase in attempt to align with the applied EM waves which increases the internal kinetic energy elevating the tissue temperature. Heat transfer in biological tissues and the conversion of microwave energy into thermal energy is described by Bio-Heat equation as in (1) (Hancock, et al., 2015; PENNES, 1949)

$$\rho c \frac{\partial T}{\partial t} = \nabla \cdot k \nabla T + J \cdot E - h_{bl}(T - T_{bl}) - Q_{el} + Q_m, \quad (1)$$

$$h_{bl} = \rho_{bl} c_{bl} \omega_{bl},$$

Where ρ : Tissue density [kg/m^3], c : Specific heat capacity [$\text{J}/\text{kg}\cdot\text{K}$], k : Thermal conductivity [$\text{W}/\text{m}\cdot\text{K}$], $J \cdot E$: Current density [A/m^2], E : Electric Field intensity [V/m], T_{bl} : blood temperature [K], ρ_{bl} : blood density [kg/m^3], c_{bl} : Blood specific heat capacity [$\text{J}/\text{kg}\cdot\text{K}$], ω_{bl} : blood perfusion rate [s^{-1}], h_{bl} : heat transfer coefficient due to blood perfusion [W/m^3], Q_m : energy generated by the metabolic process [J] and Q_{el} : electromagnetic energy transferred between the applicator and tissue [W/m^3].

The term $J \cdot E$ in (1) represents the energy deposited by the applicator and converted into heat. The criterion to measure the energy absorbed by a living tissue when exposed to electromagnetic radiation is the Specific Absorption Rate (SAR). SAR indicates the absorbed power per mass of a living tissue to determine the heating ability of microwave antenna and can be calculated in (2).

$$SAR = \frac{J \cdot E}{\rho} = \frac{\sigma \cdot E^2}{\rho}, [\text{W}/\text{kg}] \quad (2)$$

Microwave heating occurs in a volume around the applicator and unlike RF energy, microwaves require no electrically conductive path for propagation, and it can pass through and heat tissues at any temperature or any water content. A common measure used to describe how efficiently a

material will absorb microwave energy is effective conductivity where high conductivity tissues (high water content) readily absorb microwaves, while low conductivity tissues (low water content) allow microwave propagation. The most commonly frequencies used in microwave ablation are 433, 915, and 2450 MHz according to ISM frequencies (Hancock, et al., 2015; Luyen, Hung, et al., 2014; Luyen, Hung, et al., 2014; Luyen, et al., 2013; Muheremu & Niu, 2014). Microwave ablation requires the application of powerful hardware and specialized software which allow predicting the heating rate in a biological tissue near the radiating element of a needle-like applicator and several simplified approaches were proposed to calculate the coupled electromagnetic heat transfer into the tumour tissue including the numerical solution of Bio-heat equation. The relative permittivity and conductivity of biological tissues are dependent on water content and temperature levels. Furthermore, the variation of dielectric and thermal properties of biological tissues during ablation are frequency dependent. Numerically modeling the frequency dependent properties of living tissue is accomplished using multi-pole Cole-Cole model in a large frequency range (Gabriel, et al., 1996; Gabriel, et al., 1996; Schwan & Li, 1955; Brandy, et al., 1981; Stuchly, et al., 1981; López, et al., 2015; Farina, et al., 2015; Wright, AS, et al., 2001). Moreover, the penetration depth of microwave field into tissue is dependent on the relative permittivity and conductivity of targeted tissue. Penetration depth, δ , of an electromagnetic field is defined as the distance required for the electric field of a plane wave to attenuate to $1/e$ (approximately 37%) of its initial value or the power to decay to $1/e^2$ (approximately 13.5%).

$$\delta = \frac{1}{\omega \sqrt{\mu\epsilon} \sqrt{\frac{1}{2} \left(\sqrt{1 + \left(\sqrt{\frac{\sigma}{\omega\epsilon}} \right)^2} - 1 \right)}} \quad (3)$$

Where δ : the depth of penetration of the electric field in biological tissue [m], σ : Conductivity [S/m], ω : Angular frequency [rad/s], μ : Magnetic permeability [H/m], ϵ : Dielectric permittivity [F/m]. As illustrated in (3), the penetration depths for blood at 2.45 GHz and 14.5 GHz are 16.12 and 1.68mm respectively, 24.303 and 2.042 mm for blood vessels, and 22.573 and 2.16 mm for dry skin, and 22.03 and 2.1 mm for wet skin, and 117.02 and 12.296 mm for fat.

Most living tissues are considered good dielectric materials for microwave ablation frequencies therefore the penetration depth can be approximated as in (4)

$$\delta \gg \frac{2}{\sigma} \sqrt{\frac{\epsilon}{\mu}} [m] \text{ for } \left[\frac{\sigma}{\omega \epsilon} \right]^2 \ll 1 \quad (4)$$

The penetration depth is inversely proportional to conductivity, but heating rate is proportional to conductivity. The calculations of penetration depth mentioned in (3) and (4) are approximated as most of the microwave energy absorbed by the biological tissues is in the near field or Fresnel regions of the antenna and may not propagate as plane waves. As stated in (4), deeper penetration occurs at the expense of slower heating.

One of the main advantages of MW ablation is that microwaves can focus its energy in the direction of the targeted tissue due to the shorter wavelength than that of RF ablation which allows faster ablation times and more uniform ablation zones. Faster and uniform ablation zone is very important parameter specially in regions with higher blood perfusion rate in the vicinity of large vessels which mediates ablation zone size because it tends to sink heat away from the ablation zone periphery (Chiang, Jason, et al., 2012; Gamez, ES, et al., 2013).

Trade-offs between penetration depth and heat generation is very important in determining which microwave frequency is suitable in treating certain tumour tissue. However, the recent research demonstrated the feasibility of using higher frequencies for tissue ablation. Despite deeper penetration depth of lower frequencies, tumour tissues not being successfully ablated were observed under the same power levels and same duration when exposed for both lower and higher frequency radiation (Chaichanyut, M, et al., 2013). Moreover, the size of ablation zones obtained using higher frequency are comparable to those obtained at lower frequencies. Additionally, higher microwave frequencies offer the advantage of smaller antenna lengths which makes microwave ablation less invasive. In addition, microwave ablation may be performed using compact multi-element array that can create ablation zones not achievable from large single element antennas used in conventional low frequency tissue ablation (Luyen, Hung, et al., 2014; Luyen, et al., 2013; Luyen, Hung, et al., 2014).

1.3. Benefits of Microwave ablation compared to other thermal ablation Techniques

Most important factor that distinguishes microwaves from other sources of thermal therapy techniques that microwaves can propagate through all types of tissues including dehydrated, charred and desiccated tissues created during the ablative process unlike RF, laser and ultrasound

energies can be substantially affected by different tissue types, especially as a result of thermal ablation. Microwaves also offer more direct and fast heating than other ablation energies, making them more potent in organs with high blood perfusion or near vascular heat sinks and provide shorter treatment time (Singal, et al., 2018; Yhamyindee, P, et al., 2012; Luyen, et al., 2017). Despite RF ablation is the most widely used modality in cancer treatment, it has several limitations and shortcomings which gave rise to the development of microwave ablation with less invasive and more effective method in cancer treatment. The differences between RF and microwave heating in each organ given that the properties of each tissue type, are demonstrated in Table 1. As illustrated in Table 1, RF heating is limited in areas of high blood perfusion rate (kidney and liver), in tissues with poor electrical and thermal conductivity (lung and bone), while microwaves offer all of the same benefits as RF energy for thermal ablation, but are not as dependent on tissue properties, have the ability to heat faster in a larger volume, less affected by perfusion and may be able to penetrate deeper into low conductivity materials (lung and bone) (Suseela, Sreekala, et al., 2013; Rosen, Arye, et al., 2002; McGahan & Raalte, 2005; Kaur & Maini, Surita, 2014; Tacke, et al., 2004; Lee, et al., 2003; Hulsey, et al., 2015; Phairoh, et al., 2015; Sanpamch, et al., 2015; Brace, 2009).ⁱ

1.4. Microwave ablation system

Microwave ablation system consists of Microwave power source such as solid state semiconductor devices or vacuum tube devices such as magnetron. Coaxial cable is used to carry the microwave power from the generator to the antenna. Most thermal ablation devices intended for percutaneous use are currently between 1.5 mm and 3 mm in diameter. Smaller antenna diameters are preferred for percutaneous applications while larger needle diameters are associated with increased risk of complications such as bleeding. On the other hand, small diameter coaxial cables have lower power handling ability which is not desirable in microwave ablation system. Increased power delivery has been associated with faster and potentially more effective treatments, particularly when targeting large tumours (Brace, Christopher L, 2010; Vojackova, Lucie, et al., 2014; Phairoh, C, et al., 2013). At the same time, input powers exceeding the cable power rating can have detrimental effects. Using only smaller size antenna will facilitate active cooling and antenna arrays can help increase energy delivery and hence produce larger ablation zones (Taj-Eldin,

ⁱ (Chou, 1995; Pop, Mihaela, et al., 2010; Liu, Zhengjun, et al., 2006; Solazzo, et al., 2005; Lee, et al., 2003; Hancock, et al., 2015; Luyen, Hung, et al., 2014; Luyen, Hung, et al., 2014; Luyen, et al., 2013; Muheremu & Niu, 2014).

Mohammed & Prakash, Punit, 2014). The antenna contains a rigid shaft and the radiating section at the distal end of the applicator as shown in Fig. 1.

Table 1. Comparison between RF and microwave ablation treatment according to organ specific consideration

Organ	RF Ablation	Microwave Ablation
<i>Liver</i>	<ul style="list-style-type: none"> -It is limited only to treat only small tumours less than 3 cm in diameter. -It is ineffective to ablate tumours in high perfusion regions such as tumours near large vessels of diameter 3mm (Hancock, et al., 2015; Singal, et al., 2018). 	<ul style="list-style-type: none"> -It can ablate tumour tissues around large vessels due to faster heating, higher temperature levels provided by microwaves in high perfusion region (e.g. Liver) (Hancock, et al., 2015). -higher effective conductivity attained in microwave ablation produced larger ablation lesions Increasing (Brace, 2009).
<i>Lung</i>	<ul style="list-style-type: none"> - RF current isnot able to penetrate through low conductivity aerated lung. -It has limited amount of power deposited into tissue due to the increased impedance seen by generator (Brace, 2009). -Poor thermal conductivity of aerated lung during RF ablation results in small ablation zone (Brace, Christopher L, 2010; Wonnell, et al., 1992). 	<ul style="list-style-type: none"> -The lower permittivity and conductivity of aerated lung allows deeper microwave penetration (Sanpamch, et al., 2015). -Microwave heating is not substantially hampered by low-conductivity tumour tissue which can actively produce larger ablation zones (Lee, et al., 2003). -Due to better propagation of microwave in low conductivity lung, better thermal gradient achieved maximum temperature exceeds 150 °C (Colebeck, Erin, et al., 2013). -Change in tissue properties during ablation procedures won't affect microwave energy as much as RF energy (Hulsey, et al., 2015).
<i>Kidney</i>	<ul style="list-style-type: none"> -It is Limited only to treat small tumours due to high perfusion rate of kidney (Pop, Mihaela, et al., 2010). -Tissue dehydration hampers RF current as the temperature increases during the procedure -It is Ineffective for treating large tumours (>3 cm in diameter) or centrally located tumours (Brace, 2009; Goldberg, SN, et al., 1998). 	<ul style="list-style-type: none"> -Higher heating rate is observed during microwave ablation procedure due to high water content of kidney (Brace, 2009). -Less sucesptable to tissue dehydration as It allows better microwave propagation (Hancock, et al., 2015). -Faster heating ability of microwave energy will overcome the high perfusion rate of kidney (Suseela, et al., 2015).
<i>Bone</i>	<ul style="list-style-type: none"> -Limited ablation zones due to poor conductivity and thermal conduction of bone (Brace, 2009; Solazzo, et al., 2005). 	<ul style="list-style-type: none"> -Microwave penetration is more effective due to low permittivity and conductivity of bone tumours (Gamez, ES, et al., 2013). -Microwave applicators are developed to provide more precised controlled ablation lesions and achieve more functioning limb after the procedure (Phairoh, et al., 2015; Martínez-Valdez, R., et al., 2017; Luján, et al., 2017).

Microwave ablation requires the application of powerful hardware and specialized software which allow predicting the heating rate in a biological tissue near the radiating element of a needle-like

(coaxial) applicator and several simplified approaches were proposed to calculate the coupled electromagnetic heat transfer into the tumour tissue including the numerical solution of EM PENNES Bio-heat equation. Furthermore, to monitor the variation of dielectric and thermal properties of biological tissues during ablation are temperature dependent. Despite recent advances in the nonlinear modelling to estimate the heating rate in the ablation zone taking into account the temperature dependent dielectric properties of the biological tissue, the results of simulations agree with experimental data only to a certain degree especially at high powers (Colebeck, Erin, et al., 2013; Komarov, 2014; Trujillo, M & Berjano, E, 2013)ⁱⁱ

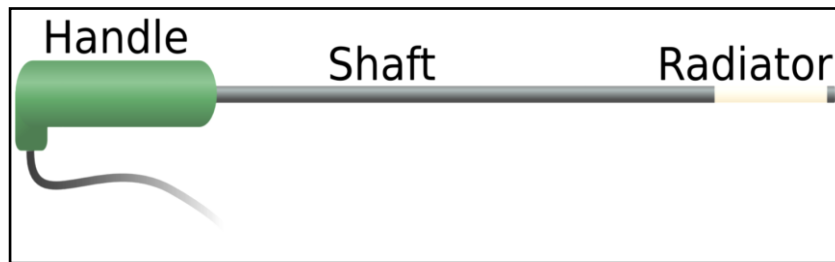


Figure 1. Coaxial cable runs the length of the shaft, with the radiating element at the distal end of the antenna. Energy is produced around the radiating element (Brace, Christopher L, 2010)

To validate the simulated and numerical results of microwave ablation, the heating pattern can be visualized by means of static phantoms and temperature variations in a fixed point of biological medium volume can be determined with fibre optical sensor. In-vivo and In-vitro monitoring techniques are also used to visualize and validate the heating pattern and temperature variation of the coagulation zone (Cepeda Rubio, Mario Francisco Jesús, et al., 2013; De Sieyes, et al., 1981). Antenna properties relevant to thermal ablation include near field radiation pattern, reflection coefficient, operating bandwidth, Specific Absorption Rate (SAR) value and temperature levels achieved during the procedure. In general, the lowest return loss is desirable to maximize power transfer from the antenna into the tissue. Power reflected from the antenna reduces tissue heating, while increasing unwanted heating of the antenna shaft. In extreme cases, high return loss may necessitate short ablation times to prevent thermal damage along the antenna shaft. Most antennas currently radiate in the normal (broadside) mode, with propagation directed radially outward from the antenna. This is especially true of antennas designed for tumour ablation applications, where the ideal radiation pattern is focused and Omni-directional to match the Advantages of approximately spherical shape of many tumours. Antennas designed in the axial (End-fire) mode

ⁱⁱ (Watanabe, et al., 2012; Ji, Zhen & Brace, Christopher L, 2011; Yang, Deshan, et al., 2007; Pop, Mihaela, et al., 2010; Asili, Mustafa, et al., 2013; Wang, Peng & Brace, Christopher L, 2012; Zhang, Huijuan, et al., 2012)

have been developed for cardiac applications to produce localized heating of a spot at the end of a catheter. Therefore, the desired antenna radiation pattern is highly dependent on the tumour cell-host organ (Gu, Zeji, et al., 1999).

1.5. Problems and Limitations Found in Microwave Ablation Technology

Despite microwave ablation is the most recent ablative technique and has several advantages over other complementary methods for cancer treatment such as low cost, smaller antenna size, shorter recovery time and effective prevention of the metastasis of tumour cells, there are still shortcomings and challenges accompanied with microwave ablation therapy needed to be fulfilled (Hassan, et al., 2018; Hassan, et al., 2016).

- The tissue impedance increases as the water content evaporates during the tissue ablation which results in shifting in the resonating frequency of the antenna. Therefore, the return loss will increase and as most of the current microwave ablation systems use narrowband antenna, this will create elongated ablation zone and damage the surrounding healthy tissues (Hulsey, et al., 2015; Hancock, 2011; Brace, Christopher L, et al., 2004; Brace, Christopher L, et al., 2005).
- The overheating of cabling used to transfer power from the generator to the applicator due to high mismatch losses between the antenna and coaxial cable while increasing unwanted heating of the antenna shaft. In extreme cases, high return loss may necessitate short ablation times to prevent thermal damage along the antenna shaft and damage of the healthy tissues along the antenna shaft and lead to shorter ablation time (Luyen, et al., 2015).
- The most common frequencies used in microwave ablation are 433, 912 and 2450 MHz which produce non uniform SAR pattern resulting in unsuccessfully ablated areas within the target tissue (Luyen, Hung, et al., 2014; Luyen, Hung, et al., 2014; Luyen, et al., 2013; Hancock, Chris P, et al., 2013; Sawicki, et al., 2015; Hodgson, et al., 1999; Yoon, et al., 2011; Komarov, 2014; Hines-Peralta, Andrew U, et al., 2006; Ahn, Hee-Ran & Lee, Kwyro, 2005). Recent studies demonstrated that nanosecond pulsed electric fields (nsPEF) used as purely electrical cancer therapy without the need of hyperthermia or drugs. nsPEF electrodes can provide acceptable level of homogeneity in SAR pattern. However, the SAR homogeneity is only confined in a small volume within the separation of the 2 electrodes and inhomogeneous in the vicinity surrounding the electrodes. It was observed that the

homogeneity of SAR pattern depends on the distance between the electrodes (Beebe, et al., 2002; Soueid, et al., 2015).

- The need of using *baluns* increases the size of the antenna which results in less comfortable and less invasive treatment procedures for percutaneous applicators which may cause complications after surgery (Lin, James C & Wang, Yu-Jin, 1996; Hancock, Chris P, et al., 2013; Maini, Surita & Marwaha, Anupma, 2012; Maini, Surita & Marwaha, Anupama, 2013; Luyen, et al., 2015; Luyen, Hung T., et al., 2015; Longo, Iginio, et al., 2003; Maini, 2016; Lara, et al., 2015).

Several scenarios have been investigated in literature regarding antenna designs proposed for microwave ablation. Nonetheless, high reflection and lack of control over heating due to use of high input power still represent the main shortcomings associated with these designs. High reflection encountered during ablation due the change of tissue properties with the increase of temperature which can be attributed to narrow band feature which hinders large portion of microwave power from being deposited within targeted tissue. This yielded using high input power to force eradication of targeted tumour at the expense of overheating of the cable and lack of control over heating. These drawbacks give rise to claim a novel antenna design to alleviate complications and overcome limitations of previously proposed applicator designs achieve successful ablation using low microwave power by confinement of heating within the targeted tissues rather than its surroundings.

1.6. Research Aim and Objectives

Major concern of this work is to alleviate complications and overcome limitations of previously proposed applicator designs especially regarding control overheating of the cable, overly-treated lesions and unconfined heating. The aim of this research is to design and develop a compact microwave antenna for treating focal tumours to achieve confined heating within targeted tumour by using low input power producing minimum reflection over a wider bandwidth.

The research aim can be achieved via the following objectives:

- Review recent research about tissue ablation therapy highlighting the pros and cons found in previously proposed work which is consolidated in a comprehensive literature.
- Determine limitations of previously proposed solutions regarding applicator designs which gave rise to the problems encountered in microwave ablation.

- Design less invasive antenna structure by choosing to operate the antenna at high microwave frequency bands which will provide smaller compact design and targeted higher thermal conductivity yielding higher absorption by the targeted region.
- Apply analytical solutions by solving Maxwell equations and boundary conditions to determine current distribution required on the antenna surface to attain highly directed axial near-field radiation which yields confined heating within targeted tumour model.
- Synthesize the antenna structure using numerical simulations so that it has less abrupt transitions which will be exploited in achieving minimum reflection over wide bandwidth.
- Apply parametric studies to the antenna structure so that it has minimum backward radiation and directed axial radiation towards the targeted tumour which helps achieving homogenous absorption within targeted tumour and reaching the temperature levels required for ablation at low power level while alleviating radiation towards healthy tissues surrounding the targeted tumour.
- Apply embedded choke approach in the antenna structure which yields compact sized applicator and minimizes return currents excited in the outer conductor of the coaxial cable. This controls overheating of the cable and reduces the damage of healthy tissues along the antenna shaft.
- Manufacturing and testing the developed antenna in either real biological tissues or synthesized solutions to prove the efficacy of the proposed design as microwave coagulator in providing successful ablation at low input power by exploiting directed axial radiation and determine the total ablated volume obtained after the procedure.

1.7. Research Contribution

The main concern of the proposed solution is to address the shortcomings of antenna designs proposed in literature to effectively overcome the related complications encountered in microwave ablation especially regarding control over heating, high reflection, and overheating of the cable. This work addresses the significance of using ultra-wideband antenna to offer low power microwave ablation by introducing teardrop flared tipped (TDFT) antenna to alleviate the limitations found in microwave cancer ablation. This is accomplished by the following findings:

- Prior understanding of tumour shape and its peripherals contributes greatly in determining electromagnetic (EM) radiation that creates a heating conformal to tumour shape and provide successful ablation. This is accomplished by calculating current distribution by building semi-analytical and numerical model that facilitates synthesising the optimum applicator structure to provide the required near-field radiation. As a result, this helps synthesize applicator structure to provide symmetrical no-null radiation and help producing nearly equal power deposition in the region surrounding TDFT antenna yielding homogeneous heating within targeted region.
- Axial End-fire radiation with higher directivity is found to be more efficient in achieving more confined heating within targeted lesion than broadside radiation associated with previously proposed designs; and minimizes unwanted radiation exposure towards surrounding healthy tissues. This highly directed radiation significantly alleviates the input power required for successful ablation –i.e. 3:5W– by 66% of the minimum power reportedly used in literature i.e.10 to over 60 W.
- Proposed UWB TDFT antenna provides minimum reflection stability– 99.17% overall efficiency over UWB including at operating frequency– and provide wideband mapping of heterogeneous dielectric properties of biological tissues operating at low input power level.
- Synthesizing antenna structure with self-imbedded choke provides more compact sized applicator– i.e. maximum diameter of the proposed TDFT applicator including dielectric shield 3.4 mm and minimum diameter of 1.025 mm–, alleviates return currents on the outer conductor of coaxial cable by approximately 36% and hence reduces overheating problem which minimizes damage of healthy tissues along antenna shaft. This is noticeably manifested from thermal simulations and ablation experiments where no cable overheating or damage of tissues along antenna shaft observed.
- TDFT antenna is distinguished by efficiently treating several cancer types such as liver, kidney, breast and bone cancer where directed axial radiation provides exceptionally confined heating of approximately 30 mm diameter tumour at lower input power of 3W in only 3 minutes comparable to that obtained at much higher input power. Experimental results also show successful ablation of a lesion of volume $16 \times 19.5 \times 19.5 \text{ mm}^3$ achieved for much less power–i.e. 1W– in 15 min comparable to that attained at higher input power reported in literature.
- TDFT antenna with highly-directed radiation noticeably creates confined heating zones which uses only 60% of the lowest input power to attain comparable successfully ablated lesions to

that recorded in literature in minimum duration of 15 mins in standard ablation operations. This reduces the input power required by microwave applicator by almost 40% of the lowest input power used in literature.

- It was found that input power used, and duration of radiation exposure greatly depend on the size and location of tumour. In addition, using lower input power helps eradicating critically located tumours such as bone tumours or tumours near large vessels which minimizes organ mal-function after ablation. This also facilitates the possibility of having longer ablation operations in much safer manner without the risk of patients being exposed to high radiation using higher input power as presented in literature.
- Therapeutic temperature level recorded using TDFT antenna is 72.375 °C for 3W input power which is much less than that required for tissue vaporization –i.e. temperatures in excess of 100 °C. In addition, ablated lesions achieved– temperatures above 50°C– in a diameter of approximately 30 mm in only 3 mins which less than typical time for ablation i.e. 15 mins. This minimizes problems previously encountered with instability of MW equipment and overheating during ablation due to tissue vaporization using higher power or longer treatment time; and gives better and more control over antenna performance in achieving temperatures in therapeutic ranges within targeted area.

1.8. Research Process

A research process is being constantly updated, searching for better ways of making observations, understanding, hypothesis, analysis and conclusions which are incorporated into set of rules and procedures of research methodology. Scientific methodology comprises of three main elements theory and background, computational results and analysis using simulation tools; and practical measurements for validation. Research process is clarified in the following steps:

Step 1: Research begins with defining what is already known about tissue ablation therapy and reviewing the literature of previously proposed studies. Determining the pros and cons found in microwave ablation therapy through observations specially in applicator designs proposed in the literature.

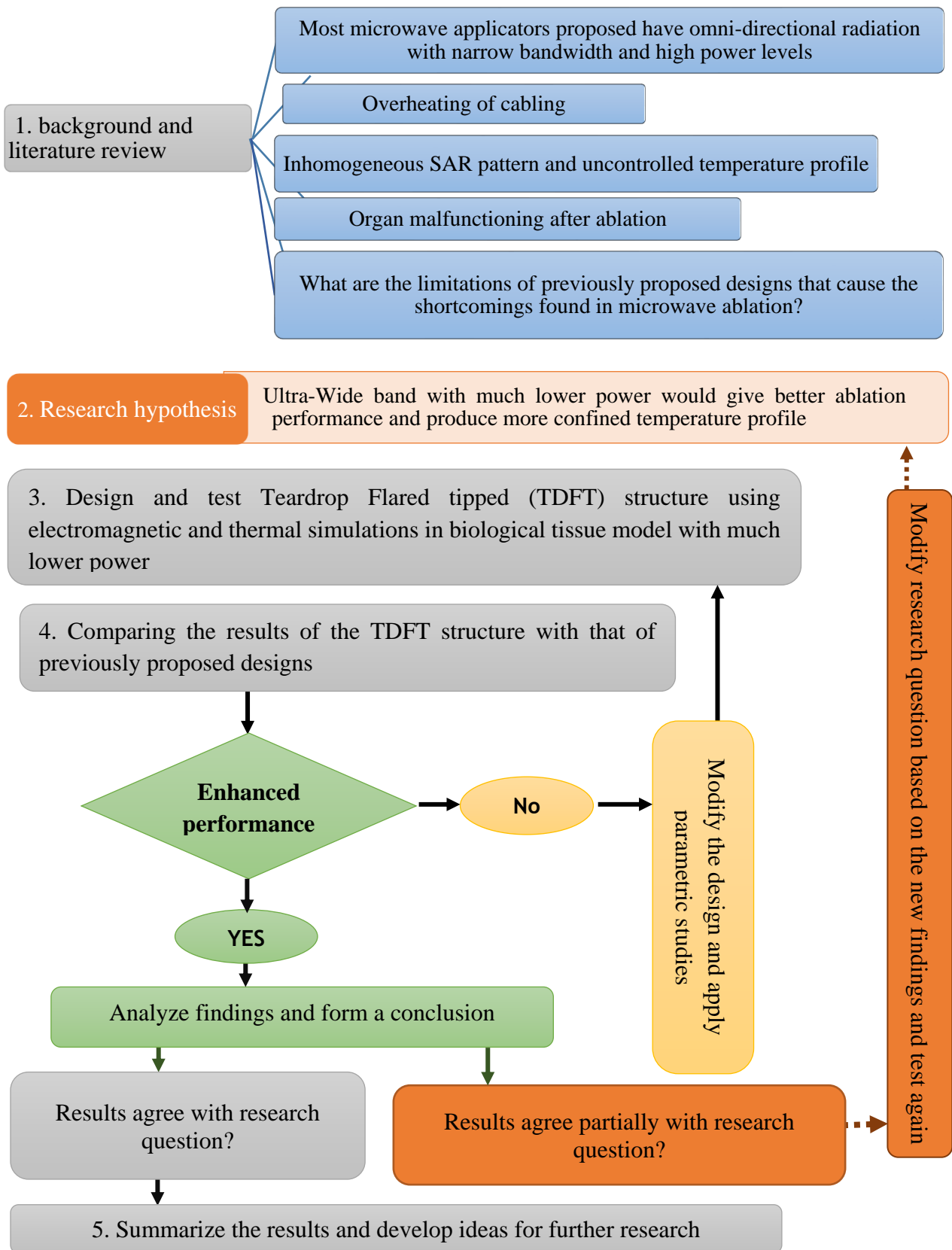
Step 2: A research question arises based on these observations which is will better ablation performance and confinement of heating zone within the targeted tissues rather than its surroundings be attained using low microwave power?

Step 3: Propose teardrop flared tipped antenna design as a solution for problems found in microwave ablation therapy of focal tumours. Modelling and simulating the antenna design in liver, saline and tumour using Electronics Desktop suite and Ansys workbench software packages.

Step 4: After analysing and applying parametric studies performed, the required results of return loss, Nearfield radiation patterns, bandwidth, SAR pattern and thermal profile are obtained and compared with that previously proposed MW applicator to determine whether better antenna performance is achieved using proposed TDFT antenna design.

Step 5: Manufacture and test the proposed antenna in Egg-white and biological tissue to validate the simulated results. The testing will determine the extent of ablated volume attained using teardrop flared tipped antenna. After finishing the validation phase, summarizing research findings and writing up the whole PhD thesis will be the final step.

1.8.1. Research Process Chart



1.9. Thesis outline

This report is structured as follows:

- **Chapter One** starts with a brief introduction to traditional cancer treatment options and an overview on various types of tumour ablation techniques focusing on the advantages microwave ablation therapy compared to other tumour ablation techniques. This chapter also highlights the problems found in microwave ablation therapy which in-turn identifies the aim, objectives and contribution of this research.
- **Chapter Two** presents a literature review of the most recent researches related to microwave ablation therapy explaining different aspects of microwave applicator design, shortcomings and limitations yet to be addressed. Research process chart is also presented in this chapter.
- **Chapter Three** introduces a semi-analytical numerical model of TDFT antenna and calculation of radiated electric field within biological tissue to be further compared to simulation and experimental results
- **Chapter Four** presents the proposed TDFT design exploited in solving the research problems stated earlier highlighting the factors that distinguish the proposed solution among previously proposed applicator designs. Simulation results (reflection coefficient, nearfield pattern, SAR patterns, temperature distribution...etc.) are presented in this chapter. In addition, reflection measurements and ablation experimental results are provided in this chapter.
- **Chapter Five** presents the assessment of TDFT antenna design highlighting the main advantages of the proposed solution and how it addresses the limitations found in literature.
- **Chapter Six** covers the conclusion of this study and future studies yet to be investigated regarding tumours exist near a vessel wall.

Chapter Two

Related Work and Literature Review

2.1. Introduction

This section consolidates more details about applicator designs proposed in the literature for microwave ablation therapy. Different topologies have been introduced regarding the structure of the antenna designs proposed as applicators for microwave ablation therapy which can be categorized as follows:

2.1.1. Linear Element Based Applicator Designs

The antenna proposed in (Preston, et al., 2018) provides a possible way to treat the inaccessible nodules. The device comprises a microwave conveying structure, 1 meter in length, capable of delivering energy at 5.8GHz. The use of a hollow structure within the cable allowed for the inclusion of a CMOS sensor for visualization and navigation through the bronchial tree. The radiative tip comprises an inner and outer conductor initially manufactured from brass enclosing a Polyether Ether Ketone (PEEK) dielectric structure and was chamfered to allow for easy penetration into tissue as shown in Fig. 2. The length of the tip was preliminary set to a quarter wavelength with geometry to provide an impedance match between the lower impedance cable and the higher impedance tissue.

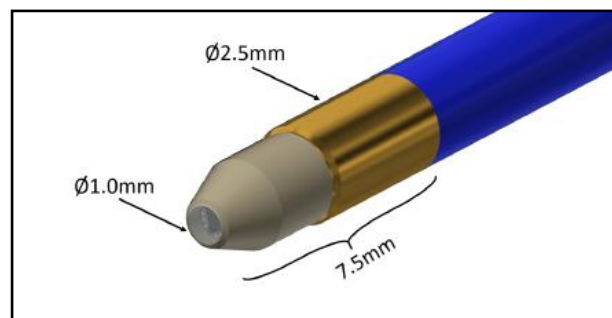


Figure 2. The radiative tip of the proposed antenna (Preston, et al., 2018).

Simulation results showed a match at 5.8GHz in the simulated S parameters of 14.87 dB or 96.8% being delivered into the tissue. Initially continuous power delivery was used, but this resulted in excess heating both at the tip and along the cable in the time needed to achieve the required ablation size. Pulsing was subsequently used to ensure that both tip and cable temperature remained within acceptable limits. Measurements of ablation zones were taken during varied time delivery with

pulsed power of 2s on, 5s off with a power of approximately 19.12W. Due to high reflection and narrowband width, large portion of the input power was absorbed by tissues along the antenna shaft which necessitates shorter ablation times.

In (Luyen, Hung, et al., 2017), A technique to reduce the overall diameter of coax-fed antennas equipped with coaxial baluns is presented. The technique involves introducing an impedance-matched air-filled coax section at the end of the Teflon-filled coax feed. Due to the lower relative permittivity of air, the air-filled coax has a smaller diameter than the Teflon-filled coax for the same inner conductor diameter and characteristic impedance. Prototypes of a Choked Dipole (CD), based on the design in (Nevels, Robert D., et al., 1998), and a Floating Sleeve Dipole (FSD), based on the design in (Yang, Deshan, et al., 2006), are modelled to demonstrate the efficacy of the proposed design concept. Simulations and ablation experiments were conducted to compare the performances of these antennas to those of conventional CD and FSD antennas.

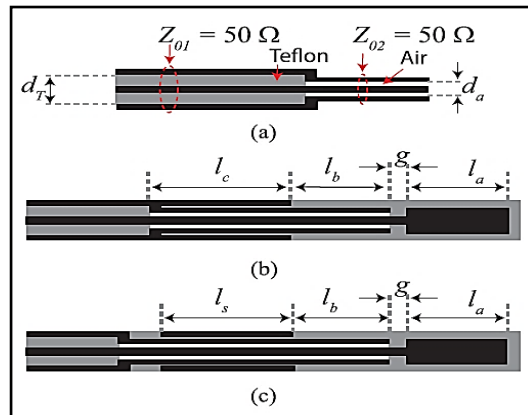


Figure 3. (a) Impedance-matched transition between a Teflon-filled and an air-filled coaxial cable. Topology of (b) a modified choke dipole and (c) a modified floating sleeve dipole implemented on the air-filled coax sections. Black represents metal, grey (Luyen, Hung, et al., 2017).

As shown in Fig. 3, Both CD and FSD antennas are embedded in a Teflon catheter with an outer diameter of 2.5 mm. The operating frequency of 7 GHz for the antennas was chosen to balance between the advantage of shorter antenna lengths and the disadvantage of higher ohmic losses. The dimensions of these antennas were optimized using CST Studio and then incorporated in transient thermal simulations to predict temperature rises in the tissues for 5 min ablation with an input power of 30 W for each antenna. At the design frequency of 7 GHz, the measured S_{11} value was -24 dB for the conventional CD, -23 dB for the modified CD, -27 dB for the conventional FSD and -18 dB for the modified FSD. The experimental results conducted in porcine liver tissue

showed ablation lesions of dimensions $4.1 \times 2.7 \text{ cm}^2$ for the conventional CD, $4.0 \times 2.8 \text{ cm}^2$ for the modified CD, $4.3 \times 2.8 \text{ cm}^2$ for the conventional FSD, and $3.7 \times 2.8 \text{ cm}^2$ for the modified FSD antenna. From the simulation results, the modified CD and FSD designs presented good impedance matching and 30% more size compactness. Nevertheless, higher reflection coefficients than that of the conventional designs were attained due to the application of air-filled coax section. Furthermore, elongated ablation zones attained may damage the surrounding healthy tissues.

In (Fallahi, Hojratollah, et al., 2017), an antenna for a minimally invasive MWA for eradicating bilateral adrenal adenomas, symptomatic of Conn's syndrome was developed in this study shown in Fig. 4. The small size of the adrenal gland and targeted adenomas ($\sim 10 \text{ mm}$ sphere), make the existing MWA devices, which have been developed for creating large ablation zones, unsuitable. Dielectric properties of different zones of adrenal glands were measured to provide the realistic parameters for MWA applicator design. First, coaxial dielectric measurement technique was employed to measure the broadband (0.5 – 20 GHz) dielectric properties of ex vivo adrenal glands to be included in electromagnetic and thermal analysis of the proposed antenna. A dielectric-loaded coaxial monopole antenna was initially chosen to operate at 2.45 GHz due to the constraints of short ablation zones. Water was selected for dielectric loading due to its high permittivity ($\epsilon_r \sim 78$ at 2.45 GHz) in addition, it serves as means to actively cool the coaxial cable, thereby limiting passive heating along the length of the device.

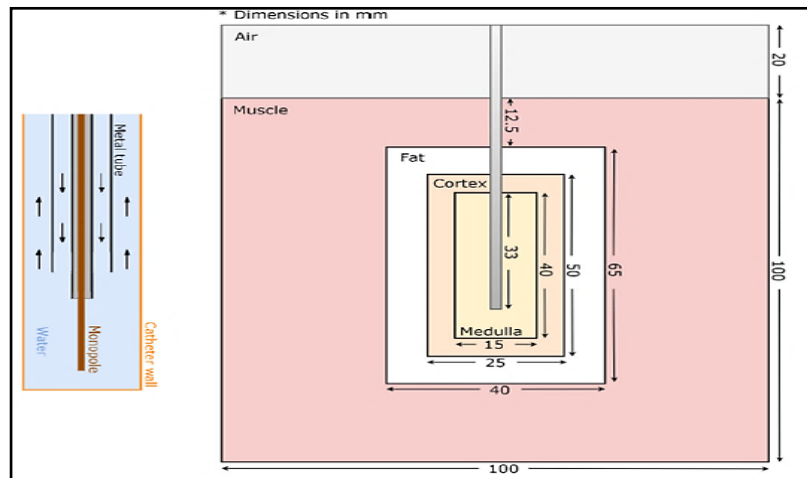


Figure 4. Illustration of the (a) antenna tip and (b) geometry employed for 2D computational model (Fallahi, Hojratollah, et al., 2017).

Compared to MWA applicators in current use, where ablation zone length is typically $\sim 30\text{-}40 \text{ mm}$, the proposed device offered improved control in heating along the length of the applicator. Water inflow/outflow channel increase the total size of the antenna which increase the invasiveness of

the antenna makes it less desirable for percutaneous applications. Further investigation and optimization of antenna designs, future efforts should characterize the relationship between applied power levels and ablation duration on ablation zone size.

Authors in (Mohtashami, Yahya, et al., 2017) presented a reflector-backed slot/monopole antenna for generation of directional heating patterns in MWA. This design constituted of a monopole antenna backed with a reflector made by extending a portion of the outer conductor of the coaxial cable as shown in Fig. 5. The presence of the reflector decreases the radiation of the monopole behind the reflector, creating an asymmetric SAR pattern. To further reduce the radiation behind the reflector, A semi-cylindrical slot is etched in the outer conductor of the feeding coaxial cable away from the base of the monopole. The electric field generated by this slot constructively interferes with that generated by slot and monopole combine destructively.

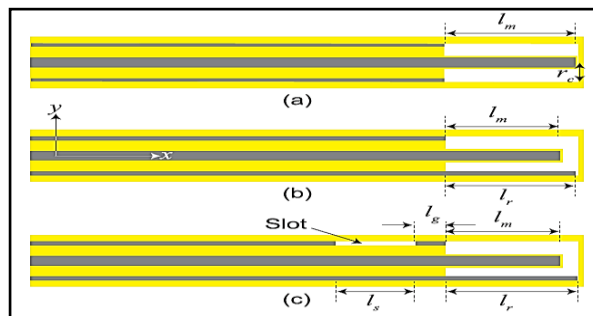


Figure 5. Topology of the three structures studied in this paper. Yellow, grey, and white represent Teflon, copper, and air, respectively. (a) Axisymmetric monopole antenna. (b) reflected backed monopole antenna (c) Reflector backed slot monopole antenna (Mohtashami, Yahya, et al., 2017).

From the simulation and thermal results, the proposed reflector-backed slot attained highly directional SAR and heating patterns in which the SAR values behind the reflector are 15 dB below the values in the region facing the slot opening and monopole. A prototype of this antenna was fabricated to perform MWA experiments in egg white at a power level of 20 W for 5 min. The proposed design is relatively narrowband (1.8%) and the resulting radiation can be prone to elongated patterns which increases the reflection during the ablation process due to shifting in the frequency of operation. Moreover, introduction of slots causes excessive backward heating along the antenna shaft without design modification.

In (Luyen, et al., 2017), authors presented a coax-fed interstitial antenna design for MWA using a tapered slot balun. The balun is created by tapering the outer conductor of the coax to make a smooth transition from a coaxial line to a parallel-wire line as shown in Fig. 6. Two tapered-slot

balun designs, a single-slot and a double-slot balun, were investigated for their use with corresponding dipole antennas. The single-slot tapered balun was created by linearly tapering outer conductor into a single strip. One arm of the dipole is created by extending the inner conductor. The other arm is placed in the slot created by tapering the outer conductor and connected to the strip at its distal end using a conductive ring. At its operating frequency, the balun provides balanced currents for two arms of the dipole.

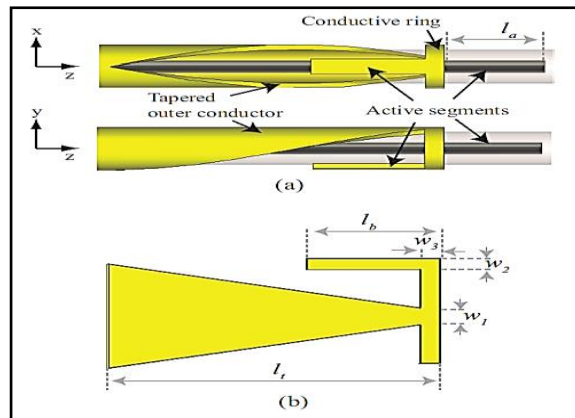


Figure 6. Topology of the interstitial antenna design with a single-slot tapered balun and two active segments (Luyen, et al., 2017).

For Single slot tapered balun antenna, simulation results revealed VSWR of approximately 1.38 corresponding to $|S_{11}|$ value of -16 dB at 6 GHz, demonstrating that the single-slot design provided a good impedance match between the dipole and the feed line. SAR levels are reduced by 20 dB near the proximal end of the second dipole arm connected to the tapered outer conductor and by 30 dB near the proximal end of the tapered balun. Thermal analysis showed that maximum lateral dimensions of the ablation zone in the two cut planes are the same and equal to 24 mm. In the y-z plane, the maximum lateral radius of the ablation zone is 13.25 mm for the lower side and 10.75 mm for the upper side. The dimensions of the double-slot balun and the three active segments of the dipole, noted in Fig. 7 were optimized in the simulations to achieve a localized SAR pattern and good impedance match at 6 GHz. From simulation results, the double-slot tapered balun achieves a slightly better impedance matching ($|S_{11}| = -20$ dB) than the two-segment dipole at the operating frequency of 6 GHz. Thermal analysis revealed that antenna using the double-slot balun produced a compact volume enclosed by the -30 dB contours, of which the lateral diameter (about 26 mm) is even larger than that of the single slot design.

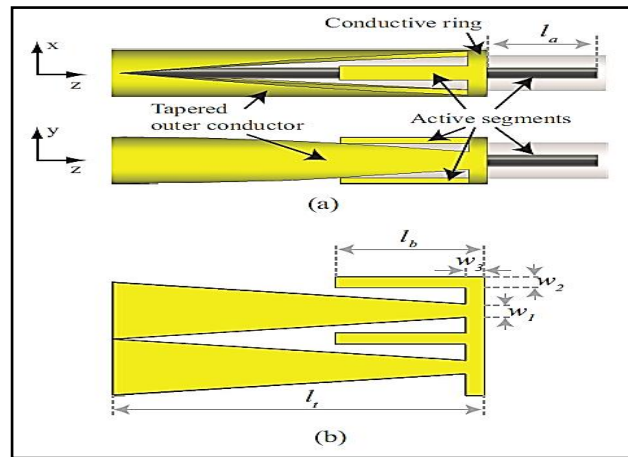


Figure 7. Topology of the interstitial antenna design with a double-slot tapered balun and three active segments (Luyen, et al., 2017).

A prototype of the antenna with the double-slot tapered balun was fabricated to conduct ablation experiments in ex vivo bovine livers. The antenna produced ablation zones with dimensions of up to $4.6 \times 3.5 \times 3.5 \text{ cm}^3$ for the case of a 10-minute ablation using 30W input power. Given the complexity of the design to achieve more compact SAR Pattern, asymmetrical SAR patterns were obtained in both single and double slot tapered balun antennas along with elongated ablation zones which may damage the healthy tissues along the insertion path of the antenna.

In (Tal & Leviatan, 2017), authors proposed another method to reduce the microwave ablation antenna diameter where they didn't use antennas whose input impedance matches that of a standard 50Ω coaxial cable feed-line. In this work, an extremely thin antenna shown in Fig. 8. designed for liver tumour treatment at 10 GHz. The diameter of the central conductor is 0.5 mm, the inner and outer diameters of the outer conductor are 0.7 mm and 1.1 mm, respectively. This results in a characteristic impedance of 14Ω . The antenna is then assumed to be embedded in a homogeneous lossy dielectric mimicking the liver tumour. Simulations of the antenna that have been performed with CST Multiphysics studio, reveal nearly spherical ablated zone around the antenna tip.

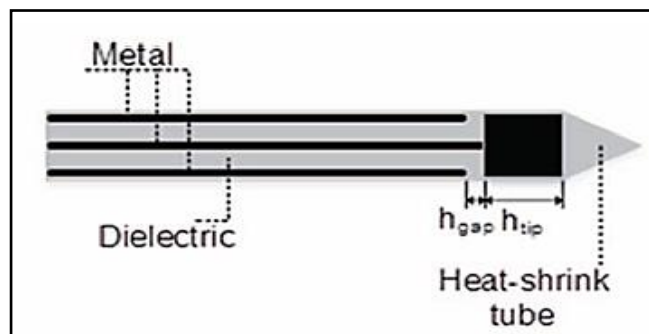


Figure 8. Proposed MWA antenna cross section area (Tal & Leviatan, 2017).

From simulation results, the proposed design achieved nearly spherical ablation zone. However, on the other hand, operating the antenna at such high frequencies as 10 GHz increases the ohmic losses which was clearly observed from high mismatch loss of -8 dB at 10 GHz. Operating the antenna at frequencies such as that proposed in (Luyen, Hung, et al., 2017) compromised between smaller antenna size and higher ohmic losses. In addition, coaxial feed with small diameters hinder the power handling capabilities of the coax cable which leads to less power deposited in the targeted tissue.

In (Alnassan, Hussein, et al., 2014), numerical simulation of microwave ablation was proposed as a step in the implementation of system design to calculate the temperature distribution of targeted radiation dipole antenna for microwave ablation at 2.45GHz. This experiment achieved power in the range 50W, 60W and 70W through the temperature profile around the antenna. In addition, the ablation time was set in the range 300s, 600s and 900s. The goal was to develop a device for directional tumour ablation avoiding destruction of healthy structures. The antenna was designed and simulated by varying the directive windows angle during the ablation. A metal catheter with diameter of 3mm was chosen to guide the generated electromagnetic waves to the dielectric window as shown in Fig. 9.

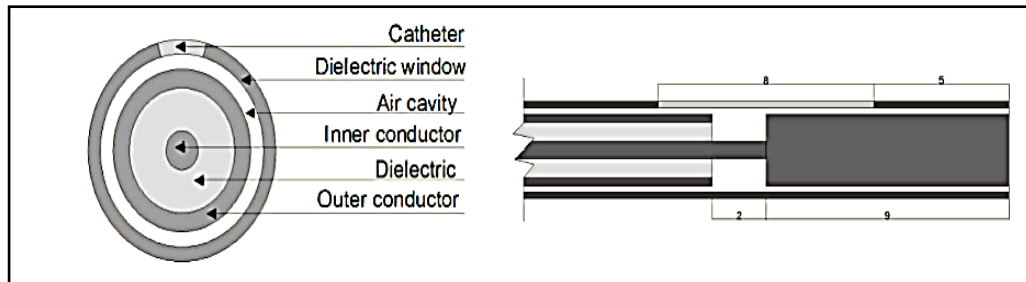


Figure 9. Antenna top and side section (Alnassan, Hussein, et al., 2014).

This model was designed using COMSOL 4.3 computer simulation for temperature distribution around the antenna tip on two opposite sides (active window side and non-active side). The numerical simulation showed ablation zone on active side with radius of 2cm and 1 cm on non-active side for 600s. One other feature of this device is the SAR patterns are clearly uneven on the opposed sides that means the difference values of absorbed heat energy by tissues.

The feasibility of using high frequency microwaves for tissue ablation by comparing the performance of a 10 GHz microwave ablation system with that of a 1.9 GHz system was

demonstrated in (Luyen, Hung, et al., 2013; 2014). Two 1.9 GHz and 10 GHz floating sleeve dipole antenna prototypes were designed and simulated using CST Microwave Studio. In the full-wave EM simulations, the sleeve lengths were optimized to achieve localized SAR patterns at 1.9 GHz and 10 GHz. The ablation experiments were conducted in bovine liver. At the frequencies where the ablation experiments are conducted, an S_{11} of lower than -15 dB was achieved.

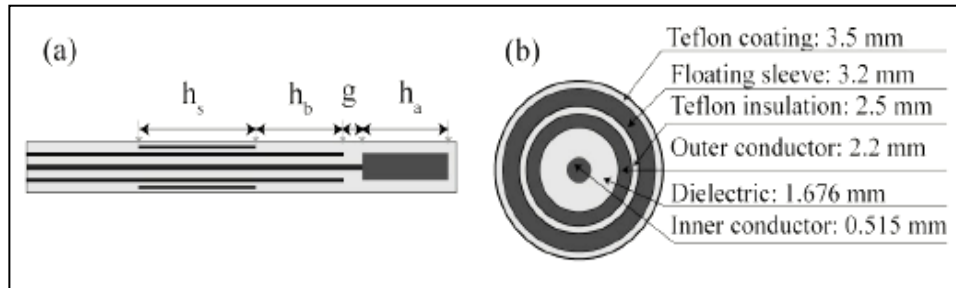


Figure 10. Topology of the floating sleeve dipole antenna used in ablation experiments. (a) Side view. (b) Cross-sectional view (Luyen, Hung, et al., 2013; 2014).

Figure 10 shows the floating sleeve antennas designed and fabricated for use in ex vivo experiments with bovine liver. The 10 GHz and 1.9 GHz experiments resulted in comparable ablation zone dimensions. While at higher frequencies the penetration depth of EM waves into biological tissues reduces, the higher conductivity at these frequencies results in significantly higher temperature levels near the antenna. This high temperature level in conjunction with thermal diffusion is believed to be responsible for creating the large ablation zone observed at 10.0 GHz (Thongsopa & Thosdeekoraphat, 2013; Vojackova, Lucie, et al., 2014). The multi floating sleeve antenna proposed added to the total diameter of the applicator which leads to less intrusive design which is less desirable by the patients undergo such treatment procedures.

In (Maini, Surita & Marwaha, Anupama, 2013), a new multi section floating sleeve interstitial coaxial antenna for microwave ablation was proposed. The antenna has an asymmetrical floating sleeve featuring a split tip on the tip as shown in Fig. 11. Performance of the antenna has been evaluated numerically, taking into account the temperature distribution, antenna impedance matching, size and shape of the thermal lesion at the operating frequency 2.45GHz. A power of 60 Watt provided to the proposed design for 66 sec. The corresponding increase in temperature has been evaluated by the Bio heat equation. COMSOL Multiphysics FEMLAB version 3.4 has been used as primary computer simulation tools.

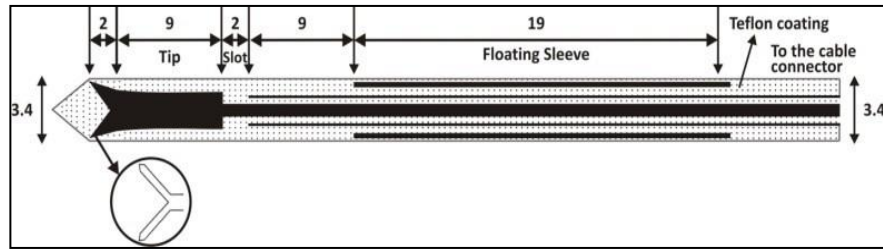


Figure 11. Schematic diagram of multi-section floating sleeve antenna (Maini, Surita & Marwaha, Anupama, 2013).

The proposed antenna results depicted that with reflection coefficient -27 dB, the antenna was well matched and having capability of creating spherical ablation zones up to 2 cm in radius using 60-Watt input power at 2.45 GHz. In addition, the surface heat is well distributed and strong near the tip of the antenna of spherical shape, leading to the high temperatures, but heat lesion gets weaker as it goes far from the antenna tip. The multi section floating sleeve antenna proposed a good agreement between temperature distribution, heat lesion, and reflection coefficient in comparison with the floating sleeve antenna. The multi floating sleeve antenna proposed had much larger diameter than the conventional floating sleeve antenna.

Taj-Eldin, Mohammed and Prakash, Punit (2014) compared microwave ablation with interstitial single and multi-antenna configurations operating at 915 MHz vs. 2.45 GHz while controlling transmitted power and treatment duration. Full Wave finite element method (FEM) simulations were employed to compare sizes and patterns of ablation zones achievable after 10 min ablations. Coaxial dipole antenna was designed and employed to radiate into liver tissue at 915 MHz and 2.45 GHz, as well as an intermediate frequency of 1.5 GHz as shown in Fig. 12.

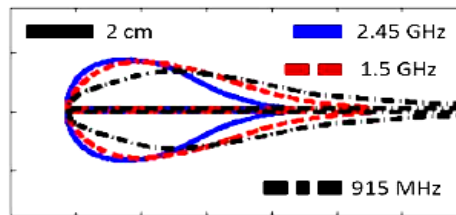


Figure 12. Simulated heating patterns (Taj-Eldin, Mohammed & Prakash, Punit, 2014).

Simulation and experimental results indicated that a single antenna operating at 2.45 GHz yielded an ablation zone diameter $\sim 25\%$ larger than an antenna operating at 915 MHz when powered with 30 W for 10 min and at higher frequencies, shorter antenna lengths lead to shorter and more spherical ablation zones. Experiments performed in ex vivo muscle tissue were in good agreement with simulation; more spherical ablation zones were observed for the synchronous array (48 mm

× 46 mm) compared to the asynchronous array (57 mm × 42 mm). These results suggest that antennas operating at 2.45 GHz may be better suited for rapid creation of spherical ablation zones in liver tissue.

The applicator design proposed in (Maini, 2016) is basically a floating sleeve antenna with miniaturized tapered cap, which is electrically connected to inner conductor as shown in Fig. 13. The structure of tapered cap floating sleeve antenna has been optimized with finite element modelling of MWA antennas. It can be observed that with the optimized length of the tapered cap of 5 mm with a base diameter of 0.25 mm and angle of 28° the antenna resonates at the operating frequency of 2.45 GHz.

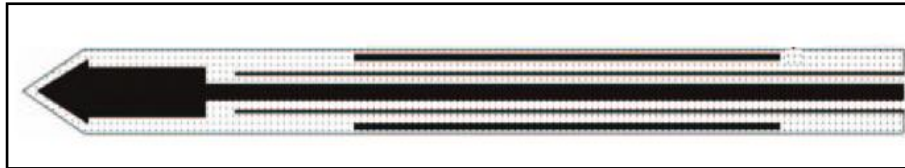


Figure 13. Schematic diagram of multi-section floating sleeve antenna (Maini, 2016)

At 2.45 GHz the value of reflection coefficient S_{11} is of the order of -24.8 dB. The ablation lesion produced was more of elliptical shape than spherical shape which might not be suitable for treating spherical focal tumours and might damage the healthy tissues surrounding the tumour. Several designs proposed in the literature provided lower reflection which results in more deposited power in the centre and surface of the tumour.

In (Maini, Surita & Marwaha, Anupma, 2012), heating characteristics of coaxial dipole antenna and coaxial slot antenna were studied. The two-dimensional finite element method (FEM) were used to measure and simulate the results of the coaxial ring slot antenna and coaxial dipole antenna. The tip of the dipole antenna is a whole piece of metal, while the inside of the tip of a slot antenna is the dielectric of the coaxial cable as shown in Figs 14 and 15, respectively.

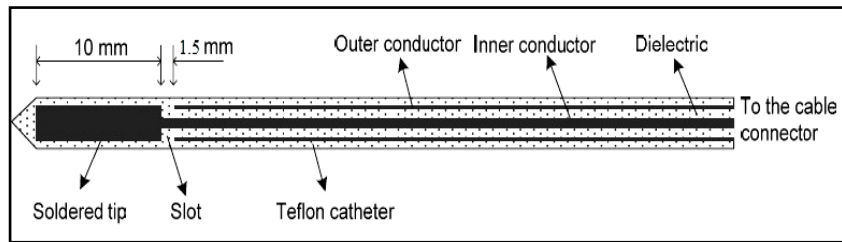


Figure 14. Schematic of the coaxial dipole antenna (Maini, Surita & Marwaha, Anupma, 2012).

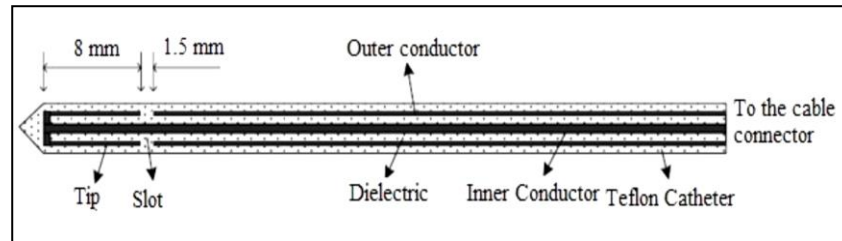


Figure 15. Schematic of the coaxial slot antenna (Maini, Surita & Marwaha, Anupma, 2012).

It was found that from the surface temperature distribution, dipole coaxial antenna had a long tail and more prone to backward heating which causes detrimental tissue heating along the antenna insertion region with respect to coaxial slot antenna. The lesion produced depend upon the power supplied to the antennas, when the input power was increased, larger lesions produced, but with backward heating problem caused burning of healthy tissues which poses a huge challenge for microwave antenna designs. In the proposed designs, specific tumour geometries needed to be modelled. Array configurations of both designs could enhance the results for more localized heating pattern.

The design and development of a multi-functional near-field antenna that met the challenge of matching the impedance of a rigid 2.2 mm diameter coaxial transmission line to the impedance of cancerous tissue was proposed in (Hancock, Chris P, et al., 2013), enabled in situ tissue type/state measurements to be made, and allowed biopsy samples to be extracted from (or material to be introduced into) the body, all in a single structure. The antenna structure supports the propagation of microwave energy at 14.5 GHz for 50W at the distal end was delivered into tissue. The first phase of the design was based around a small diameter antenna structure for near-field propagation into biological tissue that could be used to perform tissue ablation and measurement only. The second phase included the design of an integrated hollow channel to remove material from, or introduce material into, the body as shown in Fig. 16.

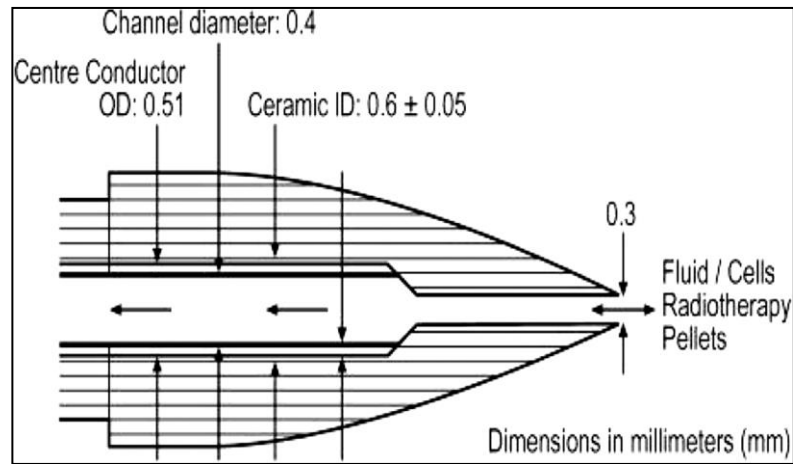


Figure 16. Close-up of the design of the radiating tip that includes the channel used to transport biological tissue or introduce radioactive pellets (Hancock, Chris P, et al., 2013).

The near-field antenna structures were designed and simulated using Computer Simulation Technology Microwave Studio. A biopsy tube was modelled running down the axis of the centre conductor of the coaxial line, and through the end of the ceramic tip. The arrangement of the 4 holes between the inner and outer conductors was modified and spaced by 180° to try to reduce the mismatch and loss. In the proposed design, there was lowering of the peak absorption with introduction biopsy sample in the hollow channel as the power was spread over a larger volume, as there was more power absorbed near the tip, and biopsy worsens the match of the antenna, so less total power is delivered to tumour tissue.

2.1.2. Slot Based Applicator Designs

The authors in (Liu, et al., 2017) introduced minimally invasive multiple-slots antennas with a large radiation pattern for microwave tissue ablation at 2.45 GHz and 60 W. this work presented multiple-slots antenna to perform ablation slices within liver tumours of large sizes. The following model illustrated in Fig. 17 which contains a basic liver tissue and three multiple-slots coaxial antenna. The simulation was carried out in commercial software MULTIPHYSICS COMSOL.

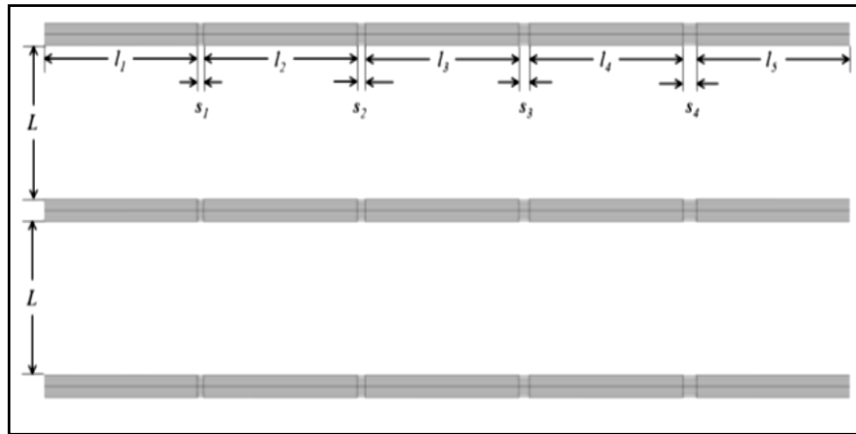


Figure 17. 3D representation of the proposed structure (Liu, et al., 2017).

From simulation results, the ablation has a width of 10 cm and a length of 15 cm. The simulation results will do a great help to the actual application process when the tumours in patients have large size. According to the results, the microwave power was absorbed in the tissue creating cylindrical shape around the antenna and its highest values obtain close to the slot. The simulated heating area formed a flat plane, which will be helpful for the operation. From the results proposed above directional and flat shaped radiation could be achieved using microstrip antenna designs to minimize the complications associated with multiple incisions which may cause superficial burns from excessive backward heating with the high-power level used above.

The work presented in (Luján, et al., 2017) consists of the modelling of two microwave antennas to treat bone tumours. The main goal to design antennas to treat specifically bone tumors is to focus the electromagnetic energy to the bone while the surrounding healthy tissue is minimally affected. The several study scenarios were proposed to evaluate the performance of each antenna: 1) slot length, 2) antenna insertion, 3) antenna irradiating bone 4) antenna irradiating a multi-layer tissue and 5) input power and application time. Figure 18 describes the geometry of the proposed antennas. 2.45 GHz was chosen as a work frequency.

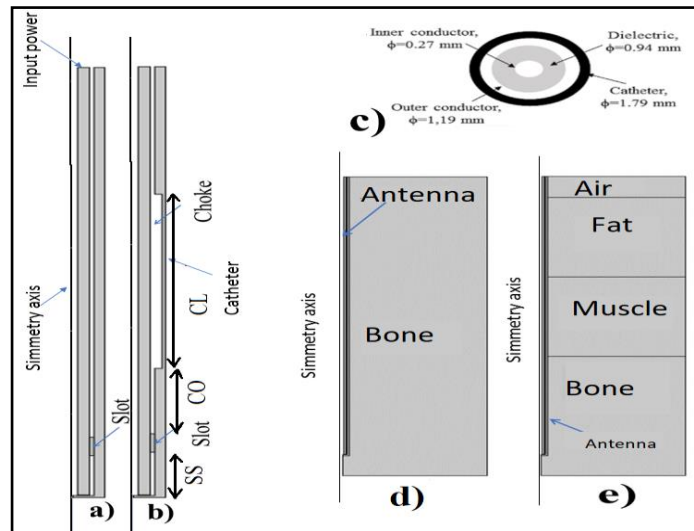


Figure 18. Geometry description of the proposed antennas. a) One Slot antenna, b) One slot choked antenna, c) Transversal description of the antenna body, d) Model used to predict the outcome when bone tissue is irradiated, e) Model used to predict the outcome when a multi-layer tissue is irradiated (Luján, et al., 2017).

From thermal results, tissue overheating was observed near slot which can be attributed to the lack of control on the amount of power and long duration of radiation exposure. The temperature levels required to perform bone drilling or eradicating bone lesions as proposed in literature exceeds 100°C (Phairoh, C, et al., 2013) which using either proposed designs may hinder necessary longer ablation times to provide more confined zones and protect surrounding healthy tissues.

In (Trujillo-Romero, CJ, et al., 2017), a new micro-coaxial double slot antenna for thermal ablation in bone was analysed. The antenna was modelled to predict temperature increase in bone, due to the MW energy. The ability to heat up bone tissue at hyperthermia, ablation and vaporization levels, among other parameters, was analysed. A double slot micro-coaxial antenna was proposed with each slot guide the EM radiation to the targeted tissue. The operating frequency of the antenna was chosen to be 2.45 GHz. As shown in Fig. 19, a 3D model, which consists of a micro-coaxial antenna and a femur section, was proposed. The antenna was made of micro-coaxial cable and the slots were located over the external conductor as a ring.

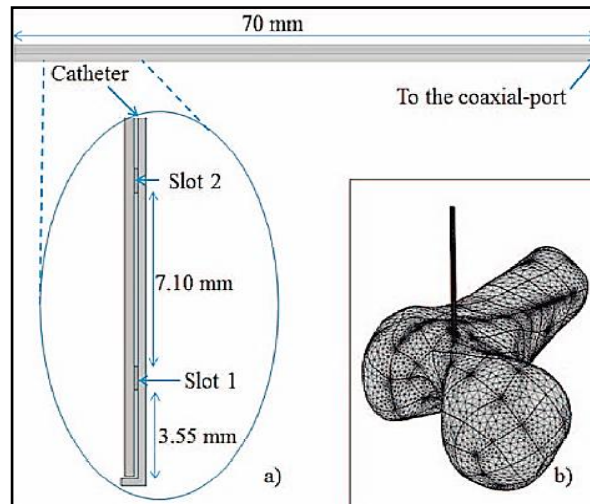


Figure 19. Geometries used to model the micro-coaxial antennas. a) 2D Axisymmetric view of the 3D double slot antenna, b) 3D model of the antenna inserted in the bone section to be heated, and an example of the mesh used for the analyses based on the finite element (Trujillo-Romero, CJ, et al., 2017).

First the EM simulations were completed and the specific absorption rate (SAR) was calculated which was used as an input to the thermal models. To know the performance and the efficiency of the double slot antenna to generate thermal ablation in bone, the next case scenarios were analysed. Three input power levels were studied. Two constant input powers (5 W and 10 W) and a variable input power (analytical function, which describes an input power varying from 8 W to 3 W during the 15 minutes of treatment). For variable input power, performance of the antenna is better. The volume of tissue under vaporization was lower and the volumes of the tissue under hyperthermia and ablation (therapeutic effect) were kept at the highest values. From simulation results, Reduction of the treatment time may be considered to avoid overheating ($>100^{\circ}\text{C}$) and therefore reduction of the amount of tissue under vaporization. Reduction of the input power levels to achieve therapeutic temperatures may result in longer ablation time. In addition, the applicator must be moved to cover more volume in case of low input power which might be inconvenient for patients undergo such procedure.

In (Martínez-Valdez, R., et al., 2017), A 2D axisymmetric model, which consists of the micro-coaxial antenna and a rectangular section to simulate the bone tissue, was proposed. The antenna was made of micro-coaxial cable and the slot was located over the external conductor as a ring. EM simulations were completed and the specific absorption rate (SAR) was calculated which was used as an input to the thermal models. Parametric studies were applied to determine the worst and the best parameters (frequency, slot length and location), to get the worst and the best results regarding SWR and area covered by therapeutic temperatures. From simulation results, Reduction

of the treatment time may be considered to avoid overheating ($>100^{\circ}\text{C}$) and therefore reduction of the amount of tissue under vaporization. Slot based antennas suffers from excessive backward heating which necessitates the use of baluns to minimize the damage of healthy tissues along the antenna shaft.

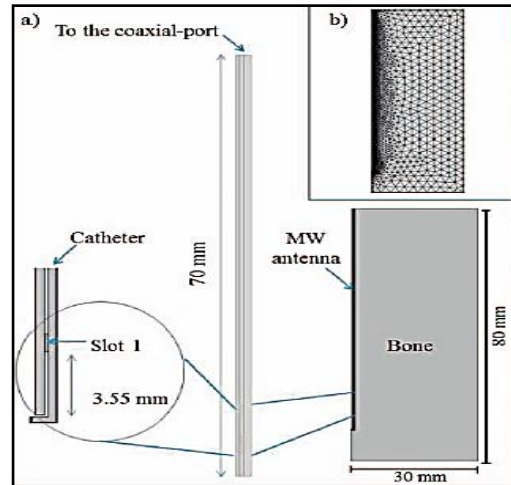


Figure 20. Geometry used to model the micro-coaxial antenna. a) 2D axisymmetric view of the micro-coaxial antenna with one slot and its insertion in bone tissue, b) example of the mesh used for the analyses based on the finite element method (Martínez-Valdez, R., et al., 2017).

In (Sawarbandhe, Mahesh D., et al., 2016), coaxial slot antenna was designed as shown in Fig. 21(a). Copper is used as inner and outer conductor while dielectric between them is PTFE. The distance of slot from the tip is one fourth of effective wavelength; because that the slot antenna behaves same as dipole antenna. Return Loss recorded in simulation and experimental results - 13.3 dB and -18.7 dB respectively. Radiation pattern of the proposed antenna is omnidirectional and the obtained VSWR was found to be 1.54 at the operating frequency.

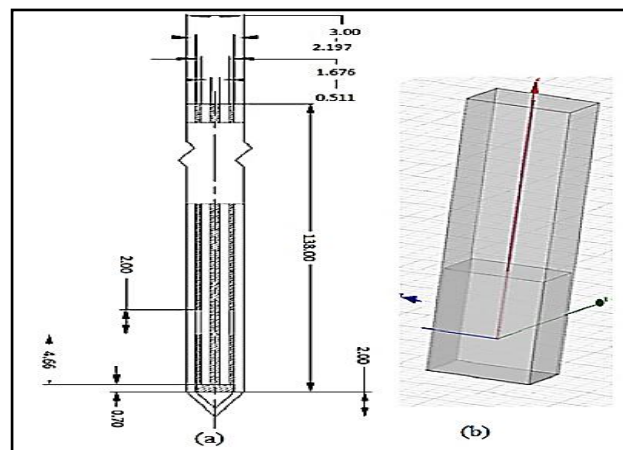


Figure 21. (a) Structure of Coaxial Antenna (all units in mm), (b). HFSS simulation of Antenna (Sawarbandhe, Mahesh D., et al., 2016).

From the simulation and experimental results, the reflection recorded was so much higher than that of several slot-based coaxial antennas introduced in literature which hinders the antenna to effectively eradicate the tumour tissues.

In (Razib, Alimul, et al., 2016), the simulation analysis of single slot Microwave Coaxial Antenna (MCA) for different slot positions was studied. Figure 22 shows 3D model of a basic breast tissue with a tumor and a single slot coaxial antenna which using COMSOL with different slot positions. MCA was excited at operating frequency of 2.45 GHz with a power of 10 W.

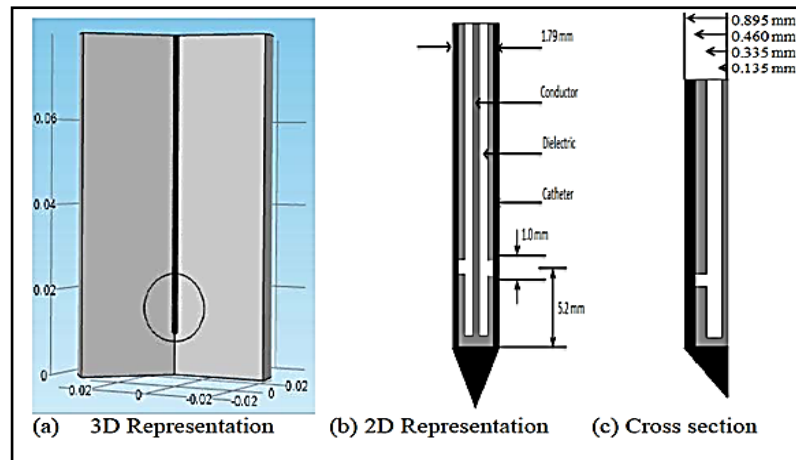


Figure 22. Schematic diagram of a breast tissue with tumor (Razib, Alimul, et al., 2016).

From simulation results, the highest surface temperature is 477K for $t = 2$ min and the slot position is at 50% of the tumor where the tumour gets fully burnt with less damage to normal tissues. However, more healthy tissues get damaged and tumour was not fully destroyed for slot position of 75% and 25% of the tumor. In addition, in all cases, the microwave power was absorbed in the tumor creating ellipsoidal shape around the antenna slot and its highest values obtain close to the slot and decreases with the distance. From the simulation analysis, microwave power absorption, SAR distribution, temperature distribution was directly dependent on slot positions. From the analysis, when the antenna is placed in the centre of tumour tissue, equal distribution of microwave power will be generated within the cancerous cells results in tissue being successfully ablated after the ablation procedure. In addition, lower power levels are recommended as they provide more control over the resulting ablated lesion and minimize radiation exposure of surrounding healthy tissues. Temperature levels generated in all cases will produce charred or desiccated tissues which degrades the antenna performance during the procedure.

(Gas & Szymanik, 2018) described the coupled electro-thermal problem of local heating of hepatic tumors during microwave ablation treatment using proposed multi-slot coaxial antenna. A 2D axisymmetric model of multi-slot antenna has simple structure as illustrated in Fig. 23. Such thin needle applicator is made of two coaxial conductors separated by a cylindrical dielectric layer with a 50-ohm feeding.

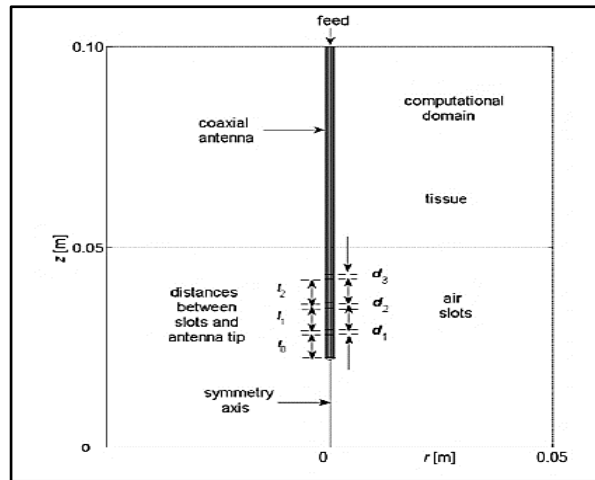


Figure 23. multi-slot coaxial antenna and its model including the antenna dimensions (Gas & Szymanik, 2018).

S-parameter was found to be -44.24 dB at 2.45 GHz. A 20.53 W power achieved ablation zone of radius 8.5 mm. The obtained S11- parameter distribution confirmed that, for new dimensions of the antenna slots and their arrangement, the antenna resonant frequency. In the next step of optimization procedure, the total input power elevations of the microwave applicator were selected in such a way that the tissue temperature does not exceed the limit values for thermal ablation, i.e. 50 – 110°C.

2.1.3. Looped, Helical Based Applicator Designs

Authors in (Maini & Shekhawat, 2018) proposed Copper Tube Sleeve Coaxial Spiral Antenna. The proposed design was optimized with 10 numbers of turns for liver at a frequency of 2.45 GHz as shown in Fig. 24. The important feature of the proposed antenna is that it increases the area of conduction of microwaves which increases the capacitance per unit length of the coaxial line, which can be considered as effective parallel capacitors.

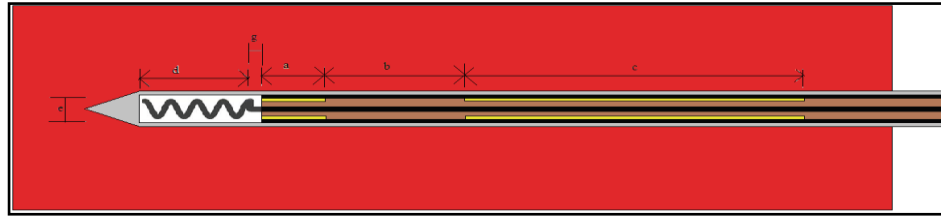


Figure 24. Copper Tube Sleeve Coaxial Spiral Antenna (Maini & Shekhawat, 2018).

From simulation results, it was found that the proposed design provides reflection coefficient (S_{11}) of the order of -37.19 dB for number of turns 10. SAR was observed that 9.99 watt was accepted by the liver from 10-Watt incident power. For the entire tissue mass 0.538 Kg with the average power of -17.27 dBm, the total SAR in terms of power is 42.64 dBm/kg. From the electromagnetic and thermal analysis of the proposed design, despite the compact size of the antenna, the radiation within the liver model is rectangular shaped pattern, therefore, it more suitable for treating tumours with rectangular shapes. Operating the antenna at low frequency bands produces inhomogeneous SAR patterns and the ablation process will be prone to hot spots in the targeted lesion.

In (Vojackova, Lucie, et al., 2014), the article demonstrated the possibility of utilization of interstitial applicators virtually organized in several configurations for the treatment of the breast cancer by microwave thermos-ablation. The interstitial helix antenna was adapted and numerically tested, using full wave EM simulator SEMCAD X, at the 2.45 GHz shown in Fig. 25. A simple homogeneous breast phantom with a 2mm skin layer considered here was taken from literature. For this study a spherical tumour of diameter $d = 20$ mm was virtually placed into the breast phantom. First, one applicator was examined, and results showed that part of power was absorbed by skin and healthy tissue, also it was obvious that the SAR distribution quantity was not homogenous in the whole tumour volume. Then two applicators were placed and SAR in the volume of a sphere is more homogeneous.

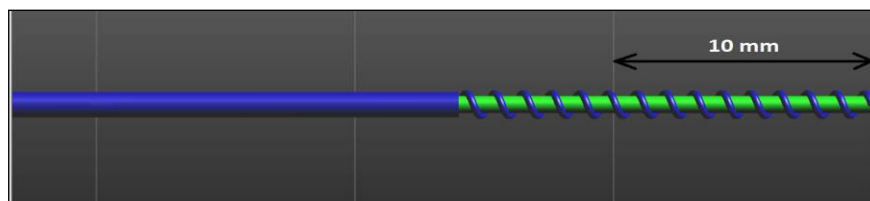


Figure 25. Detail of a helix modelled in SEMCAD X (Vojackova, Lucie, et al., 2014).

Thermal simulations for the configurations with one and two applicators were done to ensure thermos-ablation procedure (temperature higher than 45). It was found that due to the tumour volume the use only one or two applicators was enough. Usage of two applicators is better because the temperature in skin is not so high in comparison to the case with one applicator. Array configuration of the proposed applicator may not be suitable for treating tumours near vessels which need more directional heating patterns depending on the tumour shape to avoid radiation exposure to vessels or healthy tissues (Karampatzakis, Andreas, et al., 2013; Thongsopa & Thosdeekoraphat, 2013; Ortega-Palacios, Rocío, et al., 2012; McWilliams, Brogan, et al., 2015).

In (Luyen, Hung T., et al., 2015), two new classes of recently developed in (Luyen, et al., 2015; 2014) for interstitial MWA were discussed. The first class of antennas comprises a balun free helical radiator fed at its base with a coaxial cable shown in Fig. 26. When this antenna is operated at its second resonant frequency, the feed point acts as a natural high impedance point and chokes the current flow on the outer surface of the feeding coaxial cable. Due to the large impedance mismatch between the feeding coaxial cable and the antenna, an impedance matching network is used within the feeding coaxial cable that matches the high feed-point impedance to the lower impedance of the feeding cable.

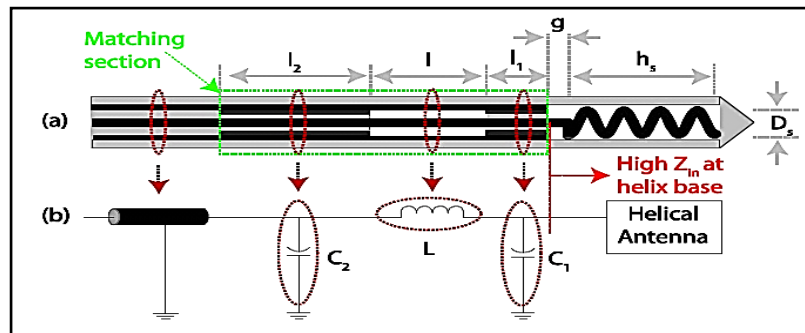


Figure 26. (a) Topology of the proposed helical antenna and matching section. Dark grey represents copper, light grey represents Teflon, and white represents air. (b) Equivalent circuit model of the matching section (Luyen, Hung, et al., 2015; 2014).

The second class of antennas comprises balanced dipole or loop antennas fed with balanced, shielded two-wire transmission lines. In this case, the balanced two-wire line is placed inside a hollow conductor that acts as a floating shield and does not allow the fields of the line to penetrate the surrounding region. The antennas were operated at 10 GHz. Figure 27 shows an example of a dipole and a loop antenna fed using such a line. In such a structure, the current flowing on one

conductor of the feeding line (and one antenna arm) is balanced by the current flowing on the other conductor (and the other antenna arm). Therefore, no RF current flows on the outer surface of the floating shield.

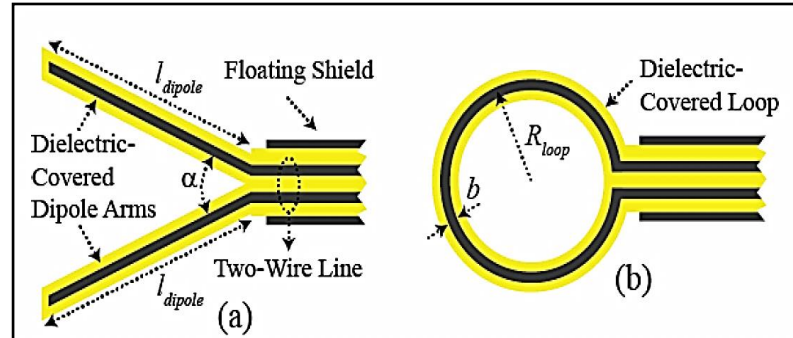


Figure 27. Topology of a balanced dipole (a) and loop (b) antenna fed with a shielded two-wire line (Luyen, Hung T., et al., 2015).

In aforementioned designs, limitations of the fabrication process yielded to use lower performance pi matching network instead of using better performance quarter wavelength transformer (i.e. broader bandwidth and better impedance matching). Smaller diameter of catheter is needed for smaller sized antennas to achieve more comfortable less invasive procedures for the patients.

2.2. Critical Evaluation of Literature

Several antenna designs have been proposed in the aforementioned literature to achieve more compact applicator with low return loss to increase the power deposited within the tumour tissue and in turn achieve the required temperature levels and SAR value for successful ablation procedure. Most of antenna designs proposed use either linear element or coaxial slot as their primary mode of radiation and can be categorized as follows:

- Designs primarily comprised of a linear element include monopoles, dipoles, tri-axial, cap disk and tapered cap antenna design as shown in Fig. 28. These antennas are highly efficient with good broadside radiation patterns. However, without design modification they are relatively narrowband and have elongated patterns. Moreover, Broadside radiation is found not to be suitable radiation for ablating large focal tumours with nearly spherical shape. These designs may result in existing tumour tissues not being successfully ablated which justified the use of high input power to force full destruction of untreated cancerous lesions (Sanpamch, et al.,

2015; Brace, Christopher L, et al., 2005; Alnassan, Hussein, et al., 2014; Hürter, W, et al., 1991; Labonte, Sylvain, et al., 1996; Tal, et al., 2015; Huang, Chi-Fang, et al., 2014; Schaller, Gerd, et al., 1996; Strickland, AD, et al., 2002).



Figure 28. Schematic cross sections of monopole, dipole, tri-axial, Cap Disk and Tapered Cap antenna designs for microwave ablation.

- Coaxial or slot antenna designs radiate from a smaller point and can be designed to produce relatively low reflections with acceptable radiation patterns and their smaller radiation point can be desirable for ablation of small volumes. However, single slot antennas suffer from excessive backward heating along the antenna shaft without design modification which may damage healthy tissues surrounding the tumour and antenna shaft. *Baluns* such as floating sleeves and chokes are proposed to overcome the backward heating problem associated with coaxial slots as depicted in Fig. 29. However, *baluns* add to the total antenna diameter, making them less attractive for use in percutaneous applications. The word *balun* is referred to the structure that links a *balanced* two-conductors' transmission line to *unbalanced* line such as coaxial transmission line (John & Ronald , 2002). Natural chokes are proposed in the literature by selecting the operating frequency to be at the second harmonic frequency with much higher reflection which necessitate the use of matching sections such as quarter wavelength transformer or pi-network to lower the high reflection at the selected operating frequency and minimize the damage of the surrounding healthy tissues due to backward heating (Luyen, Hung T., et al., 2015; Lin, James C & Wang, Yu-Jin, 1996; Hancock, Chris P, et al., 2013; Maini, Surita & Marwaha, Anupma, 2012; Maini, Surita & Marwaha, Anupama, 2013; Longo, Iginio, et al., 2003; Luyen, et al., 2015; Hamada, L, et al., 2000; Gas & Szymanik, 2018).

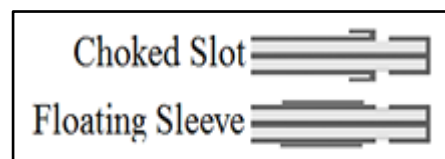


Figure 29. Schematic cross sections of choked and floating sleeve coaxial slot antennas.

- Looped and helical antenna designs illustrated in Fig. 30 have been reported for tissue ablation treatment. Looped antenna designs have been described for cardiac ablation (Gu, et al., 1999; Shock, et al., 2004; Reimann, Carolin, et al., 2016; Mays, R. Owen, et al., 2016). With the advantage of size compactness and homogenous SAR distribution, helical antennas operating in normal mode have been described for liver and breast ablation treatment (Vojackova, et al., 2014; Luyen, et al., 2015; Yu, Nam C, et al., 2006).

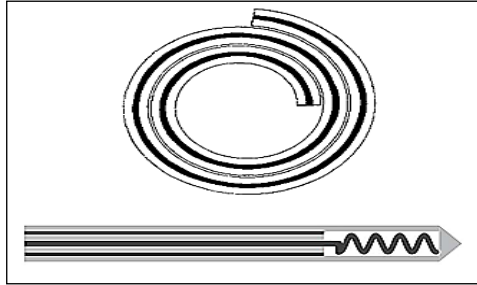
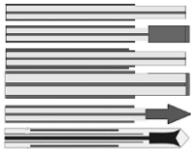
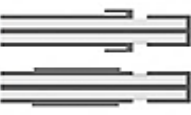



Figure 30. Schematic cross section of spiral and helical antenna presented in the literature for tumour ablation.

Since the helix dimensions are very small fraction compared to wavelength, helix will operate in normal mode ($n L \ll \lambda$) where n is the number of turns and L is the length of single turn. Its radiation pattern is an Omni-directional pattern similar to short straight conductor parallel to the helix axis. However, helical antenna designs operating in normal mode given the critical dimensions of the helix provide omni-directional patterns and large portion of the applied power was absorbed by the skin and healthy tissues surrounding the targeted tumour due to high mismatch losses.

A brief comparison between antenna designs proposed in microwave ablation therapy is illustrated in Table 2 highlighting the advantages and drawbacks of each design approach and expected solutions suggested by previous research which still have limitations yet to be alleviated.

Table 2. Comparison between Antenna Designs proposed in Literature

Antenna type	Structure	Features	Shortcomings yet to be solved	Proposed Solutions
Linear based Design		<ul style="list-style-type: none"> -Highly efficient -Omni-directional radiation 	<ul style="list-style-type: none"> -Relatively narrowband -Elongated patterns -Unsuitable for ablating large focal tumours with nearly spherical shape (cancer cells not being successfully ablated). 	<ul style="list-style-type: none"> - Floating sleeves and chokes are proposed as baluns to overcome the backward heating problem. - Increased antenna size which may lead to superficial skin burns . - Less desirable for percutaneous applications (Martínez-Valdez, R., et al., 2017; Sawarbandhe, Mahesh D., et al., 2016; Brace, Christopher L, 2010; Luyen, Hung, et al., 2017; Luján, et al., 2017; Preston, et al., 2018; Fallahi, Hojjatollah, et al., 2017; Mohtashami, Yahya, et al., 2017).
Slot based Design		<ul style="list-style-type: none"> -Relatively low reflections -Acceptable radiation patterns -Suitable for ablation of small volumes. 	<ul style="list-style-type: none"> -Excessive backward heating along the antenna shaft which may damage healthy tissues surrounding the tumour and antenna shaft. 	
Helical or Looped Based Design		<ul style="list-style-type: none"> -Compact size -Homogenous SAR distribution due to high power density 	<ul style="list-style-type: none"> -High Mismatch losses -Large portion of applied power absorbed by skin and healthy tissues surrounding the targeted tumour. 	

A brief overview on several conventional designs was presented in the literature. These designs were classified as a linear element, coaxial slot, looped, or helical-based designs. These are highly power efficient designs, with good broadside radiation patterns. However, they are relatively narrowband, and radiation can be prone to hot spots or elongated patterns. In addition, coaxial or slot antennas are designed to produce relatively low reflections with acceptable radiation patterns and are desirable for ablation of only small volumes. However, proposed slot antenna designs suffer from excessive backward heating along the antenna shaft without design modification. Coaxial chokes were proposed to reduce the backward heating by eliminating the current on the outer conductor of the coaxial cable. However, chokes add to the total antenna diameter, making them less desirable for use in percutaneous applications. Continually improving antenna performance such as minimum reflection, wider bandwidth, size compactness along with focused energy radiation are considered indispensable and most challenging requirements of antenna design to ensure optimal microwave ablation treatment procedure.

2.3. Applicator Design Considerations for Successful Ablation

The following applicator design considerations are summarized to narrow down the basic requirements to attain optimum applicator design and successful ablation

- Prior understanding of tumour shape and its peripherals helps synthesizing the required electric field which generates heating conformal to the actual tumour shape and minimizes unnecessary radiation exposure.
- Creating EM radiation conformal to a cancerous lesion shape is manifested by calculating current distributions on antenna surface using Maxwell equations and applying boundary conditions to reach the desired EM radiation.
- Highly-directed (End-Fire) radiation within targeted region is more efficient in creating confined homogeneous heating reaching sufficient temperature levels required for successful ablation i.e. temperature greater than or equal 50°C rather than omni-directional (Broadside) radiation with zero-radiation regions and undesired radiation towards surrounding healthy tissues (Hancock, 2014; Brace, Christopher L, et al., 2005; (Balanis, Constantine A., 2005).

- ▶ Achieving the acceptable ablation safety margins where 50°C contour encompasses and eradicates a radial distance extending from 5 to 10 mm of surrounding healthy tissues away from tumour boundary to assure no transfer of cancerous cells through blood vessels ensure complete eradication of tumour and its peripherals. This alleviates the possibility of cancer recurrence (Prakash, Punit, 2010; Poulou, Loukia S, et al., 2015; Singh & Repaka, 2017).
- ▶ Operating at higher frequencies than 0.9, 1.5 and 2.45 GHz commonly used in microwave ablation targets higher thermal conductivity which in-turn increases energy absorption within targeted regions and provide more size compactness of the applicator and confined heating (Hulsey, et al., 2015; Hancock, 2011; Brace, Christopher L, et al., 2004; Brace, Christopher L, et al., 2005).
- ▶ Directed radiation helps lower the input power required for ablation and provide more control over heating within the targeted lesion.
- ▶ Maintaining less than -10-dB reflection (maximum acceptable voltage standing wave ratio VSWR is 2.0) stability over wide frequency range is indispensable to overcome increase in reflection during ablation (Balanis, Constantine A., 2005).
- ▶ Heterogeneous dielectric properties and disparity of water content in single biological tissue hinder creating successfully ablated lesion using narrowband operation which enquires wide band feature to helps provide minimum reflection stability during ablation, save as much healthy tissues as possible and alleviates possibility of tissue not being successfully ablated.

Chapter three

Semi-analytical Numerical Nearfield Calculation of TDFT Antenna

3.1. Introduction and Overview of Opened-Out Coaxial Line Antennas

Research began with investigating several types of antenna designs, differentiating between the performance of each antenna based on the previous considerations by identifying the drawbacks and advantages of each design. It was found that most commonly used antenna designs have a narrowband feature and used high input power which was ineffective in treating a single biological tissue with such heterogeneous properties according to the percentage of water content and fats within the tissue. Moreover, choosing the antenna design is basically determined by the shape of the radiation and the consequent thermal heating desired to successfully eradicate the targeted lesion. Slot based designs as mentioned earlier in chapter 2, suffer from excessive backward heating and it is basically suitable for small tumours. In addition, looped or helical antennas have the advantage of providing high power density. But on the other hand, helical antennas with normal mode operation have critical dimensions and offer a narrowband feature which hinders the stability of antenna performance as it significantly deteriorates with the shifting of the operating frequency during ablation. This can be observed in overheating of the cable and high reflection encountered with helical antennas yielding superficial skins burns and complications during ablation (Vojackova, Lucie, et al., 2014; Maini & Shekhawat, 2018).

For linear based element such as dipole, monopole and triaxial designs, they are distinguished by easy of insertion and high efficiency over a very narrow band and inhomogeneous radiation especially in the axial direction which cause the antenna performance to be susceptible to change in frequency of operation as a result of tissue dehydration and provide tissues not being successfully destroyed after ablation (Brace, Christopher L, 2010).

Also, it was believed that designing a specific type of antenna to create a customized thermal profile is one of the major limitations of these designs as it requires selectively heating targeted lesion with minimum radiation exposure towards surrounding healthy tissue. Existing microwave applicators produce unconformable electromagnetic radiation which yields inhomogeneous energy deposition and results in tissues not being successfully eradicated.

In this section, we investigate that controlling the shape of applied electric field yields to control SAR pattern which in-turn synthesizes controlled and confined temperature profiles using low input power. As demonstrated from literature, temperature distribution is found greatly dependent on SAR pattern and applied electric field which can be evaluated by identifying the corresponding current distribution on the antenna surface. Synthesizing a customized temperature profile was proposed in literature using an array of linear-based antennas to achieve the desired electric field distribution, by using a linear-based array of discrete current sources (Sharma, Shashwat & Sarris, Costas D., 2016).

This research proposes a synthesized microwave antenna to provide axially and rotationally uniform directed electric field yielding homogeneous and confined heating within the targeted cancerous lesion. Using low power along with alleviating high reflection due to shift in frequency of operation during ablation associated with narrow-band designs, ultra-wide band feature was chosen to overcome such limitations providing enhanced performance and maintaining minimum reflection stability during ablation.

Antenna types are defined and categorized based on how they are initially synthesized for instance wire, stubs, slots and aperture antenna designs. These types are classified and arranged as an evolutionary sequence from wide to narrow bandwidth over various studies and research. Due to the advent of modern digital communication techniques, several antenna designs have been developed over the years to fulfil the grown demand in higher-bandwidth antennas. Ultra-Wideband (UWB) is a widely recognized in wireless technology for low power, interference immune and high data rate applications like radar imaging, position localization, sensor data collection and medical imaging. Therefore, numerous antenna designs have been proposed in literature to achieve the most significant requirements for UWB technology.

Applicator designs as previously mentioned in section 2.2 such as slot-based designs are suitable for treating only small tumours and excessive backward heating hinders these designs to apply confined heating with minimum damage towards surrounding healthy tissues. In addition, due to critical dimensions of helical-based designs and change in dielectric properties of the surrounding tissues during ablation, antenna performance deteriorates significantly during ablation and as they provide broadside radiation, undesired radiation towards surrounding healthy tissues is encountered and damage large portion of the organ after the procedure. Therefore, investigating linear-based radiator to achieve more directed axial radiation with wide band feature is the main

challenge in this work to provide directed EM radiation and hence confined heating within the targeted area.

One of commonly known designs evolved for UWB technology are opened-out coaxial-line based designs. Figure 31 illustrates the classification of coaxial-line based antennas. They are introduced in such a way that provides better understanding of how one type evolves into another. It is clearly observed from Fig. 31, that antennas with abrupt discontinuities have large reflections such as conventional monopole antenna where reflections cancel over very narrow frequency bands, while antennas with small and gradual discontinuities such as volcano-smoke antenna have small reflections over wide frequency bands (Kraus, John D & Marhefka, Ronald J, 2002).

As shown in Fig. 31, Opened-out coaxial line antennas are evolved from the very broadband gradually tapered “Volcano-smoke” through intermediate bandwidth “Conical antennas” to the narrowband of quarter-wavelength monopole antenna. In addition, these designs are omnidirectional in the azimuth plane with null radiation along the vertical (zenith) direction.

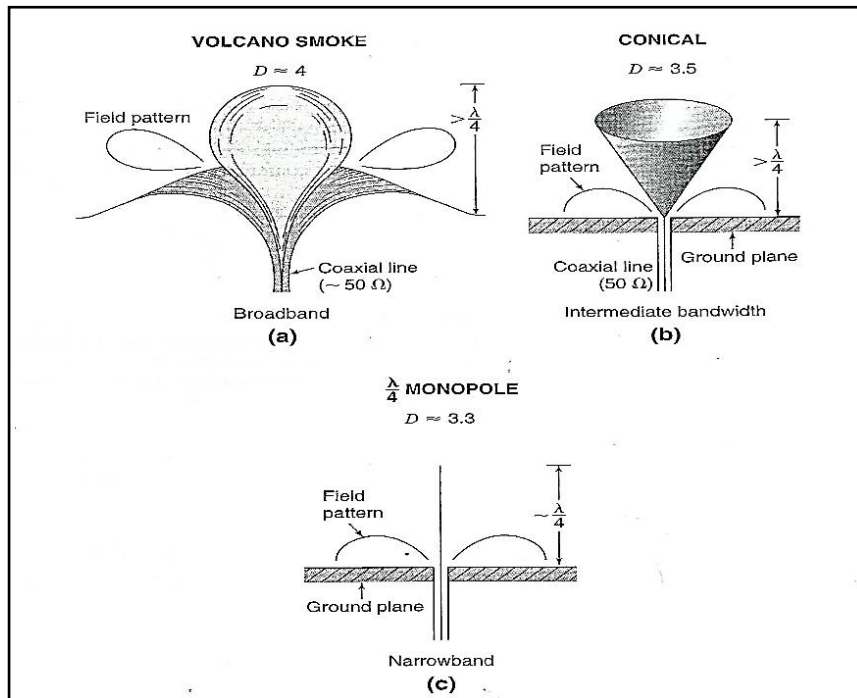


Figure 31. Evolution from (a) broadband gradually tapered volcano smoke through (b) intermediate bandwidth Conical antenna to (c) narrow bandwidth $\lambda/4$ monopole (John & Ronald , 2002).

It is believed that the volcano smoke antenna (VSA) topology offers the unique advantages of simplicity, exceptional bandwidth over other broadband antennas. Nevertheless, one of the

limitations associated with VSA is the fabrication process which is prone to inaccuracy and leads to inadequate results. Due to the abrupt transition between the coaxial cable and 3D bulb structure associated with conventional VSA, high impedance mismatch occurs at the junction between the bulb and coaxial feed which affects all frequencies of operations and lead to disruption of VSWR (Lopez, Aida Garcia, et al., 2013; Paulsen, Lee, et al., 2003). In addition, all antenna designs presented in Fig. 31 have relatively low directivities and offers broadside radiation with null along the antenna axis.

Several antenna designs are widely evolved in the history of UWB development activities due to constant demand of higher data rate and multiservice wireless applications (Yeoh & Rowe, 2015; Schantz, 2012). One of which are conical-based antenna designs. Several examples of conical antennas are proposed in the literature, such as conventional conical monopole and biconical antenna (Balanis, Constantine A., 2005), and the planar inverted cone antenna (PICA) (Suh, et al., 2004). Conical monopole antenna is adopted in this work because of its exceptional wideband feature, compact size and ease of implementation. Extensive parametric studies distinctly presented in literature of conical structures to achieve impedance matching over ultra-wide bandwidth for several wireless applications. Figure 32 shows an example of conical antenna design and its radiation pattern at different operating frequencies. As stated in (Yeoh & Rowe, 2015), it was noticeably showed that the wider the flaring of radiating end of the antenna structure is, the narrower the beam-width of the radiation pattern is, hence more directional radiation especially at higher frequencies when antenna dimensions become larger compared to wavelength as depicted in Fig. 32 (Yeoh & Rowe, 2015). It was also investigated that wider flaring angle gives shorter conical length at the same frequency of operation (Yeoh, et al., 2010).

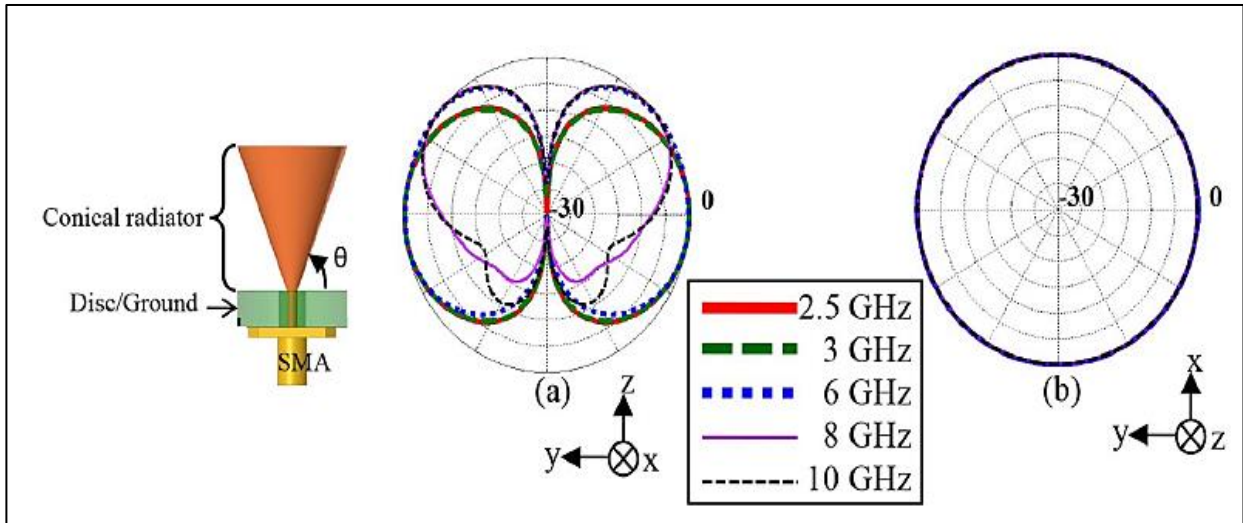


Figure 32. Conical monopole antenna and its radiation pattern in both elevation (on the left) and azimuth planes (on the right) (Yeoh & Rowe, 2015).

Nevertheless, their exceptional impedance matching over ultra-wide bandwidth, most conical monopole antennas have a flat truncated tip which abruptly minimizes currents excited on the antenna tip and gives broadside radiation with null along cone axis regardless how wide the cone angle θ is. To provide EM radiation equally distributed within the selected area as mentioned earlier, axially directed radiation is essential to directed maximum power within the selected tumour. This directional radiation helps creating confined heating and reaching temperature levels required for complete cell destruction i.e. temperatures exceed $50\text{ }^{\circ}\text{C}$ where irreversible changes of tissue properties occur and results in instantaneous cell death when temperatures reach $60\text{ }^{\circ}\text{C}$ and above. To provide such radiation, a study of structural optimization of conical monopole antenna is performed to investigate the potential of axially directed EM radiation in providing confined heating and successful ablation. In order to achieve axial directed radiation, a taller and fine elongated tip is implemented on a classical conical monopole antenna as a new radiating element to create longer path for currents excited on the antenna surface and cause slow deceleration of charges on the antenna tip which generates electric field in the axial direction perpendicular to direction of currents excited on the antenna tip according to boundary conditions of electric field illustrated in the following equations (Balanis, Constantine A., 2005; John & Ronald, 2002).

$$n_{12} \times (E_2 - E_1) = 0$$

$$n_{12} \times (D_2 - D_1) = \sigma_s$$

Where n_{12} is the normal vector on the interface surface between medium 1 and medium 2, E_2 and E_1 are Electric field intensities in medium 2 and medium 1, respectively. D_2 and D_1 are electric displacement field in medium 2 and 1, respectively and σ_s surface charge on interface surface. Proven from Faraday's law i.e. Difference in electric field and any tangential component on the interface surface have a dot product equal to zero and therefore electric field has only one component parallel to normal vector (n_{12}) and its cross-product with normal vector (n_{12}) to the interface surface is equal to zero (Balanis, Constantine A., 2012).

Extensive parametric analysis is to be conducted taking into consideration that there are critical factors to be preserved when designing an antenna as microwave applicator of cancer ablation which are listed as follows:

- Maximum diameter of the antenna should not exceed 3.5 mm in order not to cause complications after the ablation procedure (see chapter 1 section 1.4) (Brace, Christopher L, 2010; Brace, 2009; Hancock, et al., 2015).
- Minimum diameter of the antenna to facilitate fabrication, give better power handling capability of the coaxial feed and to dissipate heat especially at high frequencies is 1mm.

With considerations mentioned above, there will be constraints on the degree of gradient of conical angle i.e. flaring of conical tip to attain the performance required for successful ablation (see section 2.3 in chapter 2). In the next section, analytical and computational evaluation of the current distribution and consequent nearfield distribution produced by the new radiating MW applicator is presented and will be further compared and validated using the one obtained using commercial software packages.

3.2. Synthesis of Antenna geometry

New hemispherical tipped conical monopole antenna is presented in this chapter. Since the new antenna is teardrop like structure, it is referred as teardrop flared tipped (TDFT) antenna and illustrated in Fig. 33. TDFT design is proposed as interstitial microwave applicator for treating focal spherical hepatocellular tumours to provide more precise ablation zones. TDFT design is evolved from a conventional monopole antenna where a hemispherical cap is introduced to excite currents and its subsequent electric field in the axial direction of the antenna unlike fields produced by conventional monopole antenna. TDFT structure consists of a hemispherical tip connected to

an inverted conical structure hypothetically connected at its vertex lowermost to a feed point i.e. assumed to be inner conductor of a coaxial cable whose central axis is coaxially aligned with the axis of the teardrop structure as depicted in Fig. 33. The semi-vertical angle of the conical structure is θ_o and H, R_o, a are cone height, slant cone height and upper radius of the inverted cone, respectively. The height of the inner conductor of a coaxial feed are denoted as h_o . The radius of the hemispherical tip is the same as the upper radius of the inverted cone at $z = H$ and ψ is the semi-subtended angle that extends along the perimeter of the hemispherical tip as shown in Fig. 33.

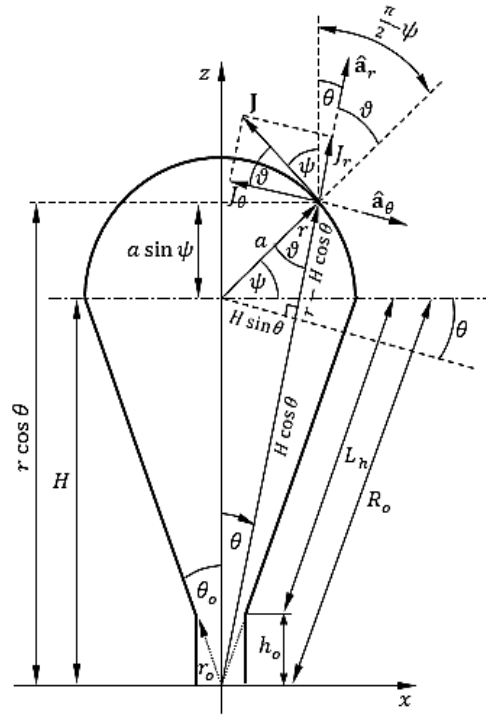


Figure 33. Geometrical representation of proposed TDFT antenna.

3.2.1. Geometrical Relations on the Hemisphere

The upper hemispherical surface has a radius a and center point at $(x = 0, y = 0, z = H)$ and is described by the following equation in Cartesian coordinates (Balanis, Constantine A, 2012),

$$x^2 + y^2 + (z - H)^2 = a^2 \quad (1)$$

To get equation (1) in spherical coordinates, one can use the following relations.

$$r^2 = x^2 + y^2 + z^2 \quad (2-a)$$

$$z = r \cos \theta \quad (2-b)$$

Where r is the radial distance, θ is the polar angle and ϕ is the azimuthal angle.

This results in the following expression for the spherical surface equation

$$\boxed{r^2 - 2Hr \cos \theta + H^2 = a^2} \quad (3-a)$$

Equation (3-a) can be rewritten as:

$$\theta = \cos^{-1} \left(\frac{H^2 - a^2 + r^2}{2Hr} \right) \quad (3-b)$$

The following partial derivatives can be obtained from (3)

$$\frac{\partial r}{\partial \theta} = -\frac{Hr \sin \theta}{r - H \cos \theta} \quad (4-a)$$

$$\frac{\partial r}{\partial \theta} = -r \frac{\sin \vartheta}{\cos \vartheta} \quad (4-b)$$

$$\boxed{\frac{\partial \theta}{\partial r} = -\frac{r - H \cos \theta}{Hr \sin \theta}} \quad (4-b)$$

$$\boxed{\frac{\partial \theta}{\partial r} = -\frac{1 \cos \vartheta}{r \sin \vartheta}} \quad (4-c)$$

The spherical surface can be described by the following equations.

$$a \cos \psi = r \sin \theta \quad (5-a)$$

$$a \sin \psi = r \cos \theta - H \quad (5-b)$$

$$\psi = \sin^{-1} \xi \quad (6-a)$$

$$\cos \psi = \sqrt{1 - \xi^2} \quad (6-b)$$

where,

$$\zeta = \frac{1}{a} (r \cos \theta - H) \quad (7)$$

From the antenna geometry shown in Fig. 33, one can notice

$$\frac{\pi}{2} - \psi = \vartheta + \theta \quad (8)$$

$$\sin \vartheta = \frac{1}{a} H \sin \theta \quad (9-a)$$

$$\cos \vartheta = \frac{1}{a} (r - H \cos \theta) \quad (9-b)$$

$$r = a \cos \vartheta + H \cos \theta \quad (9-c)$$

$$\boxed{\frac{\partial \vartheta}{\partial r} = -\frac{1 \cos \theta}{r \sin \theta}} \quad (10)$$

$$\boxed{\frac{\partial \vartheta}{\partial \theta} = \frac{H \cos \theta}{a \cos \vartheta}} \quad (11)$$

Making use of the relations given by (1) - (7),

$$\frac{\partial \psi}{\partial \theta} = \frac{1}{\sqrt{1 - \xi^2}} \frac{\partial \xi}{\partial \theta} = \frac{-r \sin \theta + \frac{\partial r}{\partial \theta} \cos \theta}{a \sqrt{1 - \xi^2}} = \frac{-r \sin \theta}{a \cos \psi} \left(1 + \frac{H \cos \theta}{r - H \cos \theta} \right) = \frac{-r}{r - H \cos \theta} \quad (12-a)$$

$$\boxed{\frac{\partial \psi}{\partial \theta} = \frac{-r}{r - H \cos \theta}} \quad (12-b)$$

Then it can be reduced to

$$\boxed{\frac{\partial \psi}{\partial \theta} = \frac{-r}{a \cos \vartheta}} \quad (12-c)$$

$$\frac{\partial \psi}{\partial r} = \frac{1}{\sqrt{1-\xi^2}} \frac{\partial \xi}{\partial r} = \frac{-r \sin \theta \frac{\partial \theta}{\partial r} + \cos \theta}{a\sqrt{1-\xi^2}} = \frac{\left(\frac{r-H \cos \theta}{H} + \cos \theta\right)}{a \cos \psi} = \frac{1}{H \sin \theta} \quad (13-a)$$

$$\boxed{\frac{\partial \psi}{\partial r} = \frac{1}{H \sin \theta}} \quad (13-b)$$

Then it can be rewritten as

$$\boxed{\frac{\partial \psi}{\partial r} = \frac{1}{a \sin \vartheta}} \quad (13-c)$$

Half the perimeter of the longitudinal section of the TDFT structure can be expressed as

$$\mathcal{L} = R_o - r_o + \frac{\pi}{2} a \quad (14)$$

3.3. Current Distribution on the Antenna Surface

Current distribution on antenna surface varies significantly with antenna length (\mathcal{L}) compared to wavelength at the operating frequency. Two study scenarios are considered in the analytical model adopting two forms of current distributions, one for free space radiation and the other when antenna is immersed in a lossy homogeneous dielectric medium i.e. biological tissue. Wavelength λ can be calculated using the following formula (John & Ronald , 2002),

$$\lambda_{eff} = \frac{c}{f\sqrt{\epsilon_r}}$$

Where c is the speed of light in vacuum 3×10^8 m/s, f is the frequency of operation in Hz and ϵ_r is the complex relative dielectric permittivity of the surrounding medium (John & Ronald , 2002).

$$\epsilon_r = \epsilon_r - j \frac{\sigma}{\omega \epsilon_o}$$

where, ϵ_o is the permittivity of free space, ϵ_r is the dielectric constant of the medium and σ is electrical conductivity of dielectric medium in S/m.

3.3.1. Current Distribution on Electrically Short Antenna ($\mathcal{L} < \lambda/2$)

For free space radiation, antenna length is considered electrically short compared to the wavelength. Therefore, on the conical surface, the current has only a radial component J_r and can be described as (John & Ronald , 2002; Balanis, Constantine A, 2005),

$$\mathbf{J} = J_o \frac{\mathcal{L} - (r - r_o)}{\mathcal{L}} \hat{\mathbf{a}}_r, \quad r_o \leq r \leq R_o, \quad \theta = \theta_o \quad (15)$$

While on the surface of the hemisphere, the current has two components J_r and J_θ and can be described as (John & Ronald , 2002; Balanis, Constantine A, 2005),

$$\mathbf{J} = J_o \frac{a}{\mathcal{L}} \left(\frac{\pi}{2} - \psi \right) [\cos(\theta + \psi) \hat{\mathbf{a}}_r - \sin(\theta + \psi) \hat{\mathbf{a}}_\theta], \quad R_o < r \leq H + a, \quad 0 \leq \theta \leq \theta_o \quad (16-a)$$

The last expression (16-a) can be rewritten as

$$\mathbf{J} = J_o \frac{a}{\mathcal{L}} (\theta + \vartheta) [\sin \vartheta \hat{\mathbf{a}}_r - \cos \vartheta \hat{\mathbf{a}}_\theta], \quad R_o < r \leq H + a, \quad 0 \leq \theta < \theta_o \quad (16-b)$$

Also, the last expression (16-b) can be rewritten as

$$\mathbf{J} = \frac{J_o}{\mathcal{L}} (\theta + \vartheta) [H \sin \theta \hat{\mathbf{a}}_r - (r - H \cos \theta) \hat{\mathbf{a}}_\theta], \quad R_o < r \leq H + a, \quad 0 \leq \theta < \theta_o \quad (16-c)$$

$$J_r = J_o \frac{a}{\mathcal{L}} (\theta + \vartheta) \sin \vartheta, \quad R_o < r \leq H + a, \quad 0 \leq \theta < \theta_o \quad (17-a)$$

$$J_\theta = -J_o \frac{a}{\mathcal{L}} (\theta + \vartheta) \cos \vartheta, \quad R_o < r \leq H + a, \quad 0 \leq \theta < \theta_o \quad (17-b)$$

3.3.2. Current Distribution on Electrically Long Antenna ($\mathcal{L} \geq \lambda/2$)

For radiation in lossy homogeneous dielectric medium, antenna length becomes greater fraction of wavelength and it is considered electrically long compared to wavelength. Therefore, on the conical surface, the current has only a radial component J_r and can be described as (John & Ronald , 2002; Balanis, Constantine A, 2005)

$$\mathbf{J}^c = J_o (1 - r_c) \cos \kappa r_c \hat{\mathbf{a}}_r, \quad r_o \leq r \leq R_o, \quad \theta = \theta_o \quad (18)$$

where,

$$r_c = \frac{r - r_o}{\mathcal{L}} \quad (19)$$

$$\kappa = \frac{2\pi\mathcal{L}}{\lambda} \quad (20)$$

On the surface of the hemisphere, the current has two components J_r and J_θ and can be described as (John & Ronald , 2002; Balanis, Constantine A, 2005),

$$\mathbf{J}^s = J_o (1 - \xi) \cos \kappa \xi [\sin \vartheta \hat{\mathbf{a}}_r - \cos \vartheta \hat{\mathbf{a}}_\theta], \quad R_o < r \leq H + a, \quad 0 \leq \theta \leq \theta_o \quad (21)$$

where,

$$\xi = \frac{R_o - r_o + \psi a}{\mathcal{L}} \quad (22)$$

The expression (21) can be rewritten as

$$J_r^s = J_o (1 - \xi) \cos \kappa \xi \sin \vartheta \quad (21-a)$$

$$J_\theta^s = -J_o (1 - \xi) \cos \kappa \xi \cos \vartheta \quad (21-b)$$

Superscript s and c denoted to current component on the spherical and conical structure, respectively.

3.4. Evaluation of the Near Field Distribution

For a current distribution \mathbf{J} flowing on conducting medium of surface area S, the radiated electric field can be obtained as follows (John & Ronald , 2002; Balanis, Constantine A, 2005),

$$\mathbf{E} = -j\omega\mathbf{A} - \nabla\Phi \quad (23)$$

where \mathbf{A} is the vector magnetic potential, it can be expressed as (Balanis, Constantine A, 2005),

$$\mathbf{A} = \frac{\mu}{4\pi} \int_S \mathbf{J} G(R) dS \quad (24)$$

and Φ is the scalar electric potential, it can be expressed as (Balanis, Constantine A, 2005),

$$\Phi = \frac{j}{4\pi\epsilon\omega} \int_S (\nabla \cdot \mathbf{J}) G(R) dS \quad (25)$$

where $(\nabla \cdot \mathbf{J})$ is the surface divergence of \mathbf{J} at a point on the antenna surface and $G(R)$ is the Green's function (Balanis, Constantine A, 2005),

$$G(R) = \frac{e^{-jkR}}{R}, \quad R = |\mathbf{r}_f - \mathbf{r}'| \quad (26)$$

Where $\mathbf{r}_f = (r_f, \theta_f, \phi_f)$ is the position vector of a point in radiation zone (near or far) and $\mathbf{r}' = (r', \theta', \phi')$ is the position vector of a point on the antenna surface.

Let us set the following,

$$\mathbf{A} = \frac{\mu}{4\pi} \mathbf{J} \quad (27)$$

where,

$$\mathbf{J} = \int_S \mathbf{J} G(R) dS \quad (28)$$

and,

$$\Phi = \frac{j}{4\pi\epsilon\omega} \mathcal{G} \quad (29)$$

where,

$$\mathcal{G} = \int_S (\nabla_s \cdot \mathbf{J}) G(R) dS \quad (30)$$

Making use of (26) and (28), the expression (22) for the radiated electric field can be written as follows,

$$\mathbf{E} = -\frac{j\mu\omega}{4\pi}\mathbf{J} - \frac{j}{4\pi\epsilon\omega}\nabla\mathcal{G} \quad (31)$$

The vector \mathbf{J} can be expressed in terms of its components as

$$\mathbf{J} = J_r \hat{\mathbf{a}}_r + J_\theta \hat{\mathbf{a}}_\theta + J_\phi \hat{\mathbf{a}}_\phi = J_x \hat{\mathbf{a}}_x + J_y \hat{\mathbf{a}}_y + J_z \hat{\mathbf{a}}_z \quad (32)$$

where,

$$J_x = \int_S J_x G(R) dS, \quad J_y = \int_S J_y G(R) dS, \quad J_z = \int_S J_z G(R) dS \quad (33)$$

The vector magnetic potential \mathbf{A} cannot be evaluated directly in the spherical coordinates using (24) or, alternatively, (27). Instead, it can be evaluated using the integrals in (33). This requires the transformation of the current distribution vector \mathbf{J} into the Cartesian coordinates as follows (Balanis, Constantine A, 2005),

$$\begin{pmatrix} J_x \\ J_y \\ J_z \end{pmatrix} = \begin{pmatrix} \sin \theta \cos \phi & \cos \theta \cos \phi & -\sin \phi \\ \sin \theta \sin \phi & \cos \theta \sin \phi & \cos \phi \\ \cos \theta & -\sin \theta & 0 \end{pmatrix} \begin{pmatrix} J_r \\ J_\theta \\ J_\phi \end{pmatrix} \quad (34)$$

The integrals in (32) can, then, be used to evaluate the components of the vector magnetic potential \mathbf{A} in the Cartesian coordinates. The following transformation should be done to get the components of \mathbf{A} expressed in the spherical coordinates (Balanis, Constantine A, 2005).

$$\begin{pmatrix} A_r \\ A_\theta \\ A_\phi \end{pmatrix} = \begin{pmatrix} \sin \theta_f \cos \phi_f & \sin \theta_f \sin \phi_f & \cos \theta_f \\ \cos \theta_f \cos \phi_f & \cos \theta_f \sin \phi_f & -\sin \theta_f \\ -\sin \phi_f & \cos \phi_f & 0 \end{pmatrix} \begin{pmatrix} A_x \\ A_y \\ A_z \end{pmatrix} \quad (35)$$

The expression in (26) can be used to evaluate the components of \mathbf{A} . The numerical operations to get the components of \mathbf{A} in the spherical coordinates can be carried out as follows,

$$J_r = J_r^s + J_r^c \quad (36-a)$$

$$J_\theta = J_\theta^s + J_\theta^c \quad (36-b)$$

$$\mathcal{J}_\phi = \mathcal{J}_\phi^s + \mathcal{J}_\phi^c \quad (36-c)$$

The terms denoted by superscripts s and c refer to the integrals being evaluated on hemispherical and conical surfaces, respectively which contribute in calculation of the components of magnetic vector potential \mathbf{A} . For simplicity, let us assume that the evaluation of magnetic vector potential \mathbf{A} is at a point in radiation zone (near or far) (r_f, θ_f, ϕ_f) on x-z plane where $\phi_f = 0$

The contribution of the current flowing on the hemispherical surface to the vector magnetic potential \mathbf{A} can be expressed as follows,

$$I_r^s = J_r^s (\sin \theta_s \cos \phi_s \sin \theta_f + \cos \theta_s \cos \theta_f) + J_\theta^s (\cos \theta_s \cos \phi_s \sin \theta_f - \sin \theta_s \sin \theta_f) \quad (37-a)$$

$$I_\theta^s = J_r^s (\sin \theta_s \cos \phi_s \cos \theta_f - \cos \theta_s \sin \theta_f) + J_\theta^s (\cos \theta_s \cos \phi_s \cos \theta_f + \sin \theta_s \sin \theta_f) \quad (37-b)$$

$$I_\phi^s = J_r^s \sin \theta_s \sin \phi_s + J_\theta^s \cos \theta_s \sin \phi_s \quad (37-c)$$

The contribution of the current flowing on the conical surface to the vector magnetic potential \mathbf{A} can be expressed as follows,

$$I_r^c = J_r^c (\sin \theta_c \cos \phi_c \sin \theta_f + \cos \theta_c \cos \theta_f) \quad (38-a)$$

$$I_\theta^c = J_r^c (\sin \theta_c \cos \phi_c \cos \theta_f - \cos \theta_c \sin \theta_f) \quad (38-b)$$

$$I_\phi^c = J_r^c \sin \theta_c \sin \phi_c \quad (38-c)$$

$$\mathcal{J}_r = \int_{\text{Hemisphere}} I_r^s G^s dS + \int_{\text{Cone}} I_r^c G^c dS \quad (39)$$

$$\mathcal{J}_\theta = \int_{\text{Hemisphere}} I_\theta^s G^s dS + \int_{\text{Cone}} I_\theta^c G^c dS \quad (40)$$

$$J_{\phi} = \int_{\text{Hemisphere}} I_{\phi}^S G^S dS + \int_{\text{Cone}} I_{\phi}^C G^C dS \quad (41)$$

3.5. Evaluation of Surface Integrals

3.5.1. Infinitesimal Surface Area in Spherical Coordinates

In spherical coordinates, consider a small infinitesimal length element between 2 points which can be decomposed into (Balanis, Constantine A, 2005),

$$d\mathbf{l} = dr \hat{\mathbf{a}}_r + r d\theta \hat{\mathbf{a}}_{\theta} + r \sin\theta d\phi \hat{\mathbf{a}}_{\phi} \quad (42)$$

Where $\hat{\mathbf{a}}_r$ is the radial unit vector, $\hat{\mathbf{a}}_{\theta}$ is the unit vector that points in the direction of increasing θ and $\hat{\mathbf{a}}_{\phi}$ is the unit vector rays in the direction of increasing ϕ .

For a surface of revolution around the z-axis (the surface equation is independent of ϕ), the infinitesimal surface element can be expressed as (Balanis, Constantine A, 2005),

$$d\mathbf{S} = (dr \hat{\mathbf{a}}_r + r d\theta \hat{\mathbf{a}}_{\theta}) \times (r \sin\theta d\phi \hat{\mathbf{a}}_{\phi}) \quad (43)$$

Performing the cross product in (43), one gets

$$d\mathbf{S} = (r d\theta \hat{\mathbf{a}}_r - dr \hat{\mathbf{a}}_{\theta}) r \sin\theta d\phi \quad (44)$$

By implicit differentiation of both sides of (3) one gets,

$$dr = -\frac{H r \sin\theta}{r - H \cos\theta} d\theta \quad (45)$$

$$d\theta = -\frac{r - H \cos \theta}{H r \sin \theta} dr \quad (46)$$

Substituting from (29) into (27), one gets the infinitesimal surface element on the hemispherical surface which can be expressed as,

$$d\mathbf{S}_s = -\left(\frac{r - H \cos \theta}{H \sin \theta} \hat{\mathbf{a}}_r + \hat{\mathbf{a}}_\theta\right) r \sin \theta dr d\phi \quad (47)$$

$$dS_s = |\mathbf{dS}| = \frac{r}{H} \sqrt{r^2 - 2Hr \cos \theta + H^2} dr d\phi \quad (48)$$

Substituting from (3) into (48), one gets the following expression for the hemispherical surface described above,

$$dS_s = \frac{a}{H} r dr d\phi \quad (49)$$

From the geometrical representation of TDFT structure illustrated in Fig. 33, (49) can be written as,

$$\boxed{dS_s = \frac{a}{R_o \cos \theta_o} r dr d\phi} \quad (50)$$

To verify the correctness of the expressions in (49) and (50), let us calculate the surface area of the hemisphere by integrating dS over the domain: $R_o \leq r \leq H + a$, $0 \leq \phi \leq 2\pi$ (Balanis, Constantine A, 2012).

$$\begin{aligned} S_s &= \int_S dS_s = \int_0^{2\pi} \int_{R_o}^{H+a} \frac{a}{H} r dr d\phi = \frac{2\pi a}{H} \int_{R_o}^{H+a} r dr = \frac{2\pi a}{H} \left[\frac{r^2}{2} \right]_{R_o}^{H+a} \\ &= \frac{2\pi a}{H} \left[\frac{a^2 - (R_o^2 - H^2) + 2aH}{2} \right] = 2\pi a^2 \end{aligned} \quad (51)$$

The expression (51) is exactly the surface area of a hemisphere of radius a .

As the hemispherical surface is independent of ϕ , the expression in (49) can be further reduced to (Balanis, Constantine A, 2012),

$$dS_s = \frac{2\pi a}{H} r dr \quad \text{on the hemisphere} \quad (52)$$

On the conical surface defined as $\theta = \theta_o$, $0 \leq r \leq R_o$, the surface area element is expressed as (Balanis, Constantine A, 2012),

$$dS_c = r \sin \theta_o dr d\phi \quad (53)$$

$$\boxed{dS_c = \frac{a}{R_o} r dr d\phi} \quad (54)$$

Where r is the radial distance along the slant height of the cone, θ is the semi-vertical angle that extends from z axis where $\theta = 0$ to θ_o .

For simplicity, since the height of inner conductor of the coaxial feed h_o is very small compared to the wavelength, let us assume than the conical structure extends from the origin to a height H and slant height R_o

To verify the correctness of the expressions in (53) and (54), let us calculate the lateral surface area of the cone by integrating dS over the domain: $0 \leq r \leq R_o$, $0 \leq \phi \leq 2\pi$.

$$S_c = \int_{S_c} dS_c = \int_0^{2\pi} \int_0^{R_o} \frac{a}{R_o} r dr d\phi = \frac{2\pi a}{R_o} \int_0^{R_o} r dr = \frac{2\pi a}{R_o} \left[\frac{r^2}{2} \right]_0^{R_o} = \pi a R_o \quad (55)$$

The expression (55) is exactly the lateral surface area of a cone of radius a and slant height R_o .

As the conical surface is independent of ϕ , the expression in (54) can be further simplified to

$$dS_c = \frac{2\pi a}{R_o} r dr \quad \text{on the cone} \quad (56)$$

3.5.2. Evaluation of Surface Current Divergence on the Hemisphere

$$\nabla_s \cdot \mathbf{J} = \eta_r + \eta_\theta + \eta_\phi \quad (57)$$

Where $\eta_r, \eta_\theta, \eta_\phi$ is the divergence of current element in radial, polar and azimuthal direction, respectively.

Since current components on both hemispherical and conical surfaces are in radial and polar directions, divergence of current element in azimuthal direction is zero as expressed in (60) (Balanis, Constantine A, 2005).

$$\eta_r = \frac{1}{r^2} \frac{\partial}{\partial r} (r^2 J_r) \quad (58)$$

$$\eta_\theta = \frac{1}{r \sin \theta} \frac{\partial}{\partial \theta} (J_\theta \sin \theta) \quad (59)$$

$$\eta_\phi = \frac{1}{r \sin \theta} \frac{\partial J_\phi}{\partial \phi} = 0 \quad (60)$$

Current component in polar direction (θ) exists only on the hemispherical surface which gives a divergence in the polar direction over a surface extends only from $R_o < r \leq H + a$, $0 \leq \theta < \theta_o$ as written in (61)

$$\eta_\theta = \begin{cases} \eta_\theta^s, & R_o < r \leq H + a, \quad 0 \leq \theta < \theta_o \\ 0, & \text{Otherwise} \end{cases} \quad (61)$$

Current components in radial direction exist on both conical and hemispherical surface which gives a divergence in a radial direction as follows

$$\eta_r = \begin{cases} \eta_r^s, & R_o < r \leq H + a, \quad 0 \leq \theta < \theta_o \\ \eta_r^c, & r_o \leq r \leq R_o, \quad \theta = \theta_o \end{cases} \quad (62)$$

3.5.2.1. Expressions for η_θ^s , η_r^s and η_r^c for Short Antenna ($\mathcal{L} < \lambda/2$)

$$J_\theta = -J_o \frac{a}{\mathcal{L}} \left(\frac{\pi}{2} - \psi \right) \sin(\theta + \psi), \quad R_o < r \leq H + a, \quad 0 \leq \theta < \theta_o \quad (63-a)$$

From (8), the expression (63-a) can be rewritten as,

$$J_\theta = -J_o \frac{a}{\mathcal{L}} (\theta + \vartheta) \cos \vartheta, \quad R_o < r \leq H + a, \quad 0 \leq \theta < \theta_o \quad (63-b)$$

From (59), η_θ^s can be evaluated as,

$$\eta_\theta^s = \frac{1}{r \sin \theta} \left(J_\theta \cos \theta + \frac{\partial J_\theta}{\partial \theta} \sin \theta \right) \quad (64)$$

Where

$$\frac{\partial J_\theta}{\partial \theta} = -J_o \frac{a}{\mathcal{L}} \left[\left(\frac{\pi}{2} - \psi \right) \cos(\theta + \psi) \left(1 + \frac{\partial \psi}{\partial \theta} \right) - \sin(\theta + \psi) \frac{\partial \psi}{\partial \theta} \right] \quad (65)$$

From (12-b), expression (65) can be written as

$$\frac{\partial J_\theta}{\partial \theta} = J_o \frac{a}{\mathcal{L}} \left\{ \frac{r}{r - H \cos \theta} \left[\left(\frac{\pi}{2} - \psi \right) \cos(\theta + \psi) - \sin(\theta + \psi) \right] - \left(\frac{\pi}{2} - \psi \right) \cos(\theta + \psi) \right\} \quad (66)$$

$$\frac{\partial (J_\theta \sin \theta)}{\partial \theta} = J_o \frac{a}{\mathcal{L}} \left\{ \frac{r \sin \theta}{r - H \cos \theta} \left[\left(\frac{\pi}{2} - \psi \right) \cos(\theta + \psi) - \sin(\theta + \psi) \right] \right. \\ \left. - \left(\frac{\pi}{2} - \psi \right) [\sin(\theta + \psi) \cos \theta + \cos(\theta + \psi) \sin \theta] \right\} \quad (67-a)$$

Making use of the geometrical relations on the antenna surface shown in Fig. 33, and equation (8), equation (67-a) can be reduced to (Balanis, Constantine A, 2005),

$$\frac{\partial (J_\theta \sin \theta)}{\partial \theta} = J_o \frac{a}{\mathcal{L}} \left\{ \frac{r \sin \theta}{r - H \cos \theta} [(\vartheta + \theta) \sin \vartheta - \cos \vartheta] \right. \\ \left. - (\vartheta + \theta) [\cos \vartheta \cos \theta + \sin \vartheta \sin \theta] \right\} \quad (67-b)$$

Then

$$\eta_\theta^s = J_o \frac{a}{\mathcal{L} r \sin \theta} \left\{ \frac{r \sin \theta}{r - H \cos \theta} ((\vartheta + \theta) \sin \vartheta - \cos \vartheta) \right. \\ \left. - (\vartheta + \theta) \cos(\vartheta - \theta) \right\} \quad (68-a)$$

$$\eta_\theta^s = \frac{J_o}{\mathcal{L}} \left\{ \frac{(\vartheta + \theta) \sin \vartheta - \cos \vartheta}{\frac{1}{a}(r - H \cos \theta)} - (\vartheta + \theta) \frac{a}{r} \frac{\cos(\vartheta - \theta)}{\sin \theta} \right\} \quad (68-b)$$

Substituting from (9-b) into (68-b),

$$\boxed{\eta_{\theta}^s = \frac{J_o}{\mathcal{L}} \left[(\vartheta + \theta) \left(\frac{\sin \vartheta}{\cos \vartheta} - \frac{a}{r} \frac{\cos(\vartheta - \theta)}{\sin \theta} \right) - 1 \right]} \quad (69)$$

An alternative way to arrive at (69) can be as follows

From (58), divergence of current component in radial direction can be written as follows (Balanis, Constantine A, 2005),

$$\eta_r = \frac{1}{r^2} \frac{\partial}{\partial r} (r^2 J_r) = \frac{1}{r^2} \left(r^2 \frac{\partial J_r}{\partial r} + 2r J_r \right) \quad (70)$$

Which can be reduced to

$$\eta_r = \frac{\partial J_r}{\partial r} + \frac{2}{r} J_r \quad (71)$$

Recall from equation (16-b), current component in radial direction on the hemispherical surface can be written as

$$J_r^s = J_o \frac{a}{\mathcal{L}} (\theta + \vartheta) \sin \vartheta, \quad R_o < r \leq H + a, \quad 0 \leq \theta < \theta_o \quad (72)$$

$$\frac{\partial J_r^s}{\partial r} = \frac{J_o}{\mathcal{L}} a \left[\left(\frac{\partial \theta}{\partial r} + \frac{\partial \vartheta}{\partial r} \right) \sin \vartheta + (\vartheta + \theta) \cos \vartheta \frac{\partial \vartheta}{\partial r} \right] \quad (73)$$

From equations (4-c) and (10), equation (73) can be written as

$$\frac{\partial J_r^s}{\partial r} = -\frac{J_o}{\mathcal{L}} a \left[\left(\frac{1 \cos \vartheta}{r \sin \vartheta} + \frac{1 \cos \theta}{r \sin \theta} \right) \sin \vartheta + (\vartheta + \theta) \cos \vartheta \frac{1 \cos \theta}{r \sin \theta} \right] \quad (74)$$

Substituting in (71), η_r^s can be written as

$$\eta_r^s = \frac{J_o}{\mathcal{L}} a \left[\frac{2}{r} (\vartheta + \theta) \sin \vartheta - \frac{1}{r} (\vartheta + \theta) \cos \vartheta \frac{\cos \theta}{\sin \theta} - \frac{1}{r} \left(\frac{\cos \vartheta}{\sin \vartheta} + \frac{\cos \theta}{\sin \theta} \right) \sin \vartheta \right] \quad (75)$$

Equation (75) can be simplified to

$$\eta_r^s = \frac{J_o a}{\mathcal{L} r} \left\{ (\vartheta + \theta) \left[2 \sin \vartheta - \cos \vartheta \frac{\cos \theta}{\sin \theta} \right] - \cos \vartheta - \sin \vartheta \frac{\cos \theta}{\sin \theta} \right\} \quad (76)$$

$$\eta_r^s = \frac{J_o a}{\mathcal{L} r \sin \theta} \left\{ (\vartheta + \theta) [\sin \vartheta \sin \theta - (\cos \vartheta \cos \theta - \sin \vartheta \sin \theta)] - (\cos \vartheta \sin \theta + \sin \vartheta \cos \theta) \right\} \quad (77)$$

Then

$$\eta_r^s = \frac{J_o a}{\mathcal{L} r \sin \theta} \left\{ (\vartheta + \theta) [\sin \vartheta \sin \theta - \cos(\vartheta + \theta)] - \sin(\vartheta + \theta) \right\} \quad (78)$$

From equation (15), current component in radial direction on the conical surface can be written as

$$J_r^c = \frac{J_o}{\mathcal{L}} [\mathcal{L} - (r - r_o)], \quad r_o \leq r \leq R_o, \quad \theta = \theta_o \quad (79)$$

Then the divergence of radial current component on the conical surface can be written as

$$\eta_r^c = \frac{J_o}{\mathcal{L}} \left\{ -1 + \frac{2}{r} [\mathcal{L} - (r - r_o)] \right\} \quad (80)$$

$$\eta_r^c = -\frac{J_o}{\mathcal{L}} \left[3 - \frac{2(\mathcal{L} + r_o)}{r} \right] \quad (81)$$

3.5.2.2. Expressions for η_θ^s , η_r^s and η_r^c for Long Antenna ($\mathcal{L} \geq \lambda/2$)

Let us assume ξ to be

$$\xi = \frac{R_o - r_o + \psi a}{\mathcal{L}} \quad (22)$$

Making useful derivatives of ξ with respect to radial distance and polar angle which can be evaluated as

$$\frac{\partial \xi}{\partial r} = \frac{a}{\mathcal{L}} \frac{\partial \psi}{\partial r} \quad (82)$$

Substitute from (13-c) in (84), one gets

$$\boxed{\frac{\partial \xi}{\partial r} = \frac{1}{\mathcal{L} \sin \vartheta}} \quad (83)$$

$$\frac{\partial \xi}{\partial \theta} = \frac{a}{\mathcal{L}} \frac{\partial \psi}{\partial \theta} \quad (84)$$

From (12-c), (84) can be rewritten as

$$\boxed{\frac{\partial \xi}{\partial \theta} = \frac{-r}{\mathcal{L} \cos \vartheta}} \quad (85)$$

Making use of equation (82) and (84), one gets

$$\frac{\partial}{\partial r} [(1 - \xi) \cos \kappa \xi] = [-(1 - \xi) \kappa \sin \kappa \xi - \cos \kappa \xi] \frac{\partial \xi}{\partial r} \quad (86)$$

$$\frac{\partial}{\partial r} [(1 - \xi) \cos \kappa \xi] = -\frac{1}{\mathcal{L} \sin \vartheta} [(1 - \xi) \kappa \sin \kappa \xi + \cos \kappa \xi] \quad (87)$$

Then the differentiation of radial component of current element on hemispherical surface from (21), one can get

$$\frac{\partial J_r^s}{\partial r} = J_o \left[-\frac{1}{\mathcal{L} \sin \vartheta} [(1 - \xi) \kappa \sin \kappa \xi + \cos \kappa \xi] \sin \vartheta + (1 - \xi) \cos \kappa \xi \cos \vartheta \left(-\frac{\cos \theta}{r \sin \theta} \right) \right] \quad (88)$$

$$\frac{\partial J_r^s}{\partial r} = \frac{-J_o}{r \sin \theta} \left[\frac{r}{\mathcal{L}} \sin \theta [(1 - \xi) \kappa \sin \kappa \xi + \cos \kappa \xi] + (1 - \xi) \cos \kappa \xi \cos \vartheta \cos \theta \right] \quad (89)$$

Recall from (58) divergence of current element in radial direction on the hemispherical surface which can be written as

$$\eta_r^s = \frac{\partial J_r^s}{\partial r} + \frac{2}{r} J_r^s \quad (90)$$

Where radial component of current element on the hemispherical surface can be written from (21-a)

$$J_r^s = J_o (1 - \xi) \cos \kappa \xi \sin \vartheta \quad (21-a)$$

Then divergence of current element in radial direction on the hemispherical surface which can be evaluated as follows

$$\eta_r^s = \frac{-J_o}{r \sin \theta} \left[\frac{r}{\mathcal{L}} \sin \theta [(1 - \xi) \kappa \sin \kappa \xi + \cos \kappa \xi] + (1 - \xi) \cos \kappa \xi \cos \vartheta \cos \theta - 2 (1 - \xi) \cos \kappa \xi \sin \vartheta \sin \theta \right] \quad (91)$$

Making useful derivatives with respect to polar angle θ

$$\frac{\partial}{\partial \theta} [(1 - \xi) \cos \kappa \xi] = [-(1 - \xi) \kappa \sin \kappa \xi - \cos \kappa \xi] \frac{\partial \xi}{\partial \theta} \quad (92)$$

Substituting from (85) in (92), one gets

$$\frac{\partial}{\partial \theta} [(1 - \xi) \cos \kappa \xi] = \frac{r}{\mathcal{L} \cos \vartheta} [(1 - \xi) \kappa \sin \kappa \xi + \cos \kappa \xi] \quad (93)$$

Recall from equation (21-b), the component of current element in direction of polar angle θ on the hemispherical surface can be written as

$$J_\theta^s = -J_o (1 - \xi) \cos \kappa \xi \cos \vartheta \quad (21-b)$$

$$\frac{\partial J_\theta^s}{\partial \theta} = -J_o \left[\frac{r}{\mathcal{L} \cos \vartheta} [(1 - \xi) \kappa \sin \kappa \xi + \cos \kappa \xi] \cos \vartheta - (1 - \xi) \cos \kappa \xi \sin \vartheta \frac{H \cos \theta}{a \cos \vartheta} \right] \quad (94)$$

$$\frac{\partial J_\theta^s}{\partial \theta} = -J_o \left[\frac{1}{\mathcal{L}} [(1 - \xi) \kappa \sin \kappa \xi + \cos \kappa \xi] - \frac{H}{a} (1 - \xi) \cos \kappa \xi \frac{\sin \vartheta}{\cos \vartheta} \cos \theta \right] \quad (95)$$

$$\eta_\theta^s = \frac{1}{r \sin \theta} \left(\frac{\partial J_\theta^s}{\partial \theta} \sin \theta + J_\theta^s \cos \theta \right) \quad (96)$$

$$\eta_\theta^s = \frac{-J_o}{r \sin \theta} \left[\frac{1}{\mathcal{L}} [(1 - \xi) \kappa \sin \kappa \xi + \cos \kappa \xi] \sin \theta - \frac{H}{a} (1 - \xi) \cos \kappa \xi \frac{\sin \vartheta}{\cos \vartheta} \cos \theta \sin \theta + (1 - \xi) \cos \kappa \xi \cos \vartheta \cos \theta \right] \quad (97)$$

From (58), divergence of current element in radial direction on the conical surface can be written as

$$\eta_r^c = \frac{\partial J_r^c}{\partial r} + \frac{2}{r} J_r^c \quad (58)$$

The component of current element in radial direction on the conical surface using (18) can be written as

$$J_r^c = J_o(1 - r_c) \cos \kappa r_c \quad (18)$$

$$\eta_r^c = J_o \left[-\frac{\kappa}{\mathcal{L}} (1 - r_c) \sin \kappa r_c - \frac{1}{\mathcal{L}} \cos \kappa r_c + \frac{2}{r} (1 - r_c) \cos \kappa r_c \right] \quad (98)$$

$$\boxed{\eta_r^c = J_o \left[(1 - r_c) \left(\frac{2}{r} \cos \kappa r_c - \frac{\kappa}{\mathcal{L}} \sin \kappa r_c \right) - \frac{1}{\mathcal{L}} \cos \kappa r_c \right]} \quad (99)$$

3.6. Results and Discussions

Since TDFT antenna is intended for radiation within biological tissues, equations derived for antenna immersed in lossy dielectric medium i.e. it is considered electrically long compared to wavelength are imported in MATLAB to numerically calculate magnetic vector potential \mathbf{A} and scalar electric potential Φ in the vicinity near the antenna structure (near zone).

3.6.1. Current Distribution on Electrically Long Antenna ($\mathcal{L} \geq \lambda/2$)

Current distribution on the antenna surface is calculated by importing equations (18) and (21) in MATLAB. Figure 34 illustrates current distribution on the surface of TDFT antenna immersed in lossy biological tissue. Length of the antenna became electrically long compared to wavelength approximately $\frac{3}{2} \lambda_{eff}$ when inserted in lossy biological medium i.e. liver tissue. For electrically long antenna, current distribution varies sinusoidally along the length of the antenna and decays gradually towards the antenna end as shown in Fig. 34. Magnitude of electric current sheet is depicted in Fig. 35 along the antenna length.

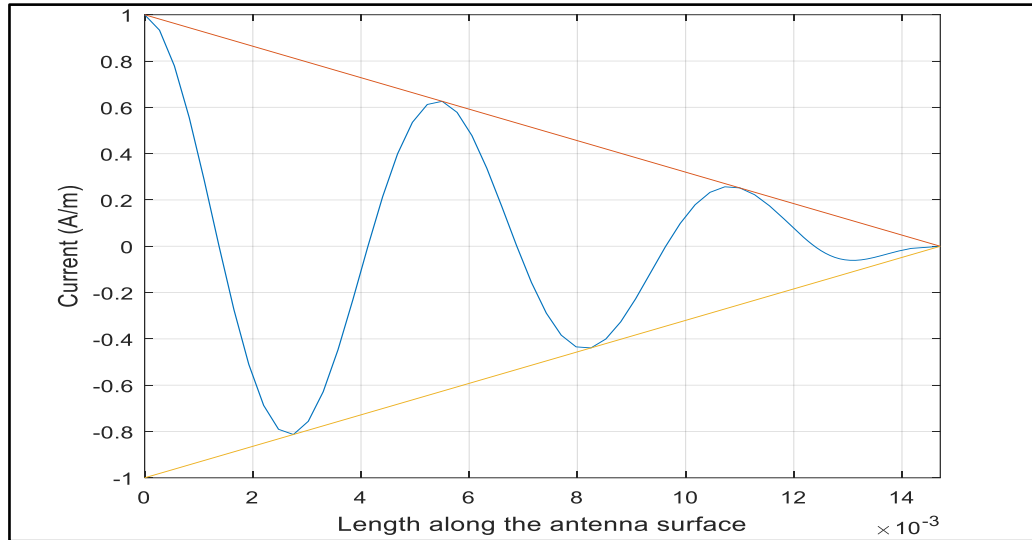


Figure 34. Distribution of the electric current sheet along the circumferential length of TDFT antenna when immersed in biological tissue.

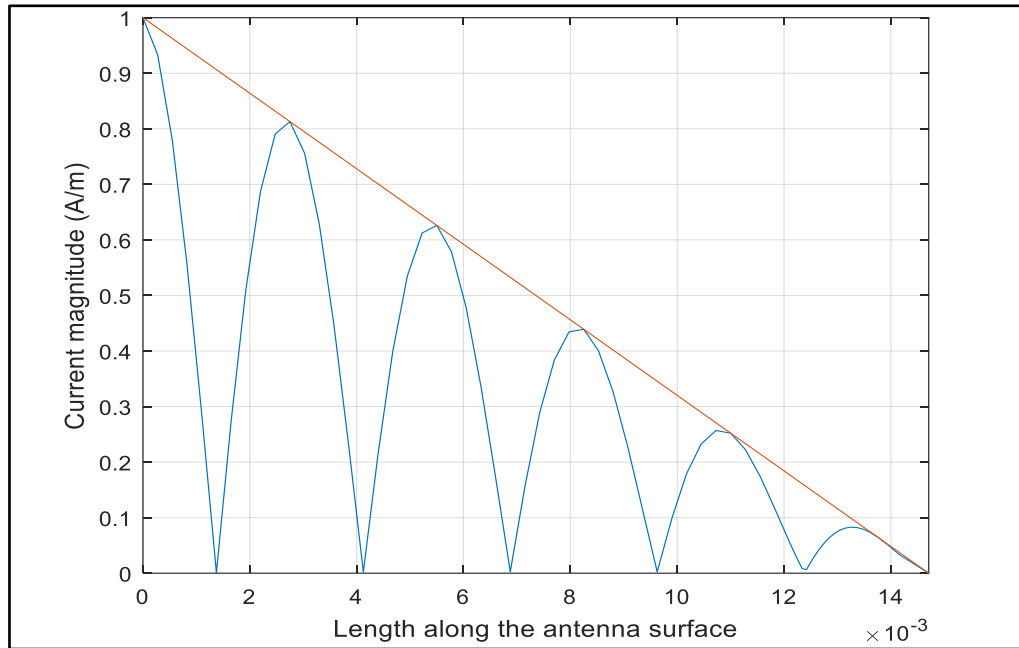


Figure 35. Distribution of the magnitude of the electric current sheet along the circumferential length of TDFT antenna when immersed in biological tissue.

3.6.2. Evaluation of the electric field distribution in the near zone

Electric field E components in the near zone can be evaluated numerically in the surrounding space using the following formulas presented in cartesian coordinates (Hussein, 2007):

$$E_x = -j\omega A_x - \frac{\Delta\phi}{\Delta x}$$

$$E_y = -j\omega A_y - \frac{\Delta\phi}{\Delta y}$$

$$E_z = -j\omega A_z - \frac{\Delta\phi}{\Delta z}$$

Prior to numerical calculations mentioned above, antenna structure and its surroundings are then modelled in MATLAB to calculate nearfield distribution at a point at radial distance r_f with respect to any point on the surface of TDFT antenna. To enable such calculation, a segmentation of antenna structure and the surrounding space is applied in such way that facilitates the numerical evaluation of magnetic vector potential \mathbf{A} and electric scalar potential Φ due to current element flowing at any point on the antenna structure $(\hat{r}, \hat{\theta}, \hat{\phi})$ and the corresponding radiated electric field at a point in the near zone (r_f, θ_f, ϕ_f) . The space around the antenna is chosen to be a sphere with radius r_f to imitate the nearfield calculation using commercial software package (ANSYS). 3D grid of TDFT antenna structure employed in the numerical calculation of radiated near field using MATLAB is depicted in Fig. 36.

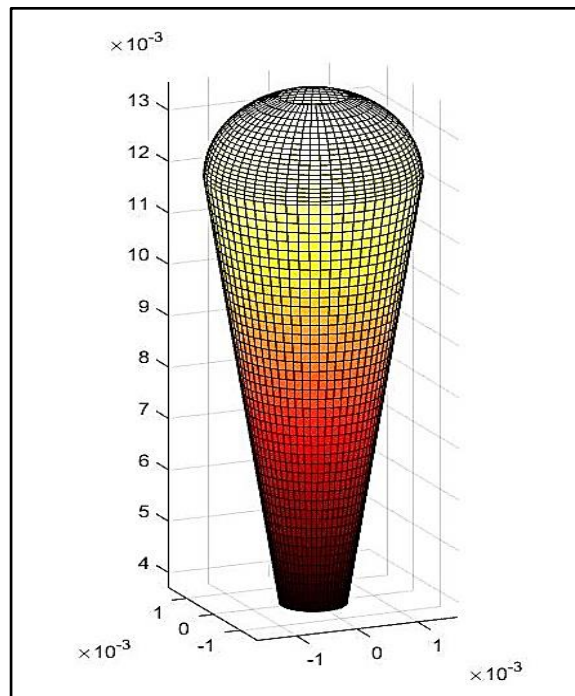


Figure 36. 3D grid representation of TDFT antenna structure in MATLAB.

A point in the near field was pre-defined to be at radial distance of 46 mm away from the antenna structure. This point was chosen to further compare the radiated electric field obtained using semi-analytical model with that using commercial software packages (ANSYS Electronic Desktop suite v.16 previously introduced as HFSS). As calculations of radiated electric field in the near zone are

performed over a specified sphere with defined radius (r_f) around the antenna model in HFSS, a decomposition of radial distance r_f in cartesian coordinates has been done in numerical calculation of the electric field using MATLAB. Radiated electric field components numerically calculated using the algorithm presented in (Hussein, 2007).

Electric field components are then transformed using (35) to calculate the radiated electric field components in spherical coordinates instead of cartesian coordinates to be further compared with the results obtained using electromagnetic simulation. Effective wavelength and other antenna parameters are also included in numerical calculation given the dielectric properties of each surrounding i.e. egg-white, liver and tumour. The radiated electric field in the elevation and azimuth planes is illustrated in Fig. 37 at radial distance of 46mm away from the antenna axis in egg-white model as these results are to be compared with that using numerical electromagnetic simulation using Ansoft HFSS (recently presented as electronic desktop suite) in chapter 4 where nearfield calculation is conducted over a sphere of radius 46mm surrounding the antenna model. 3D representation of nearfield pattern of TDFT antenna is also calculated and illustrated in Fig. 38. Electric field radiated in tumour model is also calculated in both elevation and azimuth planes and presented in Fig. 39 at radial distance 46mm away from antenna structure. 3D representation of electric field radiated in tumour model over a spherical surface of radius 46mm around the antenna is illustrated in Fig. 40. It is clearly observed that Electric field patterns has no null radiation along the antenna axis. Electric field evaluated using numerical calculations be furtherly compared to that obtained using commercial software packages (ANSYS Electronics Desktop Suite v.16).

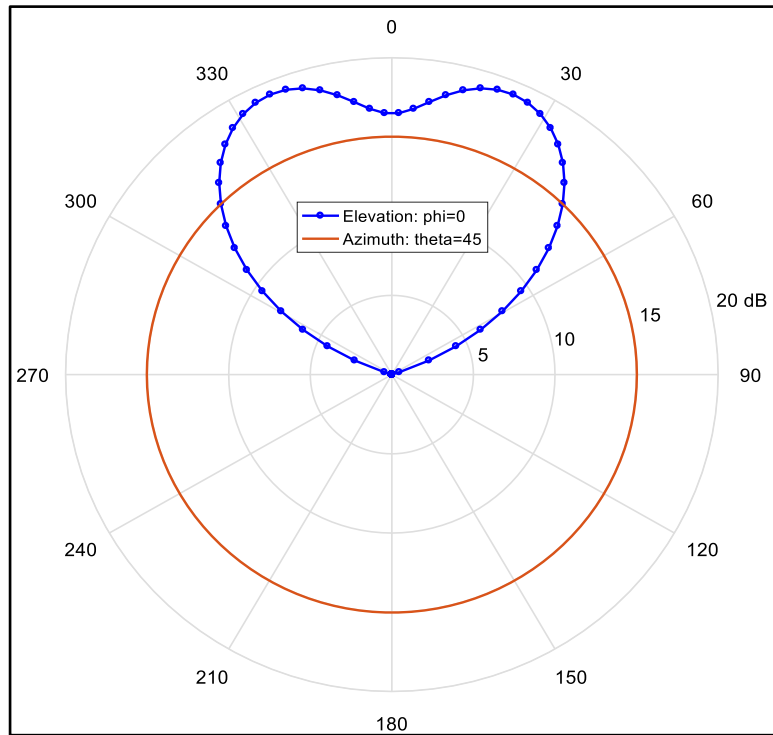


Figure 37. Near-Field patterns on a sphere of radius 4.6 cm centered at the location of TDFT antenna when immersed in egg-white ($\epsilon_r=56$, $\sigma=10$) at 7.3 GHz in the elevation and azimuth planes.

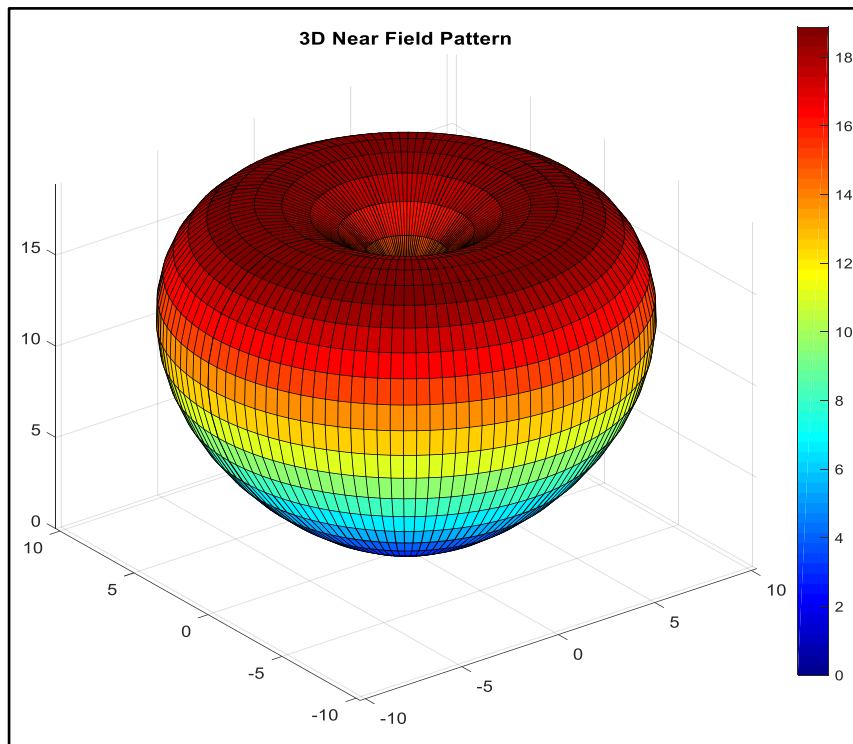


Figure 38. 3D Near field distribution on a sphere of radius 4.6 cm centered at the location of TDFT antenna when immersed in egg-white ($\epsilon_r= 56$, $\sigma=10$) at 7.3 GHz.

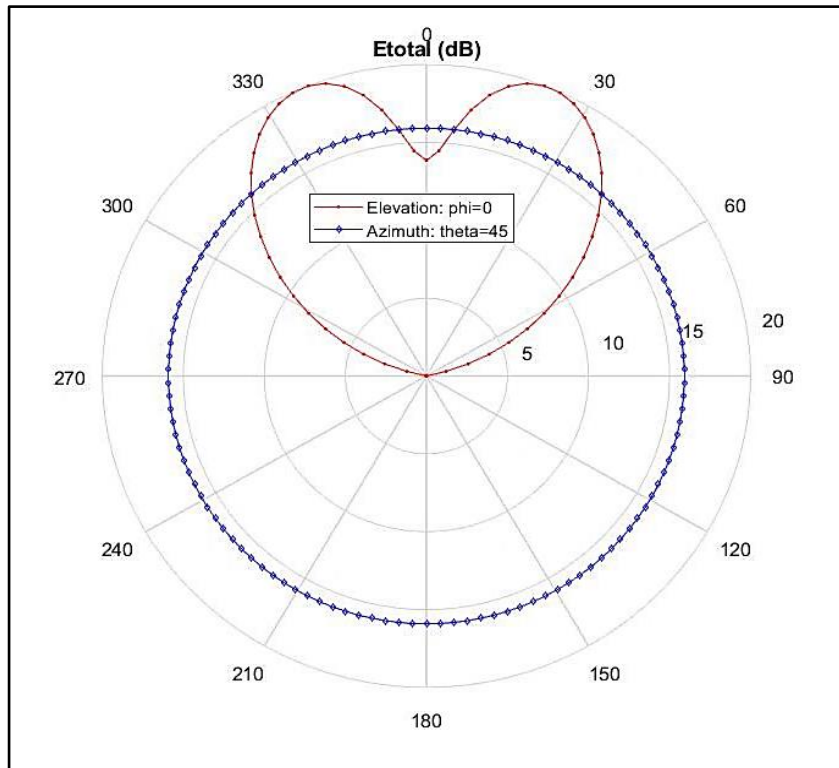


Figure 39. Near-Field patterns on a sphere of radius 4.6 cm centered at the location of TDFT antenna when immersed in tumour tissue ($\epsilon_r = 46, \sigma = 8.16$) at 7.3 GHz in the elevation and azimuth planes.

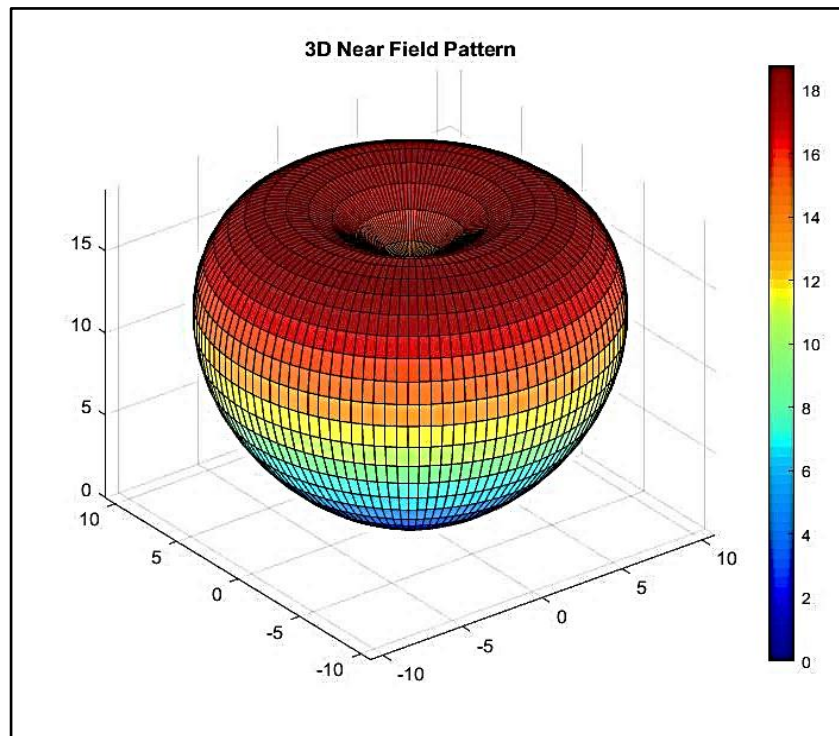


Figure 40. 3D Near field distribution on a sphere of radius 4.6 cm centered at the location of TDFT antenna when immersed in hepatic tumour model ($\epsilon_r = 46, \sigma = 8.16$) at 7.3 GHz.

Nearfield distribution is also calculated within different biological tissues such as kidney, heart, breast and bone to investigate the capability of UWB feature associated with TDFT antenna to efficiently heat tumours exist in other organs of human body and highlight the efficacy of UWB feature to provide wideband mapping of heterogeneous dielectric properties of biological tissues hindered to attain using narrowband applicators. Table 3 illustrates dielectric and thermal properties of other biological tissues included in the analytical model at 7.3 GHz (Hasgall, P.A., et al., 2015).

Table 3. Dielectric and thermal properties of biological tissues at 7.3 GHz.

Tissue Type		Conductivity σ	Permittivity ϵ_r	Mass Density ρ	Specific Heat Capacity C	Thermal Conductivity k
Kidney		7.8275	44.368	1066	3763	0.53
Heart		7.892	46.5	1081	3686	0.56
Breast	Glandes	7.89	49.6	1041	2960	0.33
	Fats	0.5456	4.2462	911	2348	0.21
Bone	Cancellous	2.776	14.294	1178	2274	0.31
	Cortical	1.5147	9.0531	1908	1313	0.32

Effective wavelength was calculated using the following equations (John & Ronald , 2002) given the dielectric properties in Table 3,

$$\lambda_{eff} = \frac{c}{f\sqrt{\epsilon_r}}$$

Where c is the speed of light in vacuum 3×10^8 m/s, f is the frequency of operation in Hz and ϵ_r is the complex relative dielectric permittivity of the surrounding medium (John & Ronald , 2002).

$$\epsilon_r = \epsilon_r - j \frac{\sigma}{\omega\epsilon_0}$$

where, ϵ_0 is the permittivity of free space, ϵ_r is the dielectric constant of the medium and σ is electrical conductivity of dielectric medium in S/m. Antenna length is found to be electrically long compared to the effective wavelength for all tissue types. Current distribution is also calculated the antenna surface given length of TDFT antenna loaded in each tissue model. Electric field distribution is calculated in the elevation and azimuth planes when TDFT antenna is loaded in Kidney, heart and illustrated in Figs 41, 42, respectively. From Figs 41 and 42, due to similarities

found between dielectric properties of liver, kidney and heart tissues, current distributions and consequent nearfield patterns are very close to that calculated within liver tissue. In addition, it is observed that electric field pattern in the elevation plane has no-null radiation region with no-backward radiation in the vicinity surrounding the antenna structure. Moreover, directed field is observed in the axial direction along the antenna axis. These results emphasize on the efficacy of TDFT antenna to provide directed radiation which in-turn creates confined heating within kidney and heart tissue.

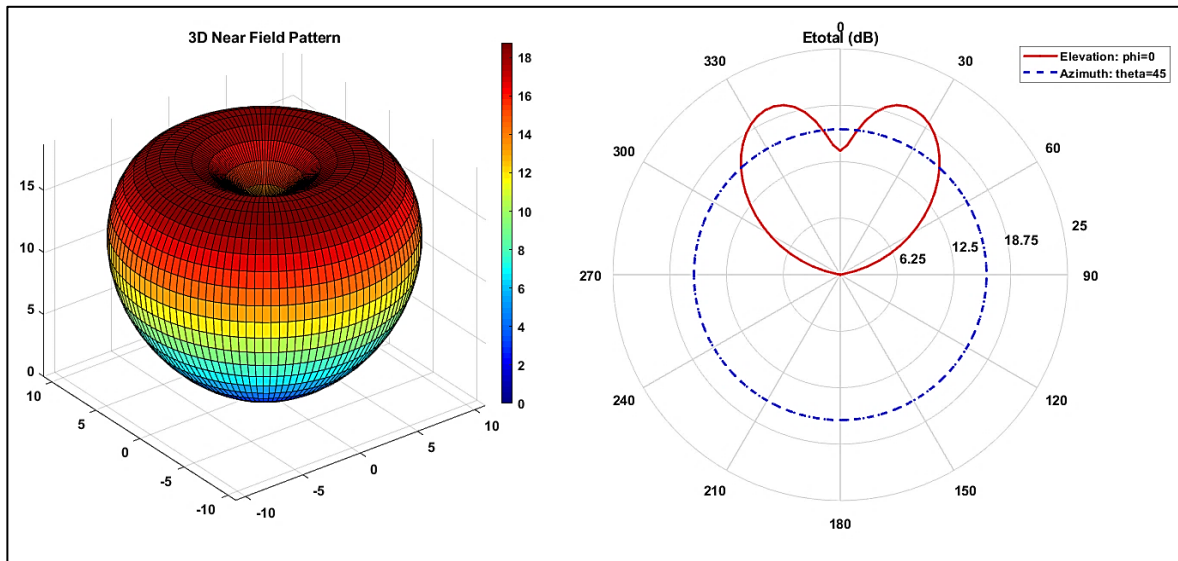


Figure 41. 3D nearfield distribution on the left and nearfield patterns on a sphere of radius 4.6 cm centered at the location of TDFT antenna when immersed in kidney tissue model on the right ($\epsilon_r = 44.368.5, \sigma = 7.8275$) at 7.3 GHz in the elevation and azimuth planes.

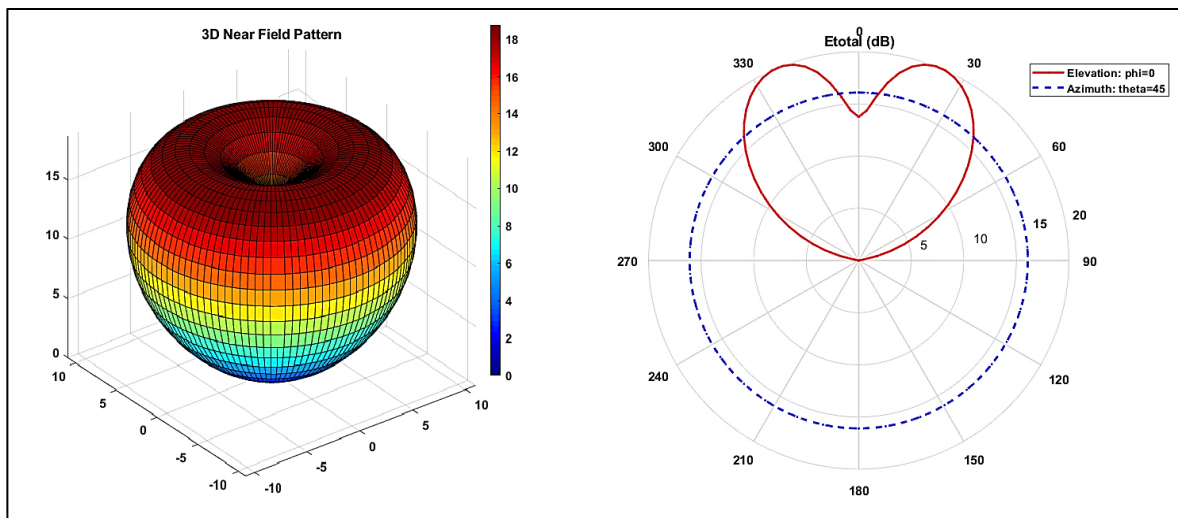


Figure 42. 3D nearfield distribution on the left and nearfield patterns on a sphere of radius 4.6 cm centered at the location of TDFT antenna when immersed in heart tissue model on the right ($\epsilon_r = 46.5, \sigma = 7.892$) at 7.3 GHz in the elevation and azimuth planes.

In addition, nearfield distributions are also calculated in glandular breast tissues and depicted in Figs 43. It is observed that TDFT antenna can also provide directed axial radiation within breast tissue. Despite the difference between dielectric properties of both glandes and fats within breast tissue model, TDFT antenna can create directed radiation and consequent confined heating.

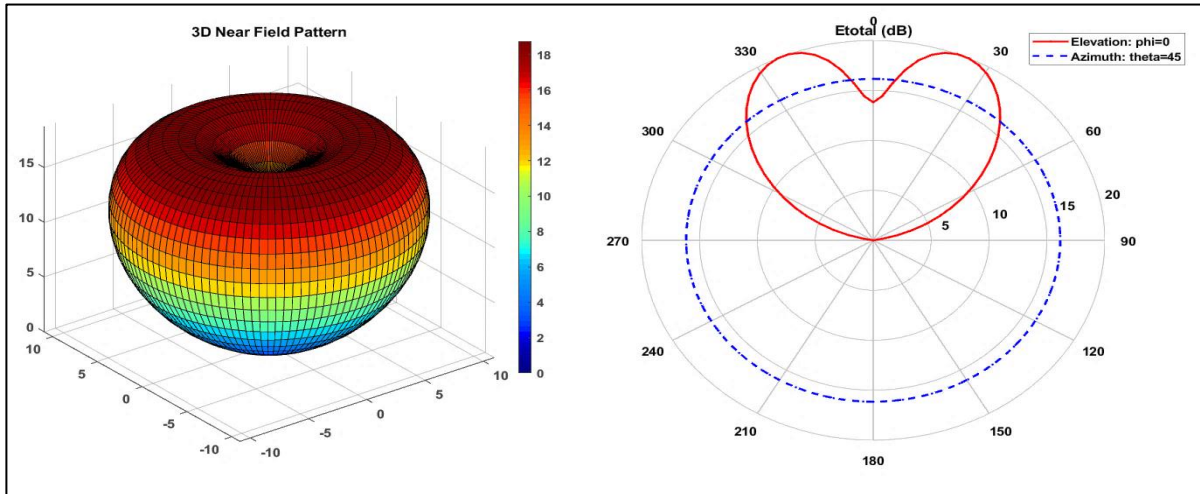


Figure 43. 3D nearfield distribution on the left and nearfield patterns on a sphere of radius 4.6 cm centered at the location of TDFT antenna when immersed in glandular breast tissue model on the right ($\epsilon_r = 49.6, \sigma = 7.89$) at 7.3 GHz in the elevation and azimuth planes.

Further Nearfield calculations are also conducted in cancellous and cortical bone tissues and illustrated in Figs 44 and 45, respectively at radial distance of 46 mm away from the antenna axis in egg-white model.

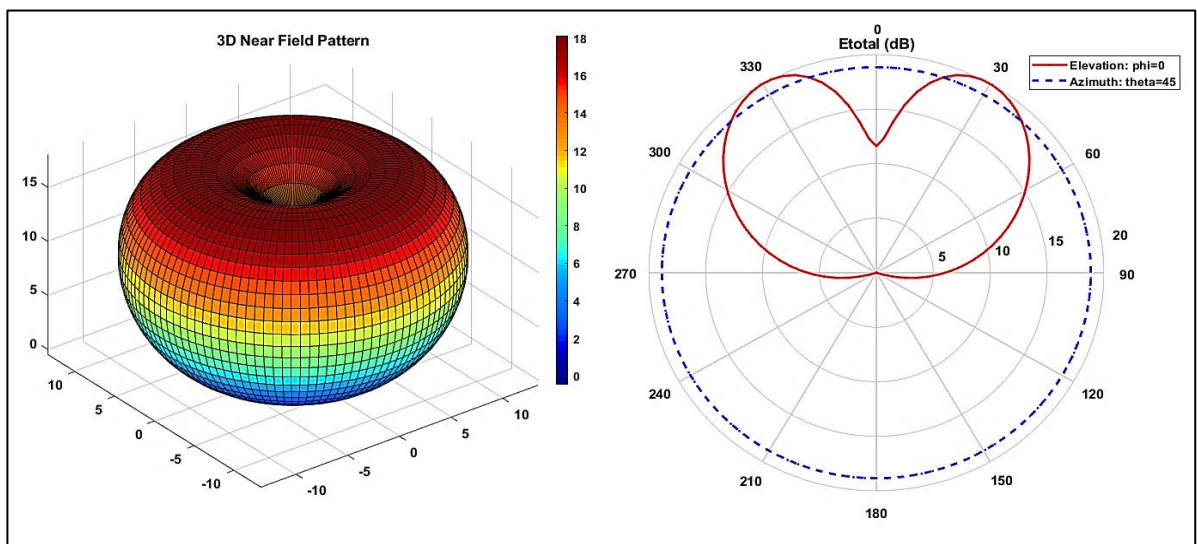


Figure 44. 3D nearfield distribution on the left and nearfield patterns on a sphere of radius 4.6 cm centered at the location of TDFT antenna when immersed in cancellous bone tissue model on the right ($\epsilon_r = 14.294, \sigma = 2.776$) at 7.3 GHz in the elevation and azimuth planes.

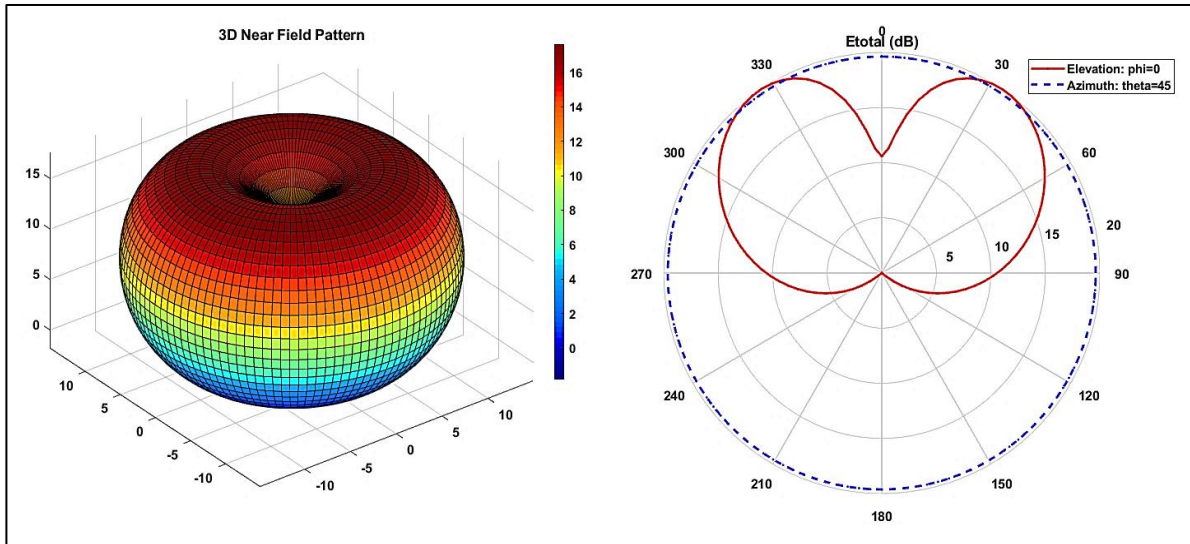


Figure 45. 3D nearfield distribution on the left and nearfield patterns on a sphere of radius 4.6 cm centered at the location of TDFT antenna when immersed in cortical bone tissue model on the right ($\epsilon_r = 9.0531$, $\sigma = 1.515$) at 7.3 GHz in the elevation and azimuth planes.

Due to significant difference between high permittivity tissue such as liver, kidney with high water content and low dielectric permittivity bone tissue, a noticeable flaring in nearfield pattern is observed. This can be attributed to low permittivity of surrounding dielectric medium creates shorter antenna length compared to effective wavelength within targeted tissue than that loaded in higher dielectric permittivity medium. As the antenna length gets slightly shorter currents excited on the antenna surface decays faster as it flows towards the tip and causes wider beam-width radiation. Nevertheless, TDFT antenna achieves radiation directed in the axial direction with no-null radiation region found around the antenna axis.

Furthermore, maxima of nearfield distributions found are approximately the same for all tissue types which helps providing homogenous SAR and consequent confined heating sufficient for successful ablation. From the analytical and numerical solutions presented above, one can observe for tissues of high dielectric permittivity and conductivity such as kidney, heart and liver, TDFT antenna with the given dimensions can efficiently provide highly directed axial radiation and confined heating within these tissues. However, for tissues with low dielectric permittivity and conductivity such as bone or fat-based tissues and higher directivity is required specially for treating varicose veins or critically located bone tumours to reduce organ malfunction, further parametric analysis is required to provide longer antenna length for the higher directivity required.

Further extensive parametric analysis using commercial software package (electromagnetic desktop suite) is conducted to find the optimum antenna dimensions including maximum diameter and length to attain minimum reflection and minimum backward radiation taking into consideration constraints of applicator dimensions (see section 3.2).

Chapter Four

Implementation and numerical modeling of Teardrop Flared Tipped antenna design

4.1. Proposed Research Design

Tear Drop Flared Tipped (TDFT) antenna design is proposed as interstitial microwave applicator for treating focal liver tumours to provide more precise ablation zones. Figure 46 illustrates the 3D geometry of tear drop flared tipped (TDFT) design proposed in this study. TDFT is adopted in this research because of its compact dimensions, ease of implementation, the ability to minimize as much reflection as possible during the ablation procedure while maintaining less backward radiation.

4.1.1. Synthesis of Teardrop Flared Tipped Antenna Structure

The synthesis of TDFT structure is distinguished from the conventional microwave applicator designs proposed in the literature as it is created by gradually changing the radius of the inner conductor of the coaxial cable towards the tip to be exploited in providing ultra-wide band feature. TDFT structure seeks to not only improve the impedance match between the feed line and antenna, but also to reduce the return currents and subsequent heating along the feed line.

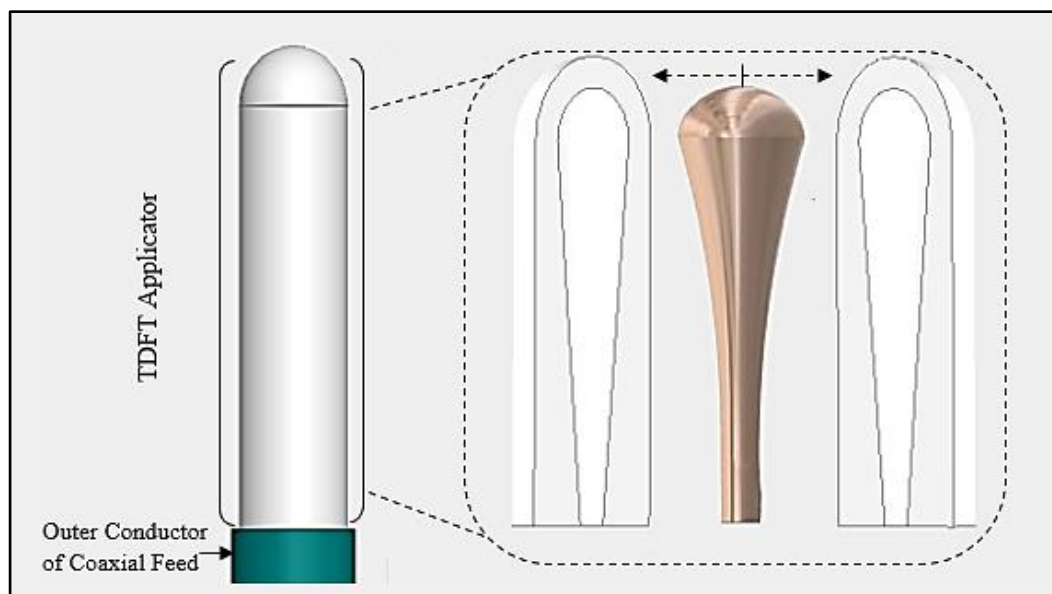


Figure 46. 3D schematic representation of the proposed TDFT antenna design.

As shown in Fig. 46, The proposed TDFT antenna is initially designed by using the inner conductor of the coaxial cable gradually flared outwards and terminated with hemispherical tip of diameter 1.66 mm to create elongated teardrop-like structure. ANSOFT HFSS is used to build a computational model of TDFT structure to be simulated at 7.3 GHz. This operating frequency was preferred because of two reasons. First, high-frequency microwave ablation was recently demonstrated to be as effective as low frequency microwave ablation in producing large ablation volumes (Sawicki, et al., 2018). Secondly, at higher frequencies, the smaller wavelength helps to reduce the active length of the antenna without compromising the size of the ablation zones which in turn reduces the invasiveness of the whole procedure (Luyen, Hung T., et al., 2015; Luyen, Hung, et al., 2014).

As most thermal ablation devices intended for percutaneous and interstitial use are currently between 1.5 mm and 2.5 mm to minimize the complication associated with larger diameter needles such as bleeding, coaxial cable adopted for TDFT feeding is with inner and outer conductors of diameters 0.496 mm and 2.159 mm respectively (Brace, Christopher L, 2010). The coaxial dielectric material used is Teflon of diameter 1.7 mm and with dielectric permittivity of 2.1. The material of coaxial feed line of inner and outer conductors is initially assigned to be perfect electric conductor (PEC).

The whole teardrop structure is enclosed entirely in Teflon to provide structural support for the antenna, ease the insertion of the applicator into the tumour tissue and avoid any adhesiveness of charred or desiccated tissues during or after the ablation process. The active length of the antenna loaded in tissue is nominally $(2n-1) \lambda_{eff}/4$ where n is an integer and λ_{eff} is the effective wavelength within the dielectric material which can be calculated using (100) to maximize energy deposition rate within the targeted tissue and less heating of the feed line is encountered (Balanis, Constantine A, 2012; Balanis, Constantine A, 2005; Kraus, John D & Marhefka, Ronald J, 2002).

$$\lambda_{eff} = \frac{c}{f\sqrt{\epsilon_r}} \quad (100)$$

Where c is the speed of light in vacuum 3×10^8 m/s, f is the frequency of operation in Hz and ϵ_r is the complex relative dielectric permittivity of the surrounding medium (John & Ronald , 2002).

$$\epsilon_r = \epsilon_r - j \frac{\sigma}{\omega\epsilon_o} \quad (101)$$

where, ϵ_o is the permittivity of free space and ϵ_r is the complex relative permittivity of the medium. Teardrop structure is initially created using a solid cone with lower diameter similar to that of the inner conductor of coaxial cable and upper diameter of 1.66 mm. Due to the abrupt transition between the coaxial cable and cone structure which may cause high increase in reflection, more smooth transition is applied by etching the outer conical surface as shown in Fig. 47 through inner surface of ring torus with inner and outer radii of 0.496 and 103.8063 mm, respectively using the following equations of characteristic impedance of $\lambda/4$ transmission line section, capacitance and inductance per unit length of transmission line (Balanis, Constantine A, 2012; Balanis, Constantine A, 2005; Kraus, John D & Marhefka, Ronald J, 2002). This chokes the currents at the starting point of the antenna which minimize the subsequent currents flowing back on the surface of the outer conductor of the coaxial feed. Choke length is found to be approximately $(2n-1) \lambda_{eff}/4$ which minimizes mismatch during ablation and acts a $\lambda/4$ transformer between low impedance upper conical structure and high impedance inner conductor of the coaxial cable (John & Ronald , 2002).

$$Z_{in} \left(L = \frac{\lambda}{4} \right) = Z_o \left(\frac{Z_L + j Z_o \tan(\beta L)}{Z_o + j Z_L \tan(\beta L)} \right)$$

$$Z_o = \sqrt{Z_{in} Z_L} , \quad \beta = \frac{2\pi}{\lambda}$$

$$C/L = \frac{2\pi \epsilon_o \epsilon_r}{\ln(D/d)}, \quad \mathcal{L}/L = \frac{\mu_o \mu_r}{2\pi} \ln(D/d)$$

Where Z_{in} is the input impedance measured at a given distance L from load impedance Z_L and β is the propagation constant, Z_o is the characteristic impedance of transmission line, C and \mathcal{L} are the capacitance and inductance of transmission line per unit lengths, respectively. D and d are the outer and inner diameters of coaxial line. μ_o and μ_r are permeability of vacuum and relative permeability of dielectric material of coaxial cable, respectively. This gradual smooth flaring provides teardrop-like structure elongated slowly from the base which exhibits wideband performance unlike the bulb structure of conventional volcano-smoke structure presented in (L. Paulsen, et al., 2003). High impedance of the slimmer section added by the introduction of embedded choke alleviates return currents excited on the outer conductor due to unbalanced nature of coaxial cabling system (John & Ronald , 2002).

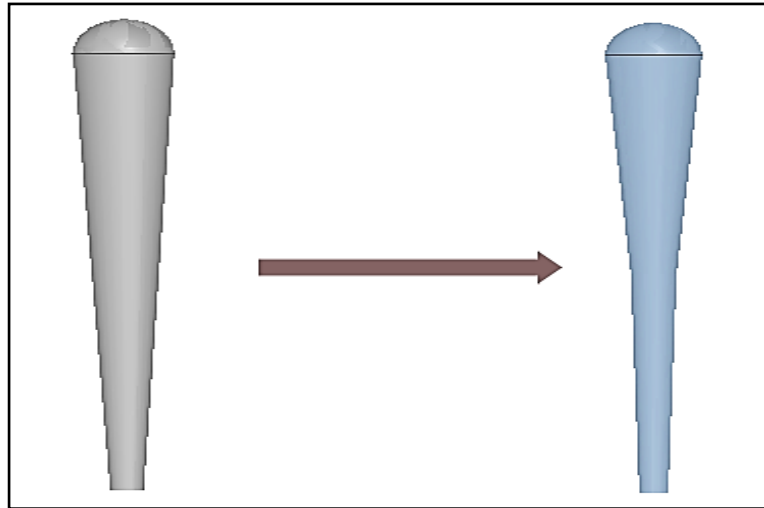


Figure 47. Synthesis of teardrop like structure by etching the outer surface of a solid cone.

Therefore, choke or sometimes referred to as *balun* i.e. a section introduced to allow more balance to coaxial cable by hindering inherently return currents flowing on outer conductor resulting in more balanced transmission (Balanis, Constantine A, 2005; John & Ronald , 2002). Moreover, the new embedded choke introduced approximately 27% total reduction in antenna size compared to original design which helps provide less invasiveness ablation.

4.1.2. Simulation Results of TDFT antenna in Saline and Healthy Liver

4.1.2.1. Electromagnetic Analysis

Finite element modelling (FEM) simulation using ANSOFT HFSS is employed to optimize the antenna design. The antenna is modelled along z-axis in both 0.9% saline and liver tissue and radiation boundary conditions were applied for both models. The analyzed model has the following assumptions, where liver tissue model is considered as linear, homogenous and isotropic medium, and the wave equation under time harmonic conditions can be written as (102)

$$\nabla \times \left[\frac{1}{\epsilon} \nabla \times \bar{H} \right] - \mu \omega^2 \bar{H} = 0, \quad (102)$$

Where H stands for magnetic field intensity (A/m), $\omega = 2\pi f$ denotes the angular frequency of EM field source (rad/s) and μ is a permeability of tissue (H/m). Moreover, the frequency-

dependent complex permittivity can be calculated using (101) where $\epsilon_0 = 8.85 \times 10^{-12} \text{ F/m}$ and ϵ_r the relative permittivity and σ is the electrical conductivity of the surrounding medium. The relative permittivity and conductivity of the liver tissue as well as 0.9% saline solution are given in Table 4 adopted from (Kim, Jung-Mu, et al., 2005; Carrara, Nello & IFAC-CNR, Italy, 2014; Hasgall, P.A., et al., 2015).

Table 4. Electrical properties of liver tissue and 0.9% Saline at 7.3 GHz.

Dielectric Material	Dielectric permittivity ϵ_r	Conductivity σ [S/m]
Liver	36.042	6.2775
0.9% Saline	68	1.55

The simplest way to understand the lossy biological characteristics is to use saline solution as a phantom material where water with additional NaCl becomes lossy dielectric material. Saline is a widely employed in surgical and clinical use to minimize the high mismatch encountered by abrupt contact of high-conductivity tumour surrounded by low-conductivity healthy tissues or *In-vitro* analysis to reduce the effect of boundaries in tissue phantom (Neelakanta, 1995).

A rectangular model for both liver and saline is considered for this study with length, width and height of 20mm, 20 mm and 30 mm, respectively to observe the antenna capabilities while it is entirely surrounded by Liver or saline which will provide good insight of the antenna performance as a microwave coagulator. The dielectric properties of both liver and 0.9% saline presented in this study are adopted from literature (Carrara, Nello & IFAC-CNR, Italy, 2014; O'Rourke, Ann P., et al., 2007; Kim, Jung-Mu, et al., 2005; Hasgall, P.A., et al., 2015). In addition, Frequency dependent dielectric properties of both liver and 0.9% saline are consolidated in the numerical simulations to obtain adequate results regarding the reflection coefficient and Near-Field pattern. FEM simulation utilizes adaptive mesh technique at frequency of 7.3 GHz for $\Delta S < 0.02$ over frequency range from 1 ~ 20 GHz using both interpolating and discrete sweep points to ensure the most accurate analysis and iterative method is applied to employ less memory for analysis. Once the nominal problem is solved, parametric studies are computed to obtain optimized results for achieving minimum mismatch losses and backward radiation. The simulation started with normalized input power of 1W as it is the default power value in HFSS using actual dielectric properties of human Liver. The dimensions of the TDFT antenna loaded in human liver and 0.9% saline at 7.3 using HFSS are given in Table 5.

Table 5. Physical parameters of the TDFT antenna

Frequency [GHz]	Active Length of TDFT [mm]	Dielectric material
7.3 GHz	11.895	Liver
	11.895	0.9% Saline

A significantly important factor to assess the antenna performance is reflection coefficient and is specified by the power losses P_r related to the total incident power P_{in} at the feeding port. The lower the mismatch is, the higher the power deposited in the surrounding tissues. Reflection coefficient denoted as S_{11} scattering parameter can be calculated using (103):

$$S_{11} = 20 \log_{10}|\Gamma| = 10 \log_{10} \frac{P_r}{P_{in}} [dB], \tag{103}$$

Choosing the active length of teardrop structure to be of length 11.895 mm $((2n - 1)/4 \lambda_{eff})$ improved return loss and reduces fields flowing back on the coaxial outer conductor. Moreover, synthesis of teardrop structure attained minimum mismatch loss stability over ultra-wide band of frequency. In-turn, more energy is deposited in the tissue. For a 11.895 mm TDFT structure loaded in 0.9% saline, Γ reflection coefficient was found to be -23.27 dB at 7.3 GHz. For the same antenna inserted in liver tissue, Γ reflection was found to be -27.81 dB at 7.3 GHz. Return loss characteristics for TDFT antenna loaded in Liver tissue and in 0.9% Saline are illustrated in Figs 48 and 49, respectively.

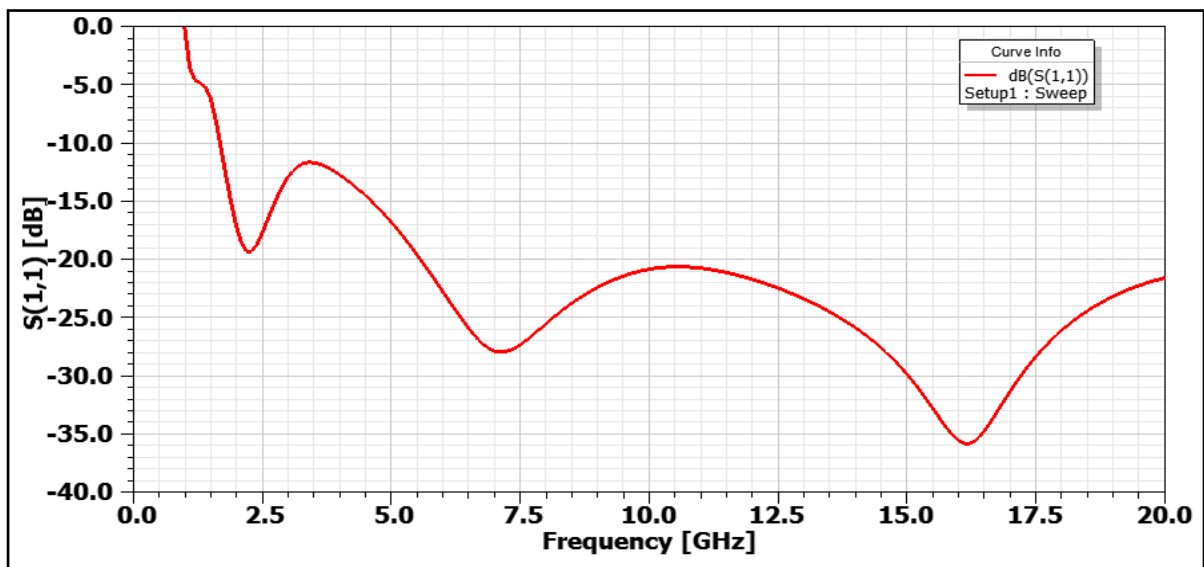


Figure 48. Return loss characteristics (S_{11}) of the TDFT antenna loaded in liver.

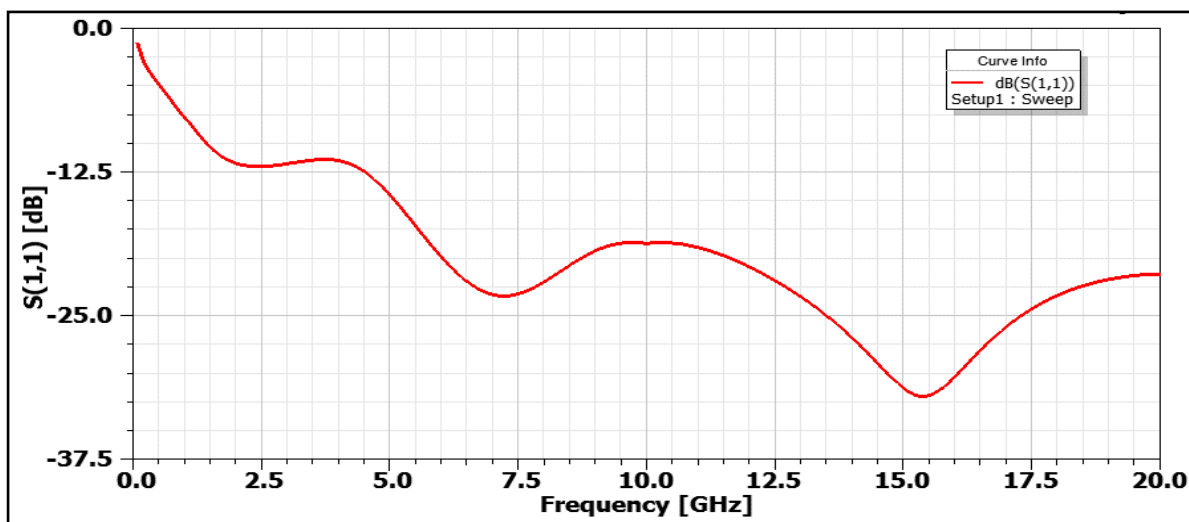


Figure 49. Return loss characteristics (S_{11}) of the TDFT antenna loaded in 0.9% Saline.

Voltage Standing Wave Ratio (VSWR) characteristics of TDFT design presented in Fig. 50 shows values less than 2 over a fractional bandwidth (FBW) more than 11.7: 1 measured from 1.7 GHz to more than 20 GHz. Overall efficiency of TDFT design is found to be 99% (VSWR less than 1.2) not only at the operating frequency 7.3 GHz but also over frequency band extended from 5.7 GHz to 20 GHz. From return loss and VSWR characteristics, ultra-wide bandwidth feature emphasizes on how the proposed TDFT design is immune to increasing reflection due to shifting in frequency of operation during the ablation process encountered in narrow bandwidth designs previously proposed in the literature (Luyen, Hung T., et al., 2015; Luyen, et al., 2015).

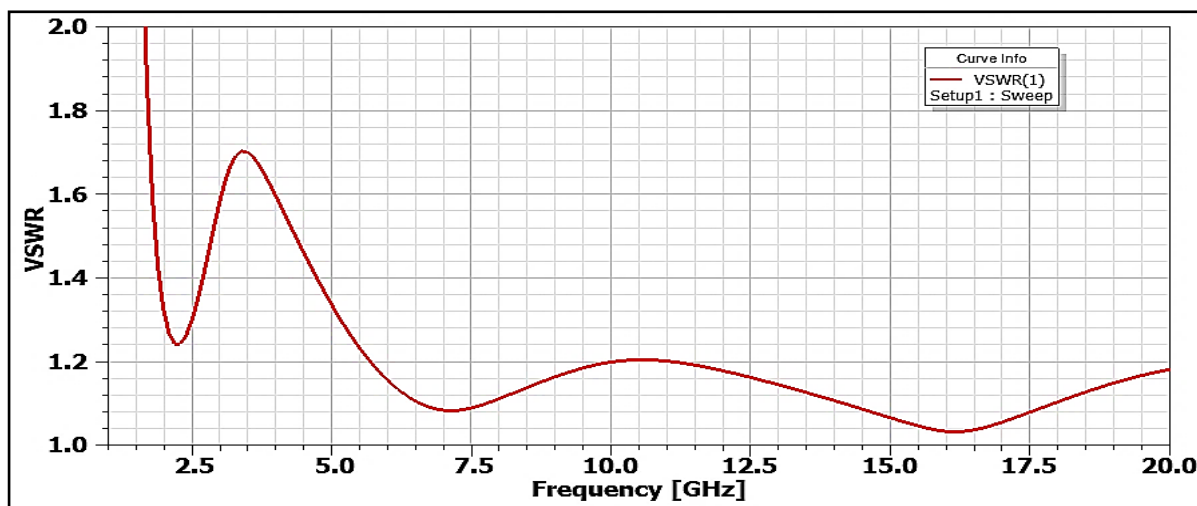


Figure 50. Voltage Standing Wave Ratio (VSWR) of the proposed TDFT antenna in liver tissue.

The current distribution along the length of TDFT structure, the inner and outer conductor of the coaxial cable at 7.3 GHz are shown in Fig. 51. Reduced fields flowing on the outer conductor of the coaxial cable can be observed in current distribution in Fig. 51 which results in less heating of the feed line and protection of healthy tissues along antenna shaft.

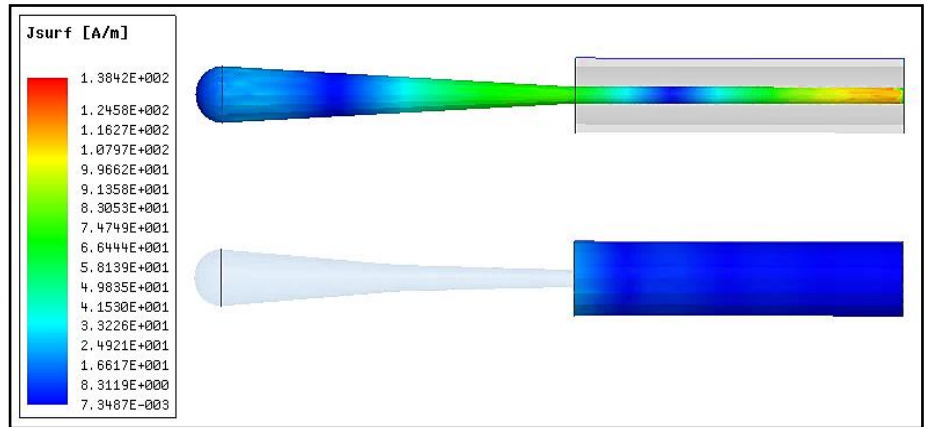


Figure 51. Current density along TDFT structure, inner and outer conductor of the entire antenna.

As illustrated in Fig. 52, etching of the conventional conical structure chokes the currents flowing at the starting point of the teardrop structure which in-turn reduces the current excited on the outer conductor of the coaxial feed by approximately 65% and alleviates the subsequent heating of the coaxial cable during the ablation process.

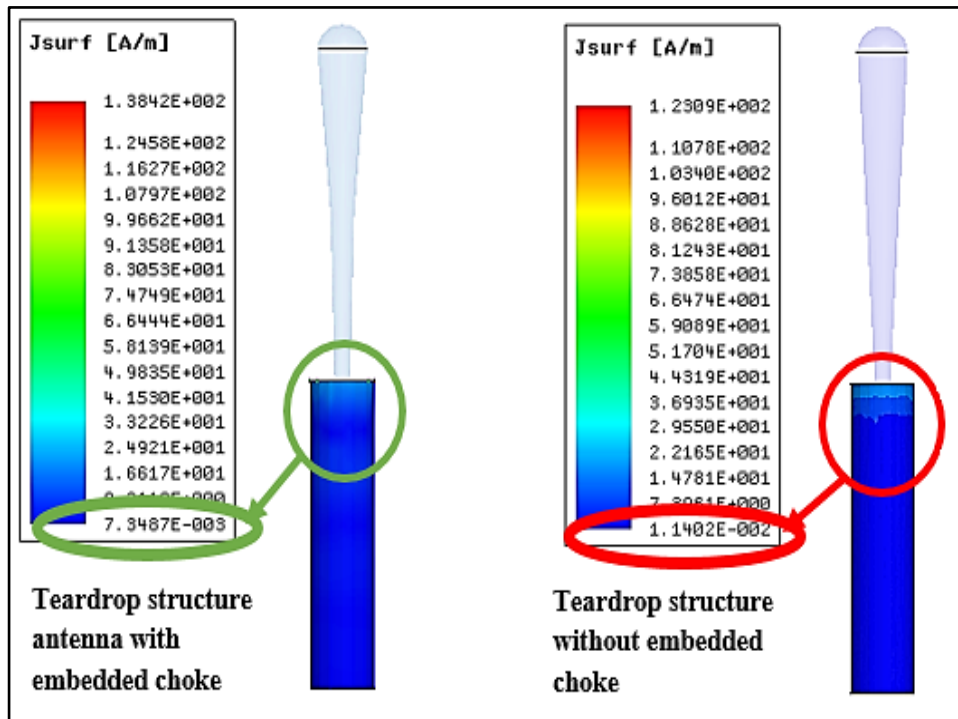


Figure 52. Comparison between current distributions on the outer conductor of the coaxial feed of Teardrop structure with and without embedded choke.

Near Field pattern is one of the indispensable considerations in designing applicators for microwave ablation therapy as it gives preliminary understanding of how the electric field around the antenna will be well-distributed. Figure 53 illustrates 3D Near field radiation pattern of the TDFT antenna loaded in Liver tissue.

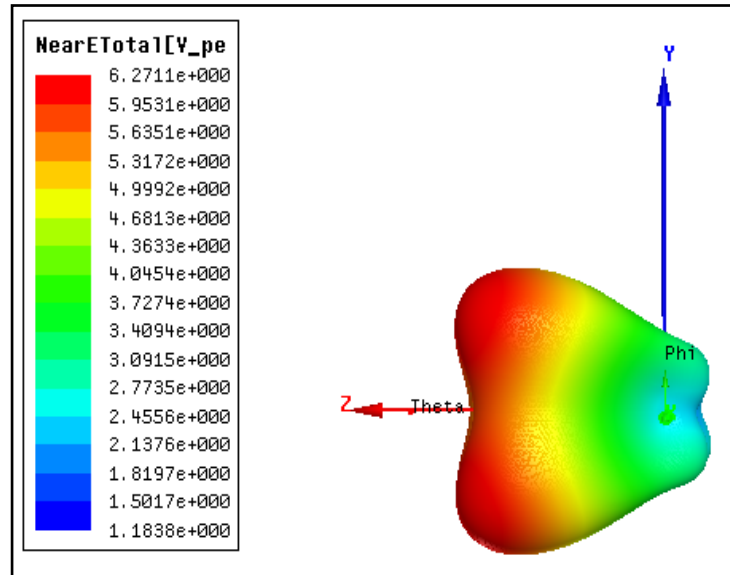


Figure 53. 3D Near Field distribution of TDFT antenna in liver.

TDFT design exhibits axial radiation and with no null along the antenna axis which can be depicted in Fig. 53. Moreover, TDFT structure provides minimum backward radiation with more localized radiation along the TDFT structure which is clearly depicted from azimuth and elevation cuts presented in Fig. 54. This can be attributed to relatively large amount of the current concentrated around the tear drop structure, which induces more electron emission (Ahn, Hee-Ran & Lee, Kwyro, 2005). Therefore, electric field intensity may be concentrated in the vicinity around the tear drop structure unlike conventional applicator with a null radiation along antenna axis which in turn produces tissues not being successfully ablated after the procedure. Consequently, the proposed TDFT structure is quite suitable for treating focal tumours.

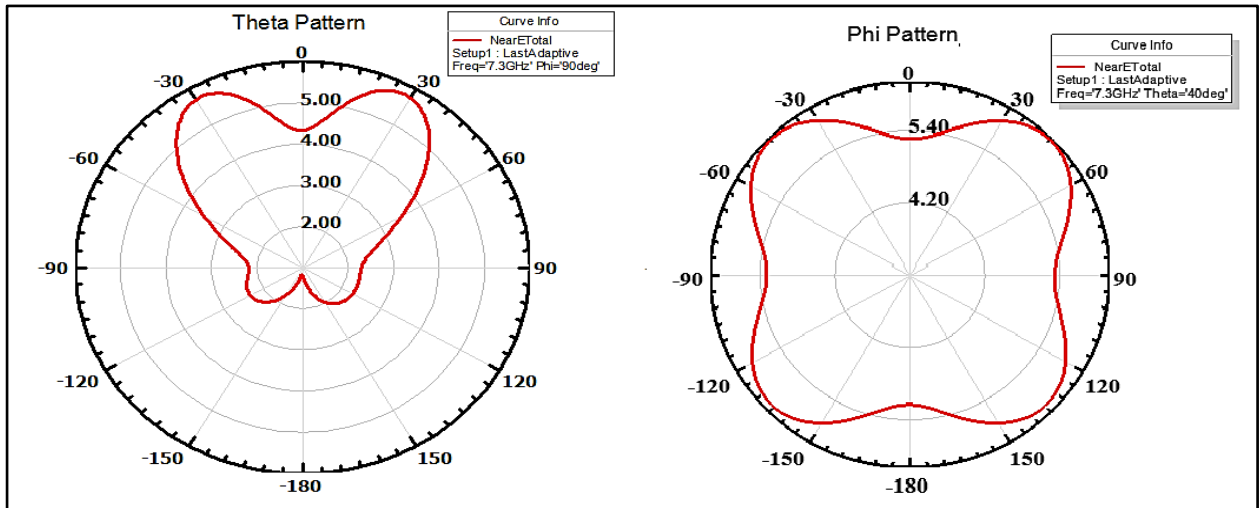


Figure 54. Near-Field radiation patterns of the proposed TDFT at 7.3 GHz in both azimuth and elevation planes.

4.1.2.2. Thermal Analysis

A critical parameter in any ablation system is specific absorption rate (SAR) which gives an insight of how the energy will be well-absorbed by biological tissues when they are exposed to electromagnetic fields. It is defined as the ratio of the power absorbed per unit volume to the tissue mass density. SAR is calculated or averaged over specific volume typically either 1 gram or 10 grams of tissue. In this research, the interaction between electromagnetic waves and dielectric biological tissue and shape of ablation volume in biological tissue is described using SAR distribution. The heating dose criterion is quantified in terms of SAR which can be expressed using the electric field intensity within the tissue (Wu, et al., 2015) as follows:

$$SAR = \frac{\text{Power absorbed}}{\rho} = \frac{\sigma \cdot E^2}{\rho}, \quad [W/kg] \quad (104)$$

Where, σ is the electric conductivity of the dielectric tissue [S/m], E is the RMS value of electric field intensity [V/m] and ρ is the tissue mass density [kg/m³]. SAR can also be calculated in non-perfused homogeneous model at the beginning of radiation exposure before thermal conduction starts to have a significant effect (Wu, et al., 2015) using (105)

$$SAR = \frac{c \nabla T}{\nabla t}, \quad [W/kg] \quad (105)$$

Where c is the specific heat capacity ($J.kg^{-1}.C^{\circ-1}$) of tissue, ΔT is change in temperature in C° within tissue and Δt is the duration of exposure. The thermal characteristics of both 0.9% saline and liver are employed to calculate SAR distribution based on the power delivered, geometry, material characteristic such as thermal conductivity, specific heat, etc. shown in Table 6 (Holmes, 2009; Hasgall, P.A., et al., 2015; Kim, Jung-Mu, et al., 2005).

Table 6. Material thermal parameters used in numerical simulation.

Material	Mass density ρ [kg/m^3]	Specific heat capacity C [$J/(kg.K)$]	Thermal Conductivity k [$W/(m.K)$]
Liver	1079	3540	0.52
0.9% Saline	998	4183	0.7

A simple homogeneous rectangular model for liver is considered for this study to evaluate SAR distribution for power level of 1 W. The applicator is inserted into Liver model with the tip of the antenna at 10 mm from its surface. SAR distribution is averaged over 1g of Liver. Figures 55 and 56 illustrate SAR values in vertical and horizontal cuts through Liver model, respectively. From Fig. 55, maxima of SAR values slowly degraded from the midpoint of the teardrop structure and as distance increases away from antenna axis, a slow decrease of SAR is observed to reach its minimum value at the boundary of Liver model as depicted in Fig. 56.

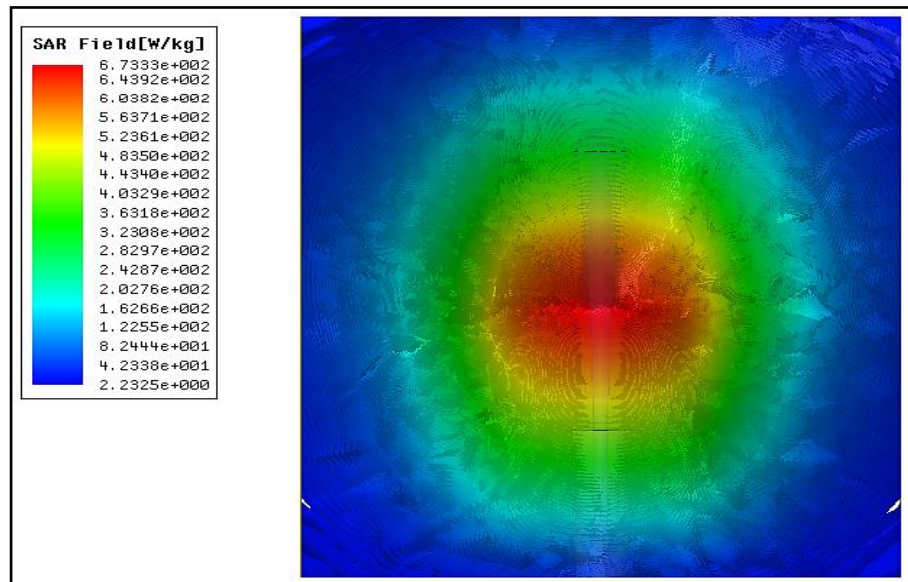


Figure 55. Distribution of SAR along central axis of the TDFT antenna.

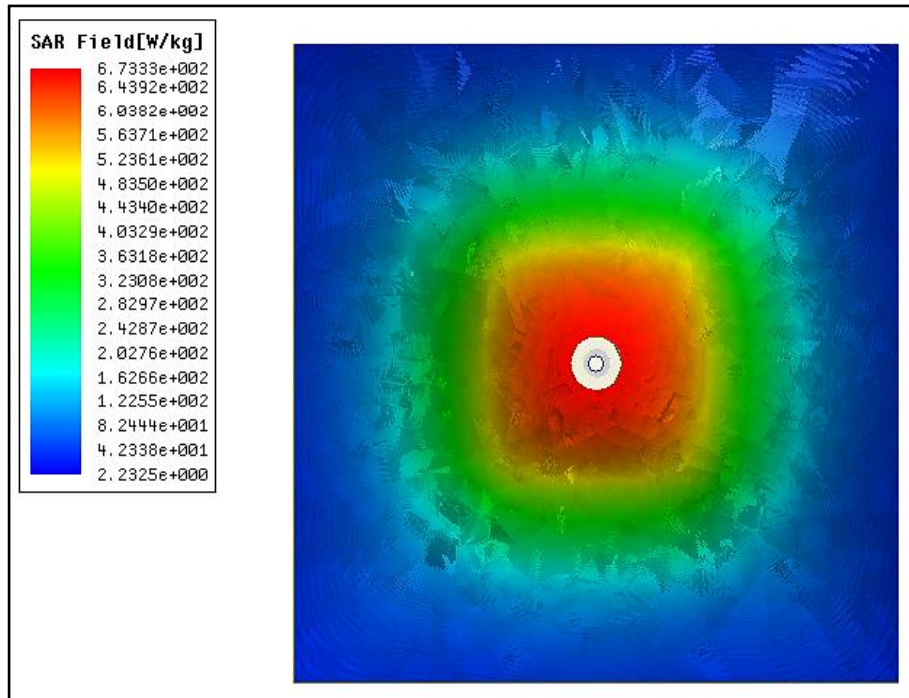


Figure 56. Transverse slice of SAR values across the TDFT structure.

Average SAR distribution is also calculated versus the central axis of antenna and plotted in Fig. 57 while SAR values are calculated over a perpendicular distance across the central axis of the antenna through midpoint of the teardrop structure illustrated in Fig. 58.

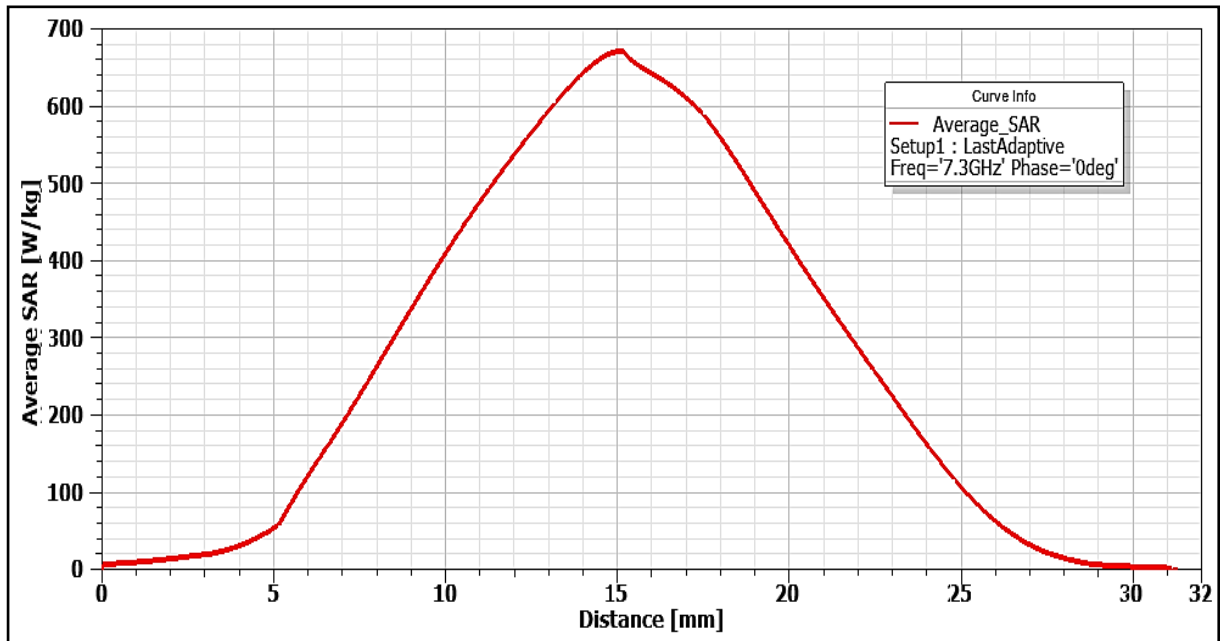


Figure 57. SAR distribution along the central axis of the TDFT antenna.

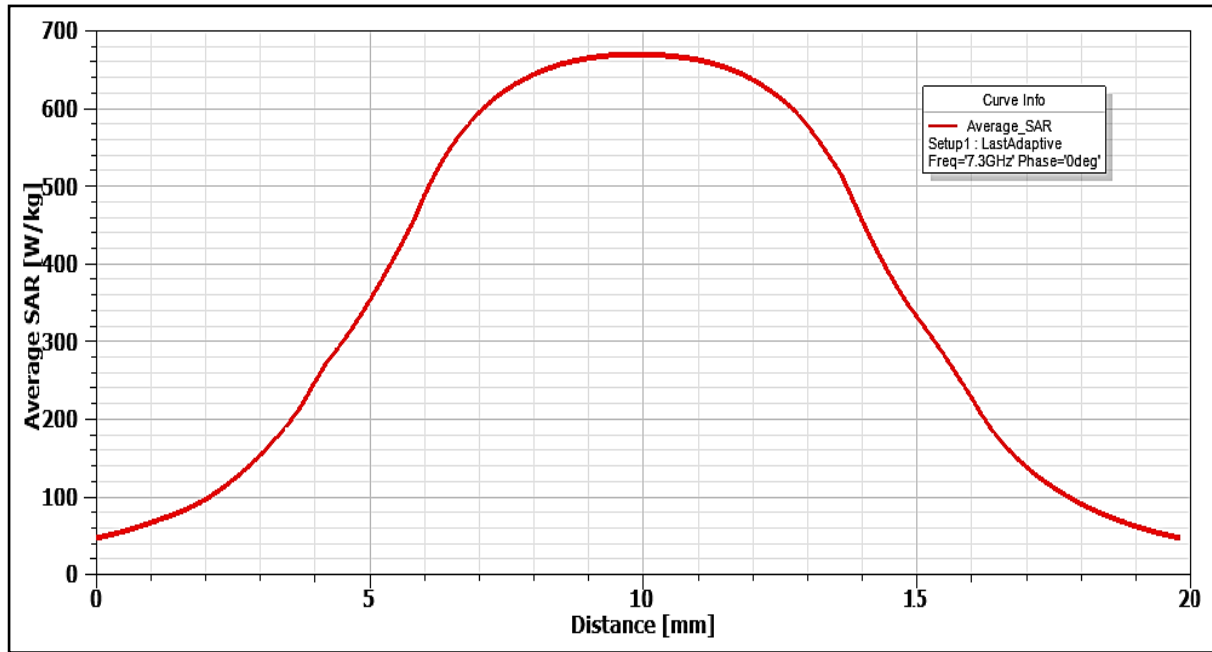


Figure 58. SAR distribution at a distance perpendicular to the central axis of the antenna through the midpoint of teardrop structure.

From Fig. 57, maxima of SAR distribution are observed along the whole length of the antenna including the midpoint of TDFT structure where SAR recorded its highest value to be approximately 669 W/kg. This high value of SAR distribution emphasises on how teardrop structure attained large energy deposition in the targeted tissue around the antenna structure. In addition, SAR values are gradually decrease as the distance from the antenna axis increases as depicted in Fig. 58 which illustrates slow energy absorption by surrounding tissues to ensure how effectively the proposed design destroys the surrounding targeted tissues while maintains minimum radiation exposure towards the healthy tissues. SAR results showed homogeneous distribution in both vertical and horizontal cuts which minimizes the possibility of tissues being unsuccessfully ablated after the procedure.

4.1.3. Simulation Results of TDFT in Malignant Tissue

4.1.3.1. Electromagnetic Analysis

A simple spherical portion of Liver tumour of diameter 20 mm surrounded by healthy liver tissue is modelled using ANSOFT HFSS where tumour tissue is placed at 10 mm from the surface of the liver tissue. The antenna is inserted into tumour with its tip at the centre of the tumour. Frequency

dependent dielectric properties of both healthy and malignant tumour tissues of Liver such as relative permittivity ϵ_r and conductivity σ are adopted from (Holmes, 2009; O'Rourke, Ann P., et al., 2007; Carrara, Nello & IFAC-CNR, Italy, 2014) and illustrated in Table 7.

Table 7. Dielectric properties of healthy liver tissue and malignant tumour tissue at 7.3 GHz

Tissue Type	Dielectric permittivity ϵ_r	Conductivity σ [S/m]
Healthy liver	36.042	6.2775
Malignant liver	46.8546	8.16

FEM simulation of TDFT antenna revealed that reflection is minimized for active length of 11.895 mm. Figure 59 shows the return loss of TDFT antenna loaded in tumour model. Γ reflection was found to be -23 dB at 7.3 GHz. Choosing $(2n-1) \lambda_{eff}/4$ length of teardrop structure reduces fields flowing back on the coaxial outer conductor allowing more power deposition within the tumour tissue.

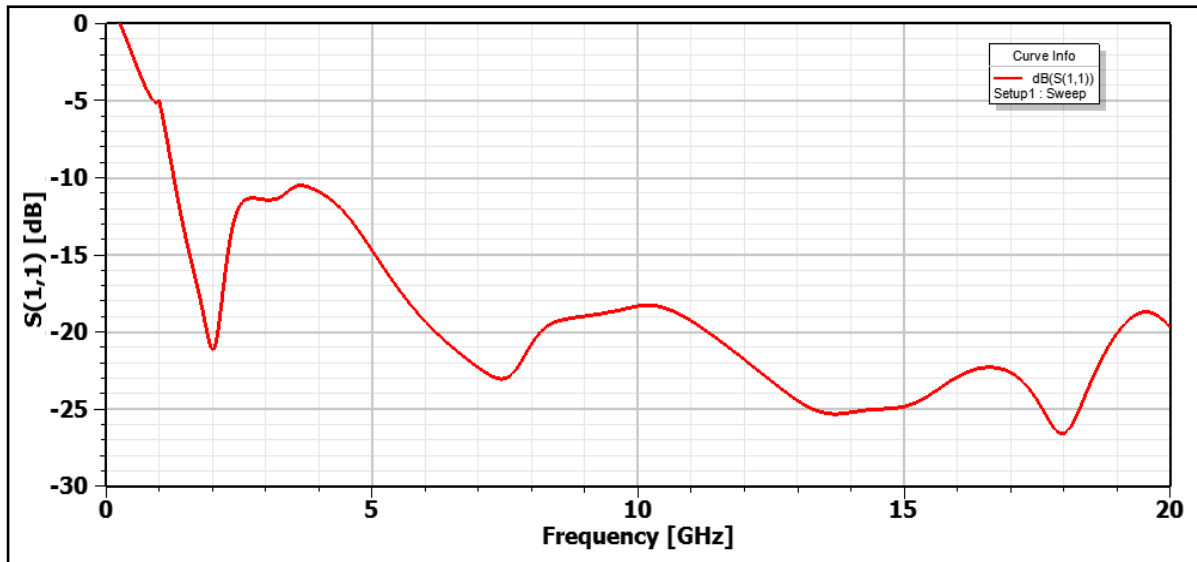


Figure 59. Return Loss of TDFT antenna inserted in tumour tissue surrounded by healthy Liver tissue.

VSWR shows values less than 2 from 1.3 GHz till more than 20 GHz. Overall efficiency is observed to be 98.2 % not only at the operating frequency but also extending from 5.5 GHz to more than 20 GHz showed in Fig. 60. From VSWR results, ultra-wide bandwidth feature of teardrop structure was attained despite the change in the dielectric properties of the surrounding tissue.

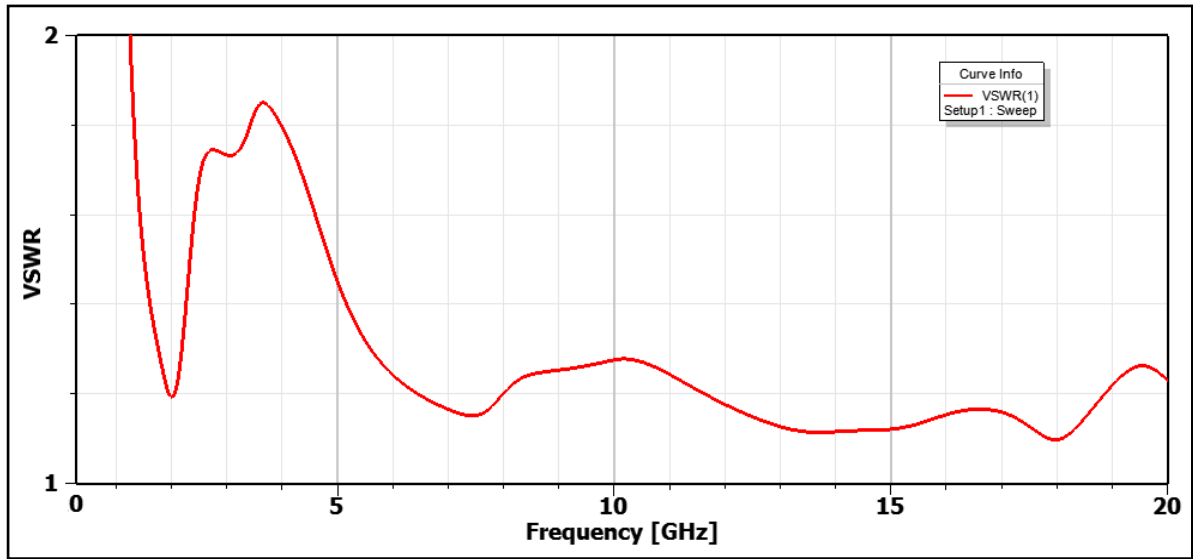


Figure 60. VSWR of TDFT antenna inserted in tumour tissue of Liver

Current distributions along the length of TDFT structure and the outer conductor of the coaxial cable at 7.3 GHz are shown in Fig. 61. Reduced fields flowing on the outer conductor of the coaxial cable can be observed from current distribution illustrated in which results in less heating of the feed line and protection of healthy tissues along antenna shaft.

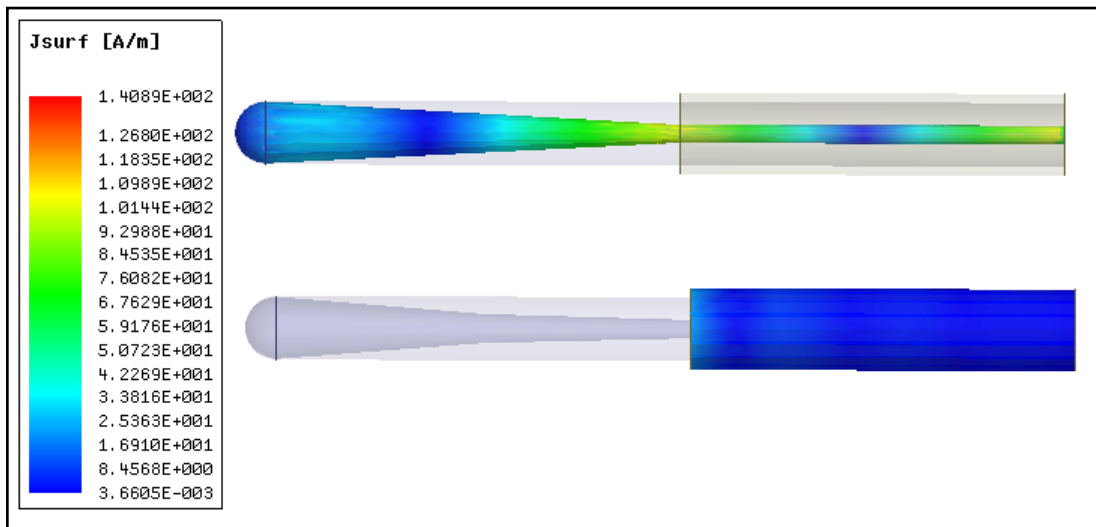


Figure 61. Current distributions along TDFT antenna and outer conductor of the coaxial cable.

Near Field pattern shows how the electric field around the antenna will be well-distributed. Figure 62 illustrates 3D Near field radiation pattern of the TDFT antenna loaded in tumour tissue.

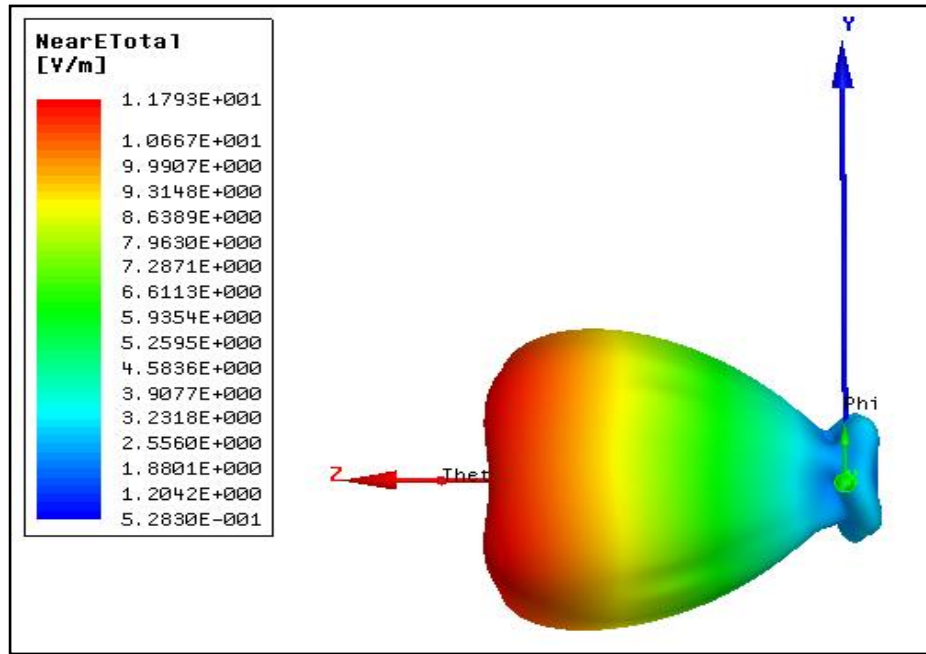


Figure 62. 3D plot of Nearfield pattern of TDFT antenna loaded in Liver tumour.

From Fig. 62, Nearfield distribution is nearly spherical along the TDFT structure and with maximum axial radiation towards the antenna tip unlike omnidirectional patterns proposed in literature. The nearly spherical radiation provides equal distribution of microwave power within the tumour tissue which results in tissues being successfully ablated after the procedure. Moreover, TDFT structure provides minimum backward radiation which is clearly depicted from azimuth and elevation cuts through 3D Nearfield pattern presented in Fig. 63.

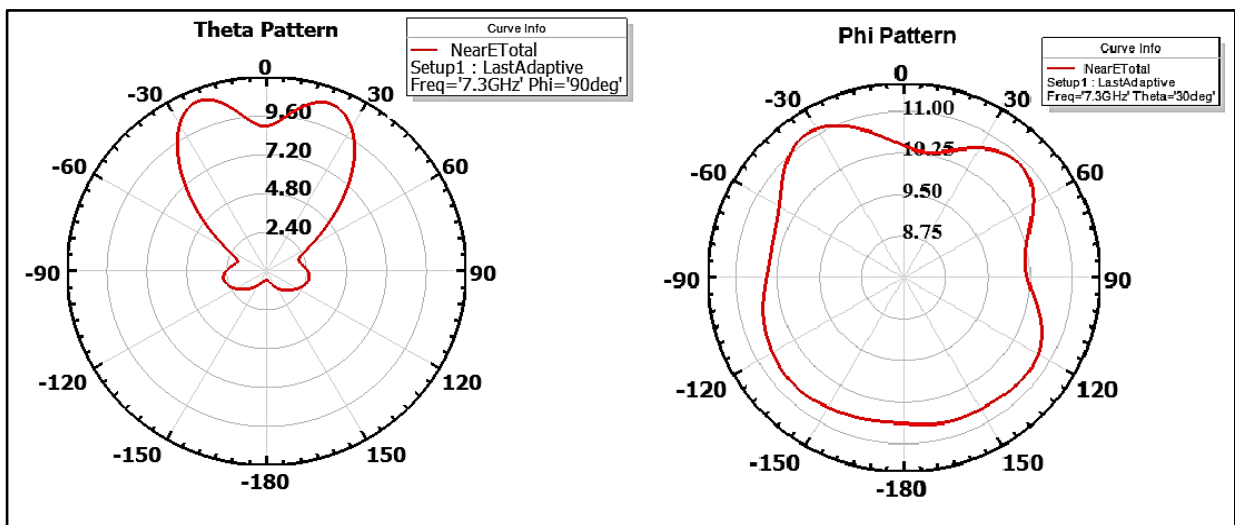


Figure 63. Near-Field radiation patterns of TDFT antenna loaded in tumour tissue at 7.3 GHz in both azimuth and elevation planes.

4.1.3.2. Thermal Analysis

Average SAR is calculated over 1g of tissue where thermal characteristics of both healthy and malignant tissues of Liver are adopted from (Suseela, et al., 2015; Hasgall, P.A., et al., 2015) such as thermal conductivity, specific heat, etc. and illustrated in Table 8.

Table 8. Thermal characteristics of healthy and malignant of Liver

Tissue type	Mass density ρ [kg/m ³]	Specific heat capacity c [J/(kg.K)]	Thermal Conductivity k [W/(m.K)]
Healthy Liver	1079	3540	0.52
Malignant liver	1043	3621	0.5

Figure 64 illustrates SAR distribution along the antenna axis while Figure 65 shows SAR values in transverse slice cut through the midpoint of the teardrop structure. Maxima of SAR values started from the midpoint of the antenna and thermal energy slowly diffused within the tumour model as depicted in Fig. 65. On the other hand, as distance increases from the antenna, SAR decreases gradually which produces homogenous SAR pattern within tumour. Therefore, the teardrop structure provides localized precise ablation zone which is suitable for treating focal tumours of diameter less than or equal to 10 mm.

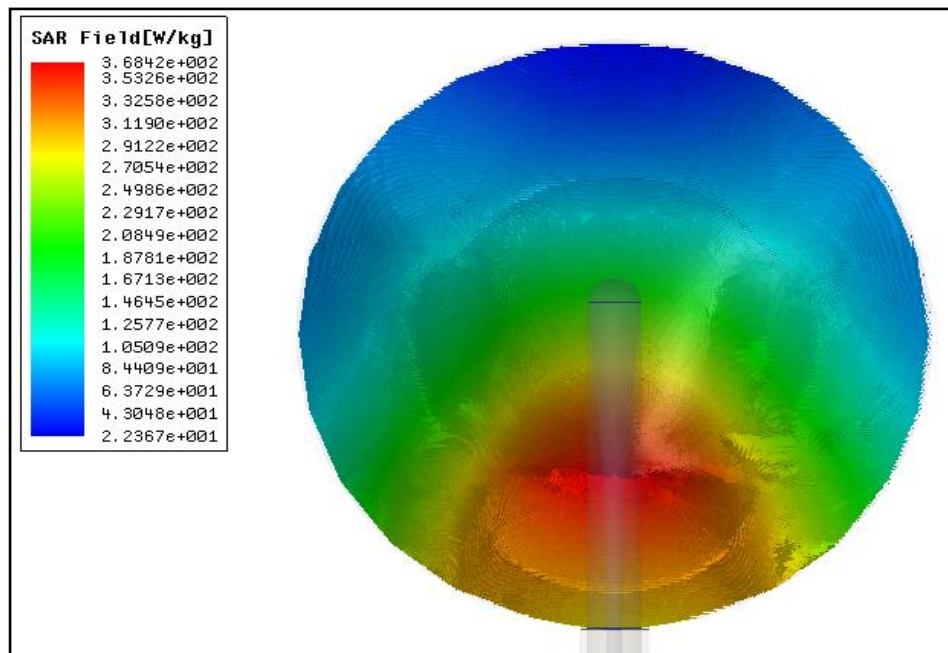


Figure 64. Distribution of SAR along central axis of the TDFT antenna within Tumour model.

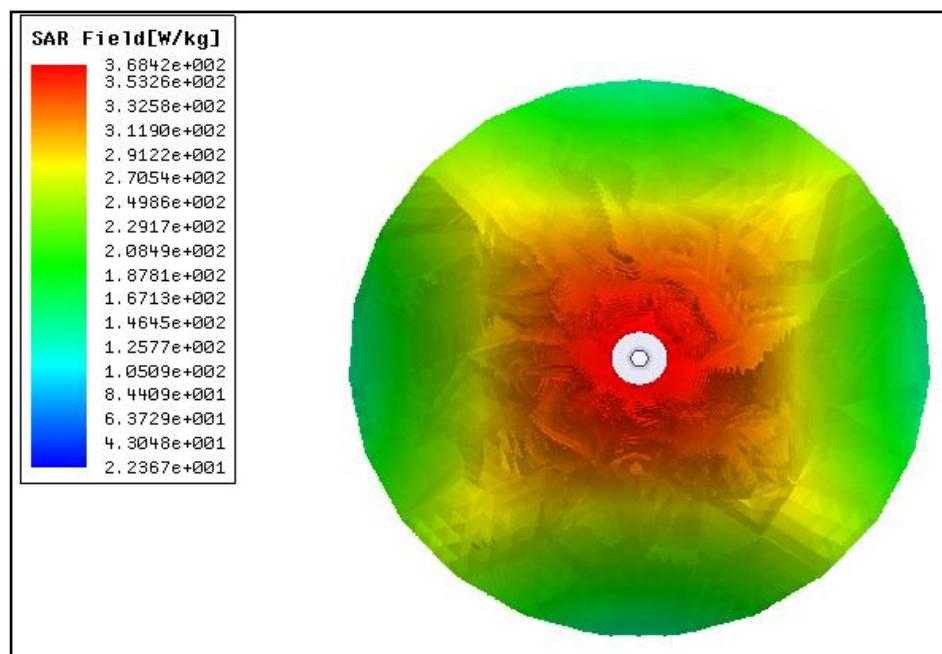


Figure 65. Transverse slice illustrating SAR values through the midpoint of Teardrop structure.

Variation of average SAR is also observed versus the distance along the central axis of antenna which is depicted in Fig. 66. In addition, Figure 67 illustrates SAR values versus distance perpendicular to antenna axis at the midpoint of the teardrop structure.

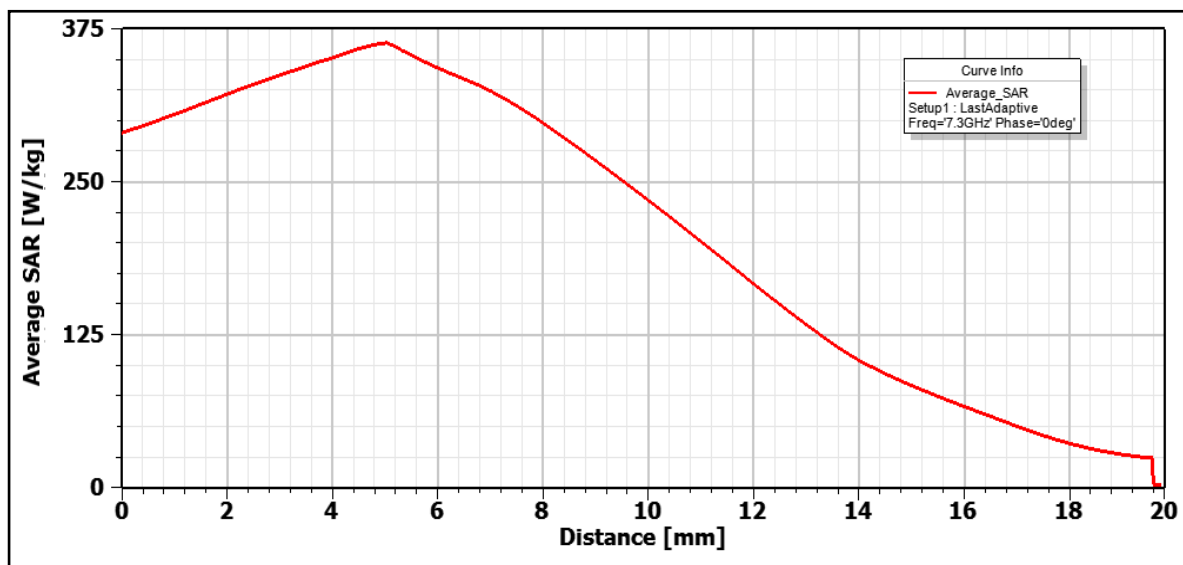


Figure 66. SAR values in the vicinity along the length of the teardrop structure.

From Fig. 66, highest values of SAR are distributed within tumour model along the whole length of the antenna specially at the midpoint of TDFT structure where it recorded its maximum to be approximately 368 W/kg. The peak SAR value emphasises on how TDFT structure attained

minimum reflection along with high power deposition in the targeted tissue around TDFT structure.

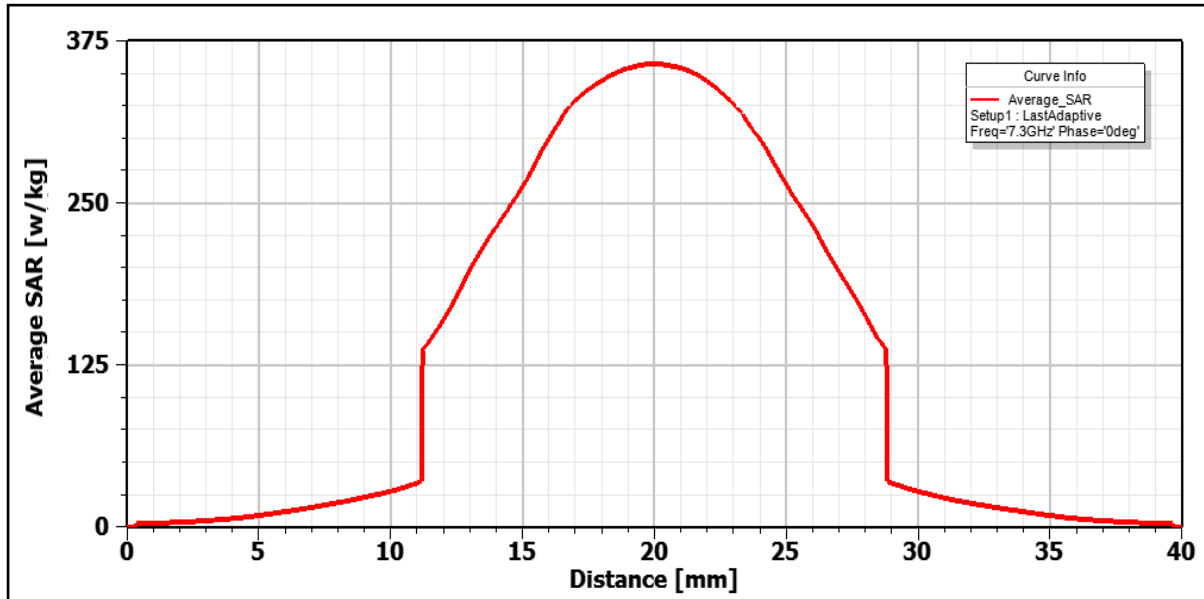


Figure 67. SAR values along a distance through the midpoint of the teardrop structure.

SAR values gradually decrease as the distance from the antenna axis increases. Abrupt decrease in SAR is observed to be 27 W/kg near the tumour/Liver interface which is depicted in Fig. 67. From SAR analysis, SAR pattern recorded its highest values concentrated within tumour model which ensure homogeneous SAR pattern can be attained using TDFT structure.

SAR peak is also investigated using different power levels along a distance perpendicular to the antenna axis through its mid-point to observe the extent of the ablated lesion that could be attained using TDFT structure. One can observe from Figs 68 and 69 that the higher power level applied, the wider the extent of the ablated lesion attained. In addition, maxima of SAR are centred within the tumour model approximately at the mid-point of teardrop structure for all values of power starting from 1 to 4 Watts. Even though TDFT antenna operates at such low power level (1W), high value of SAR is attained to be 368 W/kg and slowly distributed within the tumour unlike maximum SAR obtained in literature using the same power level (Suseela, et al., 2015). Using low power level in addition to ultra-wide band feature provides more control over the energy deposited and achieves more confined SAR lesion than that generated by the conventional antenna designs with narrow bandwidth and much higher power level (Trujillo-Romero, CJ, et al., 2017; Zhang, Huijuan, et al., 2012).

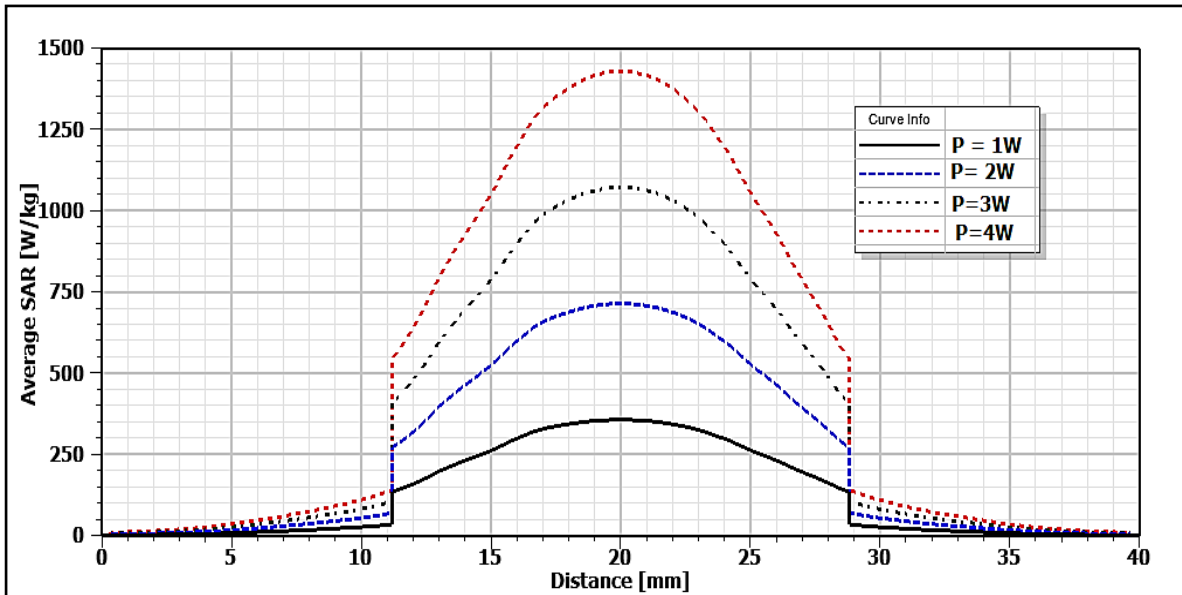


Figure 68. SAR values versus distance through the midpoint of TDFT structure for different power levels.

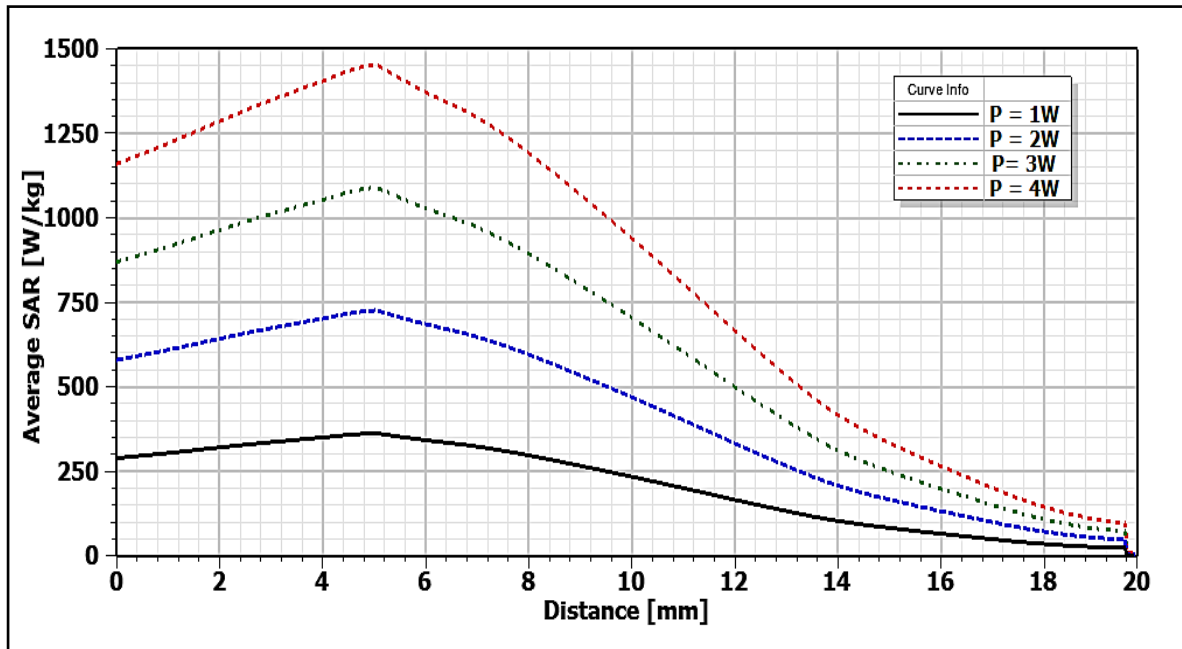


Figure 69. SAR values versus axial distance through TDFT antenna length for different power levels.

The SAR outside the tumour recorded a value of 27 W/kg which slowly decreased away from the tumour model. To give more realistic power loss distribution within the tumour and the surrounding liver model, material properties for TDFT antenna and outer conductor of the coaxial feed were modified from perfect electric conductor (PEC) to Copper. In Addition, an input power of 2 Watts (the default input power is 1W in HFSS) was chosen to check the minimum power level that could achieve the temperatures required for successful ablation. Electromagnetic analysis was

then re-conducted to ensure no difference in the electromagnetic and SAR results previously presented.

ANSYS software package can interpret electromagnetic results evaluated in Ansoft-HFSS and compute steady-state as well as transient temperature response. HFSS – recently known as ANSYS Electronics Desktop starting from 2016– and ANSYS are two separate commercial software packages based on two different platforms integrated together to model accurately the electromagnetic- thermal interaction, i.e., finding the thermal map corresponding to power loss distribution within any given model. In ANSYS, information exchange between different modules is a built-in feature of the software, so that the model can be established by one single software and related data can be transferred easily and more efficiently between the two packages (Ansoft Corporation, 2016; ANSYS Inc, 2016).

Temperature rise in any given material when exposed to electromagnetic radiation can be attributed to either inherent conductor loss or dielectric losses. Herein, A coupled electromagnetic-thermal analysis was performed to attain the temperature profile and consequent ablation lesion in tumour and surrounding liver model based on the power delivered, duration and material characteristics such as density, thermal conductivity and specific heat capacity.

Electromagnetic analysis using HFSS was first performed and different types of losses obtained. First, surface loss density [W/m^2] which results from conductor loss was evaluated on the surfaces of both TDFT structure and the outer conductor of the coaxial feed. Second, Volume loss density [W/m^3] which attributed to dielectric lossy material was evaluated within Teflon, malignant and surrounding healthy non-perfused liver model. HFSS model and Losses are then imported into ANSYS Workbench to thermally analyze TDFT antenna in tumour/liver model. Each evaluated loss represents different imported thermal load in ANSYS Workbench i.e. surface loss density is imported as heat flux load to compute the temperature distribution on the conductor surface while volume loss density is imported as internal heat generation load to evaluate the temperature profile within a dielectric medium. The temperature on the boundary of the model was set to 37°C similar to normal healthy liver with surrounding blood circulation. Figure 70 illustrates the schematic of HFSS - ANSYS Workbench link analysis. Prior steady state thermal analysis is conducted to determine the temperature level reached within the tumour model and then transient thermal analysis is applied to examine the ablated volume attained with increasing time intervals.

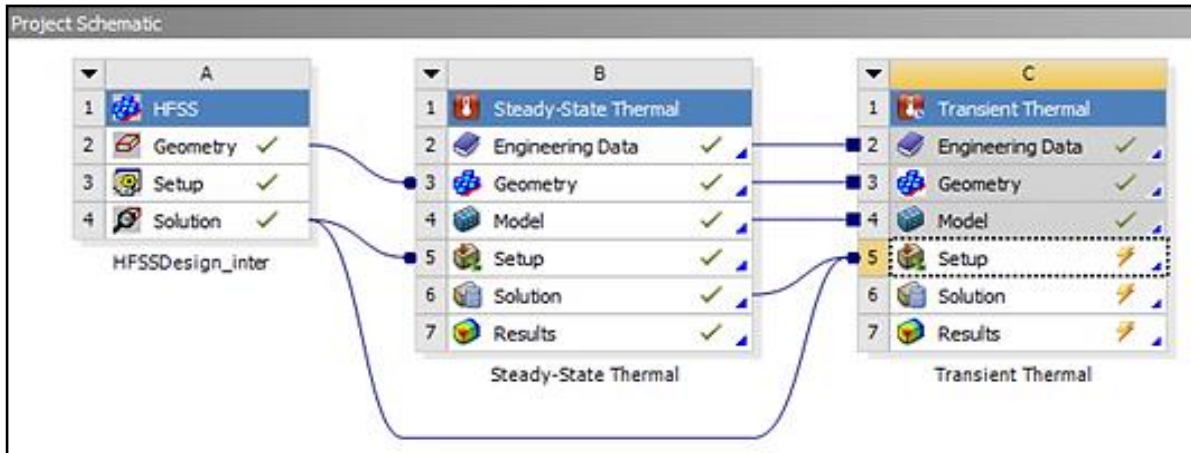


Figure 70. The schematic of HFSS - ANSYS Workbench link analysis.

Figures 71 and 72 depict the temperature levels within the tumour and the surrounding liver models based on steady state thermal analysis. High agreement between SAR results and temperature profile attained where maximum temperature of 65.159 °C reached at the midpoint of TDFT antenna. From steady state thermal analysis, temperatures above 50°C extend to a diameter of approximately 20 mm in the horizontal direction and 18 mm in the vertical direction observed through the midpoint of the teardrop structure within the tumour model where irreversible changes in tissue properties occur as a result of dehydration which in-turn cause instantaneous cell death (Rossmann & Haemmerich, 2014).

In addition, one can notice that 60°C contour is confined within a diameter of 14 mm from the midpoint of the teardrop structure. From Fig. 72, minimum temperature was observed along the antenna shaft which can be attributed to the nature of teardrop design itself acting as a current choke as it was first synthesized by slightly etching a solid cone at its base. Therefore, currents flowing back on the outer conductor of the coaxial feed were minimized which alleviates the consequent overheating of the antenna shaft. In addition, one can observe that maximum temperature of 56 °C is attained at the tumour-liver interface and then sharply decreases to 50 °C within 5 mm away from tumour boundary which satisfies the acceptable ablation safety margin of surrounding healthy tissue to ensure complete eradication of tumour and alleviates the possibility of cancer recurrence (Prakash, Punit, 2010; Poulou, Loukia S, et al., 2015; Singh & Repaka, 2017). This emphasizes on the efficacy of TDFT antenna to produce confined and more controlled ablated lesion.

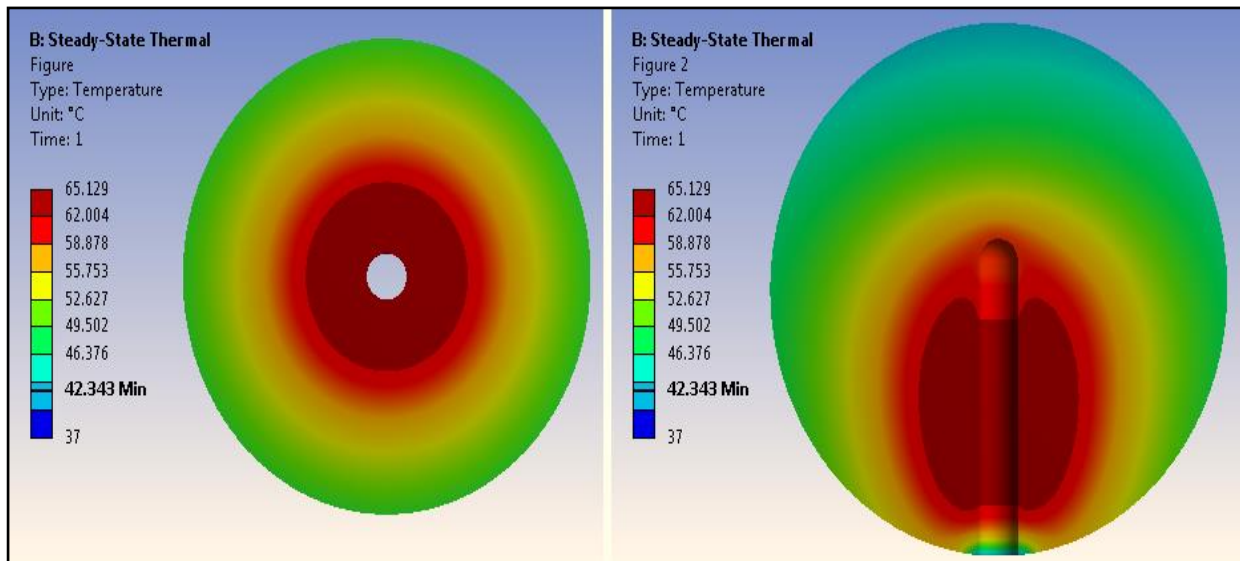


Figure 71. Steady-state temperature levels through horizontal and vertical cuts within the tumour model .

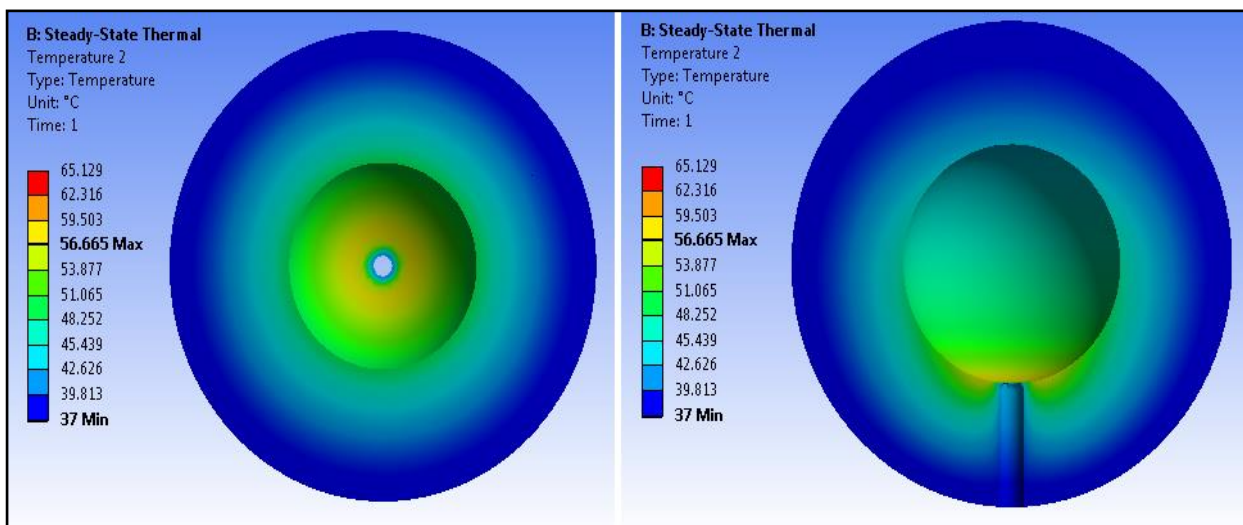


Figure 72. Steady-state temperature levels in the surrounding healthy liver model.

Transient thermal analysis is then conducted for input power of 2 Watts and time duration of 60 secs (1 minute). Similarly, surface loss and volume loss densities are imported in Transient thermal model where each evaluated loss represents different imported thermal load in ANSYS Workbench i.e. surface loss density is imported as heat flux load to compute the temperature distribution on the conductor surfaces while volume loss density is imported as internal heat generation load to evaluate the temperature distribution within a dielectric medium. Steady-state thermal solution was imported as initial temperature condition in the transient thermal analysis to determine the extent of thermal map that could be achieved using TDFT antenna at different time intervals and to make sure therapeutic temperature range is attained within the targeted lesion without reaching vaporization level which may results in instability of microwave equipment.

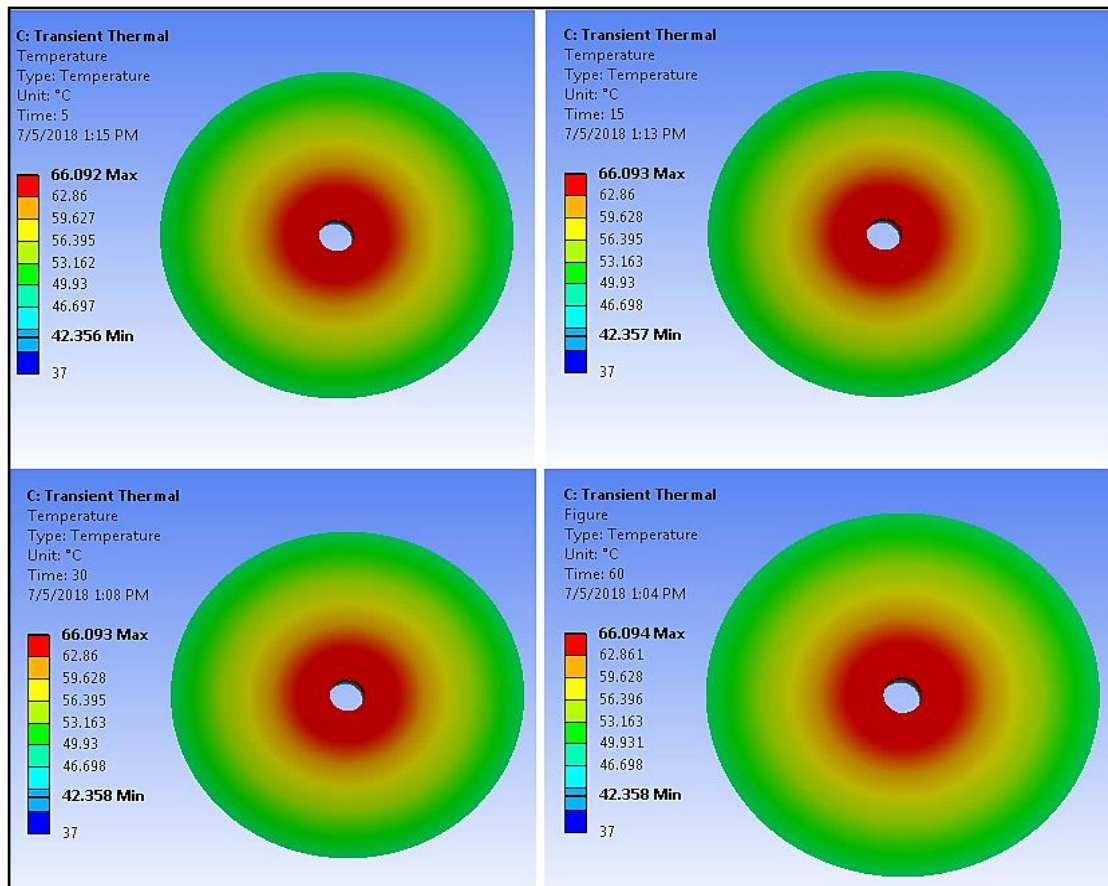


Figure 73. Temperature distribution in horizontal cut for different time durations 5, 15, 30 and 60 secs.

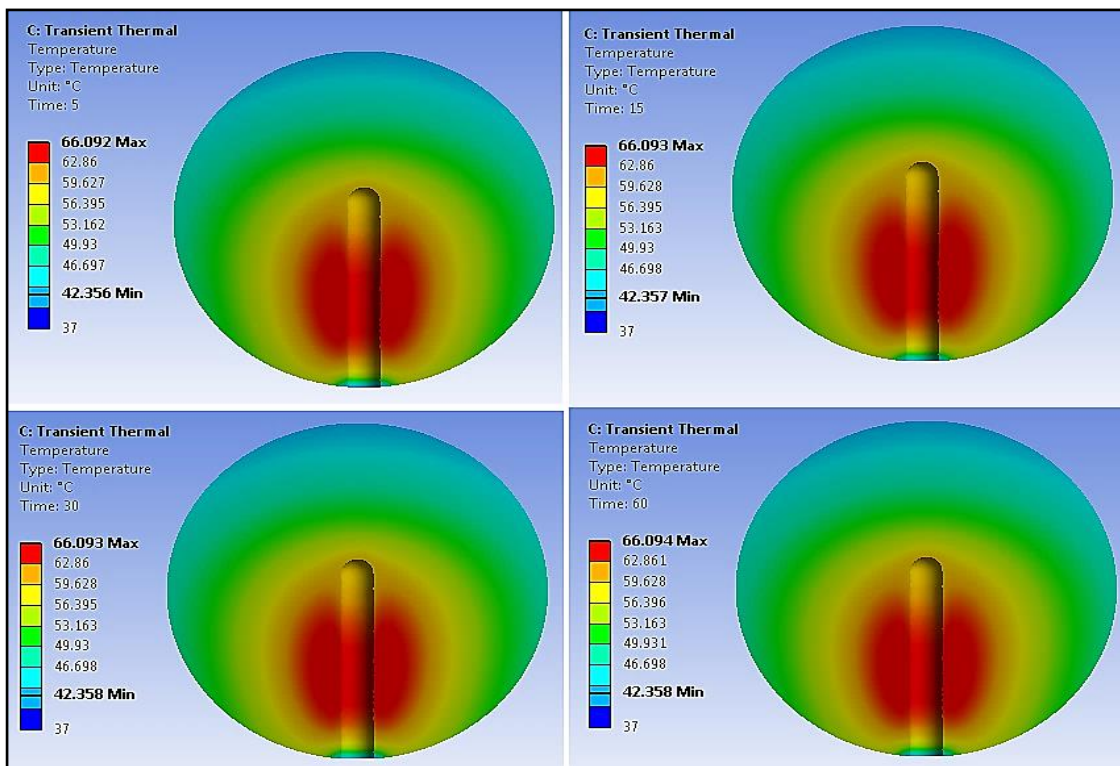


Figure 74. Temperature distribution in vertical cut for different time durations 5, 15, 30 and 60 secs.

As the steady state thermal analysis was imported into transient simulation, the variation in the maximum temperatures increases very slowly as the tissue dehydration was already reached at 60 °C yielding tissue coagulation and instantaneous cell death. Temperature profiles in horizontal and vertical cuts within the tumour model are showed in Figs 73 and 74, respectively for different time durations of radiation exposure where maximum temperature was found to be 66.093 °C for total time duration of 60 secs (1 minute) which provide a final ablated volume of 14.3 mm diameter where 60 °C contour circularly distributed and full eradication of cancerous cells occurs.

In addition, as application time increases, no tissue vaporization was observed – i.e. temperatures in excess of 100 °C– and temperatures are slowly elevated after reaching 60 °C limit which assure normal operation and avoid abrupt termination of ablation due to instability of microwave equipment during ablation (Hancock, et al., 2015). From Fig. 74, temperatures above 50°C contour encompass a diameter of 20 mm and 19 mm observed in the horizontal and vertical directions respectively through the mid-point of the antenna where irreversible changes in tissue properties are encountered due to tissue dehydration.

Temperature distributions in the surrounding healthy liver model are also calculated in transverse and longitudinal cuts and illustrated in Figs 75 and 76, respectively. From Fig. 75, one can observe that maximum temperature of 56.67 °C is attained at the tumour-liver boundary and then gradually decreases to 50 °C in 5 mm contour away from tumour boundary which satisfies the acceptable ablation safety margin of healthy tissue to ensure complete eradication of tumour and alleviates the possibility of cancer recurrence. Temperatures along the antenna shaft were clearly minimized as shown in Fig. 76 as the proposed TDFT antenna design chokes the currents following back on the outer coaxial feed which in-turn reduces the consequent overheating of the antenna shaft. Transient thermal analysis highly agrees with SAR results as temperature distribution recorded its highest value at the mid-point of TDFT antenna.

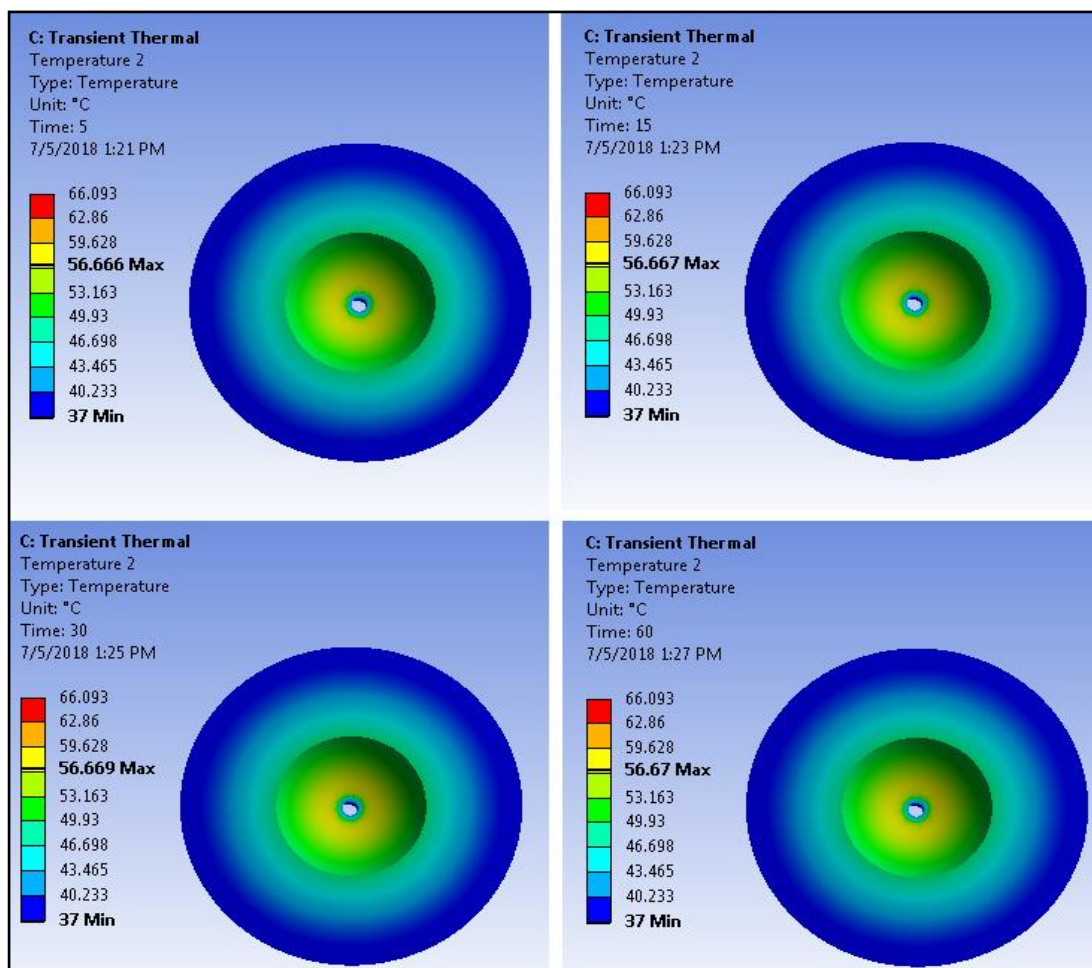


Figure 75. Temperature distribution in transverse cut for different time durations 5, 15, 30 and 60 secs in the surrounding liver model.

From SAR results and thermal analysis, TDFT antenna proved to be a standalone microwave applicator in producing comparable ablated zones to that proposed in literature at the same frequency band and much higher microwave power as introduced in (Luyen, Hung, et al., 2017; Mohtashami, Yahya, et al., 2017). Structure of the proposed TDFT antenna was synthesized such that a natural current choke embodied in the teardrop structure itself which increases the compactness of the applicator size and hinders the possibility of using any additional external chokes as previously presented in (Luyen, Hung, et al., 2017).

The efficacy of TDFT antenna as a microwave coagulator is clearly depicted in producing circularly ablated lesion of 14.3 mm diameter and up to approximately 20 mm zone of irreversible changes in tissue properties yet to be fully destroyed using only 2 Watts of microwave power in 60 seconds of radiation exposure. Moreover, ultrawide band feature of TDFT antenna facilitates the introduction of low power microwave ablation which proved to be more efficient in providing

more control over the heating zone within the targeted section (Trujillo-Romero, CJ, et al., 2017; Fallahi, Hojjatollah, et al., 2017; Zhang, Huijuan, et al., 2012).

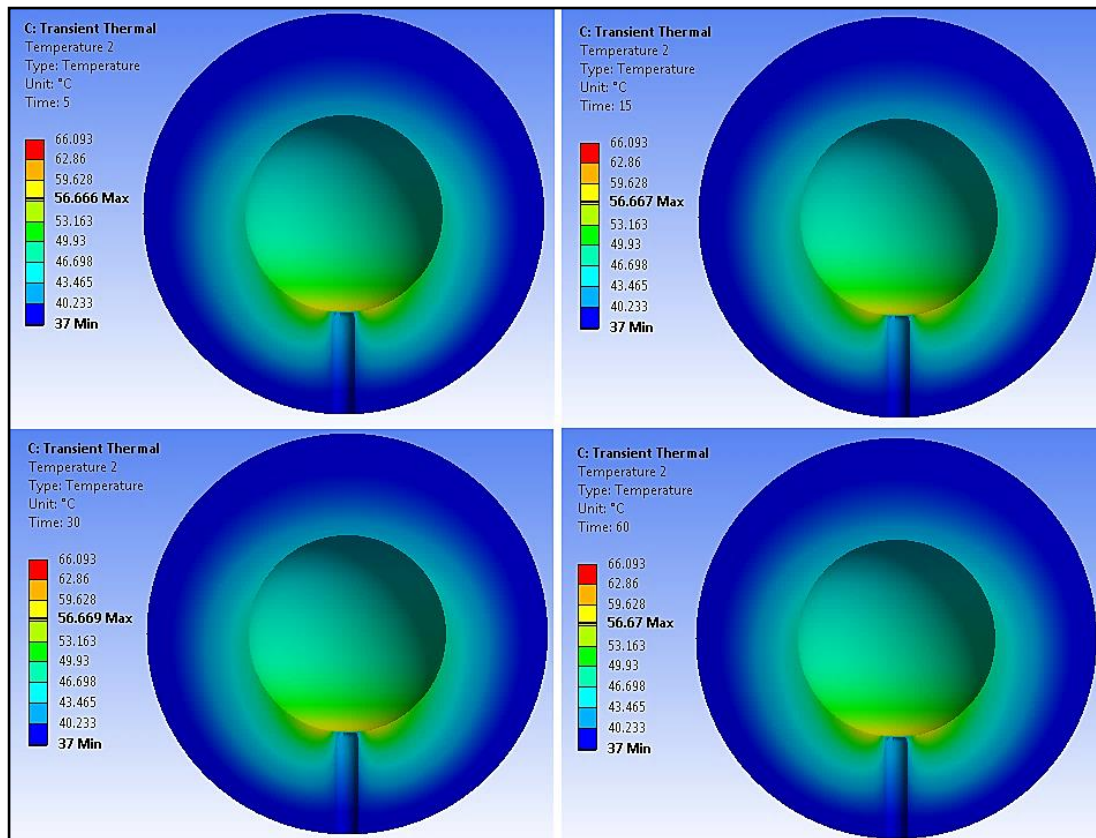


Figure 76. Temperature distribution in longitudinal cut for different time durations 5, 15, 30 and 60 secs in the surrounding liver model.

In addition, TDFT antenna achieved the safety margin of healthy tissues required to ensure successful ablation of tumour and reduce of the possibility of having cancer metastasis condition in cancer patients. Despite low frequencies have higher penetration depth which was claimed to achieve larger ablated volume, studies proved that at low frequency bands, inhomogeneous heating zones with tissue not being successfully ablated were attained after the procedure. Therefore, choosing frequency of operation to be 7 GHz unlike the conventional frequency bands associated with previously proposed designs such 915 MHz and 2.45 GHz (Neagu, 2017; Martínez-Valdez, R., et al., 2017; Luyen, et al., 2017) has significant advantages such as: at higher frequency bands, thermal conductivity of biological tissues and power absorption rate in both non-perfused and strongly perfused regions are found to be higher than that at lower frequencies (Sawicki, et al., 2018) which was exploited in providing homogeneous ablated zones and more confined heating dose within targeted areas as clearly depicted in temperature profiles of the proposed TDFT

antenna. Furthermore, more flexibility and size compactness of antenna is rather achieved at higher frequency than that at low frequencies. Low temperature along the antenna shaft and outer conductor of coaxial cable was clearly depicted from thermal analysis which can be attributed to the synthesis of TDFT antenna structure with natural choke at the starting point of the coaxial feed. Consequently, overheating problem encountered in microwave ablation procedure is noticeably alleviated and protection of healthy tissues along is significantly achieved using TDFT antenna (Mays, R. Owen, et al., 2016; Sharma, Shashwat & Sarris, Costas D., 2016).

The electromagnetic and thermal analysis of the TDFT antenna introduced above gives a preliminary idea on the antenna performance in different dielectric mediums and the extent of the temperature distribution especially the 55-60 °C contours where irreversible changes in tissue properties and instantaneous cell death attained. In the next section a study regarding the realization of TDFT antenna is conducted which includes modifications introduced in the prototype design to facilitate its manufacturing. Further studies are then applied to observe the effect of the input power on the duration of radiation exposure and the total ablated volume attained. Thermal analysis also investigates the total duration of radiation exposure to reach the temperature levels required to fully destroy the targeted tumour and its peripheries.

4.2. Realization of Prototype of TDFT antenna

As mentioned earlier, Teardrop structure has such significant features that distinguish it as a standalone design among other microwave applicators proposed in literature. nevertheless, the only difficulty encountered is its fabrication as stated by Eng. Aiden in Maker space at university of SALFORD “it is a very small structure to be manufactured in a traditional manner at the tolerances given for many reasons.” One of which is that the smallest diameter to be manufactured as checked with a couple of manufacturing companies is 1mm while the current smallest diameter of TDFT antenna is 0.5 mm. Therefore, TDFT antenna should be re-scaled a in bigger size provided that there are no significant differences in the simulated results attained before.

The most important factors to be considered in re-scaling the antenna in bigger size are:

- Maximum diameter of the antenna doesn't exceed 3.5 mm in order not to cause complications after the ablation procedure (see chapter 1 section 1.4) while minimum diameter of the antenna should be no less than 1mm.

- Minimum reflection S_{11} is required to minimize the currents excited on the outer conductor of the coaxial feed.
- Homogeneous distribution of electric field (E) is required which in-turn provides homogenous temperature profile.
- Acceptable SAR values to achieve the temperature levels required for successful ablation.

Parametric studies were applied to teardrop structure loaded in tumour/Liver model using ANSYS Electronics Desktop v.16 (previously introduced as Ansoft HFSS) to obtain the optimum dimensions of TDFT antenna to achieve the specifications required for successful ablation. With the new design considerations mentioned above, coaxial cable is chosen to be 50-ohm low loss semi-rigid coaxial cable with inner conductor, dielectric and outer conductor diameters are 1.025, 3.4, 3.9 mm, respectively. The coaxial dielectric material used is Teflon with dielectric permittivity of 2.1. The material of inner and outer conductors is assigned as copper. Teardrop structure is then created using a solid cone with lower diameter similar to that of the inner conductor of coaxial cable. Due to the abrupt transition between the coaxial cable and conical structure which may increase reflection, more smooth transition is applied by etching the outer conical surface using inner surface of ring torus with inner and outer radii of 0.5125 and 64.3439 mm, respectively to choke and minimize the currents flowing back on of the outer conductor of the coaxial feed which in-turn reduce the consequent overheating of the cable.

Several study scenarios were modelled and simulated electromagnetically using Electromagnetic Desktop suite (previously named as HFSS) and thermally using ANSYS Workbench such as different cone radius, the length of conical structure. First, a study of different cone radii is conducted with changing the length of conical structure to reach the optimum upper cone radius where minimum possible reflection is achieved. Table 9 shows the minimum reflection attained at 7.3 GHz for different cone lengths with respect to different cone upper radii as depicted in Fig. 77.

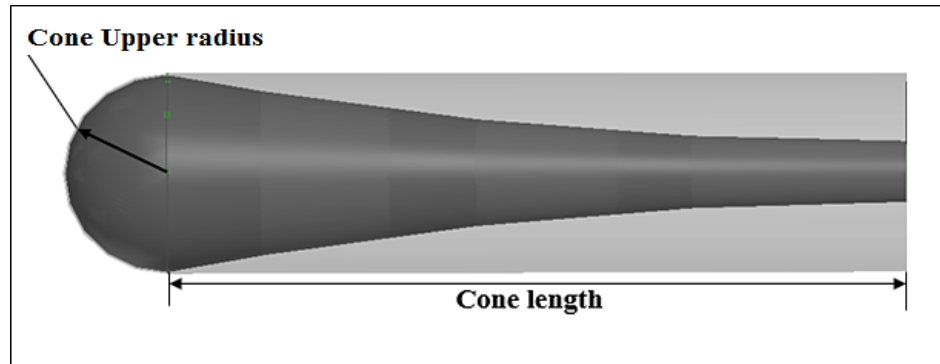


Figure 77. Side view of TDFT antenna.

Table 9. Parametric study of different cone radius and lengths versus reflection attained at 7.3 GHz

Cone length [mm]	Cone upper radius [mm]	Reflection at 7.3 GHz (S_{11})
9	1.1	-16.6775
10		-15.7474
11		-14.7032
11	1.2	-16.029
11	1.5	-20.857
11	1.66	-22.1008

From the simulated results provided in Table 9, the smaller the cone radius, the higher the reflection attained at fixed length. One can also observe that reflection increases with the increase of cone length at fixed upper cone radius while with increasing the upper cone radius at fixed cone length, reflection noticeably decreases. 1.66 mm cone radius showed the minimum reflection of -22.18 dB which is the closest value to that previously provided with the smaller version of teardrop design. In addition, 1.66 mm cone radius gives maximum antenna diameter of 3.3 mm which is considered a good compromise as the whole structure of the antenna is yet to be coated with a Teflon layer which minimize any adhesiveness with desiccated or charred tissues after the ablation. Therefore, cone radius of 1.66 mm was chosen for further parametric study to reach the optimum cone length to achieve axial radiation with lowest possible backward radiation and acceptable SAR level at 7.3 GHz. Table 10 illustrates the study of different lengths of conical structure with corresponding minimum reflection at 7.3 GHz and maximum SAR value obtained. From the simulation results obtained in Table 10, the longer the cone length is, the less is the reflection attained. However, on the other hand, SAR values decreases with increasing the length of the conical structure which might affect the temperature levels required for successful ablation (≈ 50 to 60 °C).

Table 10. Study of different cone lengths with corresponding reflection and maximum SAR value attained

Cone upper radius of 1.66 [mm]	Cone Length [mm]	Reflection at 7.3 GHz	Maximum SAR attained [W/kg]
	8.63	-25.1643	370.9
	8.75	-24.2525	368.86
	9	-24.4541	364.81
	10.235	-23.341	345.62
	11.065	-25.0566	333.35
	12	-25.8888	322.46
	13	-27.6855	313.84
	14	-30.2184	308.28
	15	-29.3912	304.13

Choosing the optimum teardrop length necessitates further thermal analysis to ensure homogenous temperature levels with nearly spherical distribution achieved. To minimize the time consumed by thermal analysis, temperature distribution won't be presented at all cone lengths mentioned above in Table 10. Figure 78 shows the steady state temperature distribution of cone lengths 10.235, 11.065, 12 and 14 mm for input power of 2W. High agreement were found between SAR results and temperature distribution attained for different teardrop lengths presented in Fig. 78. The highest temperature was found to be 61.453 °C for teardrop length of 10.235 mm which can be attributed to the highest SAR value obtained among all teardrop lengths encompassed in the thermal analysis while lowest temperature attained was 45.294 °C for 14 mm teardrop length as it has the lowest SAR value among all teardrop lengths presented in Fig. 78.

From the temperature profiles presented in Fig. 78, all teardrop lengths achieved the temperature level required for successful ablation at the same power level except 14 mm cone length. The low SAR results and hence low temperature distributions when increasing antenna length can be attributed to as the longer the antenna length is, more directive radiation pattern is, which makes the radiated fields produced less susceptible to be well absorbed by the surrounding tissues. Nevertheless, longest cone lengths i.e. 12mm and 14mm produce nearly spherical and confined heating zones around the antenna structure than that produced by smaller cone lengths.

Despite 10.235- and 11-mm cone lengths achieve the highest temperature level and SAR values, 50 °C contours in the temperature distributions were found to have more elliptical shapes through the vertical cuts along tumour model presented in Fig. 78 (highlighted in dashed black line). On the other hand, 12 mm teardrop length achieves more spherical and confined temperature

distribution where the highest temperature found at approximately the midpoint of teardrop structure is 60.589 °C and gradually decreases towards the tumour/liver interface. Thus, choosing 12 mm cone length is more power efficient than 14 mm as it will require less power to reach the temperature levels required for successful ablation in addition to creating nearly spherical confined ablation zone Nevertheless, to compensate the lower SAR value associated with 12 mm cone length, input power will be increased to meet the safety margin standard i.e. less than 10 mm of healthy tissues fully eradicated around the tumour to minimize the possibility of having cancer recurrence.

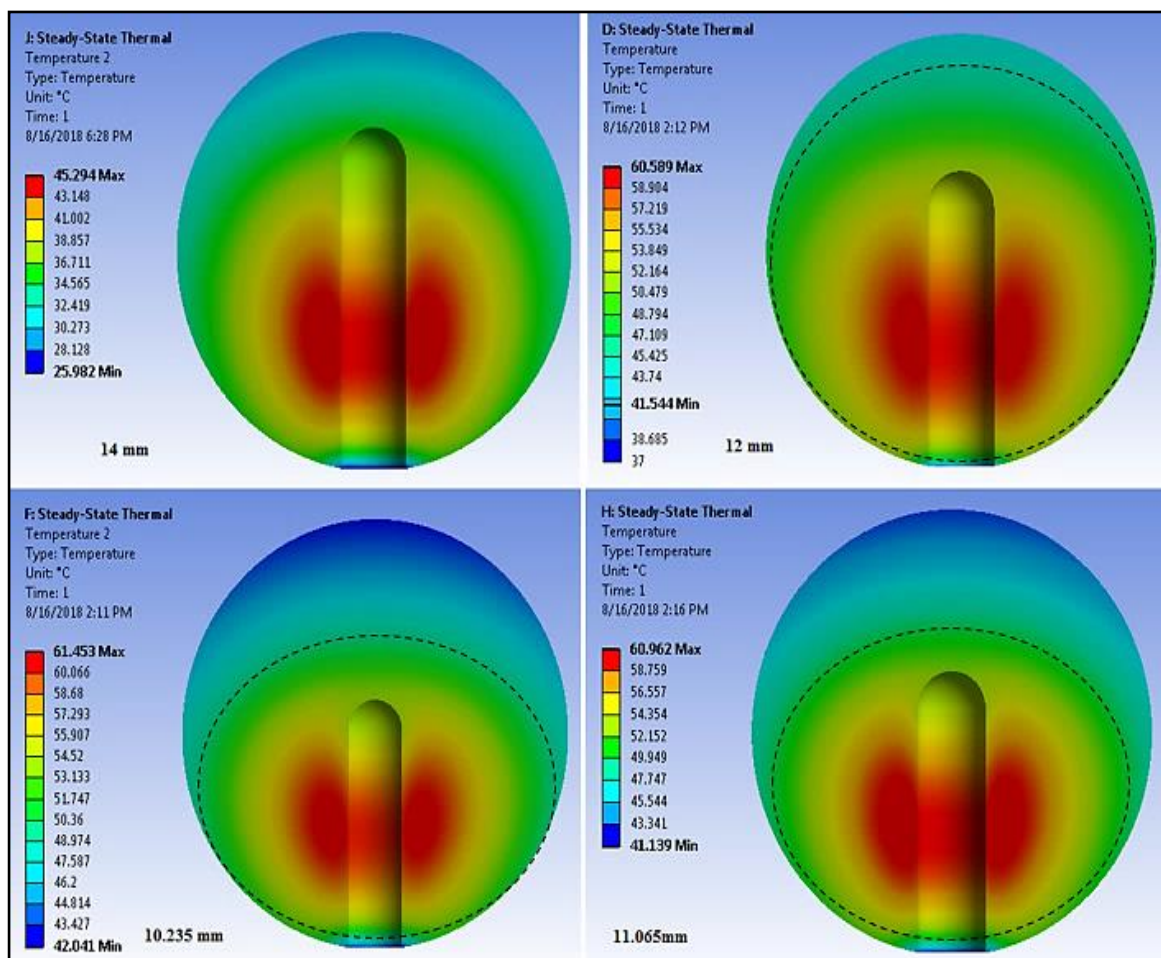


Figure 78. Steady state temperature distribution of cone lengths 10.235, 11.065, 12 and 14 mm for input power of 2W.

4.2.1. Simulation Results of TDFT in Malignant Tissue

4.2.1.1. Electromagnetic Analysis

ANSYS Electronics Desktop V.16 is then used to build a computational model of TDFT antenna of new total length of 13.66 mm which composed of cone length and cone upper radius at the hemispherical tip to be simulated at 7.3 GHz with 3W input power. The new dimensions of TDFT antenna and coaxial feed are shown in Table 11 as depicted in Fig. 79.

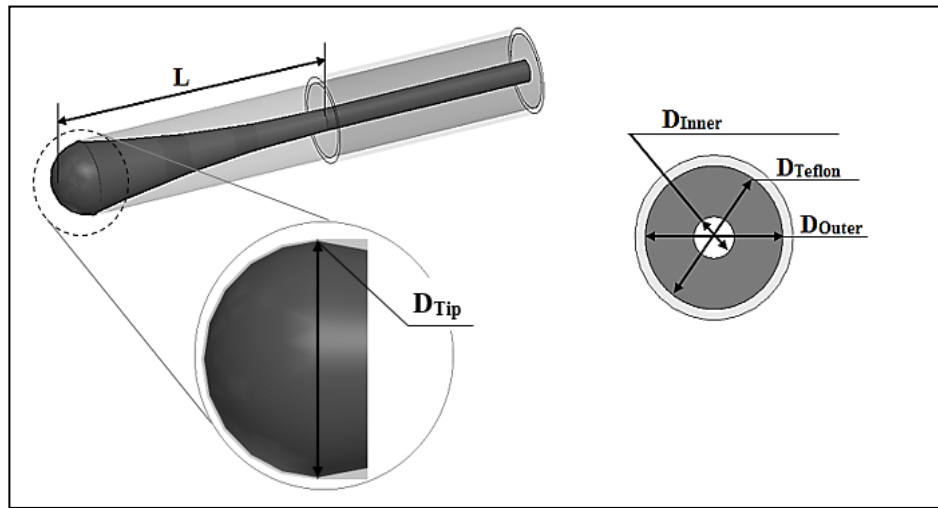


Figure 79. Structure of the new TDFT antenna

Figure 80 shows the return loss of TDFT antenna loaded in tumour model. Γ reflection was found to be -25.89 dB at 7.3 GHz. Reflection less than 15 dB is maintained all over a bandwidth extending from 3 GHz to more than 20 GHz. VSWR shows values less than 2 from 1.5 GHz till more than 20 GHz as depicted in Fig. 81. Overall efficiency is observed to be 99.17 % (reflection less than 20 dB) not only at the operating frequency but also extending from 4.6 GHz to 17.6 GHz. From VSWR and S_{11} results, the new dimensions of TDFT antenna achieved less reflection than that of the smaller version of TDFT antenna previously presented.

Table 11. New dimensions of TDFT antenna and coaxial cable

Dimension		Units in [mm]
D_{Inner}	Diameter of Inner conductor of coaxial feed	1.025
D_{Teflon}	Diameter of Teflon Dielectric	3.4
D_{Outer}	Diameter of outer conductor of coaxial feed	3.9
L	Total Length of TDFT antenna	13.66
D_{Tip}	Maximum diameter of TDFT at the tip	3.32

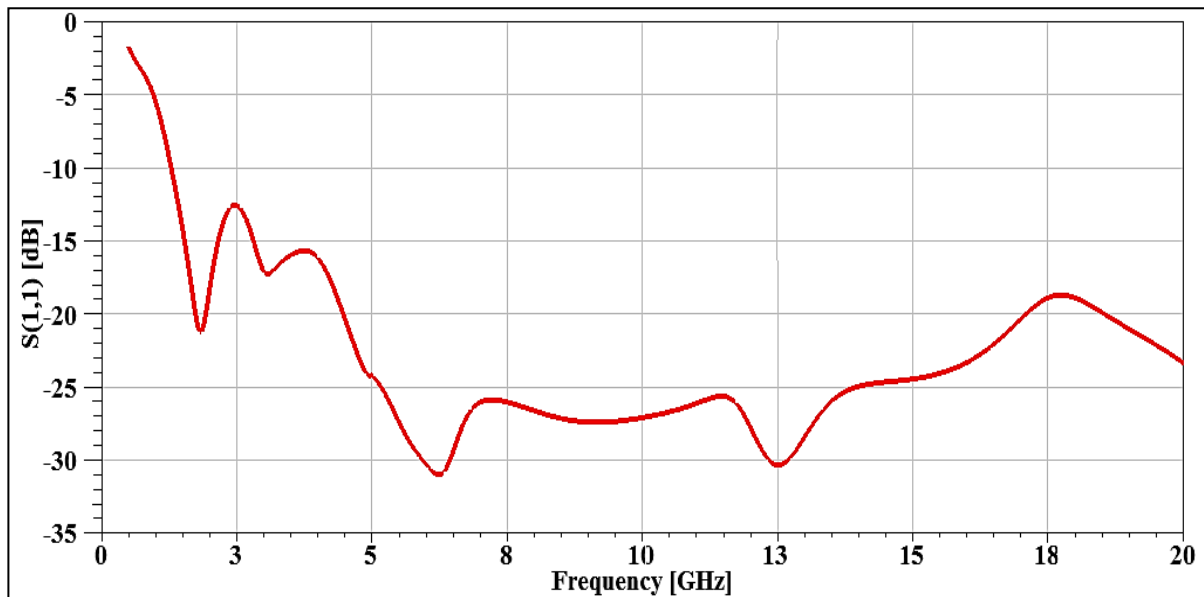


Figure 80. Return loss of TDFT antenna loaded in tumour model.

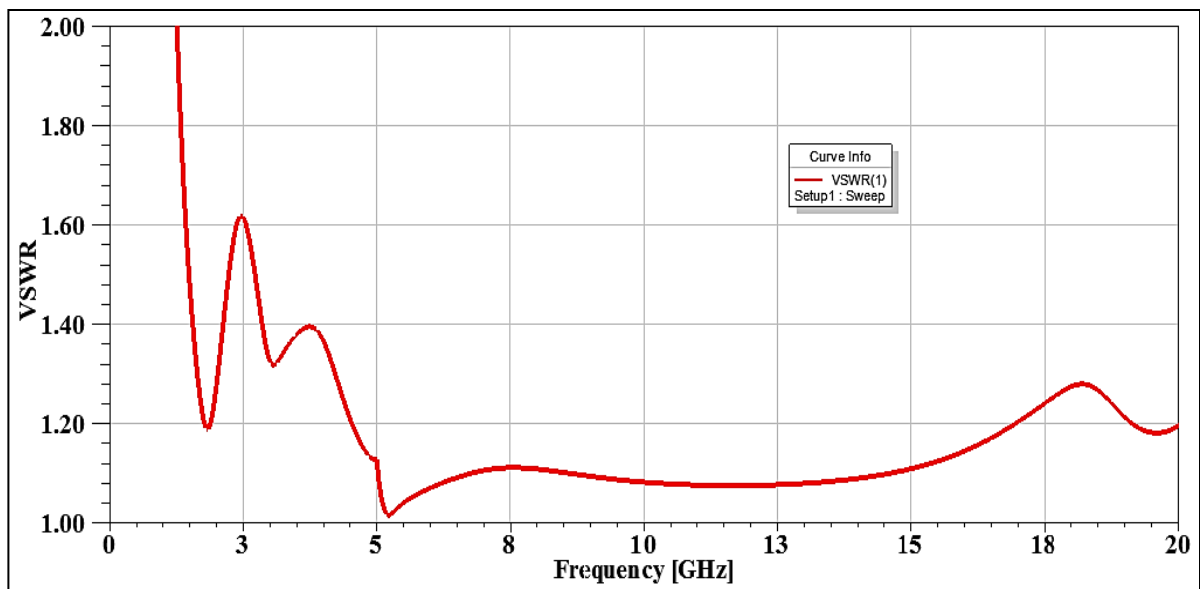


Figure 81. VSWR of TDFT antenna loaded in tumour model

Current distributions along the length of TDFT structure and the outer conductor of the coaxial cable at 7.3 GHz are shown in Fig. 82. Reduced currents are clearly noticed flowing back on the outer conductor of the coaxial cable which results in less heating of the feed line and protection of healthy tissues along antenna shaft.

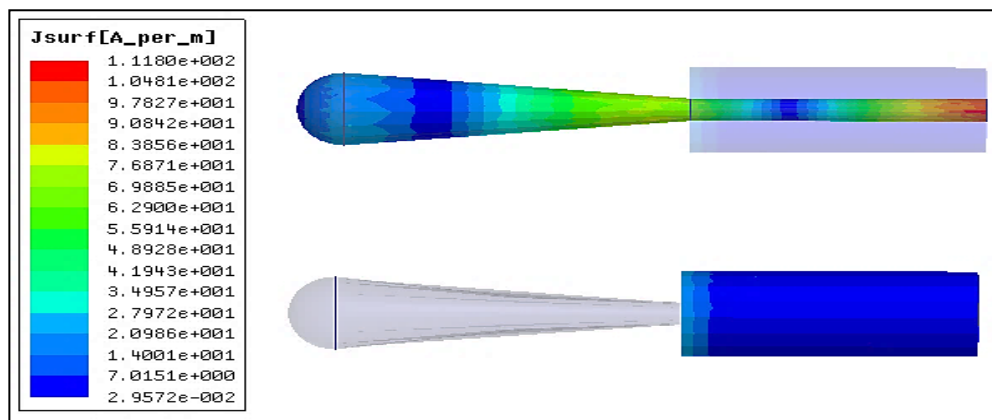


Figure 82. Current distributions along the length of TDFT structure and the outer conductor of the coaxial cable at 7.3 GHz.

Figure 83 illustrates 3D Near field radiation pattern of the TDFT antenna loaded in tumour model and the distribution of electric field in both azimuth and elevation plans is depicted in Fig. 84. TDFT antenna recorded higher values of nearfield along the TDFT structure than that obtained in the smaller design with maximum axial radiation towards the antenna tip unlike omnidirectional patterns proposed in literature. This nearly spherical radiation participates in providing spherical heating zone within the tumour tissue which alleviates the possibility of tissues not being successfully ablated using TDFT antenna. Moreover, minimum backward radiation is clearly observed from Fig. 84 which may help protect the healthy tissues along the antenna shaft.

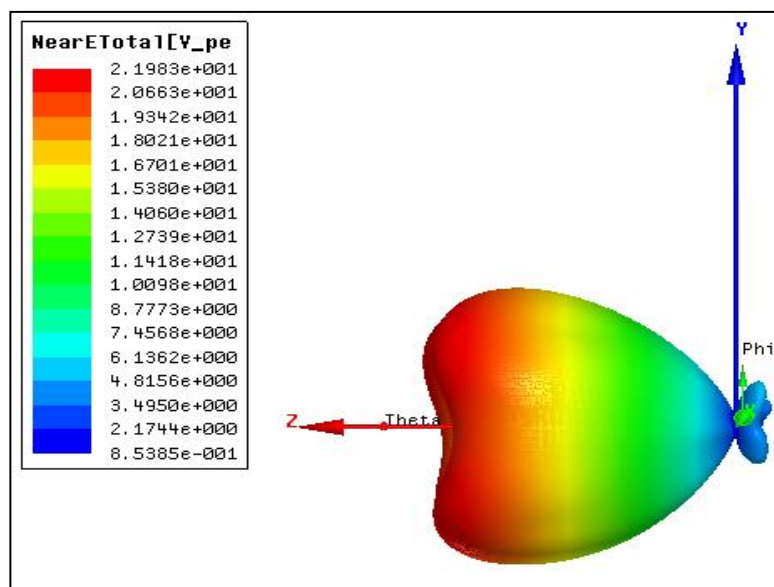


Figure 83. 3D plot of Nearfield of TDFT antenna.

Furthermore, nearfield results illustrated in Fig. 84 showed a significantly good agreement with the electric field distribution attained using numerical model illustrated in Figs 39 and 40 at the same radial distance from the antenna structure. This emphasizes on the efficacy of semi-analytical numerical calculation of electric field distribution due to a current sheet flowing on the antenna surface.

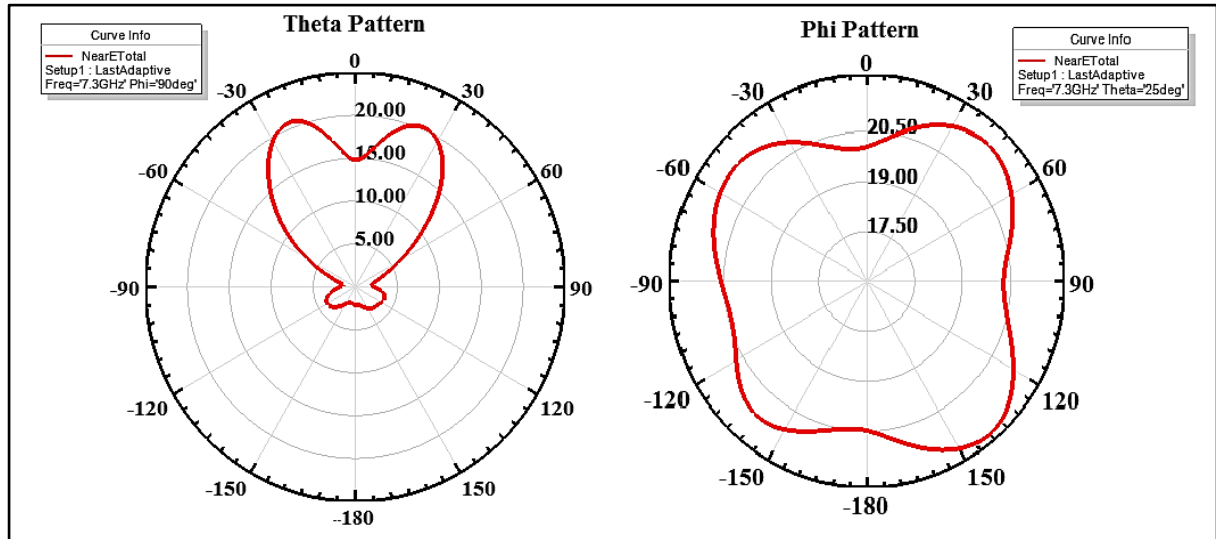


Figure 84. Near-Field radiation patterns of TDFT antenna loaded in tumour tissue at 7.3 GHz in both azimuth and elevation planes.

4.2.1.2. Thermal Analysis

Average SAR was then calculated for 3W input power averaged over 1 gram of tissue including thermal characteristics of both healthy and malignant tissues of Liver as illustrated in Table 8. Figure 85 illustrates SAR distribution along the antenna axis while Figure 86 shows SAR values in transverse slice cut through the midpoint of the teardrop structure. Maxima of SAR values started from the midpoint of the antenna and slowly diffused within the tumour model. On the other hand, as distance increases from the antenna, SAR decreases gradually which produces homogenous SAR pattern within tumour. High SAR values obtained for only 3W input power emphasizes on the efficacy of TDFT antenna as a microwave applicator among previously proposed designs with bigger size and much higher power level.

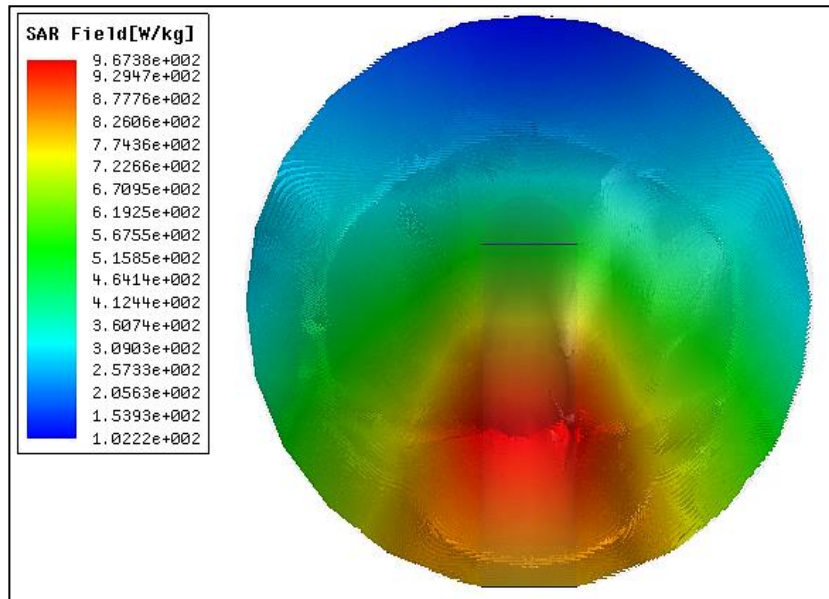


Figure 85. SAR distribution along the antenna axis.

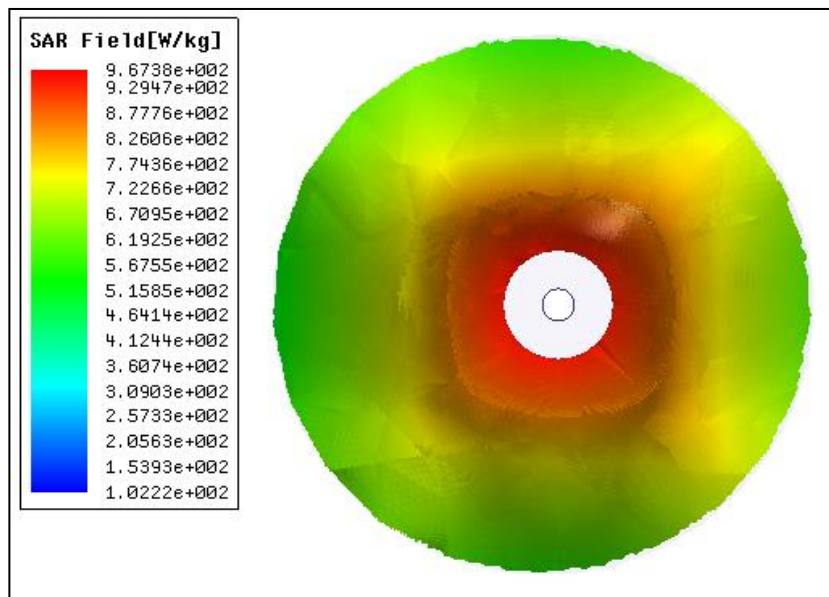


Figure 86. SAR values in transverse slice cut through the midpoint of the teardrop structure.

Variation of average SAR is also observed versus the distance along the central axis of antenna which is depicted in Fig. 87. In addition, Figure 88 illustrates SAR values versus distance perpendicular to antenna axis at the midpoint of the teardrop structure.

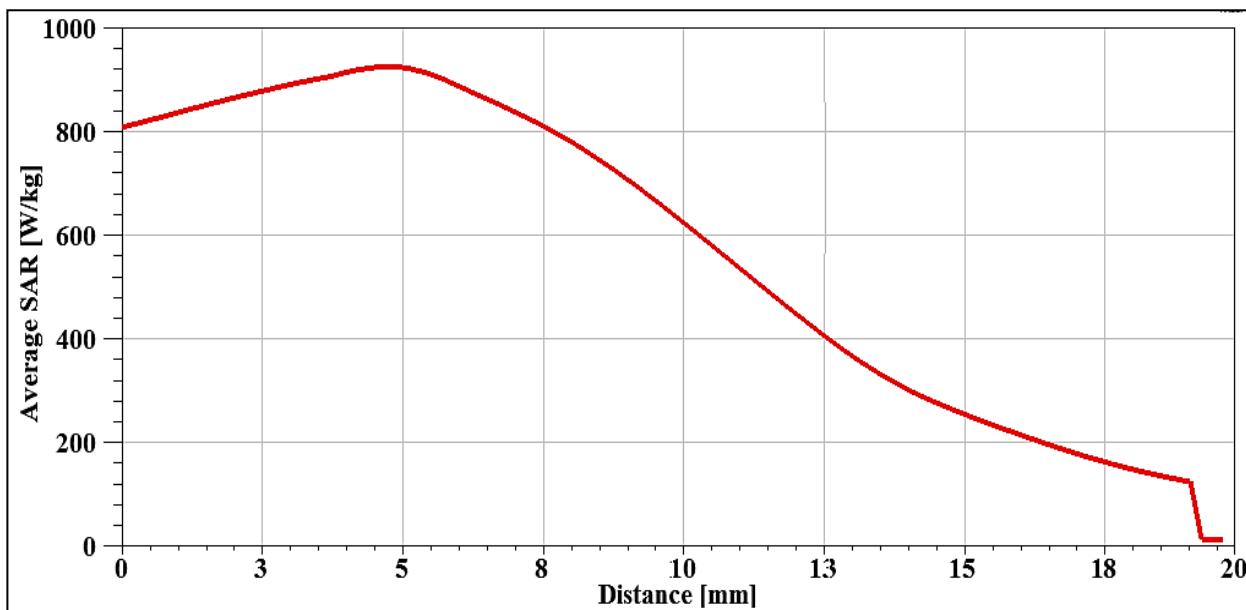


Figure 87. Average SAR is also observed versus the distance along the central axis of antenna.

From Fig. 87, highest values of SAR are distributed within tumour model along the whole length of the antenna at approximately the midpoint of TDFT structure where it recorded its maximum to be 967.38 W/kg. SAR gradually decreases as the distance from the antenna axis increases as depicted in Fig. 88 which provides homogeneous SAR pattern with its highest values concentrated within tumour model. SAR at tumour boundary abruptly decreases to 129.6 W/kg and gradually decays over a radial distance between 5 mms away from the tumour model.

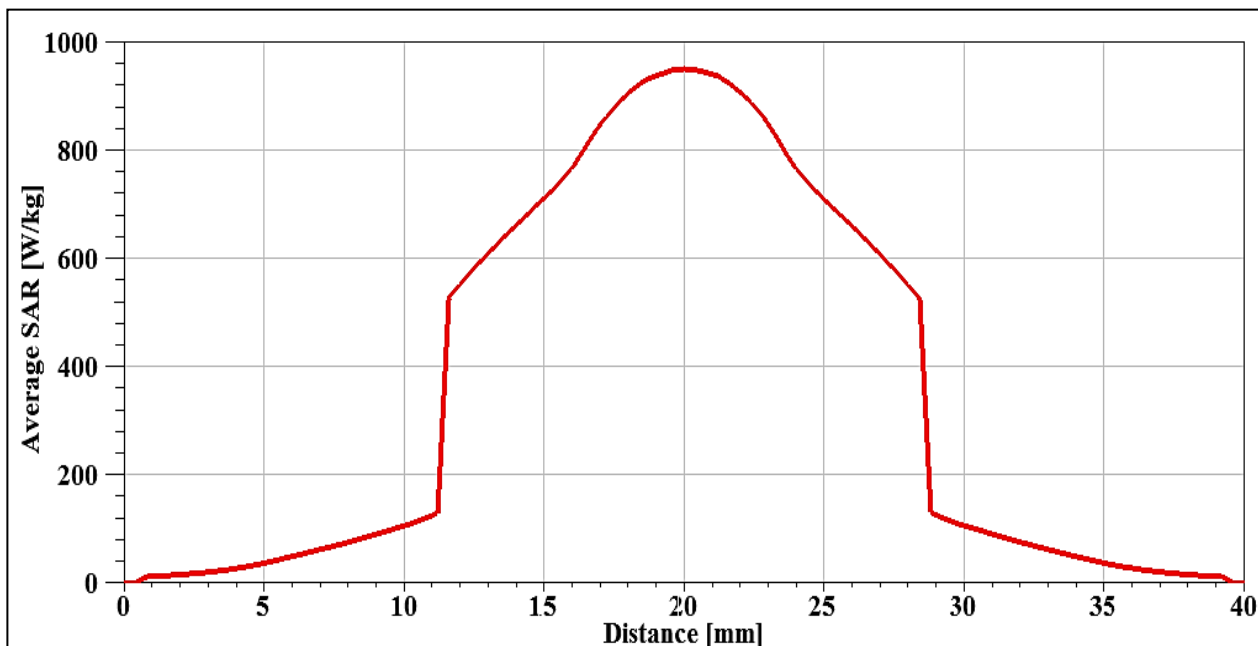


Figure 88. SAR versus distance perpendicular to antenna axis at the midpoint of the teardrop structure.

To ensure full eradication of any peripheral tumours and satisfy the safety margin standard of less than 10 mm of surrounding healthy tissues which prevent tumour metastasis in any other part of the body, a coupled electromagnetic-thermal analysis was performed to attain the temperature profile and consequent ablation lesions in tumour and surrounding liver model based on the power delivered, duration and material characteristics such as density, thermal conductivity and specific heat capacity...etc.

After performing electromagnetic and SAR analysis using ANSYS Electronics Desktop v.16, different types of losses obtained. First, surface loss density [W/m^2] which results from conductor loss was evaluated on the surfaces of both TDFT structure and the outer conductor of the coaxial feed. Second, Volume loss density [W/m^3] which can be attributed to dielectric lossy material was evaluated within Teflon, malignant and surrounding healthy non-perfused liver model. Losses are then imported into ANSYS Workbench to thermally analyze TDFT antenna loaded in tumour/liver model. Each evaluated loss represents different imported thermal loads in ANSYS Workbench i.e. surface loss density is imported as heat flux to compute the temperature distribution on the conductor surface while volume loss density is imported as internal heat generation to evaluate the temperature distribution within a dielectric medium. The temperature on the boundary of the model was set to $37\text{ }^\circ\text{C}$ similar to that of normal healthy liver with surrounding blood circulation.

Figures 89 and 90 depict the temperature levels found within the tumour and the surrounding liver models based on steady state thermal analysis. High agreement between SAR results and temperature profile obtained where maximum temperature of $72.375\text{ }^\circ\text{C}$ reached at approximately the midpoint of TDFT antenna.

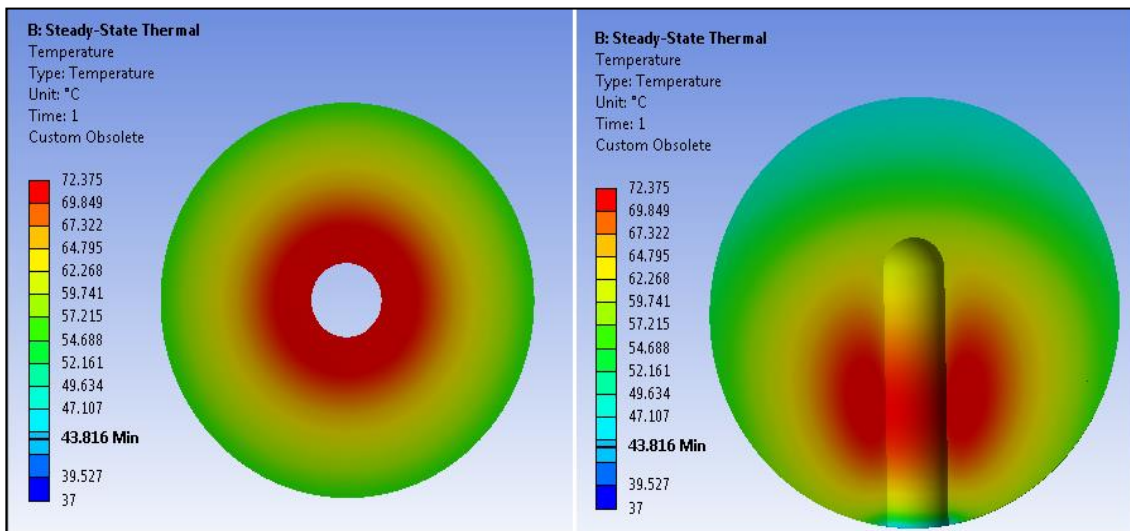


Figure 89. Temperature distribution in vertical and horizontal cuts through tumour model.

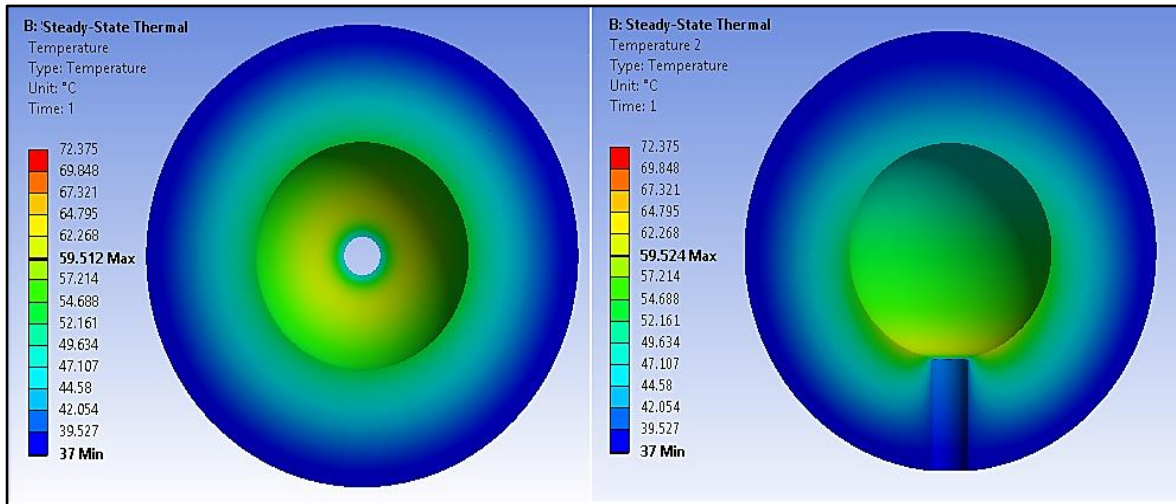


Figure 90. Temperature distribution in vertical and horizontal cuts through tumour model

From Figs 89 and 90, temperatures above 50°C exceeded the tumour boundary to a diameter of approximately 30 mm in the horizontal direction and 28.6 mm in the vertical direction through the midpoint of the teardrop structure where irreversible changes in tissue properties occur as a result of dehydration which in-turn causes instantaneous cell death (Rossmann & Haemmerich, 2014). In addition, one can notice that 60°C contour is confined within a horizontal diameter of 18 mm from the midpoint of the teardrop structure and 15 mm vertical diameter along the antenna length.

In addition, maximum temperature of 59.524 °C is attained at the tumour-liver interface and then sharply decreases to 50 °C within a radius of approximately 4.5 mm away from tumour boundary to ensure complete eradication of tumour and alleviates the possibility of cancer recurrence. Figure 91 illustrates the temperature on the surface of the outer conductor of the coaxial cable. Maximum temperature observed on the surface of the outer conductor of the coaxial feed is 41.52 °C which is much less temperature level than that required for hyperthermia (above 45°C) or ablation (50-60°C). Minimum temperature was attained along the antenna shaft as observed from Fig. 91 can be attributed to the nature of teardrop design itself acting as a current choke as it was first synthesized by slightly etching a solid cone at its base. Therefore, currents flowing back on the outer conductor of the coaxial feed were minimized which in-turn alleviates the consequent overheating of the antenna shaft.

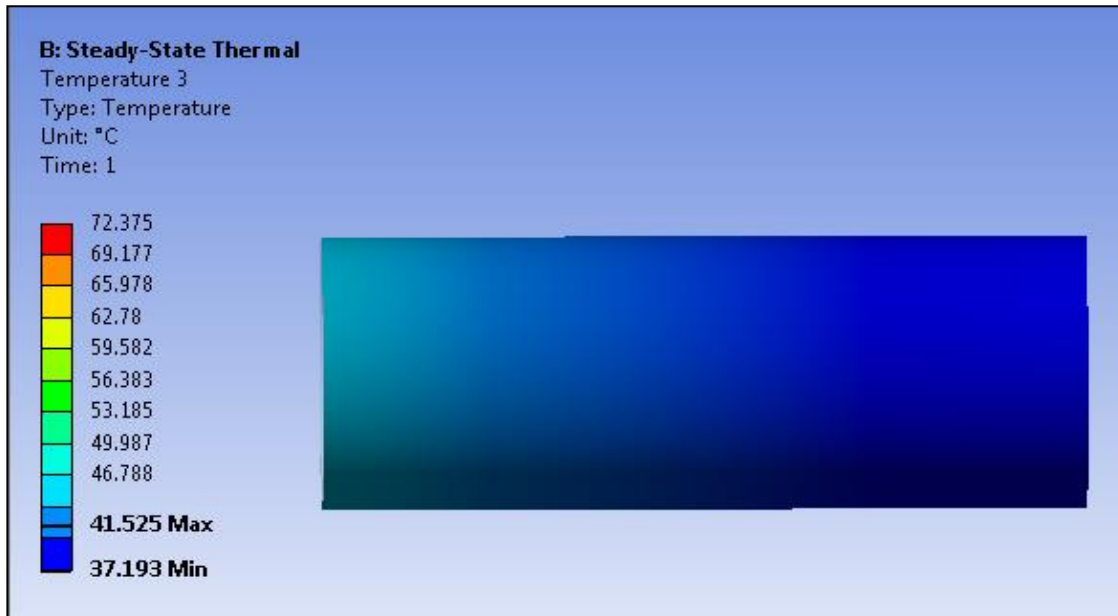


Figure 91. temperature on the surface of the outer conductor of the coaxial cable.

Steady state analysis mentioned above introduces the extent of temperature levels within the tumour and liver model to be reached using TDFT antenna. However, to observe the total duration of radiation exposure required to reach this steady state temperature, transient thermal Analysis is conducted with initial condition is applied to the whole model where initial temperature is set to 37°C which is the normal body and blood circulation temperature. Similar to prior steady state thermal analysis, surface loss density [W/m^2] -evaluated on the surfaces of both TDFT structure and the outer conductor of the coaxial feed- and volume loss density [W/m^3]-attributed to dielectric lossy material evaluated within Teflon, malignant and surrounding healthy non-perfused liver model- are imported into ANSYS Workbench to inspect the antenna performance due to transient radiation exposure within the tumour/liver model. Each evaluated loss represents different imported thermal loads in ANSYS Workbench i.e. surface loss density is imported as heat flux to compute the temperature distribution on the conductor surface while volume loss density is imported as internal heat generation to evaluate the temperature distribution within a dielectric medium. The temperature on the boundary of the model was set to 37 °C similar to that of normal healthy liver with surrounding blood circulation.

Due to long time consumed and large disk space needed to simulate transient thermal simulation, transient analysis was set to simulate the model for a total duration of only 180 secs (3 minutes) to inspect the total time needed to reach the temperature level required for ablation. Figures 92 and 93 illustrate the transient thermal analysis in horizontal and vertical cuts through the tumour model

at different time intervals 30, 60, 120 and 180 secs. Temperature profile of TDFT antenna within the tumour model shows homogeneous distribution of temperature along the antenna length through horizontal and vertical cuts within tumour model as illustrated in Figs 92 and 93, respectively. In addition, contours of highest temperatures noticeably increase in spherical manner within the tumour model.

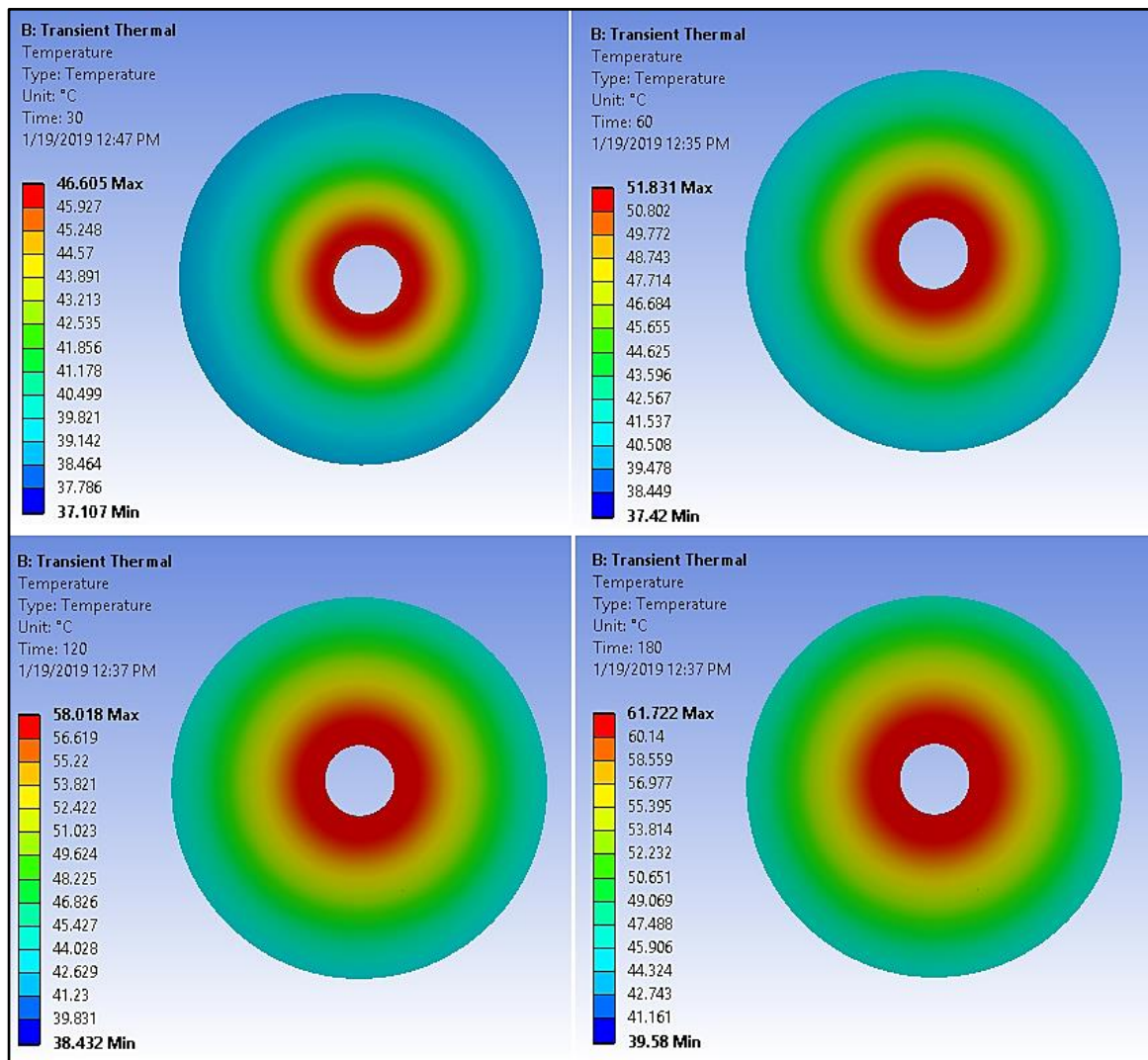


Figure 92. Transient thermal analysis in horizontal cut through tumour model at different time intervals 30, 60, 120 and 180 secs.

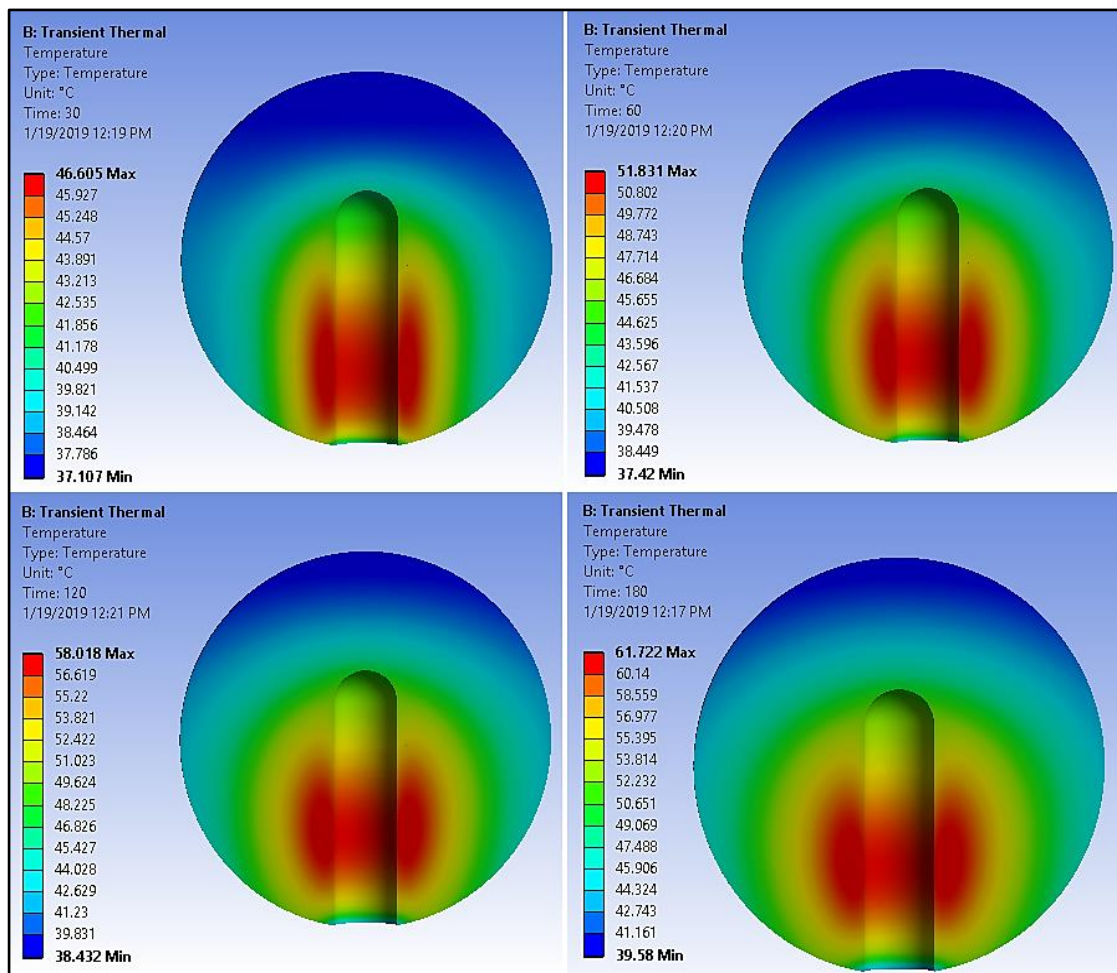


Figure 93. Transient thermal analysis in vertical cuts through tumour model at different time intervals 30, 60, 120, 180 secs.

Maximum temperature of 61.722 °C is observed at approximately the mid-point of TDFT antenna which highly agrees with SAR results and steady state thermal analysis. For 3 minutes of radiation, 50 °C contours are distributed in nearly spherical manner within the tumour model achieving a horizontal and vertical diameter of 17.4 and 16.3 mms, respectively within the tumour model where irreversible changes in dielectric properties and instantaneous cell death occurs as illustrated in Figs 92 and 93, respectively. Transient thermal analysis is also evaluated in the surrounding non-perfused healthy liver model at different time intervals 60, 120, 180 secs and depicted through horizontal and vertical cuts in Figs 94 and 95, respectively.

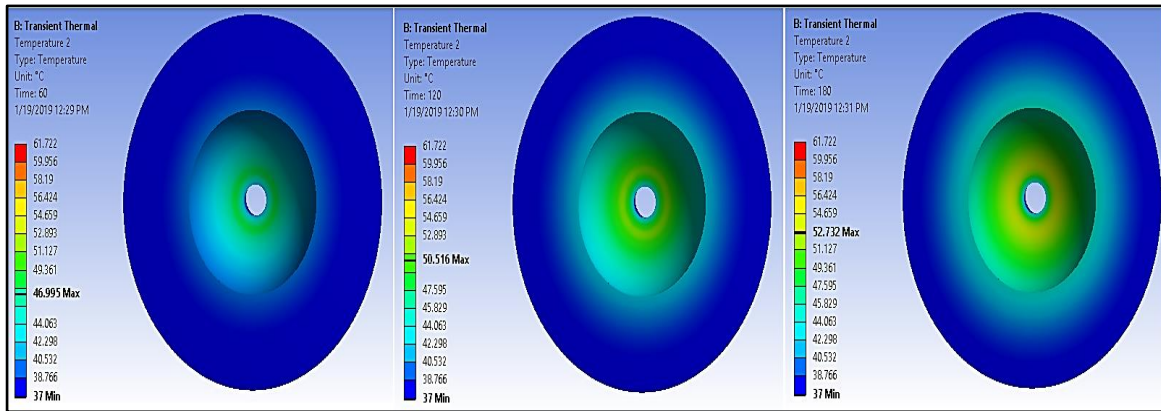


Figure 94. Transient thermal distribution in horizontal cut in the surrounding liver model at different time intervals 60, 120 and 180 secs.

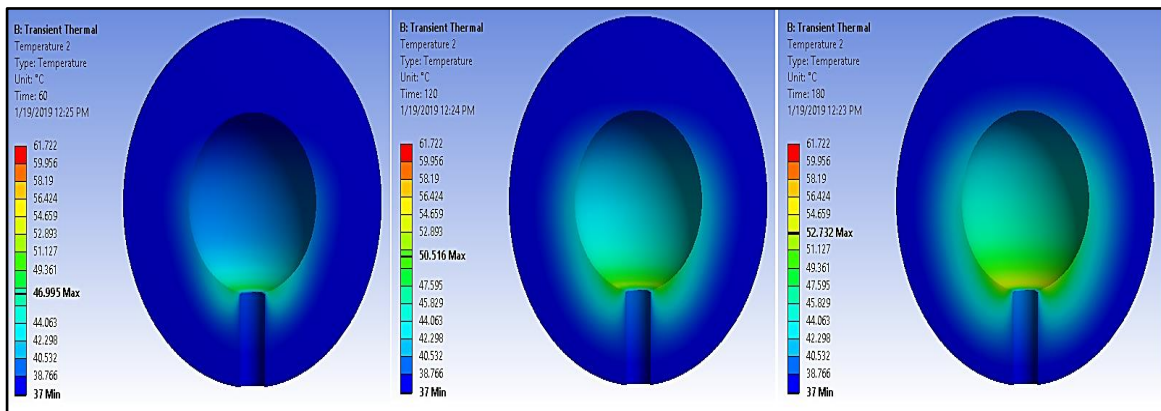


Figure 95. Transient thermal distribution in vertical cut in the surrounding liver model at different time intervals 60, 120 and 180 secs.

From Figs 94 and 95, maximum temperature of approximately 48°C is found in the surrounding tissues for 180 secs of radiation. Thermal profile of TDFT antenna shows a significant agreement with the total nearfield of the antenna where more microwave power deposited and confined significantly within the tumour model than that in the surrounding healthy tissues. In addition, thermal profile recorded a temperature of 40.3°C in the tissues along the antenna shaft which is lower temperature level than that required for hyperthermia (45-50°C). Minimum backward radiation was observed which reduces the consequent thermal damage associated with previously proposed designs. To achieve the required safety margin i.e. from 5 to 10 mm from surrounding healthy tissues to be eradicated, longer radiation duration or higher input power is recommended.

From transient and steady state thermal analysis, TDFT antenna has an exceptional capability of providing thermal confinement within the targeted area, reducing radiation exposure and consequent thermal damage in the surrounding healthy tissues and successfully reaching the

temperature levels required for cancer ablation at such low power level in short duration (3 minutes) of radiation.

Transient thermal analysis was also conducted to evaluate the temperatures recorded on the outer surface of the outer conductor of the coaxial cable which illustrated in Fig. 96. Maximum temperature on the outer conductor of the coaxial cable was found to be 40.269 °C at 180 secs of radiation which can be clearly illustrated in Fig. 96.

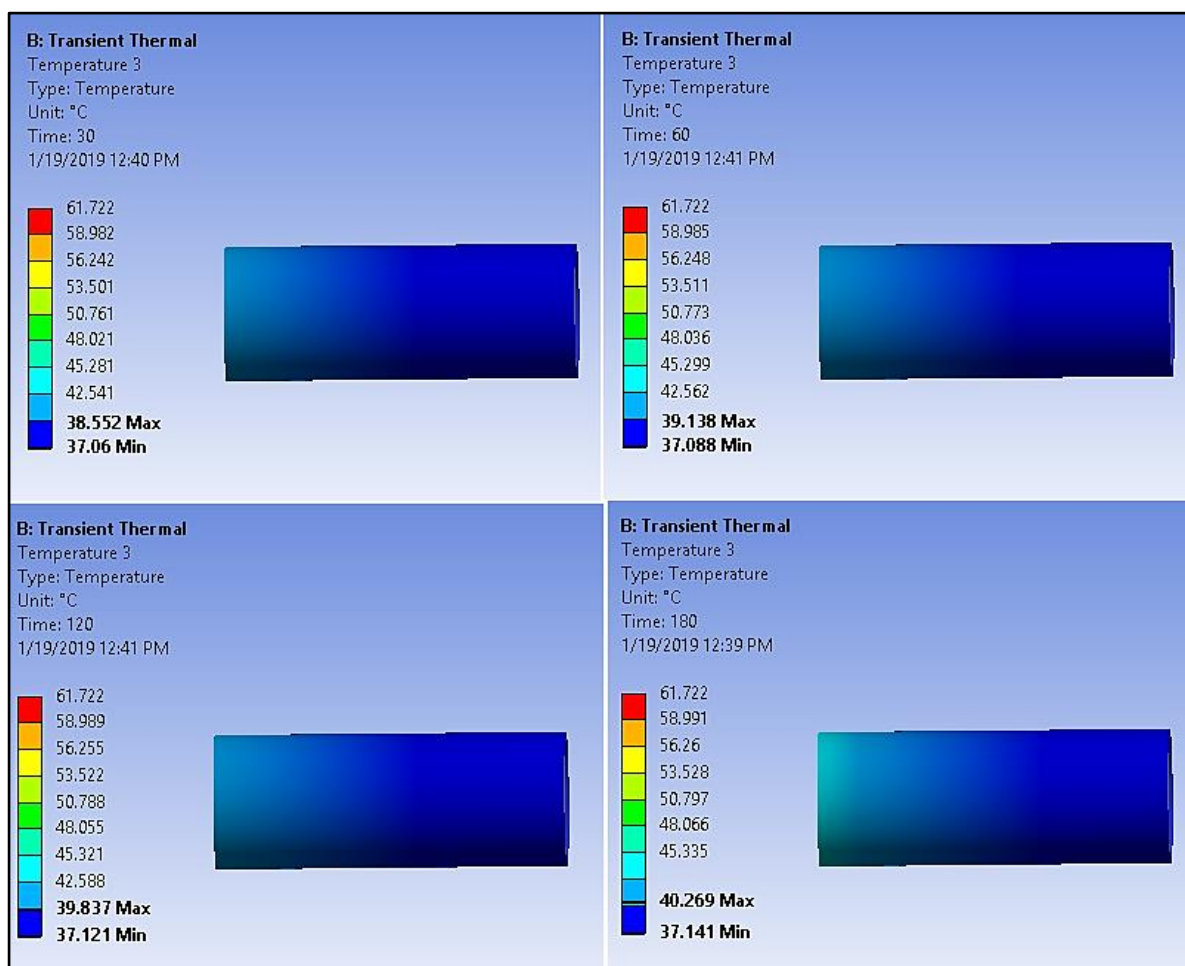


Figure 96. Transient thermal analysis on the outer conductor of the coaxial cable during the ablation process at different time intervals 30, 60, 120, 180 secs.

From Fig. 96, minimum temperature levels are achieved on the outer conductor of the coaxial cable during the ablation which can be attributed to the nature of TDFT antenna where is initially synthesized to choke the currents flowing back on the outer conductor of the coaxial cable and minimize the overheating of the cable during ablation. Reducing the overheating of the coaxial

cable contributes greatly in protecting the healthy tissues along the antenna shaft and alleviating the complications encountered with thermal ablation after the procedure.

4.2.1.3. Testing TDFT in Egg white

Prior to microwave ablation experiments, numerical simulations of TDFT antenna was performed in Egg white model to give a preliminary idea on the shape and extent of the ablation lesion that could be achieved using the antenna proposed. The whole antenna enclosed in Teflon was inserted in egg white where the antenna tip placed at the centre of a spherical model of egg white. Frequency dependent dielectric properties in addition to thermal properties of egg-white were adopted from (Mohtashami, Yahya, et al., 2017; Abbasnezhad, Behzad, et al., 2016) and imported in Electronics desktop suite (HFSS) to perform full wave EM simulation and in Ansys workbench to perform steady-state thermal analysis, respectively. Table 12 illustrates dielectric and thermal properties of Egg-white imported in numerical simulations.

Table 12. Dielectric and thermal properties of Egg-white imported in numerical simulation.

Dielectric permittivity ϵ_r [F/m]	56.196
Electrical conductivity σ [S/m]	10.973
Mass Density ρ [kg/m ³]	1041
Thermal conductivity k [W m ⁻¹ K ⁻¹]	0.55
Specific heat capacity c [J kg ⁻¹ K ⁻¹]	3800

Antenna length was determined by frequency of operation and dielectric properties of the surrounding mediums. Figure 97 illustrates S_{11} result for TDFT antenna in egg white which revealed that 13.66 mm length gives -22.27 dB reflection with minimum backward radiation at 7.3 GHz. From simulation results, reflection ≤ -10 dB can be observed at frequencies starting from 2.5 GHz till more than 20 GHz.

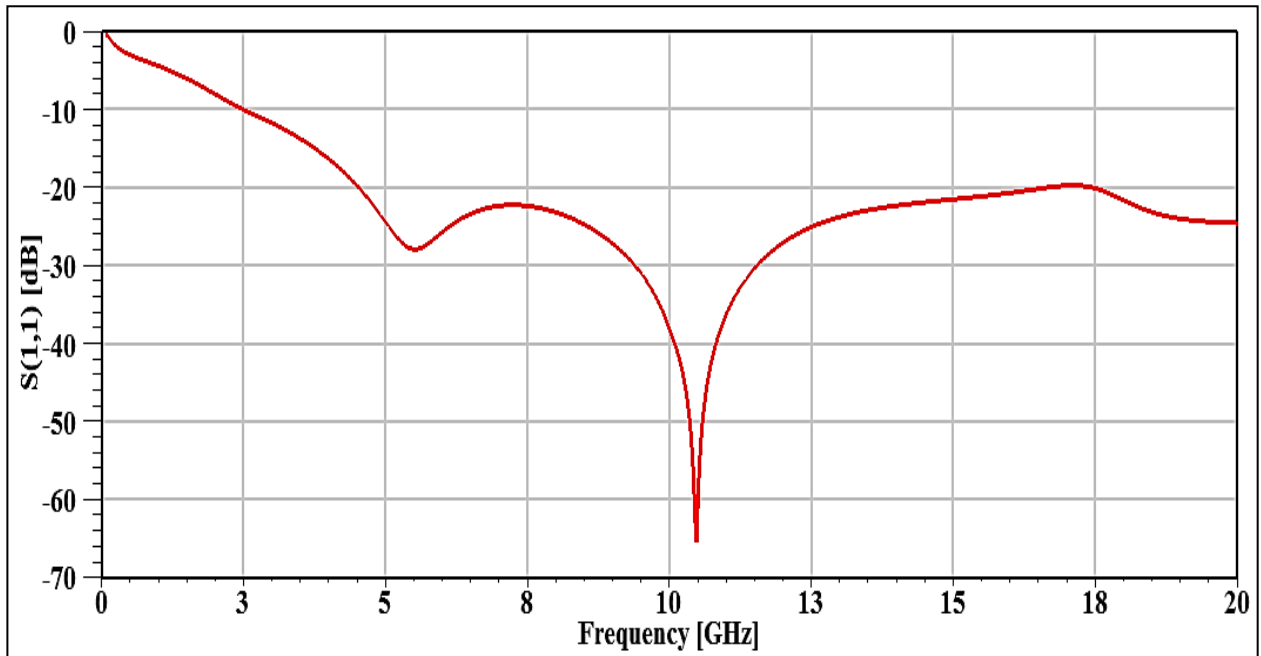


Figure 97. S_{11} results of TDFT antenna in Egg white

Nearfield is also evaluated in egg white model surrounding the antenna illustrated in Fig. 98 where axial radiation is attained along the antenna axis. Although antenna length of 13.66 mm doesn't have the minimum possible reflection attained all over the bandwidth, this length was chosen as a compromise between minimum backward radiation and minimum acceptable reflection at the operating frequency. A good agreement between numerical calculation of radiated electric field shown in Fig. 38 with that obtained by electromagnetic simulation illustrated in Fig. 98.

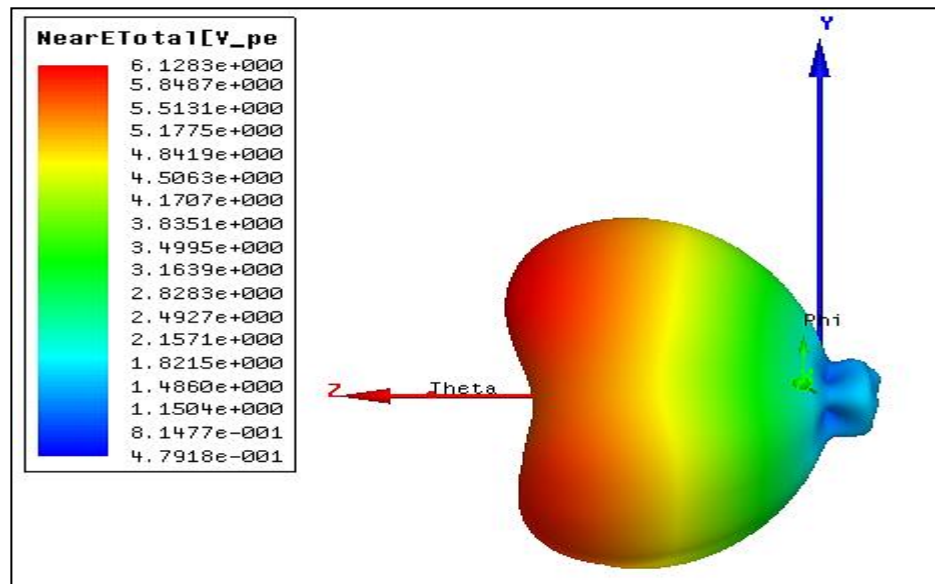


Figure 98. Nearfield pattern of TDFT antenna loaded in Egg white model.

4.3. Disparity of Ablated Lesion Size Based on the Applied Microwave Power and the Application Time

Two study scenarios were considered to investigate the effect of different power levels and the duration of radiation exposure on the total ablated volume obtained.

4.3.1. Ablated Lesion Size Dependence on the Applied Microwave Power

Prior to thermal analysis, electromagnetic analyses were conducted using Electronics Desktop suite to analyze TDFT antenna at different input power separately. Then the surfaces and volume losses were imported into steady state thermal analysis using Ansys workbench to determine the extent of ablated volume achieved at each input power. Figures 99, 100 and 101 illustrate the temperature distribution within the tumour model for 3, 4- and 5-Watts input power, respectively.

60 °C contour represents the total ablated volume by TDFT antenna where instantaneous cell death occurs while temperature above 50 °C represent irreversible changes in tissue properties due to blood coagulation and cell necrosis. 60°C noticeably expands as the power increases which can be clearly illustrated in Fig. 99. For input power of 3W, 60°C contour was observed in a horizontal diameter of 18 mm from the midpoint of the teardrop structure and 15.2 mm in vertical direction. In addition, maximum temperature of 59.524 °C is attained at the tumour-liver interface and then decreases to 50 °C within a radial distance of approximately 4 mm away from tumour boundary which satisfies the acceptable ablation safety margins of surrounding healthy tissue to ensure complete eradication of tumour and alleviates the possibility of cancer recurrence as shown in Fig. 99. On the other hand, for input power of 4W, 60°C was found horizontally in a diameter of 22.7 mm through the mid-point of the antenna and vertically in 17.3 mm diameter while for 5W input power, a diameter of 24.27 mm in the horizontal direction and 19.2 mm in the vertical direction through the mid-point of TDFT antenna was completely covered by 60 °C contour as illustrated in Figs 100 and 101.

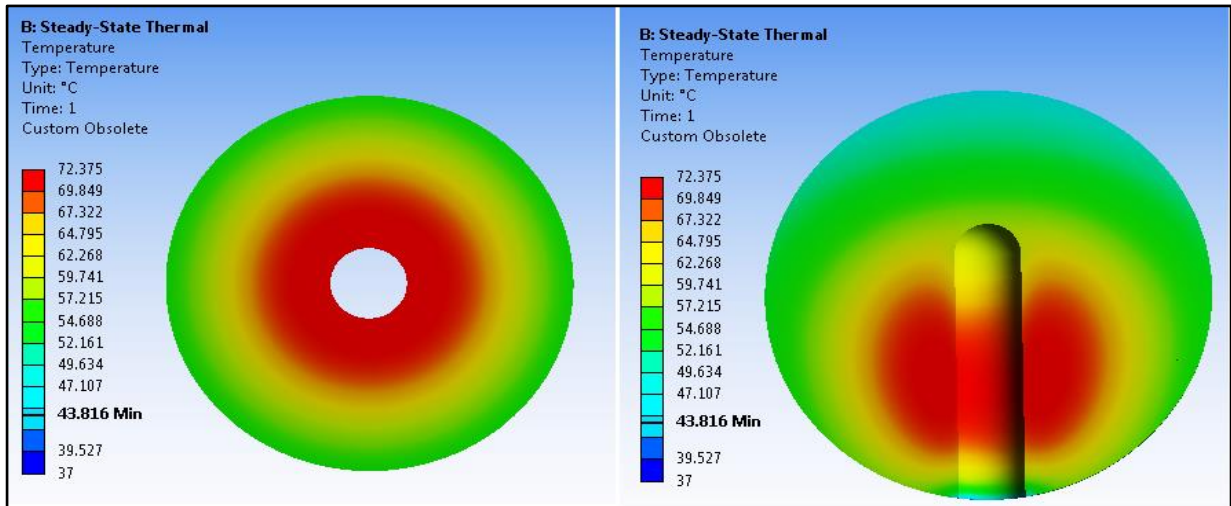


Figure 99. steady state temperature within tumour model for 3W input power.

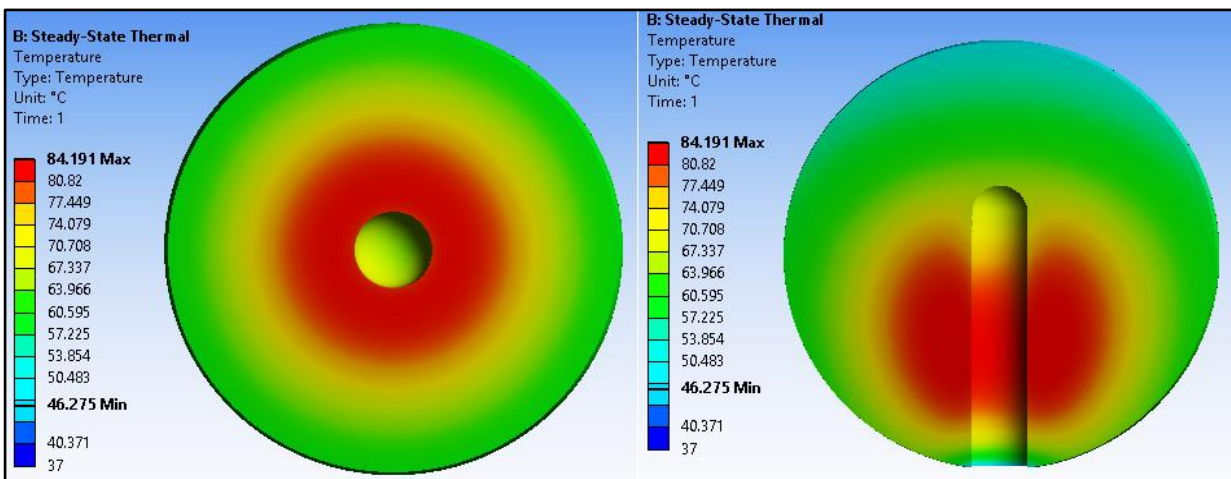


Figure 100. Steady state temperature within tumour model for 4W input power.

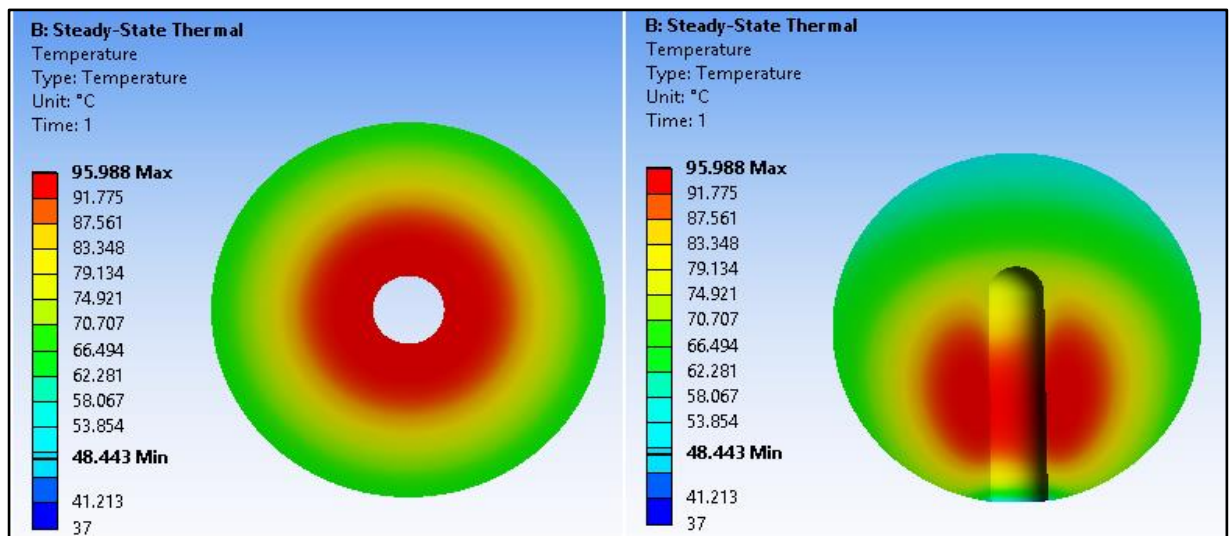


Figure 101. Steady state temperature distribution within tumour model for 5W input power.

Furthermore, the safety margin achieved in the surrounding healthy tissues as shown in Fig. 102 changes with the increase of input power. Safety margins achieved for 3W, 4W and 5W were found to be approximately 4 mm, 5 mm and 5.8 mm, respectively in a radial distance away from the tumour/liver boundary which satisfies the acceptable safety margin to ensure total eradication of tumour and its peripherals in the surrounding healthy tissues which minimizes the possibility of cancer metastasis.

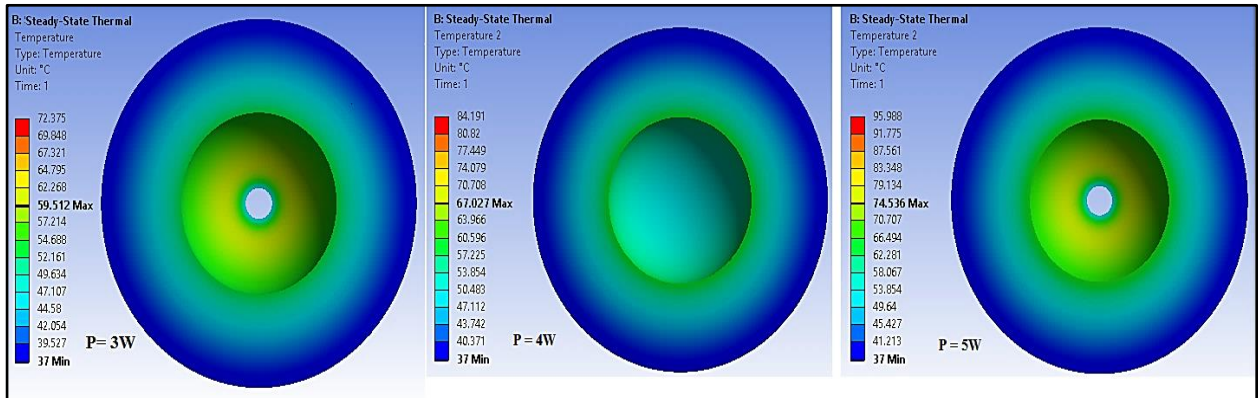


Figure 102. Temperature distribution in the surrounding tissues indicating safety margin achieved for each power level.

Figure 103 shows the total ablated volume attained for each power level. One can notice that increase of input power significantly dispartate the total ablated volume attained by TDFT antenna. In addition, thermal diffusion of the energy deposited within the targeted tissue is equally distributed in the transverse direction across the tumour model while thermal energy is slightly confined in the longitudinal direction along the antenna length away from the tumour/liver boundary.

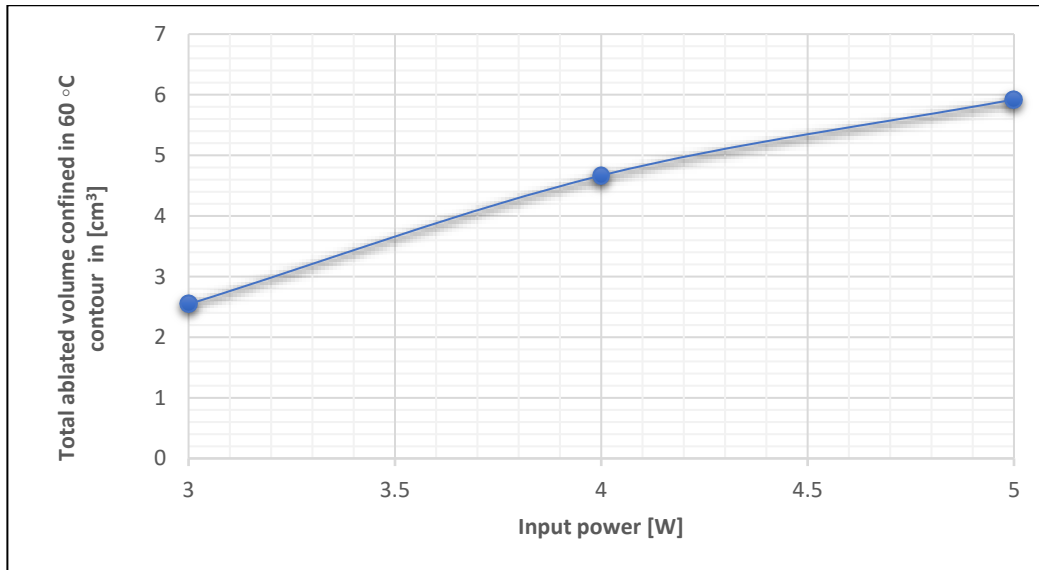


Figure 103. total ablated volume attained based on 60°C contour for each power level.

Steady state temperature was also calculated in the outer conductor of the coaxial cable and compared for different input powers. Figure 104 depicts the maximum temperature obtained on the outer conductor of the coaxial cable for 3, 4 and 5 W respectively. From Fig. 104, one can observe that maxima of temperature achieved doesn't exceeds the temperatures for hyperthermia (45-50°C) or ablation (50-60°C) which emphasizes on the significance of TDFT antenna to choke the currents excited on the outer conductor of the coaxial feed which in-turn minimizes the overheating of cabling encountered with previously proposed designs. From steady state thermal analysis, one can observe that the higher the input power is, the larger the ablated volume attained (Preston, et al., 2018; Luyen, Hung T., et al., 2015; Gas, 2015; Brace, Christopher L, et al., 2009).

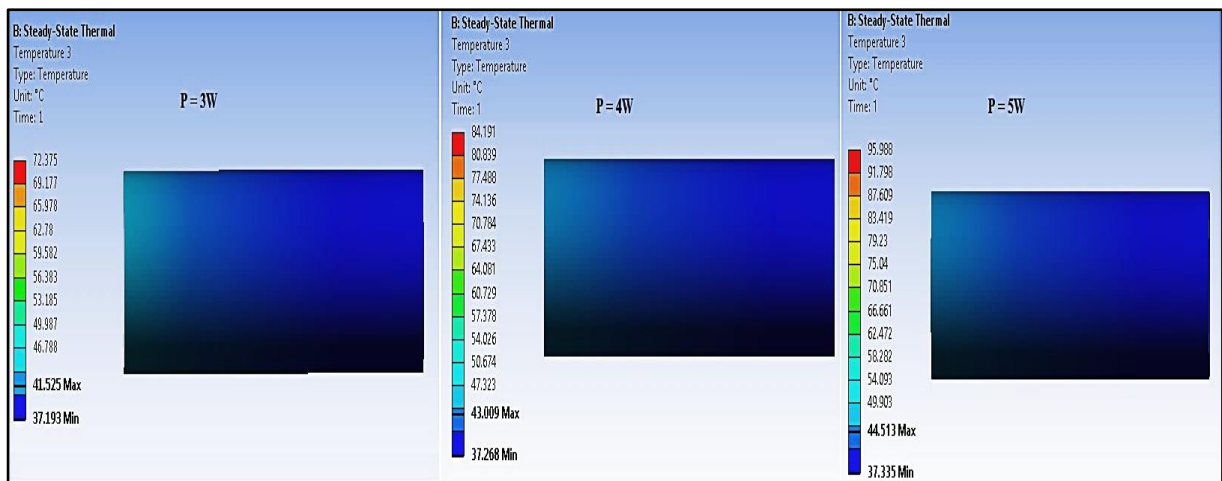


Figure 104. Temperature distribution along the outer conductor of the coaxial cable for different input power

4.3.2. Ablated Lesion Size Dependence on the Application time

To investigate the effect of radiation application time, transient thermal Analyses were then employed and compared at each power level of 3, 4, and 5W. Due to the long time and large disk space consumed by transient analysis, this simulation was performed on a server with CPU E3-1240 v5 @ 3.5 GHz, 3.5 GHz under 64 bits windows server 2012 R2 Standard operating system, 64 GB of Ram and 9 Terabytes hard disk to study the effect of changing the radiation exposure time on the ablated volume.

Figures 105 and 106 show transient thermal analysis at different time intervals of a total time duration of 180 seconds (3 minutes) for power of 3, 4 and 5 W through horizontal and vertical cuts within tumour model, respectively. One can observe the 50 °C contour expands as the duration of radiation exposure increases where the thermal conductivity of both tumour and liver takes over the thermal convection within tumour and surrounding tissues. In addition, the higher the power level is, the wider the ablated volume attained. For 3 minutes, Irreversible changes in tissue properties confined in 50 °C contour were found at diameter approximately of 16, 16.4, 17.44 mm along the antenna axis for 3, 4 and 5 W, respectively. It also extended horizontally to a diameter of 15.6, 16.07, 17.2 mm through approximately the midpoint of the antenna for input power 3, 4 and 5 W, respectively.

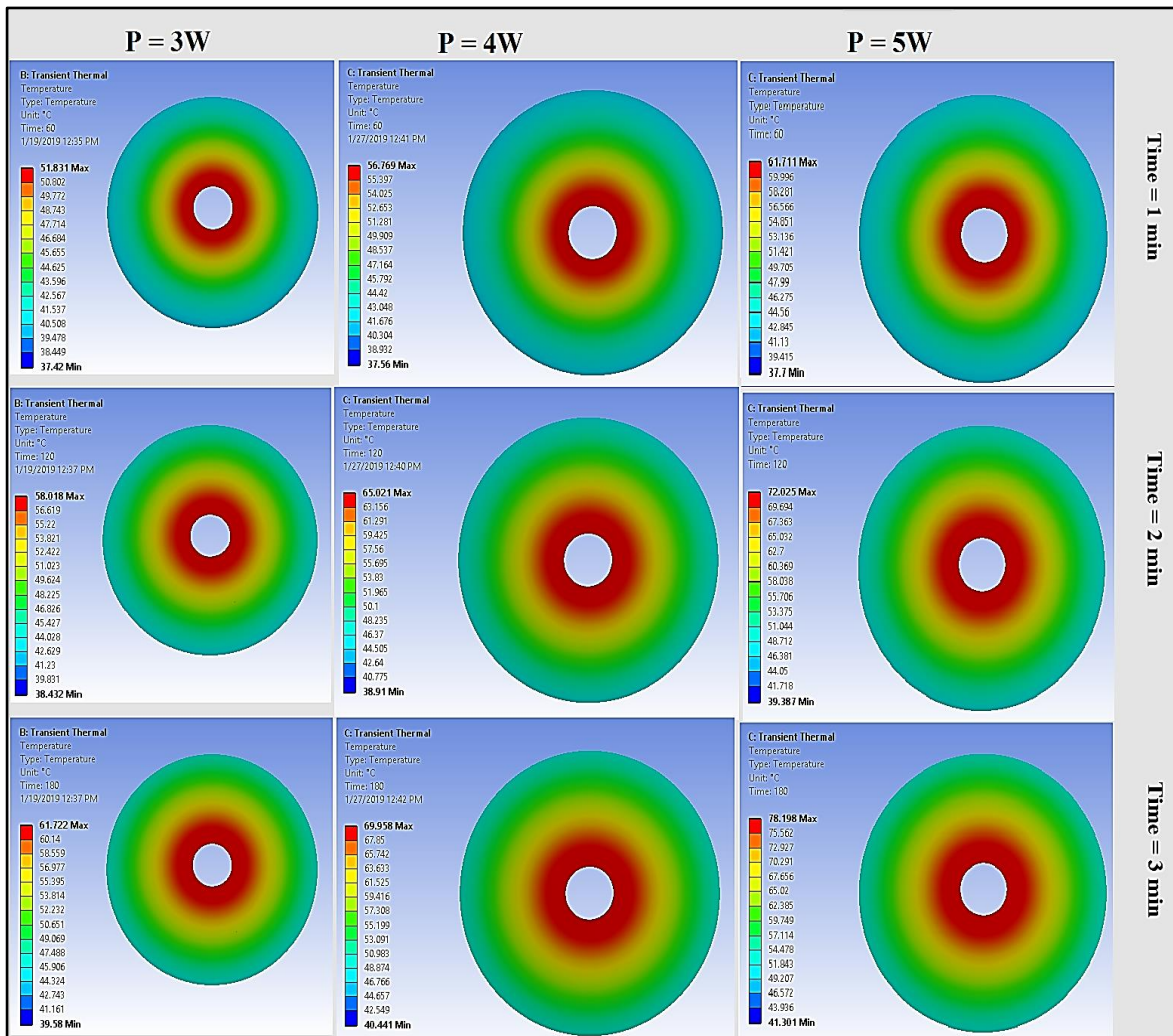


Figure 105. Transient thermal analysis at different time intervals (60, 120 and 180 secs) for input power of 3, 4 and 5 W through horizontal cut within tumour model.

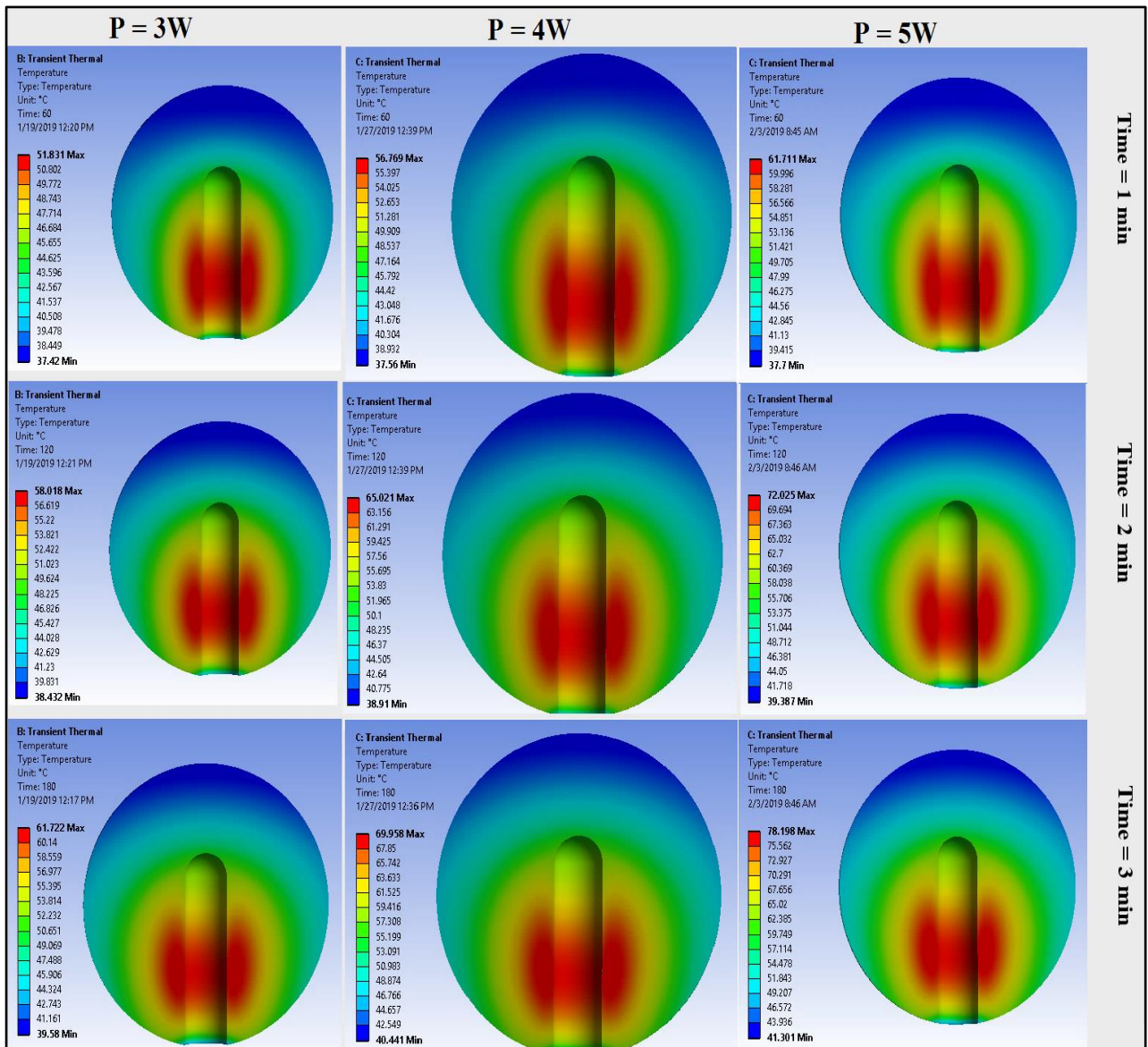


Figure 106. Transient thermal analysis at different time intervals (60, 120 and 180 secs) for input power of 3, 4 and 5 W through vertical cut within tumour model.

From transient thermal analysis, TDFT antenna can produce a nearly spherical ablation which is noticeably showed from spherical expansion of 60°C contour with the increase of application time and applied power. Moreover, thermal profiles presented in Figs 105 and 106 are significantly in a good agreement with the nearfield distribution and SAR Pattern of TDFT antenna where maximum temperature distributed from the midpoint of TDFT antenna and expands spherically towards tumour/liver boundary. Transient thermal analysis presented in Figs 105 and 106 showed that TDFT antenna can produce symmetrical ablated lesion around the antenna axis in a plane perpendicular to the antenna axis from its midpoint. This agrees with nearfield distribution as

TDFT antenna has a rotationally symmetrical structure which generates a rotationally symmetrical nearfield distribution around the antenna axis.

Temperature gradient within tumour model for each input power is illustrated in Fig. 107. From Fig. 107, Temperature gradient increases as the application time increases to reach its maximum value of approximately 78.1 °C at the longest application time (180 secs) for the highest applied power (5W). Furthermore, for application time less than 30 secs, temperature gradient increases almost linearly for each power level. However, as application time increases more than 30 secs, temperature increases nonlinearly which can be attributed to thermal conductivity of tumour which takes over the thermal convection within tumour and its surroundings. Moreover, temperature gradients recorded for each input power were noticeably diverged from the start of the ablation process and as the application time to reach 3 min, temperature gradient increased from 20 °C to almost 40°C for each input power. In addition, maximum temperature attained was elevated by 10 °C as input power increases by 1W.

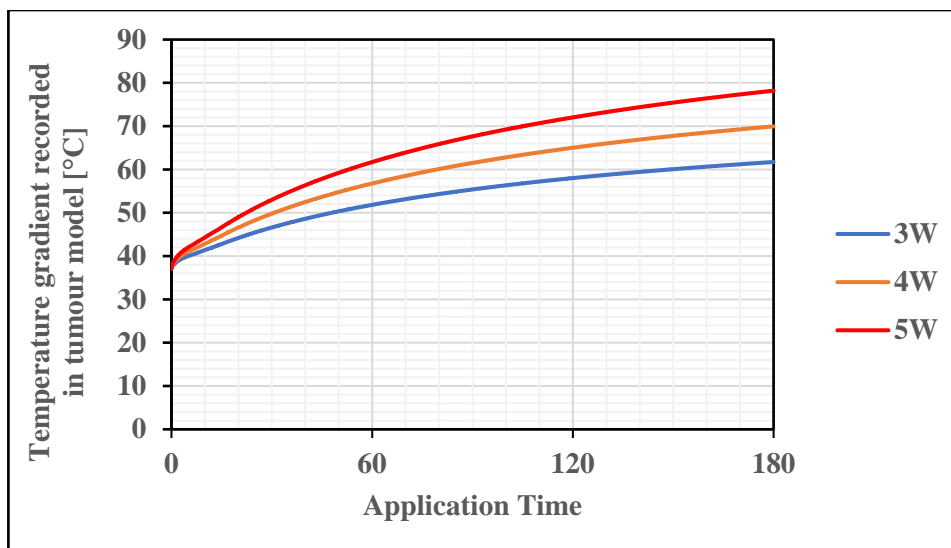


Figure 107. Temperature gradient within tumour model for each input power.

The lateral and longitudinal radii of the ablated lesion within 50°C contour was presented at different time intervals and illustrated in Table 13. One can also notice that ablated lesions expand in a spherical manner clearly depicted in the closeness between the vertical and horizontal radii of the ablated lesions presented in Table 13. In addition, as the application time and applied power increase, the total ablated volume increases which can be observed from the expansion of 50°C

contour volume. The total volume confined in 50°C contour is calculated using (106) where a and b are lateral and longitudinal radii of the total ablated lesion, respectively. Geometrical representation of ablated lesion is illustrated in Fig. 108.

$$V = \frac{4}{3} \pi a^2 \times b \quad (106)$$

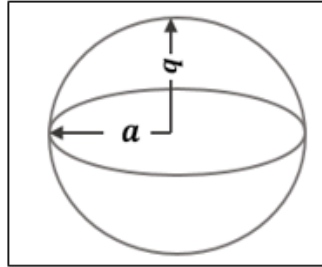


Figure 108. Geometrical representation of ablated volume.

Lesion spherical ratio (L.S.R.) can be expressed as the ration between lateral radius and longitudinal radius of the ablated lesion as stated in (107). L.S.R. equals to 1 means the shape of ablated lesion is exactly sphere. From Table 13, ablated lesion is found to be more spherical with the increase of the applied power for application time of 1 minute which clearly observed from LSR values approaching unity. The minimum LSR values were found at the start of the ablation process (application time ≤ 1 minute) for each applied power. For fixed applied power, ablated lesion tends to be more spherical as the application time increases.

$$\text{Lesion Spherical Ratio (L.S.R)} = \frac{\text{Lateral Radius (a)}}{\text{longitudinal Radius (b)}} \quad (107)$$

Table 13. Radii of ablated volume at different time interval for each input power

Applied power	3W			4W			5W		
Time interval	a [mm]	b [mm]	L.S.R	a [mm]	b [mm]	L.S.R	a [mm]	b [mm]	L.S.R
60 s	4.183	4.683	0.893	5.235	6	0.873	6.623	7.3255	0.904
120 s	6.765	7.0885	0.95	7.291	7.4	0.985	7.81	8.2555	0.946
180 s	7.7975	8.0455	0.97	8.035	8.2	0.98	8.6	8.725	0.986

Volume of the ablated lesions attained for each input power at different time intervals is calculated using (106) and presented in Table 14. As the application time increases, volume of the ablated

lesion increases. The largest ablated lesion attained of volume 3.6 cm³ centered at the midpoint of TDFT antenna at input power 5W for 180 secs.

Table 14. Volume of the ablated lesion in cm³ for different input power at different time intervals.

	Volume of ablated lesion in cm ³		
	3W	4W	5W
60 s	0.3	0.92	1.795
120 s	1.79	2.2	2.81
180 s	2.73	2.96	3.60

From Tables 13 and 14, As the applied power increases, heating grows faster, and ablated lesion expands wider than that at lower input power. TDFT antenna can achieve a successful ablation of cancerous lesions with diameters of 15.5, 16 and 17.5 mm in 3 minutes for input power of 3, 4 and 5W, respectively where 50°C contour encompasses irreversible changes in tissue properties yielding blood coagulation and cell necrosis. Transient thermal simulations of longer ablation time should be conducted using servers with much higher specifications to determine the application time needed for eradicating tumours of 3 cm diameter.

4.4. Fabrication of The Proposed TDFT Antenna Design

The prototype of TDFT antenna and its dielectric shield were fabricated to verify their performance in either biological substance such as Egg-white solution or in *ex vivo* liver ablation experiments. Due to the nature of TDFT antenna design and its outer dielectric shield, there were certain constraints found regarding its fabrication which governs the pace and adequacy of manufacturing. These constraints necessitate applying design modifications in order to facilitate the manufacturing process of the whole design using lathe.

First, the structure of TDFT antenna was made of pure Copper and it was slightly modified by introduction of a flat cylindrical area to the rear of the hemispherical tip with a minimum length of 2 mm to make it easier for holding the Copper part in the lathe. After applying the design modifications recommended, TDFT antenna were re-modeled in the numerical simulations again to ensure there is no significant changes in the simulated results obtained before. Figure 109 shows the original and modified TDFT antenna. Second, manufacturing of the dielectric Polytetrafluoroethylene (PTFE) -brand name Teflon- shield was very challenging as it is very difficult to carve out the PTFE shield to the exact outer shape of the Copper core of TDFT antenna without it slipping or deforming massively. In addition, considering splitting the dielectric shield in two halves would make it easier to machine using lathe, but the issue comes when attempting to stick it back together again as the key selling point of PTFE (brand name Teflon) is its non-stick properties.

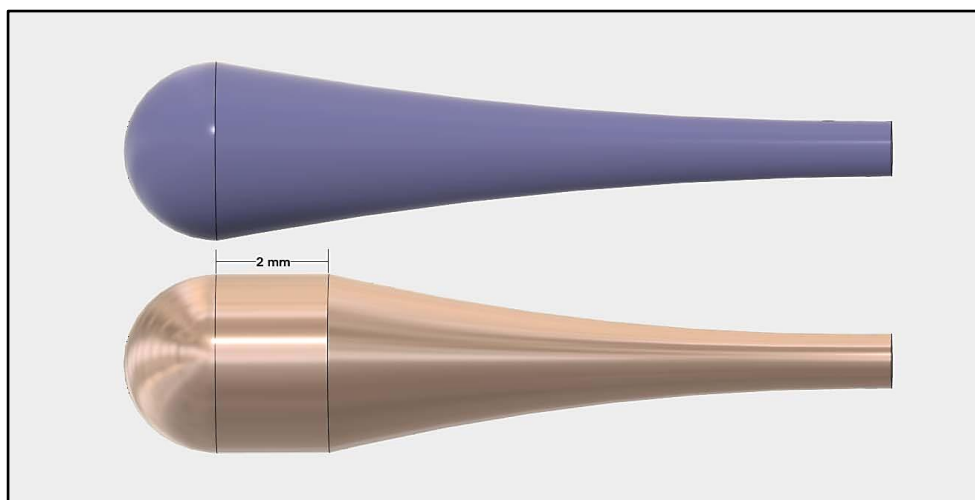


Figure 109. The original and modified Copper structure of TDFT antenna.

Due to the difficulty of manufacturing the dielectric shield at the tolerances given using traditional manner and the slippery nature of PFTE material, a hollow cylinder shaped like a test tube was considered when manufacturing the dielectric shield and securing the part to TDFT antenna with adhesive resin. The thicker the wall of the tube is, the better and much easier to machine to facilitate its fabrication without exceeding the total diameter allowed for microwave applicator (≤ 3.5 mm). Figure 110 shows the fabricated prototype of TDFT antenna and its dielectric Polytetrafluoroethylene (PFTE) shield.



Figure 110. The fabricated prototype of TDFT antenna and its dielectric PFTE shield.

Flexible low loss 50-ohm Pasternack coaxial cable (PE-300) was employed to connect TDFT antenna to the signal generator. Due to the difficulty faced in attaching the inner conductor of the coaxial cable to TDFT antenna using regular tin solder, the antenna tip and the inner conductor of the coaxial cable were inserted into a hollow metallic pin – shown in Fig. 111 – to effectively help supporting both the antenna tip and the inner conductor of the coaxial feed. The metallic pin was enclosed by PFTE cylinder and a part of outer conductor to minimize the losses that might encountered using the metallic pin.



Figure 111. Hollow metallic pin used to hold both antenna tip and the inner conductor of the coaxial cable.

TDFT antenna is then enclosed by the dielectric shield and a heat-shrink tube was then employed to help holding the dielectric shield with the coaxial cable. Final prototype of TDFT antenna connected to the coaxial cable is shown in Fig. 112. The resulting antenna has a diameter of 3.4 mm including the dielectric Teflon (PFTE) shield insulation, and it doesn't include a cooling mechanism.



Figure 112. Fully assembled prototype of TDFT applicator connected to the coaxial cable.

Two studies scenarios were conducted in one in egg-white solution and the other in Bovine liver. First, eggs were picked up on the day of experiment to monitor the total reflected power in egg-white solution first and then apply an input power of 1W to determine the volume of solidified egg-white. Secondly, Bovine liver was procured from the slaughterhouse on the morning of lab experiments where it was stored in a chiller in the slaughterhouse. Reflection measurements and ablation experiments were conducted on the day of pickup to prevent spoilage. Prior to conducting the ablation experiments, antenna was inserted into both bovine liver sample and egg-white solution to measure its reflection coefficient using a vector network analyzer VNA (Agilent Technologies, FieldFox microwave analyzer, N9918A, 26.5GHZ, now Keysight Technologies). The Experimental setup and verification of reflection for TDFT antenna in bovine liver and egg-white solution is illustrated in Figs 113 and 114, respectively.

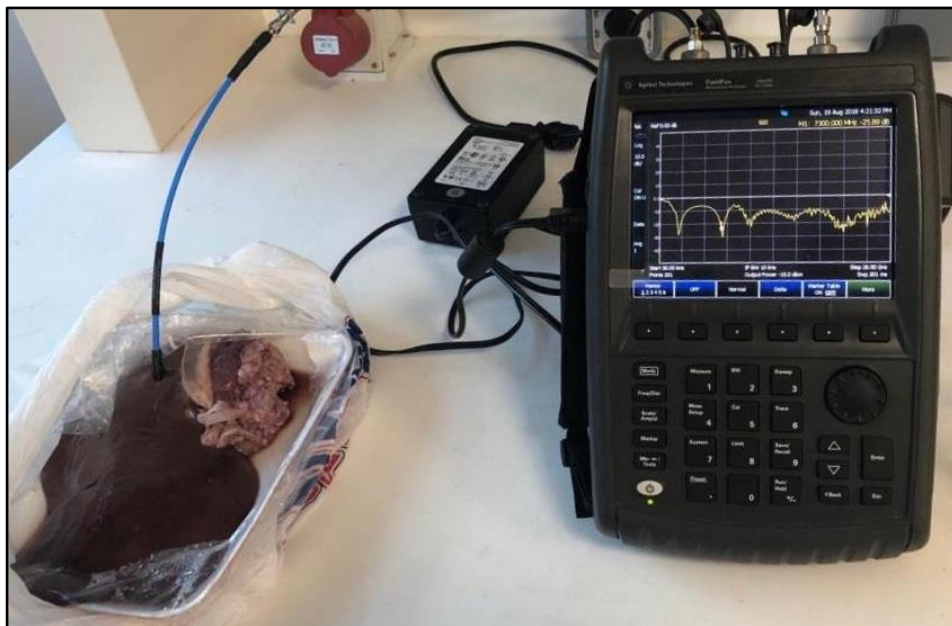


Figure 113. Experimental setup and verification of reflection for TDFT antenna in Bovine Liver sample.

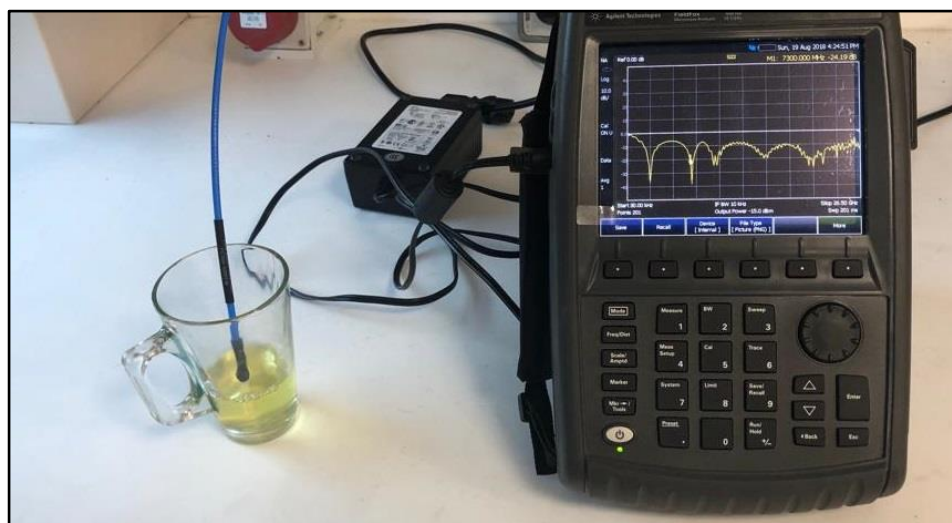


Figure 114. Experimental setup and verification of reflection for TDFT antenna in egg-white solution.

Figures 115 and 116 illustrate a comparison between the simulated and measured results of reflection for TDFT antenna in Bovine liver and egg-white solution, respectively. Reflected power was monitored for each experiment which didn't exceed 10% of the source output power for different insertion depths at the frequency of operation. Moreover, a good agreement between the simulated and measured results was found from Fig. 115 and 116 where TDFT antenna recorded a reflection of -24.19 dB when inserted in Bovine liver sample while a reflection of -25.9 dB was monitored in egg-white solution at 7.3 GHz. From return loss measurements, the total reflected power of TDFT antenna was consistently in the range of ~ 0.003 W at the frequency of operation.

From reflection measurements, TDFT antenna can operate efficiently in different surroundings whether inserted in a single tissue or in different mediums with different dielectric properties. In addition, reflection measurements showed that TDFT antenna can operate at different frequency bands unlike previously proposed designs where more than one applicator was used at each frequency band separately (Sawicki, et al., 2018)

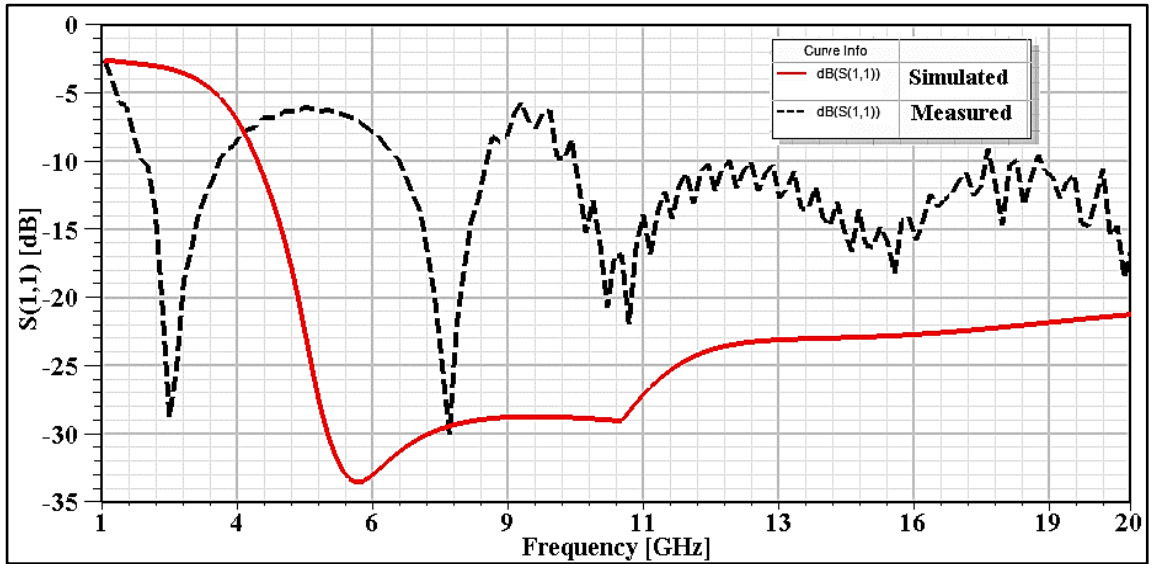


Figure 115. Comparison between simulated and measured S_{11} of TDFT antenna in bovine liver sample.

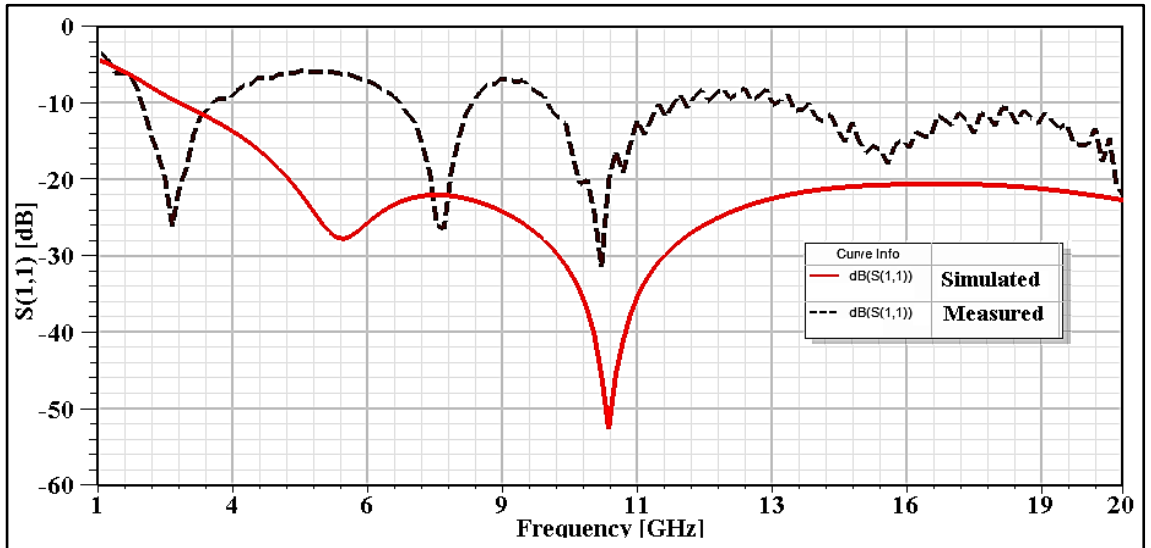


Figure 116. Comparison between simulated and measured S_{11} of TDFT antenna in egg-white solution.

The difference between measured and simulated results of S_{11} can be attributed to difficulties encountered in soldering the antenna to the inner conductor of the coaxial cable and introducing a

metallic pin – shown in Fig. 111 – at the antenna base to hold both the antenna tip and inner conductor of the coaxial cable yielding an increase of the length of TDFT antenna which in-turn increases the ohmic losses of whole structure and the possibility of introducing air-gaps between the inner conductor and the antenna structure. Nevertheless, ultra-wide band operation was clearly observed from a total bandwidth of approximately 2 GHz between where reflection measurements attained ≤ -10 dB.

For ablation experiments, the antenna was driven by a PSG Vector signal generator (Agilent Technologies E8267D 250KHz - 44GHz) connected to mini-circuits amplifier (ZVE-8G+ ~31dBm gain over 2 - 8GHz) for 7.3 GHz ablation as shown in Fig. 117. Due to the restrictions and government regulations regarding using high gain microwave amplifiers in Egypt, maximum available input power offered in Microwaves lab at Electronics research institute in Cairo, Egypt where ablation experiments were conducted was limited to only 1 W at the frequency of operation using microwave amplifier with approximately 31dBm gain. Therefore, ablation experiments for both egg-white solution and Bovine liver was performed at only 1W input power which entailed a longer application time of input power than that provided earlier in the numerical simulations to achieve solidified lesion in egg-white or ablated tissue in bovine liver.

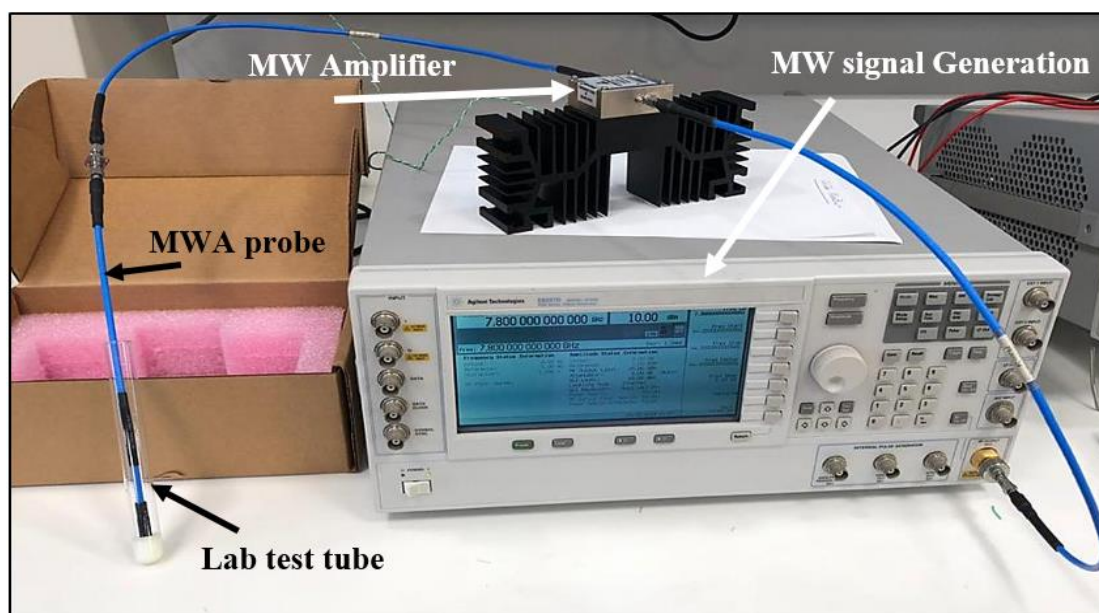


Figure 117. Microwave generation equipment and experimental setup of ablation in egg-white solution.

A small volume of egg-white solution was used to demonstrate the ablation experiment due to the limitation of total available power (1W). Snapshots of the ablated volume of TDFT antenna in

egg-white solution are presented at different time intervals in Fig. 118. It is observed that the highest temperature attained at the midpoint of TDFT antenna where a solidified white mass of egg-white is noticeably formed at the beginning of the ablation experiment (at 5 and 7 mins) which agrees with thermal simulation where the temperature maxima were observed at the mid-point of TDFT antenna. Moreover, a spherical white mass of egg-white was clearly observed at application time of 9 min which agrees with steady-state thermal profile of TDFT antenna attained in egg-white solution for 1W input power shown in Fig. 119.

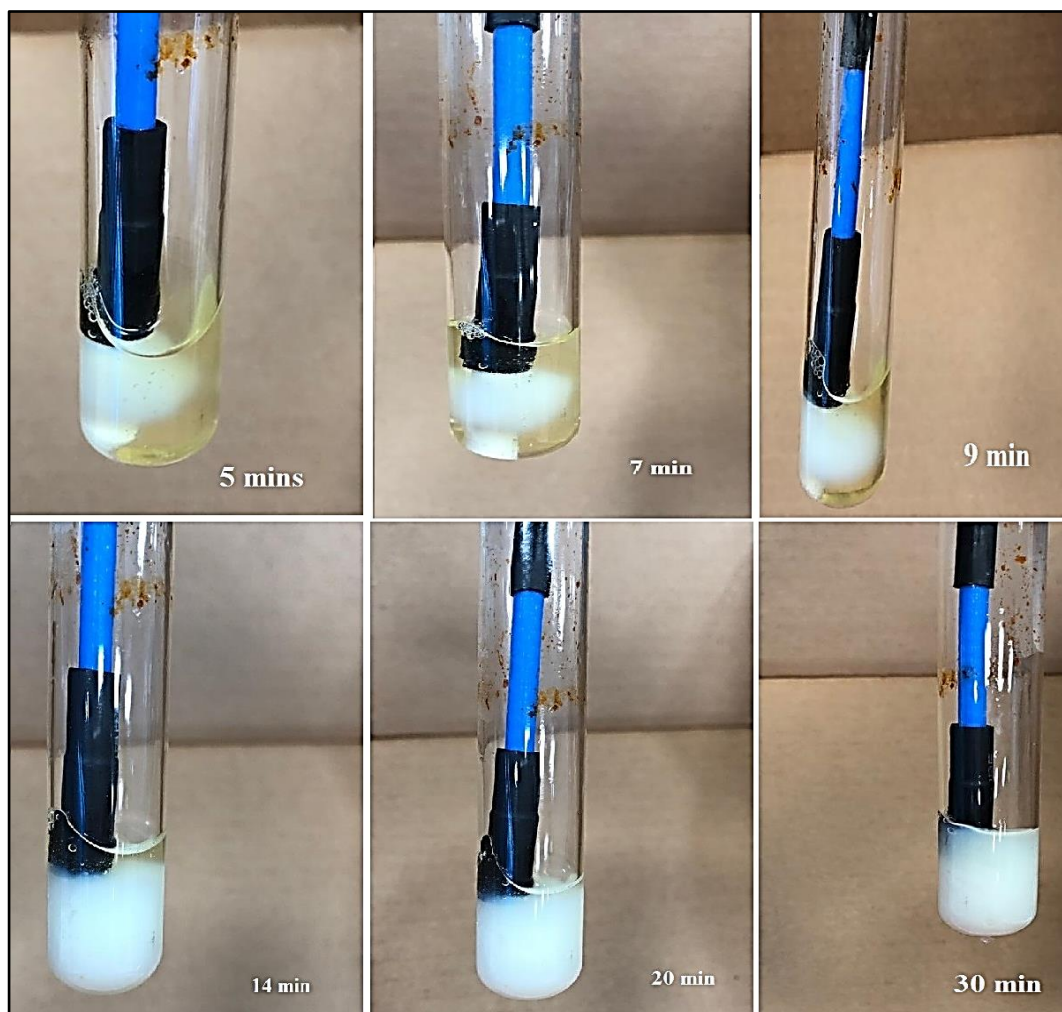


Figure 118. Snapshots of the ablated volume of TDFT antenna in Egg-white solution at different time intervals.

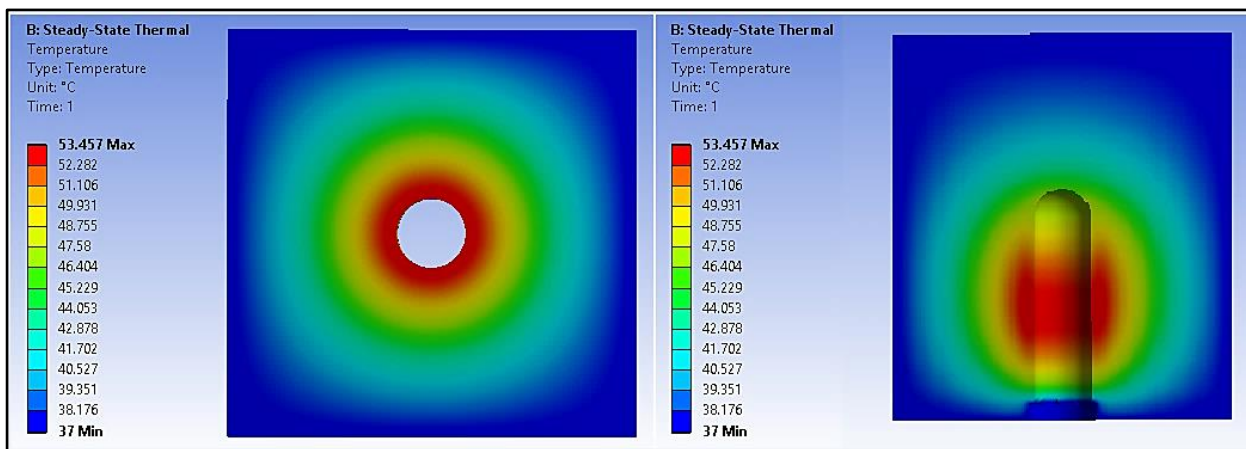


Figure 119. steady-state temperature distribution of TDFT antenna in Egg-white model.

From Fig. 106, one can observe that 50°C contour extends spherically within a diameter of 9.5 mm from the mid-point of TDFT antenna where temperature distribution recorded its maxima to be 53.457 °C through horizontal and vertical cuts in egg-white model. Figure 120 illustrates a close-up of solidified white mass of egg-white solution demonstrating a complete ablation where a total volume of 1.355 cm³ of egg-white (a height and diameter of 1.5 cm contained in test tube shown in Fig. 120) was successfully ablated in approximately 30 min for input power of 1W. Egg-white ablation experimental results agrees with SAR results and thermal analysis of TDFT antenna in egg-white solution.

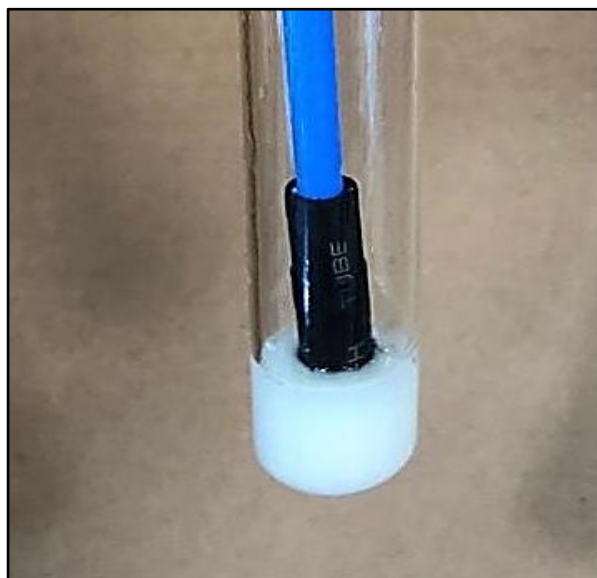


Figure 120. A close-up of solidified white mass of egg-white solution demonstrating a complete ablation.

TDFT antenna was then inserted through three liver samples, each for different application time at a position where the organ was thick enough so that the active length of TDFT antenna was completely enclosed. Experimental setup and microwave generation for liver ablation is shown in Fig. 121.

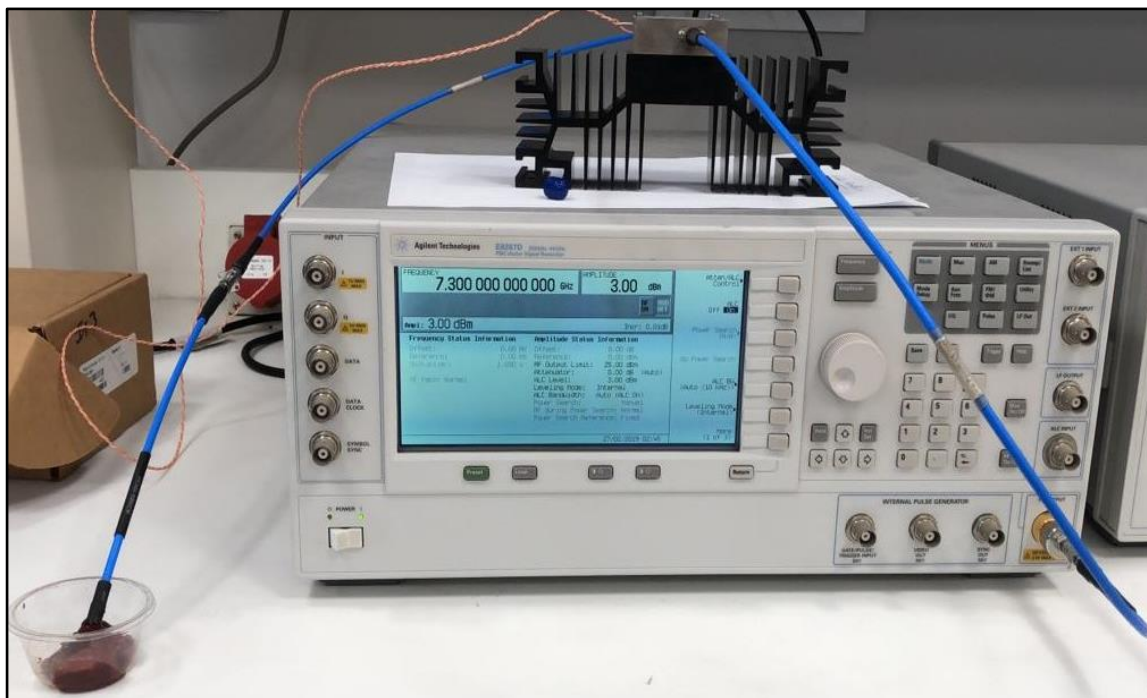


Figure 121. Microwave generation equipment and experimental setup of liver ablation.

Small liver samples were chosen to compensate the limited input power allowed for ablation experiments. Each sample was kept in a plastic beaker for each ablation experiment to maintain a consistent non-perfused portion of the organ and occlude heating within the targeted sample. The antenna position was fixed while 1W of continuous microwave power was applied for different application time 15, 30 and 90 mins. Figure 122 illustrates a close-up of TDFT antenna inserted in liver sample and a sample punctured after first ablation experiment.

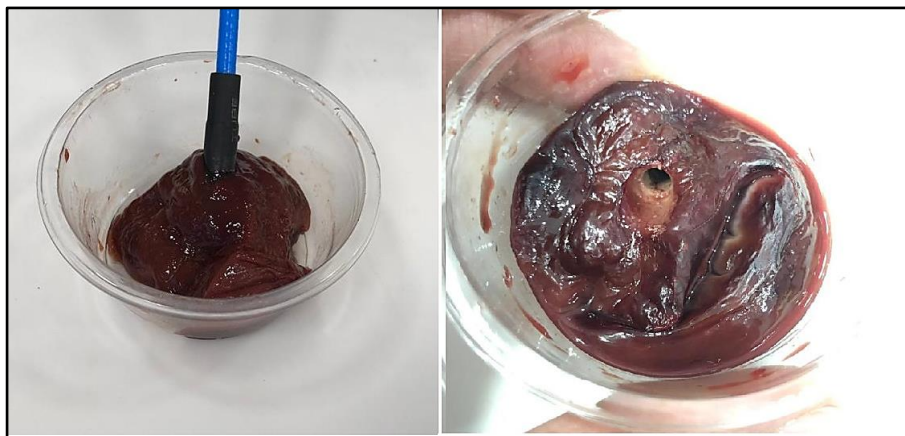


Figure 122. A close-up of TDFT antenna inserted in liver sample and a sample punctured after 90-min ablation experiment.

For each ablation experiment, liver sample was bisected along the antenna axis to examine the size of the ablated lesion achieved at each application time. Figure 123 presents the total ablated lesion achieved for 15-, 30- and 90-min ablation experiment. The boundary of the ablated volume was considered between the dark red (unaffected) tissue and peach/light brown coagulated tissue. For 15-min ablation, longitudinal and lateral diameters were found to be approximately 16 and 19.5 mm, respectively. However, as the application time increases, ablated lesion expanded to be approximately within longitudinal and lateral diameters of approximately 24 and 25.2 for 30 min ablation and for 90-min experiment, ablated volume was found to be approximately 28.5 and 32 mm in longitudinal and lateral directions. The shape of each ablated lesion was slightly deformed which can be attributed to the inconsistency often found in thickness of each liver sample.

Nevertheless, ablation started to form a spherical light orange/brown lesion and become firmer as the application time increased which is clearly depicted at 15-min ablation shown Fig. 123. Moreover, maximum temperature was found at the mid-point of TDFT antenna which can be depicted from the slightly darker brown portion in each liver sample. This agrees with numerical results of SAR and temperature distribution of TDFT antenna. In addition, coagulated tissues were found along the antenna shaft which is clearly noticed from 15- and 30-min ablation experiments as heating zones was noticeably confined along the antenna length. No ablated tissues were found in the reverse direction which emphasizes on that backward heating is noticeably diminished by TDFT antenna.

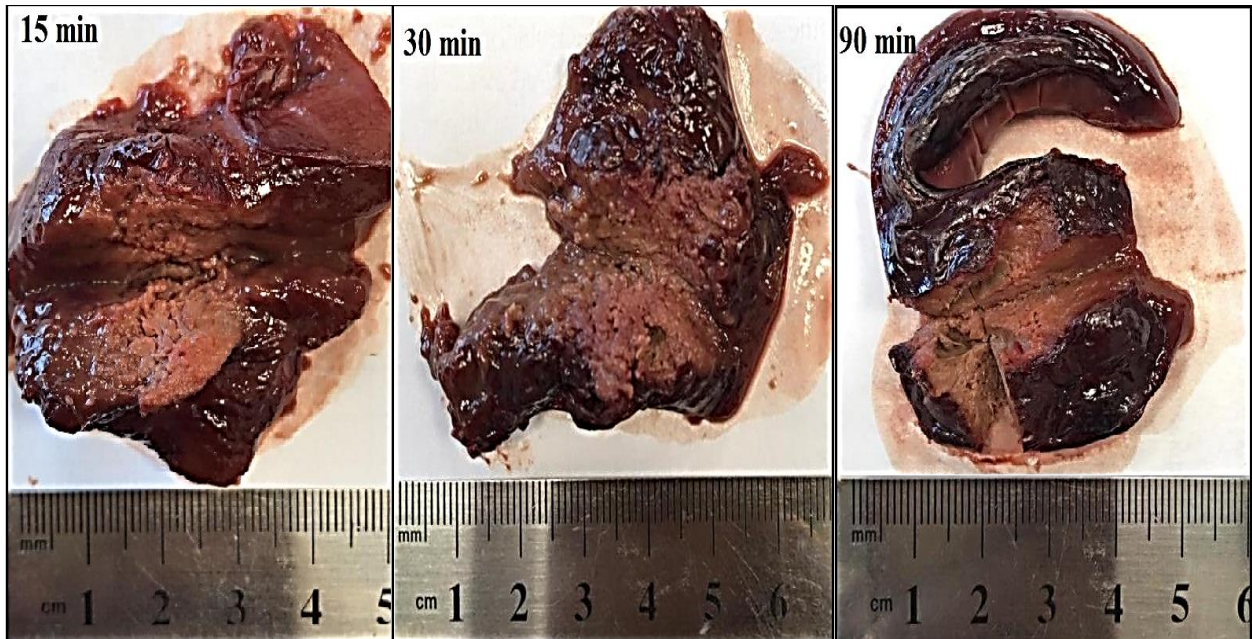


Figure 123. Total ablated lesion achieved for 15, 30- and 90-min ablation experiment.

EM and thermal analysis of TDFT antenna in liver model was also re-simulated for 1W microwave input power to study the agreement between simulated and measured results attained in ablation experiments. Due to long time and large disk space consumed by transient thermal simulation, time settings for transient analysis were set to only 10 mins application time for isotropic non-perfused liver model to determine the thermal extent that could be achieved using TDFT antenna at 1W input power. Figure 124 illustrates temperature distributions through horizontal and vertical cuts within liver model at 2 different time intervals 5 mins (300 secs) and 10 mins (600 secs), respectively. Temperature gradient slowly increases as the application time increases which can be found in the extension of 50 °C contour at 300 and 600 secs to be approximately 6.7 and 9.75 mm along the antenna axis; and 7.7 and 10 mms measured perpendicularly to the antenna axis at its mid-point, respectively. From Fig. 124, one can observe that size of the ablated lesion attained using numerical simulation is close to the one obtained in 15-min ablation experiment. Numerical simulation and ablation experiments have proven that TDFT antenna is efficiently capable of creating a nearly spherical confined ablated lesion at such low power level.

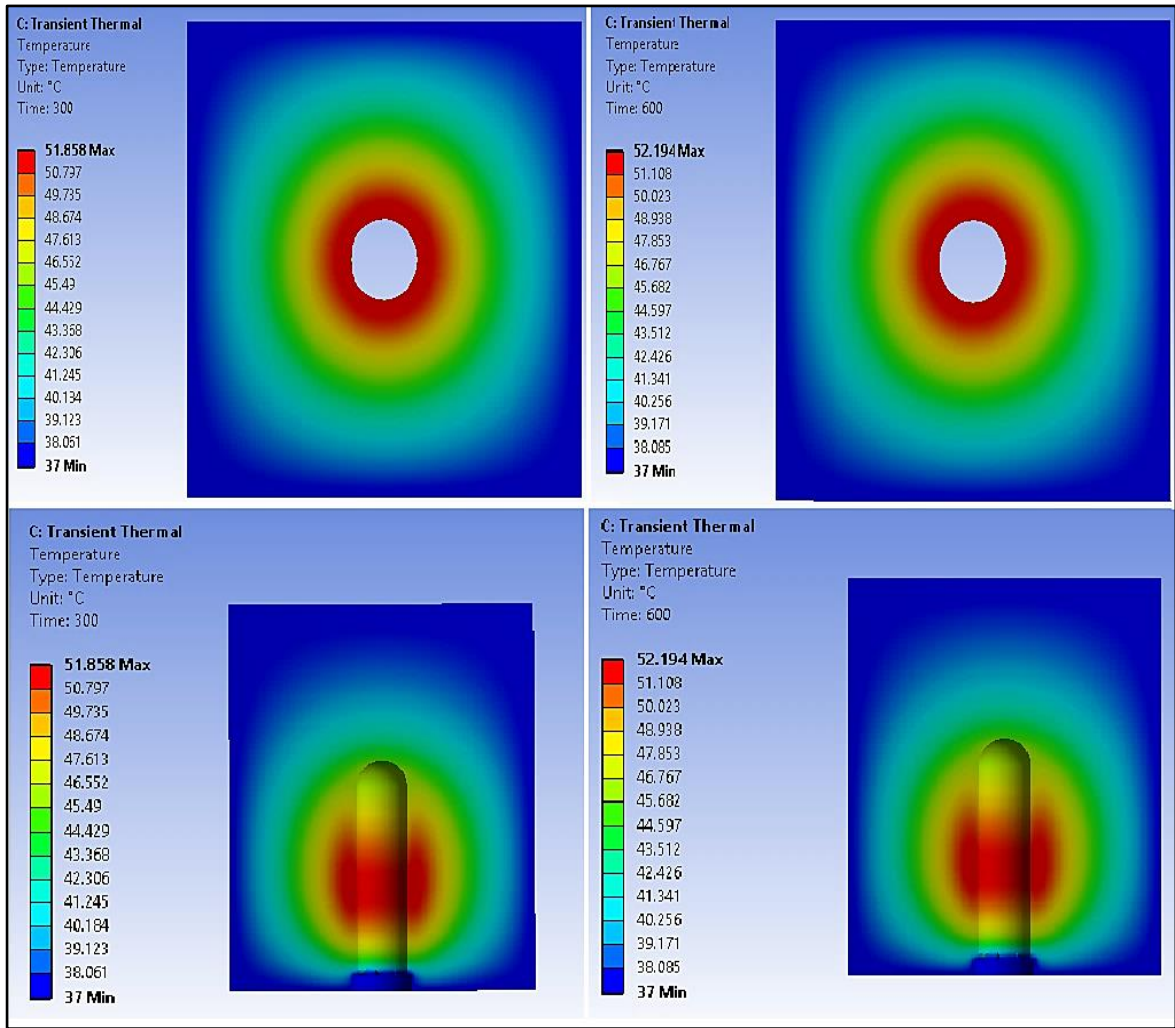


Figure 124. Transient thermal profile of TDFT antenna through horizontal and vertical cuts within Liver model for 300 secs and 600 secs at 1W input power.

Chapter Five

Evaluation of TDFT Design Compared to Previously Proposed Designs

5.1. TDFT antenna parameters compared to that attained in MWA therapy

Assessment of proposed TDFT antenna is achieved through numerical and thermal simulations and it is compared with previously proposed designs according to several parameters such as reflection, bandwidth, radiation pattern, current distribution and SAR values achieved as illustrated in Table 15 (née Reimann, et al., 2019; Preston, et al., 2018; Luyen, Hung T., et al., 2015; Gas, 2015; Brace, Christopher L, et al., 2005).

TDFT antenna provides low power cancer ablation with self-embedded choke to create confined heating by generating homogenous current distribution on the antenna surface. TDFT antenna was modelled and analysed in several dielectric surroundings such as egg-white, healthy and malignant tissue models. Symmetrical ablated lesion with no backward radiation attained using TDFT design helps overcome the nonuniform broadside radiation associated with commonly used designs. Electromagnetic simulations proved that TDFT antenna achieved -25.89 dB reflection over a bandwidth of more than 7:1 in malignant/healthy tissue model. Thermal simulations emphasize the capability of TDFT antenna of creating a confined uniform heating. Highest SAR value attained of 967.3 W/kg for 3W input power emphasized on the confined heating that can be achieved using TDFT antenna. Thermal analysis also revealed that TDFT antenna can fully ablate cancerous lesions of 15.5 mm diameter in 3 minutes for 3W input power. TDFT antenna was fabricated and tested in egg-white and bovine liver where a good agreement was attained between measured and simulated results. Minimum reflection was found to be -24.19 dB and -25.9 dB at 7.3 GHz in bovine liver and egg-white, respectively which highly agrees with numerical simulations using commercial software package and emphasizes on high power deposition and suppressing back currents of TDFT antenna. Ablation experiments were conducted in egg-white and bovine liver for 1W input power where feasibility of TDFT antenna was observed in destroying lesions of $16 \times 19.5 \times 19.5 \text{ mm}^3$ for 15-min ablation. TDFT antenna facilitates operation at variable frequency bands only for cancer treatment but also for other numerous clinical uses deploying low input power in achieving desired heating.


Table 15. TDFT antenna parameters versus most commonly used microwave applicators in cancer ablation.

Antenna Characteristics	TDFT	Other Microwave applicators	
Reflection	Minimum reflection attained is -27.81 dB in liver tissue, -23.27 dB in saline and -25.89 dB in tumour	Linear	~ -19 dB : - 46 dB
		Slot	~ -29 dB
		Helix	~ -22 dB
Bandwidth	More than 13:1 with VSWR less 2 (less than 1.2 over a bandwidth extending from 4.6 GHz to more than 17 GHz).	Linear	~ 3.5:1
		Slot	~ 2:1
		Helix	~ Narrow bandwidth of nearly 200 MHz
Radiation Pattern	Nearly spherical axial radiation pattern with no null along the antenna axis in both liver and tumour tissue	Linear	Ellipsoidal elongated pattern
		Slot	Elongated Pattern
		Helix	Omnidirectional pattern
Current distribution	Minimum currents on the outer conductor without the need of using <i>baluns</i> . Maximum temperature recorded on the surface of the outer conductor is 41 °C which is much less temperature level required for hyperthermia or ablation.	Linear	Reduced current distribution using metallic needle surrounding the antenna structure
		Slot	Overheating of the antenna shaft due to high current distribution on the outer conductor
		Helix	Large portion of power absorbed by tissues and skin along the antenna shaft
SAR and thermal profile	Homogeneous confined SAR pattern with maximum of 967.38 W/kg in tumour model for only 3W input power. Spherical lesion fully eradicated (within 60°C contour) is of 20 mm diameter. 50°C contour is approximately 30 mm within tumour model.	Linear	Elongated SAR pattern
		Slot	inhomogeneous elongated SAR pattern with its maximum near the slot
		Helix	Elongated SAR pattern with high radiation exposure toward healthy tissue along the insertion depth of the antenna.

5.2. A comparison between TDFT antenna and other MW applicators presented in Literature

In this section, performance of TDFT antenna has been assessed numerically and experimentally; and compared with other previously proposed microwave applicators; and illustrated in Table 16.

Table 16. Assessment of TDFT antenna performance compared to previously proposed designs in literature

Design	f [GHz]	S ₁₁ [dB]		Input Power [W]				Application Time [min]			Ablated Lesion (D _{Longitudinal} × D _{Lateral})					
		Simulated	≤-25.89	Simulated	1	3	4	5	Simulated	3	10	Simulated	3 min	10 min	9.75 × 10	
 Proposed TDFT antenna	7.3	Measured	≤-24.19	Measured	1				Measured	15	30	90	Measured	16×19.5	23.5×25.2	28.5×32
(Luyen, Hung, et al., 2017)	7	-18		30				5			37 × 28					
(Luyen, Hung, et al., 2017)	7	-27		30				5			43 × 28					
(Luyen, Hung, et al., 2017)	7	-24		30				5			41 × 27					
(Luyen, Hung, et al., 2017)	7	-23		30				5			40 × 28					
(Preston, et al., 2018)	5.8	-14.87		19.12 (2s on-5s off)				6			24 × 20					
				19.12 (2.2s on-5s off)				5			27 × 23					
(Ahn, Hee-Ran & Lee, Kwiro, 2005)	2.45	-28.4		20				3			45 × 24.5					
(Alnassan, Hussein, et al., 2014)	2.45	-		50,60,70				5,10,15			23 on active region (directional)					
(Fallahi, Hojjatollah, et al., 2017)	2.4	-12		40				1			19.7 × 12					
(Mohtashami, Yahya, et al., 2017)	7	-20		20				5			45 × 17					

(Luyen, Hung, et al., 2014)	10	≤-10	45	10	60×40
(Maini, Surita & Marwaha, Anupama, 2013)	2.45	-27	60	1	43 × 20
(Taj-Eldin, Mohammed & Prakash, Punit, 2014)	2.45	NA	30 (Array)	10	54 × 37
(Maini, 2016)	2.45	-24.8	20	Short duration pulses	0.19 × 0.38
(Hancock, Chris P, et al., 2013)	14.5	-17	50	2	20 × 19
(Liu, et al., 2017)	2.45	NA	60 (array)	NA	100 × 150
(Trujillo-Romero, CJ, et al., 2017)	2.45	-17.5	5	10, 15	7.99 cm ³ (bone)
(Gas & Szymanik, 2018)	2.45	-44.24	3.64	6.66	0
			20.53		17 mm
(Sawicki, et al., 2018)	6	-10	25	5	25.8 × 38.8
(Fallahi & Prakash, 2019)	0.915	-20	60	3	40.5 × 65.1
(née Reimann, et al., 2019)	5.8	-15	10	10	23 × 18
			20		28 × 22
(Taplin, et al., 2018)	5.8	-20	62	1	17 × 11.5
				2	18.5 × 14
				3	18.5 × 19

From Results presented in Table 16, it was observed that with TDFT antenna created ablated lesions at input powers from 3 to 5 W comparable to that obtained at much higher power levels (19W:60W) (Preston, et al., 2018; Fallahi, Hojjatollah, et al., 2017; Alnassan, Hussein, et al., 2014; Hancock, Chris P, et al., 2013; Luján, et al., 2017; Gas & Szymanik, 2018). Moreover, TDFT antenna has a superior performance achieving more spherical ablated lesions than that obtained in (Ahn, Hee-Ran & Lee, Kwyro, 2005) at the same application time (3 min) with much less input power (20W). In addition, simulated and measured results showed the feasibility of TDFT antenna in creating confined spherical ablated lesions at lower power level (3-5W) in shorter application time i.e. 3 min than that required in (née Reimann, et al., 2019) as observed in Table 16. Furthermore, TDFT antenna created larger ablated lesion at an input power of only (1W) with shorted application time (10 min) compared that obtained in (Luján, et al., 2017) which can be attributed to confined power deposition and minimum reflection attained using TDFT antenna. Nevertheless, the input power offered for measurement was limited to 1W, TDFT antenna produced a spherical ablated lesion in only 15 min comparable to the ones obtained in (Gas & Szymanik, 2018; née Reimann, et al., 2019). More confined heating was reached using TDFT antenna at higher frequency band with much lower input powers (3-5W) than that obtained at 5.8 GHz in (Taplin, et al., 2018) for the same application time with much higher input power.

There is trade-off between which power level and time duration needed to achieve successful ablation. For instances, for tumours less than or equal 15 mm diameter, an input power of 3W for a time of 3 minutes would be suitable. On the other hand, for larger tumour sizes, 4 and 5W with 3 min or longer application time are recommended to achieve fast ablation and more confined homogenous ablated lesions yielding a full eradication of tumour and its peripherals.

The proposed TDFT design yielded an improved performance creating equally distributed EM fields resulting in confined power deposition, achieving homogeneous temperature distribution and attaining return loss being minimally affected by the change in dielectric properties of the surrounding tissues with diminished backward heating. Simulation and experimental results also emphasized on the feasibility of TDFT antenna in diminishing the shortcomings and limitations encountered with previously proposed designs using much less input power and shorter ablation time which can be attributed to providing more confined fields over the targeted lesion, alleviating the overheating of the cabling, minimizing ablation prone to hot spots or elongated lesions and reducing as much reflection as possible during ablation with ultra-wide band feature.

Furthermore, TDFT antenna with highly-directed radiation noticeably achieves confined heating that facilitates using only 60% of the lowest input power recorded in literature to attain successful ablation in standard radiation exposure time of 15 mins. This reduces the input power used by microwave applicator by almost 40% of the lowest input power used in literature. Although TDFT antenna significantly reduces the input power required by microwave applicator used and achieve successful ablation in minimum standard duration of cancer ablation i.e. 15 mins, input power used, and duration of radiation exposure depend greatly on the size and location of tumour.

In addition, it was found that using lower input power helps eradicating critically located tumours such as bone tumours or tumours near large vessels which minimizes organ mal-function after ablation. This also facilitates the possibility of applying longer ablation operations in much safer manner without the risk of patients being exposed to high radiation using higher input power levels as presented in literature. All these features distinguished TDFT antenna to help providing less invasive microwave ablation with minimum complications and faster recovery time for cancer patients.

Chapter Six

6.1. Conclusion

A comprehensive overview on thermal tumour therapy was presented highlighting advantages and drawbacks of each technique. A literature review on numerous microwave antenna designs previously proposed was demonstrated focusing on the limitations and shortcomings of each design. Solutions were presented and summarized through applicator design considerations to emphasize and narrow down the most significant factors and basic requirements needed for antenna designs to synthesize the optimum microwave applicator for future research.

Development of microwave antenna design for microwave cancer ablation is proposed in this research investigating highly-directed radiation produced by the synthesized Tear Drop Flared Tipped (TDFT) design to treat focal nearly spherical tumours. Synthesis of TDFT structure is developed by prior identification of a radiation pattern conformal to tumour shape using semi-analytical model of TDFT antenna and its surrounding was built using Matlab to calculate the current distributions on the antenna surface to generate such radiation. This gives a preliminary idea of antenna structure that provides the required radiation. TDFT antenna is then numerically loaded in Liver, 0.9% saline and tumour model to study the performance of the proposed design using ANSOFT HFSS. The gradual synthesis of TDFT structure attained ultra-wide band feature along with stability in maintaining minimum reflection over an ultra-wide bandwidth. In addition, TDFT structure improved not only the impedance match between the feed line and antenna, but also reduced the subsequent overheating of the feed line by slightly etching the teardrop structure at its base to choke the currents flowing back on the outer conductor of the coaxial feed. TDFT design is distinguished among other conventional narrowband microwave applicators as it is immune to high reflection encountered due to shifting in operating frequency during the ablation process.

TDFT active length was optimized to be approximately $(2n-1) \lambda_{\text{eff}}/4$ operating in higher frequency band which is found to provide maximum energy deposition rate within the targeted tissue, accomplish more design compactness and in-turn less invasive yet faster ablation treatment for cancer patients. Minimum reflection stability of TDFT is attained without the need of using baluns or matching networks in saline, Liver and tumour model with overall efficiency of 99.17% in malignant tissue model at the operating frequency 7 GHz. Voltage Standing Wave Ratio (VSWR)

characteristics of TDFT design demonstrated values less than 2 measured from 1.2 GHz extending to more than 20 GHz in liver model and values less 1.5 in tumour model over bandwidth extending from 5.5 GHz to more than 20 GHz. Current distributions of TDFT design showed reduced fields flowing on the outer conductor of the coaxial cable without the need of *baluns* which results in less heating of the feed line and protection of healthy tissues along antenna shaft. In addition, nearfield distribution of TDFT design is nearly spherical along the TDFT structure with no null radiation towards the antenna tip unlike omnidirectional patterns proposed in literature. The nearly spherical radiation provides equal distribution of microwave power within the tumour tissue which results in tissues being successfully ablated after the procedure.

Moreover, TDFT structure provides minimum backward radiation which was clearly depicted from azimuth and elevation cuts of 3D Nearfield pattern. Ultra-wide band feature allowed teardrop structure to operate at such low power level compared to that reported in literature yet provided highly confined nearly spherical SAR pattern with maximum of 669 and 368 W/kg in Liver and tumour model, respectively for only 1W input power. To ensure full eradication of any peripheral tumours and satisfy the safety margin standard of less than 10 mm of surrounding healthy tissues which prevent tumour metastasis in any other part of the body, a coupled electromagnetic-thermal analysis was performed to attain the temperature profile and consequent ablation lesions in tumour and surrounding liver model based on the power delivered, duration and material characteristics such as density, thermal conductivity and specific heat capacity...etc. High agreement between SAR results and temperature profile obtained where maximum temperature of 72.375 °C reached at approximately the midpoint of TDFT antenna for only 3W input power. 60°C contour was confined within a diameter of 20 mm from the midpoint of the teardrop structure and maximum temperature of 59.524 °C was found at the tumour-liver interface. Temperatures decreased gradually to 50 °C within a radius of 5 mm away from tumour-liver interface which satisfies the acceptable ablation safety margins of surrounding healthy tissue to ensure complete eradication of tumour and alleviates the possibility of cancer recurrence. Maximum temperature observed on the surface of the outer conductor of the coaxial feed was 41.52 °C which is much less than that required for hyperthermia (above 45°C) or ablation (50-60°C). Minimum temperature attained along the antenna shaft can be attributed to the nature of teardrop design itself acting as a current choke as it was first synthesized by slightly etching a solid cone at its base. Therefore, currents flowing back on the outer conductor of the coaxial feed were minimized which in-turn alleviates the consequent overheating of the antenna shaft.

Due to the limitations found regarding the manufacturing of TDFT antenna, antenna dimensions were re-scaled and parametric studies were applied to ensure no significant changes in the previously obtained results. A 3.4 mm diameter of total length 13.66 mm gives a reflection was of -25.89 dB at 7.3 GHz. Reflection less than 15 dB was maintained all over a bandwidth extending from 3 GHz to more than 20 GHz yielding VSWR values of less than 2 from 1.5 GHz till more than 20 GHz. Overall efficiency is observed to be 99.17 % (reflection less than 20 dB) not only at the operating frequency but also extending from 4.6 GHz to 17.6 GHz. In addition, Reduced currents were clearly noticed flowing back on the outer conductor of the coaxial cable which results in less heating of the feed line and protection of healthy tissues along antenna shaft. TDFT antenna recorded higher values of nearfield along the TDFT structure than that obtained in the smaller design with maximum axial radiation towards the antenna tip unlike broadside radiation patterns proposed in literature. This nearly spherical radiation participates in providing spherical heating zone within the tumour tissue which alleviates the possibility of tissues not being successfully ablated using TDFT antenna. Moreover, minimum backward radiation is clearly observed which may help protect the healthy tissues along the antenna shaft. SAR were calculated for 3W input power over 1 gram of tissue which reached its maximum value to be 967 W/kg and slowly diffused within the tumour model. Steady state thermal analysis was conducted where maximum temperature of 72.375 °C reached at approximately the midpoint of TDFT antenna for 3W input power.

In addition, temperatures above 50°C exceeded the tumour boundary to a diameter of approximately 30 mm in the horizontal direction and 28.6 mm in the vertical direction through the midpoint of the teardrop structure where irreversible changes in tissue properties occur because of dehydration which in-turn causes instantaneous cell death. Due to long time consumed and large disk space needed to simulate transient thermal simulation, transient analysis was set to simulate the model for a total duration of only 180 secs (3 minutes) to inspect the total time needed to reach the temperature level required for ablation. Maximum temperature of 61.722 °C was observed at approximately the mid-point of TDFT antenna which highly agrees with SAR results and steady state thermal analysis. For 3 minutes of radiation, 50 °C contours are distributed in a nearly spherical manner within the tumour model achieving a horizontal and vertical diameter of 17.4 and 16.3 mms, respectively. Moreover, a temperature of 40.3°C was observed along the antenna shaft which was lower temperature level than that required for hyperthermia (45-50°C). Minimum

temperature levels were achieved on the outer conductor of the coaxial cable during the ablation which alleviated the overheating of the cable during ablation.

Several study scenarios were applied to investigate the effect of applied power and application time on the final ablated lesion. It was found that the increase of total applied power and application time significantly affect the ablated volume achieved. Steady state and transient thermal studies showed that TDFT antenna can produce symmetrical ablated lesion in a plane perpendicular to the antenna axis from its midpoint. Significant agreement was found between thermal analysis and the rotationally symmetrical nearfield distribution. Furthermore, studies showed that TDFT antenna can achieve a successful ablation of cancerous lesions with diameters of 15.5, 16 and 17.5 mm in 3 mins for input power of 3, 4 and 5W, respectively where 50°C contour encompasses irreversible changes in tissue properties yielding blood coagulation and cell necrosis.

TDFT antenna was fabricated and tested in egg-white solution and bovine liver. Ablation experiments for both egg-white solution and bovine liver was performed at only 1W input power which entailed a longer application time of input power than that provided earlier in the numerical simulations to achieve solidified lesion in egg-white or ablated tissue in bovine liver. A good agreement between the measured and simulated results where minimum reflection of was of -24.19 dB and -25.9 dB attained at the operating frequency in bovine liver and egg-white, respectively. Due to the restrictions regarding using high gain microwave amplifier, ablation experiments were conducted in egg-white solution and bovine liver for only 1W input power. Ablation experiments showed the feasibility of TDFT antenna as a microwave coagulator in producing ablated lesion of $16 \times 19.5 \times 19.5 \text{ mm}^2$ for 15-min ablation. TDFT antenna facilitates the operation at variable frequency bands which is required not only for cancer treatment but also for other numerous clinical uses deploying low input power in achieving the desired heating. TDFT antenna with highly-directed radiation noticeably achieves confined heating that facilitates using only 60% of the lowest input power recorded in literature to attain successful ablation in standard radiation exposure time of 15 mins. This reduces the input power used by microwave applicator by almost 40% of the lowest input power used in literature. Although TDFT antenna significantly reduces the input power required by microwave applicator used and achieve successful ablation in minimum standard duration of cancer ablation i.e. 15 mins, input power used, and duration of radiation exposure depend greatly on the size and location of tumour.

In addition, it was found that using lower input power helps eradicating critically located tumours such as bone tumours or tumours near large vessels which minimizes organ mal-function after

ablation. This also facilitates the possibility of applying longer ablation operations in much safer manner without the risk of patients being exposed to high radiation using higher input power levels as presented in literature. All these features distinguished TDFT antenna to help providing less invasive microwave ablation with minimum complications and faster recovery time for cancer patients.

6.2. Future Work

Due to the long-time taken to ethically approve the experimental work in actual tissues, TDFT will be further tested on real tumour tissues to validate its performance as a microwave coagulator. In addition, the effect of varying the input power and application time on measuring heat generation and the total ablated volume within the actual tissues. Nevertheless, TDFT antenna has significantly enhanced features exploited in microwave cancer ablation, it is highly efficient for treating focal nearly spherical tumours of diameter ≤ 20 mm. As TDFT antenna has a capability of thermal energy confinement in the longitudinal direction, this can be further exploited in eradicating tumours that exist near large vessels without damaging the vessel wall by inserting the antenna perpendicular to the vessel axis.

Furthermore, TDFT antenna can be tuned and tested to perform local hyperthermia at power range from 1 to 2W for shorter application time to intentionally create reversible changes in tissue properties and increase the potency of drugs in chemotherapy.

In addition, testing TDFT antenna at different frequencies in real biological tissues to investigate the antenna performance in real-time *in-vivo* ablation experiments and the effect of changing frequency of operation on the size of ablated volume, temperature levels reached and confinement of heating.

Investigating different antenna designs is inevitable as cancer can be formed in any shape and inhabit critical locations of human body where one of which can be very critical to treat. For instance, bone cancer or osteosarcoma is very critical to treat as ablation of bone tumour or sometimes called bone drilling requires precise and directional thermal heating in both zenith and elevation planes to minimize the damage that might be encountered in the surrounding healthy organ and reduce the possibility of organ malfunction after the treatment.

Moreover, there are still limitations regarding the antenna manufacturing as the feasibility of producing compact antennas is still limited as it will be very beneficial in achieving less invasive

ablation treatment and eradicating tumours inhabit critical locations that cannot be reached using traditional antenna size.

References

Ji, Zhen, & Brace, Christopher L. (2011). Expanded modeling of temperature-dependent dielectric properties for microwave thermal ablation. *Physics in medicine and biology*, 56(16), 5249.

Abbasnezhad, Behzad, Hamdami, N., Monteau, J., & Hamed, V. (2016). Numerical modeling of heat transfer and pasteurizing value during thermal processing of intact egg. *Food science & nutrition*, 4(1), 42-49.

Ahn, Hee-Ran, & Lee, Kwyro. (2005). Interstitial antennas tipped with reactive load. *IEEE Microwave and Wireless Components Letters*, 15(2), 83-85.

Alnassan, Hussein, Kastler, Adrian, Wang, Xia, & Kastler, Bruno. (2014). Modified dipole antenna for directional microwave ablation using 3D numerical simulation. 2014 7th Biomedical Engineering International Conference (BMEiCON), (pp. 1-4).

Ansoft Corporation, P. P. (2016). ANSYS Electronics Desktop, 17.2. Retrieved January 4, 2016, from <https://www.ansys.com/products/electronics/ansys-electronics-desktop>

ANSYS HFSS: High Frequency Electromagnetic Field Simulation. (n.d.). Retrieved January 3, 2016, from Ansys.com: <http://www.ansys.com/Products/Electronics/ANSYS-HFSS>

ANSYS Inc, C. P. (2016). ANSYS Simulation Platform (Workbench), 17.2. Retrieved January 4, 2016, from <https://www.ansys.com/products/structures>

Asili, Mustafa, Colebeck, Erin, Green, Ron, & Topsakal, Erdem. (2013). The effect of temperature on antenna return loss for microwave ablation antennas., 2013 US National Committee of URSI National Radio Science Meeting (USNC-URSI NRSM) (pp. 1-1).

Balanis, Constantine A. (2005). *Antenna theory: analysis and design* (Vol. 1). John Wiley & Sons.

Balanis, Constantine A. (2012). *Advanced engineering electromagnetics* (Vol. 111). Wiley Online Library.

Beebe, S., Fox, P., Rec, L., Somers, K., Stark, R., & Schoenbach, K. (2002). Nanosecond pulsed electric field (nsPEF) effects on cells and tissues: apoptosis induction and tumor growth inhibition. *IEEE Transactions on Plasma Science*, , 30(1), 286-292.

Bentzen, S. (2006). Preventing or reducing late side effects of radiation therapy: radiobiology meets molecular pathology. *Nature Reviews Cancer*, 6(9), 702-713.

Borja-Benitez, Berenice, Garduño-Nolasco, Edson, Sosa-Pedroza, Jorge, & Rodríguez-Méndez, Luis M. (2013). Size reduction of volcano monopole antenna for personal communication applications. 2013 10th International Conference on Electrical Engineering, Computing Science and Automatic Control (CCE), (pp. 179-184). Mexico City, Mexico.

References

- Brace, C. L. (2009). Radiofrequency and microwave ablation of the liver, lung, kidney and bone what are the differences. *Current problems in diagnostic radiology*, 38(3), 135-143.
- Brace, Christopher L. (2010). Microwave tissue ablation: biophysics, technology, and applications. *Critical Reviews™ in Biomedical Engineering*, 38(1), 65-78.
- Brace, Christopher L, Laeseke, Paul F, van der Weide, Daniel W, & Lee Jr, Fred T. (2005). Microwave ablation with a triaxial antenna: results in ex vivo bovine liver. *IEEE Transactions on Microwave Theory and Techniques*, 53(1), 215-220.
- Brace, Christopher L, Van der Weide, Daniel W, Lee Jr, Fred T, Laeseke, Paul F, & Sampson, Lisa. (2004). Analysis and experimental validation of a triaxial antenna for microwave tumor ablation. *2004 IEEE MTT-S International Microwave Symposium Digest*, 3, pp. 1437-1440.
- Brandy, M., Symons, S., & Stuchly, S. (1981). Dielectric behavior of selected animal tissues in vitro at frequencies from 2 to 4 GHz. *IEEE Transactions on Biomedical Engineering*, BME-28(3), 305-307.
- Carrara, Nello, & IFAC-CNR, Italy. (2014). Dielectric properties of body tissues. Retrieved December 12, 2016, from IFAC-CNR: Dielectric properties of body tissues: <http://niremf.ifac.cnr.it/tisprop/>.
- Cepeda Rubio, Mario Francisco Jesús, Hernández, Arturo Vera, & Leija Salas, Lorenzo. (2013). Advanced computer modeling for microwave ablation in breast cancer. *2013 Pan American Health Care Exchanges (PAHCE)*, (pp. 1-1). Medellin.
- Chaichanyut, M, Lertprasert, P, & Tungjitkusolmun, S. (2013). Experimental studies on power control microwave ablation in vitro animal tissues with microwave percutaneous coagulator. *2013 Asia-Pacific Microwave Conference Proceedings (APMC)*, (pp. 830-832). Seoul.
- Chiang, Jason, Hynes, Kieran, & Brace, Christopher L. (2012). Flow-dependent vascular heat transfer during microwave thermal ablation. *2012 Annual International Conference of the IEEE Engineering in Medicine and Biology Society (EMBC)*, (pp. 5582-5585). San Diego, CA.
- Chou, C. (1995). Radiofrequency hyperthermia in cancer therapy. Chapter 94 in *Biologic Effects of Nonionizing Electromagnetic Fields*, CRC Press, Inc, 1424-1428.
- Colebeck, Erin, Asili, Mustafa, Green, Ron, & Topsakal, Erdem. (2013). The effect of temperature on the microwave dielectric properties of porcine liver, lung, and heart. *2013 US National Committee of URSI National Radio Science Meeting (USNC-URSI NRSIM)*, (pp. 1-1). Boulder, CO.
- De Siewes, D. C., Duple, E. B., Strohbehn, J. W., & Trembly, B. S. (1981). Some aspects of optimization of an invasive microwave antenna for local hyperthermia treatment of cancer. *Medical physics*, 8(2), 174-183.

References

- Fallahi, H., & Prakash, P. (2019). Design of a Microwave Global Endometrial Ablation Device. *IEEE Journal of Electromagnetics, RF and Microwaves in Medicine and Biology*, 1-10.
- Fallahi, Hojjatollah, Shahzad, Atif, Clausing, Daniel, O'Halloran, Martin, Denny, M Conall, & Prakash, Punit. (2017). 2017 11th European Conference on Technological Requirements for Microwave Ablation of adrenal masses. *Antennas and Propagation (EUCAP)*, (pp. 3713-3716). Paris, France.
- Farina, L., Amabile, C., Nissenbaum, Y., Cavagnaro, M., Lopresto, V., Pinto, R., Goldberg, S. (2015). Ex vivo tissue shrinking in microwave thermal ablation. 2015 9th European Conference on Antennas and Propagation (EuCAP), (pp. 1-4). Lisbon.
- Friberg, L., Tabrizi, F., & Englund, A. (2016). Catheter ablation for atrial fibrillation is associated with lower incidence of stroke and death: data from Swedish health registries. *European Heart Journal*, ehw087.
- Gabriel, S., Lau, R., & Gabriel, C. (1996). The dielectric properties of biological tissues: II. Measurements in the frequency range 10 Hz to 20 GHz. *Physics in medicine and biology*, 41(11), 2251.
- Gabriel, S., Lau, R., & Gabriel, C. (1996). The dielectric properties of biological tissues: III. Parametric models for the dielectric spectrum of tissues. *Physics in medicine and biology*, 41(11), 2271.
- Gamez, ES, Rajagopalan, Ajit, Furgeson, DY, & Lazzi, Gianluca. (2013). Antenna design for microwave cancer ablation of osteosarcoma. 2013 US National Committee of URSI National Radio Science Meeting (USNC-URSI NRSM), 1 (pp. 1-1). Boulder, CO.
- Gananadha, Sivakumar, & Morris, David Lawson. (2004). Saline infusion markedly reduces impedance and improves efficacy of pulmonary radiofrequency ablation. *Cardiovascular and interventional radiology*, 27(4), 361-365.
- Gas, P. (2015). Determination of the optimal multi-slot coaxial antenna sizes based on the microwave antenna reflection coefficient characteristics. *Selected Problems of Electrical Engineering and Electronics (WZEE)*, 2015 (pp. 1-4). Kielce, Poland.
- Gas, P., & Szymanik, B. (2018). Shape optimization of the multi-slot coaxial antenna for local hepatic heating during microwave ablation. 2018 International Interdisciplinary PhD Workshop (IIPhDW) (pp. 319-322). Swinoujście, Poland.
- Gas, P., & Szymanik, B. (2018). Shape optimization of the multi-slot coaxial antenna for local hepatic heating during microwave ablation. 2018 International Interdisciplinary PhD Workshop (IIPhDW) (pp. 319 - 322). Swinoujście, Poland.
- Gasselhuber, Astrid, Dreher, Matthew R., Negussie, Ayele, Wood, Bradford J., Rattay, Frank, & Haemmerich, Dieter. (2010). Mathematical spatio-temporal model of drug delivery from low

References

temperature sensitive liposomes during radiofrequency tumour ablation. *International Journal of Hyperthermia*, 26(5), 499-513.

Goldberg, S Nahum, Gazelle, G Scott, Solbiati, Luigi, Rittman, William J, & Mueller, Peter R. (1996). Radiofrequency tissue ablation: increased lesion diameter with a perfusion electrode. *Academic radiology*, 3(8), 636-644.

Goldberg, SN, Solbiati, L, Hahn, PF, Cosman, E, Conrad, JE, Fogle, R, & Gazelle, GS. (1998). Large-volume tissue ablation with radio frequency by using a clustered, internally cooled electrode technique: laboratory and clinical experience in liver metastases. *Radiology*, 209(2), 371-379.

Gu, Z., Rappaport, C., Wang, P., & VanderBrink, B. (1999). A 2 1/4-turn spiral antenna for catheter cardiac ablation. *IEEE Transactions on Biomedical Engineering*, 46(12), 1480-1482.

Gu, Zeji, Rappaport, Carey M., Wang, Paul J., & VanderBrink, Brian A. (1999). A 2 1/4-turn spiral antenna for catheter cardiac ablation. *IEEE transactions on biomedical engineering*, 46(12), 1480-1482.

Habash, R., Bansal, R., Krewski, D., & Alhafid, H. (2007). Thermal therapy, Part III: ablation techniques. *Critical Reviews™ in Biomedical Engineering*, 35(1-2), 37-121.

Hamada, L, Saito, K, Yoshimura, H, & Ito, K. (2000). Dielectric-loaded coaxial-slot antenna for interstitial microwave hyperthermia: longitudinal control of heating patterns. *International Journal of hyperthermia*, 16(3), 219-229.

Hancock, C. (2010, July 20). United States patent application Patent No. 13/379,623.

Hancock, C. (2011, December 7). United States patent application Patent No. 13/992,666.

Hancock, C. (2014, June 24). United States patent application Patent No. 14/313,771.

Hancock, C., Burn, P., Duff, C., Sloan, R., White, M., Bishop, J., Tsiamoulos, Z. (2015). A New Wave in Electrosurgery : A Review of Existing and Introduction to New Radio-Frequency and Microwave Therapeutic Systems. *IEEE Microwave Magazine*, 16(2), 14 - 30.

Hancock, Chris P, Dharmasiri, Nuwan, White, Malcolm, & Goodman, Andrew M. (2013). The design and development of an integrated multi-functional microwave antenna structure for biological applications. *Microwave Theory and Techniques, IEEE Transactions*, 61(5), 2230-2241.

Hasgall, P.A., Di Gennaro, F., Baumgartner, C., Neufeld, E., Gosselin, M.C., Payne, D., Kuster, N. (2015, September 01). IT'IS Database for thermal and electromagnetic parameters of biological tissues, 3.0.

Hassan, E., Takruri, H., Zaki , A., & Hope, M. (2018). Investigation of Tear Drop Flared Tipped Antenna for Therapeutic Microwave Ablation. 2018 11th International Symposium on

References

Communication Systems & Networks Digital Signal Processing (CSNDSP) (CSNDSP18). Budapest, Hungary.

Hassan, E., Takruri-Rizk, H., & Hope, M. (2016). Applicator design considerations of microwave tumor ablation. 2016 10th International Symposium on Communication Systems, Networks and Digital Signal Processing (CSNDSP) (pp. 1-6). Prague, Czech Republic.

Hines-Peralta, Andrew U, Pirani, Nadeer, Clegg, Peter, Cronin, Nigel, Ryan, Thomas P, Liu, Zhenjun, & Goldberg, S Nahum. (2006). Microwave Ablation: Results with a 2.45-GHz Applicator in ex Vivo Bovine and in Vivo Porcine Liver 1. *Radiology*, 239(1), 94-102.

Hines-Peralta, Andrew, Sukhatme, Vikas, Regan, Meredith, Signoretti, Sabina, Liu, Zheng-jun, & Goldberg, S Nahum. (2006). Improved Tumor Destruction with Arsenic Trioxide and Radiofrequency Ablation in Three Animal Models 1. *Radiology*, 240(1), 82-89.

Hodgson, D., Feldberg, I., Sharp, N., Cronin, N., Evans, M., & Hirschowitz, L. (1999). Microwave endometrial ablation: development, clinical trials and outcomes at three years. *An International Journal of Obstetrics & Gynaecology*, 106(7), 684–694.

Holmes, K. (2009). Thermal conductivity data for specific tissues and organs for humans and other mammalian species.

Huang, Chi-Fang, Tien, Yu-Wei, Chen, Chiung-Yu, & Lin, Xi-Zhang. (2014). Design techniques for antenna needles used in microwave hyperthermia therapy for tumor treatment. 2014 IEEE-APS Topical Conference Antennas and Propagation in Wireless Communications (APWC), (pp. 37-39). Palm Beach.

Hulsey, R., Asili, M., & Topsakal, E. (2015). Adjustable zone microwave ablation. 2015 USNC-URSI Radio Science Meeting (Joint with AP-S Symposium), Vancouver, BC, Canada.

Hürter, W, Reinbold, F, & Lorenz, WJ. (1991). A dipole antenna for interstitial microwave hyperthermia. *IEEE Transactions on Microwave Theory and Techniques*, 39(6), 1048-1054.

Hussein, K. F. (2007). Efficient near-field computation for radiation and scattering from conducting surfaces of arbitrary shape. *Progress In Electromagnetics Research*, 69, 267-285.

John, D., & Ronald, J. (2002). *Antennas: for all applications*. Mc Graw Hill.

Karampatzakis, Andreas, Tsanidis, George, Kuhn, Sven, Neufeld, Esra, Kuster, Niels, & Samaras, Theodoros. (2013). Computational study of the performance of single applicators and antenna arrays used in liver microwave ablation. 2013 7th European Conference Antennas and Propagation (EuCAP), (pp. 3112-3115). Gothenburg.

Kassner, E. (2000). Evaluation and treatment of chemotherapy extravasation injuries. *Journal of Pediatric Oncology Nursing*, 17(3), 135-148.

References

- Kaur, S., & Maini, Surita. (2014). Microwave Ablation Therapy For The Treatment Of Hepatocellular Carcinoma Using Double Slot Interstitial Antenna. *International Journal Of Research Computer Applications And Robotics*, 2(1), 56-61.
- Kim, Jung-Mu, Oh, Dong Hoon, Park, Jae-Hyoung, Cho, Jei-Won, Kwon, Youngwoo, Cheon, Changyul, & Kim, Yong-Kweon. (2004). Permittivity measurements up to 30 GHz using micromachined probe. *Journal of Micromechanics and Microengineering*, 15(3), 543-550.
- Kim, Jung-Mu, Oh, Dong Hoon, Park, Jae-Hyoung, Cho, Jei-Won, Kwon, Youngwoo, Cheon, Changyul, & Kim, Yong-Kweon. (2005). Permittivity measurements up to 30 GHz using micromachined probe. *Journal of Micromechanics and Microengineering*, 15(3), 543-550.
- Kim, Young-sun, Lee, Won Jae, Rhim, Hyunchul, Lim, Hyo K, Choi, Dongil, & Lee, Ji Young. (2010). The minimal ablative margin of radiofrequency ablation of hepatocellular carcinoma (> 2 and < 5 cm) needed to prevent local tumor progression: 3D quantitative assessment using CT image fusion. *American Journal of Roentgenology*, 195(3), 758-765.
- Komarov, V. (2014). Numerical study and optimization of interstitial antennas for microwave ablation therapy. *Eur. Phys. J. Appl. Phys.*, 68(1).
- Komarov, V. V. (2014). Estimation of Heating Rate in the Near Zone of Interstitial Microwave Applicator. *IEEE Microwave and Wireless Components Letters*, 24(9), 640-642.
- Kraus, John D, & Marhefka, Ronald J. (2002). *Antenna for all applications*.
- L. Paulsen, J. B. West, W. F. Perger, & J. Kraus. (2003). Recent investigations on the volcano smoke antenna. *Antennas and Propagation Society International Symposium*. 3, pp. 845-848. Columbus, Ohio, USA.
- Labonte, Sylvain, Blais, Angeline, Legault, Stéphane R, Ali, Hassan O, & Roy, Langis. (1996). Monopole antennas for microwave catheter ablation. *IEEE Transactions on Microwave Theory and Techniques*, , 44(10), 1832-1840.
- Lara, J., Vera, A., Leija, L., & Gutierrez, M. (2015). Modeling of electromagnetic and temperature distributions of an interstitial coaxial-based choked antenna for hepatic tumor microwave ablation. 2015 12th International Conference on Electrical Engineering, Computing Science and Automatic Control (CCE), (pp. 1-5). Mexico City.
- Lara, JE., Vera, A., & Leija, L. (2016). Proposal for the application of microwave ablation as a treatment for breast cancer using interstitial applicators: Antenna design and FEM modeling. 2016 Global Medical Engineering Physics Exchanges/Pan American Health Care Exchanges (GMEPE/PAHCE) (pp. 1-6). Madrid, Spain.
- Lee, F., Haemmerich, D., Wright, A., Mahvi, D., Sampson, L., & Webster, J. (2003). Multiple probe radiofrequency ablation: pilot study in an animal model. *Journal of vascular and interventional radiology*, 14(11), 1437-1442.

References

- Lee, F., Haemmerich, D., Wright, A., Mahvi, D., Sampson, L., & Webster, J. (2003). Multiple probe radiofrequency ablation: pilot study in an animal model. *Journal of vascular and interventional radiology*, 14(11), 1437-1442.
- Lee, J. M., Jin, G. Y., Li, C. A., Chung, G. H., Lee, S. Y., Han, Y. M., . . . Kim, C. S. (2003). Percutaneous radiofrequency thermal ablation of lung VX2 tumors in a rabbit model using a cooled tip-electrode: feasibility, safety, and effectiveness. *Investigative radiology*, 38(2), 129-139.
- Leuthardt, E., Duan, C., Kim, M., Campian, J., Kim, A., Miller-Thomas, M., . . . Tran, D. (2016). Hyperthermic Laser Ablation of Recurrent Glioblastoma Leads to Temporary Disruption of the Peritumoral Blood Brain Barrier. *PloS one*, 11(2), e0148613.
- Lin, James C, & Wang, Yu-Jin. (1996). The cap-choke catheter antenna for microwave ablation treatment. *IEEE Transactions on Biomedical Engineering*, 43(6), 657-660.
- Liu, D., Lin, X., Liu, W., & Jia, X. (2017). Microwave ablation antenna with ablation area being a flat section. 2017 Sixth Asia-Pacific Conference on Antennas and Propagation (APCAP) (pp. 1-3). Xi'an, China.
- Liu, Zhengjun, Ahmed, Muneeb, Weinstein, Yehuda, Yi, Ming, Mahajan, Roop L, & Goldberg, S Nahum. (2006). Characterization of the RF ablation-induced 'oven effect': the importance of background tissue thermal conductivity on tissue heating. *International journal of hyperthermia*, 22(4), 327-342.
- Longo, Iginio, Gentili, G Biffi, Cerretelli, Matteo, & Tosoratti, Nevio. (2003). A coaxial antenna with miniaturized choke for minimally invasive interstitial heating. *IEEE Transactions on Biomedical Engineering*, 50(1), 82-88.
- Lopez, Aida Garcia, Chandra, Rohit, & Johansson, Anders J. (2013). Optimization and fabrication by 3D printing of a volcano smoke antenna for UWB applications. 2013 7th European Conference on Antennas and Propagation (EuCAP), (pp. 1471-1473). Gothenburg, Sweden.
- López, J., Leija, L., & Vera, A. (2015). Development of fabrication method for a phantom emulating breast tumor tissue for percutaneous antenna coupling measurements in microwave thermotherapy. 2015 Pan American Health Care Exchanges (PAHCE), (pp. 1-4). Vina del Mar.
- Luján, F., Pinilla, B., Gutiérrez-Martínez, J., Vera-Hernández, A., Leija, L., & Trujillo-Romero, C. (2017). Theoretical model of MW antennas to treat bone tumors: One slot and one slot choked antennas. 2017 14th International Conference on Electrical Engineering, Computing Science and Automatic Control (CCE) (pp. 1-6). Mexico City, Mexico.
- Luyen, H., Hagness, S., & Behdad, N. (2013). Tissue ablation at 10 GHz vs. 1.9 GHz: Ex vivo experiments demonstrate comparable ablation zones. 2013 IEEE Antennas and Propagation Society International Symposium (APSURSI), (pp. 2042-2043). Orlando, FL.

References

- Luyen, H., Hagness, S., & Behdad, N. (2015). A Balun-Free Helical Antenna for Minimally Invasive Microwave Ablation. *IEEE Transactions Antennas and Propagation*, 63(3), 959-965.
- Luyen, H., Hagness, S., & Behdad, N. (2017). A minimally invasive, coax-fed microwave ablation antenna with a tapered balun. *IEEE Transactions on Antennas and Propagation*, PP(99), 1-1.
- Luyen, H., Hagness, Susan C, & Behdad, Nader. (2015). A Balun-Free Helical Antenna for Minimally Invasive Microwave Ablation. *IEEE Transactions on Antennas and Propagation*, 63(3), 959-965.
- Luyen, Hung T., Mohtashami, Yahya, Sawicki, James, Shea, Jacob D., Hagness, Susan C., & Behdad, Nader. (2015). Recent advances in designing balun-free interstitial antennas for minimally-invasive microwave ablation. 2015 International Symposium on Antennas and Propagation (ISAP) (pp. 1-4). Hobart, Tasmania, Australia.
- Luyen, Hung, Gao, Fuqiang, Hagness, Susan C, & Behdad, Nader. (2014). High frequency microwave ablation for targeted minimally invasive cancer treatment. 2014 8th European Conference Antennas and Propagation (EuCAP), (pp. 1478-1482). The Hague.
- Luyen, Hung, Gao, Fuqiang, Hagness, Susan C, & Behdad, Nader. (2014). Microwave ablation at 10.0 GHz achieves comparable ablation zones to 1.9 GHz in ex vivo bovine liver. *IEEE Transactions on Biomedical Engineering*, 61(6), 1702-1710.
- Luyen, Hung, Hagness, Susan C., & Behdad, Nader. (2017). Reduced-Diameter Designs of Coax-Fed Microwave Ablation Antennas Equipped With Baluns. *IEEE Antennas and Wireless Propagation Letters*, 16, 1385-1388.
- Maini, S. (2016). Design optimization of tapered cap floating sleeve antenna for interstitial microwave ablation for liver tumor. 2016 IEEE International Conference on Consumer Electronics (ICCE) (pp. 305-308). Las Vegas, NV.
- Maini, S., & Shekhawat, D. (2018). Analysis of Copper Tube Sleeve Coaxial Spiral Antenna for Interstitial Hepatic Microwave Ablation. 2018 Eighth International Conference on Information Science and Technology (ICIST) (pp. 31-34). Cordoba, Spain.
- Maini, Surita, & Marwaha, Anupama. (2013). Design and performance analysis of multisection floating sleeve antenna using FEM for interstitial microwave ablation for HCC. 2013 IEEE Point-of-Care Healthcare Technologies (PHT), (pp. 256-259). Bangalore.
- Maini, Surita, & Marwaha, Anupma. (2012). Development and analysis of coaxial slot antenna in comparison with coaxial dipole antenna for interstitial microwave ablation. *Proceedings of the 6th international conference on Communications and Information Technology, and Proceedings of the 3rd World conference on Education and Educational Technologies* (pp. 192-196). World Scientific and Engineering Academy and Society (WSEAS).

References

- Martínez-Valdez, R., Trujillo-Romero, C.J., Castellanos, L., Gutiérrez-Martínez, J., Vera-Hernández, A., Ramos, A., & Leija, L. (2017). Feasibility of the Microwave and Ultrasound ablation as alternatives to treat bone tumors. 2017 Global Medical Engineering Physics Exchanges/Pan American Health Care Exchanges (GMEPE/PAHCE), (pp. 1-6). Tuxtla Gutierrez, Mexico.
- Mays, R. Owen, Neira, L.M., Luyen, H., Wilke, L.G., Behdad, N., & Hagness, S.C. (2016). Advances in microwave ablation antennas for breast tumor treatment. 2016 10th European Conference on Antennas and Propagation (EuCAP) (pp. 1-3). Davos, Switzerland.
- McGahan, J., & Raalte, V. (2005). History of Ablation. In *Tumor Ablation: Principles and Practice* (pp. 3-16). New York, NY: Springer New York.
- McRury, I., & Haines, D. (1996). Ablation for the treatment of arrhythmias. *Proceedings of the IEEE*, 84(3), 404-416.
- McWilliams, Brogan, Schnell, Emily, Curto, Segio, Fahrbach, Thomas, & Prakash, Punit. (2015). A directional interstitial antenna for microwave tissue ablation: theoretical and experimental investigation. *IEEE Transactions on Biomedical Engineering*, 62(9), 2144 - 2150.
- Mohtashami, Yahya, Hagness, Susan C, & Behdad, Nader. (2017). A Hybrid Slot/Monopole Antenna With Directional Heating Patterns for Microwave Ablation. *IEEE Transactions on Antennas and Propagation*, 65(8), 3889-3896.
- Muheremu, A., & Niu, X. (2014). Microwave Ablation for Bone Tumors. *Orthopedic Muscul Syst*, 3(169), 2161-0533.
- Neagu, V. (2017). A study of microwave ablation antenna optimization. 2017 E-Health and Bioengineering Conference (EHB), (pp. 41-44). Sinaia, Romania.
- née Reimann, C., Bazrafshan, B., Schüßler, M., Schmidt, S., Schuster, C., Hübner, F., Jakoby, R. (2019). A Dual-Mode Coaxial Slot Applicator for Microwave Ablation Treatment. *IEEE Transactions on Microwave Theory and Techniques*, 67(3), 1255-1264.
- Neelakanta, P. S. (1995). *Handbook of electromagnetic materials: monolithic and composite versions and their applications* (1st ed.). Bosa Roca, United States: CRC Press.
- Nevels, Robert D., Arndt, G. Dickey, Raffoul, George W., Carl, James R., & Pacifico, Antonio. (1998). Microwave catheter design. *IEEE Transactions on Biomedical Engineering*, 45(7), 885-890.
- Ng, K.-C., Lam, C.-M., Poon, R.-P., Ai, V., Tso, W.-K., & Fan, S.-T. (2003). Thermal ablative therapy for malignant liver tumors: a critical appraisal. *Journal of gastroenterology and hepatology*, 18(6), 616-629.
- O'Rourke, Ann P., Lazebnik, Mariya, Bertram, John M., Converse, Mark C., Hagness, Susan C., Webster, John G., & Mahvi, David M. (2007). Dielectric properties of human normal, malignant

References

and cirrhotic liver tissue: in vivo and ex vivo measurements from 0.5 to 20 GHz using a precision open-ended coaxial probe. *Physics in medicine and biology*, 52(15), 4707-4719.

O'Rourke, Ann P., Lazebnik, Mariya, Bertram, John M., Converse, Mark C., Hagness, Susan C., Webster, John G., & Mahvi, David M. (2007). Dielectric properties of human normal, malignant and cirrhotic liver tissue: in vivo and ex vivo measurements from 0.5 to 20 GHz using a precision open-ended coaxial probe. *Physics in Medicine & Biology*, 52(15), 4707-4719.

Ortega-Palacios, Rocío, Leija, Lorenzo, & Vera, Alonzo. (2012). Tumor breast phantom vs breast phantom Microwave ablation: Thermal experimentation and electric property measurements. *Electrical Engineering, Computing Science and Automatic Control (CCE)*, 2012 9th International Conference (pp. 1-4). Mexico City.

Pacella, C., Nasoni, S., Grimaldi, F., Stasio, E., Misischi, I., Bianchetti, S., & Papini, E. (2016). Laser ablation with or without chemoembolization for unresectable neuroendocrine liver metastases: a pilot study. *International Journal of Endocrine Oncology*.

Paulsen, Lee, West, James B, Perger, WF., & Kraus, J. (2003). Investigations on the Volcano Smoke Antenna. 2003 IEEE Antennas and Propagation Society International Symposium, 3, 845-848.

PENNES, H. (1949, September). Temperature of skeletal muscle in cerebral hemiplegia and paralysis agitans. *Archives of Neurology & Psychiatry*, 72(3), 269-279.

Petrich-Munzinger, J., Item-Glatthorn, J., Maffiuletti, N., Impellizzeri, F., Naal, F., & Munzinger, U. (2014). *Orthopedics & Muscular System: Current Research*.

Phairoh, C, Sanpanich, Arthorn, Kajornpredanon, Y, Thanangkul, S, Apaiwong, C, Sroykham, W, .Roongprasert, K. (2013). Bone drilling by using microwave ablation; FEM investigation. 2013 6th Biomedical Engineering International Conference (BMEiCON), (pp. 1-5). Amphur Muang.

Phairoh, C., Sanpanich,, A., Kajornpredanon, Y., Petsarb, K., Sroykham, W., Angkhanuwat, W., . . . Pidthalek, C. (2015). Airflow effect on microwave ablation in lung model. 2015 8th Biomedical Engineering International Conference (BMEiCON) (pp. 1-4). Pattaya.

Phasukkit, P, Tungjitkusolmun, S, & Sanpanich, Arthorn. (2012). Finite element analysis on phase shift effect of multi-antenna array alignment for microwave liver ablation. 2012 IEEE EMBS Conference Biomedical Engineering and Sciences (IECBES), (pp. 326-329). Langkawi.

Phasukkit, Pattarapong, Sanpanich, Arthorn, Tungjitkusolmun, Supan, & Hamamoto, Kiichi. (2013). Effect of phase difference in multi-antenna microwave thermal ablation for breast cancer treatment. 2013 35th Annual International Conference of the IEEE Engineering in Medicine and Biology Society (EMBC), (pp. 3718-3721). Osaka.

Pop, Mihaela, Davidson, Sean RH, Gertner, Mark, Jewett, Michael AS, Sherar, Michael D, & Kolios, Michael C. (2010). A theoretical model for RF ablation of kidney tissue and its

References

- experimental validation. In F. Bello, & Stéphane Cotin (Eds.), *Biomedical Simulation* (Vol. 5958, pp. 119-129). Springer Berlin Heidelberg.
- Poulou, Loukia S, Botsa, Evanthia, Thanou, Ioanna, Ziakas, Panayiotis D., & Thanos, Loukas. (2015). Percutaneous microwave ablation vs radiofrequency ablation in the treatment of hepatocellular carcinoma. *World journal of hepatology*, 7(8), 1054.
- Prakash, Punit. (2010). Theoretical Modeling for Hepatic Microwave Ablation. *The open biomedical engineering journal*, 4, 27-38.
- Prasantamrongsiri, S, Phasukkit, P, Pintavirooj, Chuchart, Tungjitkusolmun, S, & Sanpanich, Arthorn. (2012). 3D finite element analysis for varicose vein therapy by using microwave ablation. *Biomedical Engineering International Conference (BMEiCON), 2012* (pp. 1-5). Ubon Ratchathani.
- Prasantamrongsiri, S, Phasukkit, P, Pintavirooj, Chuchart, Tungjitkusolmun, S, & Sanpanich, Arthorn. (2012). 3D finite element analysis for varicose vein therapy by using microwave ablation. *Biomedical Engineering International Conference (BMEiCON), 2012* (pp. 1-5). Ubon Ratchathani.
- Preston, S., Taplin, W., Jones, A., & Hancock, C. (2018). A Microwave Ablation System for the Visualisation and Treatment of Pulmonary Nodules and Tumours. *2018 IEEE International Microwave Biomedical Conference (IMBioC)* (pp. 103-105). Philadelphia, PA, USA.
- Razib, Alimul, Hossain, KA., & Hossain, S. (2016). Microwave ablation technique (MWA) for cancer treatment: Simulation of single Slot MCA for different slot position. *2016 International Conference on Medical Engineering, Health Informatics and Technology (MediTec)*, (pp. 1-6). Dhaka, Bangladesh.
- Reimann, Carolin, Puentes, Margarita, Sch, Martin, & Jakoby, Rolf. (2016). Design and realization of a microwave applicator for diagnosis and thermal ablation treatment of cancerous tissue. *2016 German Microwave Conference (GeMiC)* (pp. 177-180). Bochum, Germany.
- Rosen, A., Rosen, H., Hsi, R., Rosen, D., Happawana, G., Evans, G., . . . Stern, L. (2004). Advances in RF-microwave and light sources for applications in therapeutic medicine. *15th International Conference on Microwaves, Radar and Wireless Communications, 2004. MIKON-2004. 2*, pp. 461-466.
- Rosen, Arye, Stuchly, Maria A., & Vander Vorst, Andre. (2002). Applications of RF/microwaves in medicine. *IEEE Transactions on Microwave Theory and Techniques*, 50(3), 963-974.
- Rossmann, C., & Haemmerich, D. (2014). Review of temperature dependence of thermal properties, dielectric properties, and perfusion of biological tissues at hyperthermic and ablation temperatures. *Critical Reviews™ in Biomedical Engineering*, 42(6), 467–492.
- Rubinsky, B. (2000). Cryosurgery. *Annual review of biomedical engineering*, 2(1), 157-187.

References

- Sanpamch, A., Petsarb, K., Sroykham, W., Angkhananuwat, W., Phairoh, C., Kajornpredanon, Y., . . . Phasukk, P. (2015). A simulation of lung ablation using microwave thermal energy. *RF and Wireless Technologies for Biomedical and Healthcare Applications (IMWS-BIO), 2015 IEEE MTT-S 2015 International Microwave Workshop Series on* (pp. 227-228). Taipei.
- Saunders, B., Tsiamoulios, Z., Sibbons, P., & Hancock, C. (2013). 500 The “Speedboat”: a New Multi-Modality Instrument for Endoscopic Resection in the Gastrointestinal Tract. *Gastrointestinal Endoscopy*, 77(5), AB155.
- Sawarbandhe, Mahesh D., Naik, S. Bhaskara, Satpute, VR., & Sinha, Saugata. (2016). Coaxial antenna for microwave ablation. *Distributed Computing, VLSI, Electrical Circuits and Robotics (DISCOVER), IEEE* (pp. 119-122). Mangalore, India.
- Sawicki, J., Luyen, H., Mohtashami, Y., Shea, J., Behdad, N., & Hagness, S. (2018). The Performance of Higher-Frequency Microwave Ablation in the Presence of Perfusion. *IEEE Transactions on Biomedical Engineering*, 66(1), 257 - 262.
- Sawicki, J., Shea, J., Behdad, N., & Hagness, S. (2015). Investigation of high-frequency microwave ablation using floating-sleeve dipole antennas. *2015 USNC-URSI Radio Science Meeting (Joint with AP-S Symposium)*, (pp. 327-327). Vancouver, BC, Canada.
- Schaller, Gerd, Erb, Jurgen, & Engelbrecht, Rainer. (1996). Field simulation of dipole antennas for interstitial microwave hyperthermia. *IEEE Transactions on Microwave Theory and Techniques*, 44(6), 887-895.
- Schantz, H. (2012). Three centuries of UWB antenna development. *2012 IEEE International Conference on Ultra-Wideband* (pp. 506-512). Syracuse, NY, USA.
- Schwan, H., & Li, K. (1955). Measurements of materials with high dielectric constant and conductivity at ultrahigh frequencies. *Transactions of the American Institute of Electrical Engineers, Part I: Communication and Electronics*, 73, 73(6), 603-607.
- Schwartzberg, B., Abdelatif, O., Lewin, J., Brehm, J., Bu-Ali, H., Cawthorn, S., Govindarajulu, S. (2016). Abstract P3-13-03: Multicenter clinical trial of percutaneous laser ablation for early stage primary breast cancer. Results of 49 cases with radiographic and pathological correlation. *Cancer Research*, 76(4 Supplement), P3-13-03-P3-13-03.
- Sharma, Shashwat, & Sarris, Costas D. (2016). A Novel Multiphysics Optimization-Driven Methodology for the Design of Microwave Ablation Antennas. *IEEE Journal on Multiscale and Multiphysics Computational Techniques*, 1(1), 151-160.
- Shiba, K., & Higaki, Naoya. (2009). Analysis of SAR and current density in human tissue surrounding an energy transmitting coil for a wireless capsule endoscope. *2009 20th International Zurich Symposium on Electromagnetic Compatibility*, (pp. 321-324). Zurich, Switzerland.

References

- Shock, S., Meredith, K., Warner, T., Sampson, L., Wright, A., Winter III, T., Lee Jr, F. (2004). Microwave Ablation with Loop Antenna: In Vivo Porcine Liver Model 1. *Radiology*, 231(1), 143-149.
- Siegel, R., Miller, K., & Jemal, A. (2015). Cancer statistics, 2015. *CA: A Cancer Journal for clinicians*, 65(1), 5-29.
- Singal, A., Mattison, L., Soule, C., & Iaizzo, P. (2018). Effects of Ablation (Radio Frequency, Cryo, Microwave) on Physiologic Properties of the Human Vastus Lateralis. *IEEE Transactions on Biomedical Engineering*, 65(10), 2202-2209.
- Singh, S., & Repaka, R. (2017, 11 07). Quantification of Thermal Injury to the Healthy Tissue Due to Imperfect Electrode Placements During Radiofrequency Ablation of Breast Tumors. *Journal of Engineering and Science in Medical Diagnostics and Therapy*, 1(1), 1-10.
- Solazzo, S., Liu, Z., Lobo, S., Ahmed, M., Hines-Peralta, A., Lenkinski, R., & Goldberg, S. (2005). Radiofrequency Ablation: Importance of Background Tissue Electrical Conductivity—An Agar Phantom and Computer Modeling Study 1. *Radiology*, 236(2), 495-502.
- Soueid, M., Jacques, J., Yardin, C., Fontanier, S., O'Connor, R., Leveque, P., & Arnaud-Cormos, D. (2015). Microwave hyperthermia versus nanosecond pulsed electric field for in vivo tumors applications. 2015 IEEE MTT-S International Microwave Symposium (IMS), (pp. 1-4). Phoenix, AZ.
- Strickland, AD, Clegg, Peter J, Cronin, Nigel J, Swift, B, Festing, M, West, KP, Lloyd, DM. (2002). Experimental study of large-volume microwave ablation in the liver. *British Journal of Surgery*, 89(8), 1003-1007.
- Stuchly, M., Athey, T., Stuchly, S., Samaras, G., & Taylor, G. (1981). Dielectric properties of animal tissues in vivo at frequencies 10 MHz–1 GHz. *Bioelectromagnetics*, 2(2), 93-103.
- Suh, S.-Y., Stutzman, W., & Davis, W. (2004). A new ultrawideband printed monopole antenna: The planar inverted cone antenna (PICA). *IEEE Transactions on Antennas and Propagation*, 52(5), 1361-1364.
- Sun, L., Ou, G., Lu, Y., & Tan, S. (2013). Axial ratio bandwidth of a circularly polarized microstrip antenna. In *Advancement in Microstrip Antennas with Recent Applications* (pp. 229-245). InTech.
- Suseela, S., Urdaneta, M., & Wahid, P. (2015). Use of magnetic nanoparticles in microwave ablation. 2015 IEEE 16th Annual Wireless and Microwave Technology Conference (WAMICON) (pp. 1-4). Cocoa Beach, FL, USA.
- Suseela, Sreekala, Wahid, Parveen, & Mohanan, P. (2013). A catheter antenna for cardiac ablation. 2013 IEEE Antennas and Propagation Society International Symposium (APSURSI), (pp. 2046-2047). Orlando, FL.

References

- Tacke, J., Mahnken, A., Roggan, A., & Günther, R. (2004). Multipolar radiofrequency ablation: first clinical results. *RoFo: Fortschritte auf dem Gebiete der Rontgenstrahlen und der Nuklearmedizin*, 176(3), 324-329.
- Taj-Eldin, Mohammed, & Prakash, Punit. (2014). Microwave ablation at 915 MHz vs. 2.45 GHz: single and multiple-antenna considerations. 2014 IEEE Antennas and Propagation Society International Symposium (APSURSI), (pp. 1139-1140). Memphis, TN.
- Tal, N., & Leviatan, Y. (2017). A minimally invasive microwave ablation antenna. 2017 IEEE International Conference on Microwaves, Antennas, Communications and Electronic Systems (COMCAS). Tel Aviv, Israel.
- Tal, N., Oz, D., & Leviatan, Y. (2015). Study of a thin applicator for Microwave Ablation of liver malignant tumor. 2015 IEEE International Conference on Microwaves, Communications, Antennas and Electronic Systems (COMCAS), (pp. 1-4). Tel Aviv, Israel.
- Taplin, W., Preston, S., & Hancock, C. (2018). A Miniature Flexible Microwave Applicator for the Ablation of Pancreatic Tumours at 5.8 GHz. 2018 Asia-Pacific Microwave Conference (APMC) (pp. 1402-1404). Kyoto, Japan.
- Tham, Jing-Yao, Ooi, Ban Leong, & Leong, Mook Seng. (2005). Novel Design of Broadband Volcano-Smoke Antenna. 2005 IEEE Antennas and Propagation Society International Symposium. 1, pp. 573-576. Washington, DC.
- Thongsopa, C., & Thosdeekoraphat, T. (2013). Analysis and Design of Magnetic Shielding System for Breast Cancer Treatment with Hyperthermia Inductive Heating. *International Journal of Antennas and Propagation*, 12.
- Trujillo, M., & Berjano, E. (2013). Modeling Electrical and Thermal Conductivities of Biological Tissue in Radiofrequency Ablation. *The Proceedings of The 2013 COMSOL Conference*.
- Trujillo-Romero, CJ, Rico-Martínez, G., Leija-Salas, L., Vera-Hernández, A., & Gutiérrez-Martínez, J. (2017). Microwave ablation to treat bone tumors by using a double slot antenna: A modelling study. *Global Medical Engineering Physics Exchanges/Pan American Health Care Exchanges (GMEPE/PAHCE)*, 2017 (pp. 1-4). Tuxtla Gutierrez, Mexico.
- Tsiamoulos, Z., Hancock, C., Sibbons, P., Bourikas, L., & Saunders, B. (2014). PTU-186 The “speedboat-rs2”: A New Multi-modality Endoscopic Device For Gastric And Oesophageal Submucosal Dissection And Tunnelling. *Gut*, 63(suppl 1), A120-A121.
- Vojackova, L., Merunka, I., Fiser, O., & Vrba, J. (2014). Interstitial applicators for breast cancer treatment by microwave thermoablation. 2014 24th International Conference on Radioelektronika, (pp. 1-4). Bratislava.

References

- Vrba Jr, Jan, & Vrba, David. (2014). Microwave Technology Based Medical Imaging and Diagnostics. Session 3P14 Application/Effects of EM Field/Radiation in Medicine/Bio and in Ecological Industrial Technologies, 1619.
- Wang, Peng, & Brace, Christopher L. (2012). Tissue dielectric measurement using an interstitial dipole antenna. *IEEE Transactions on Biomedical Engineering*, 59(1), 115-121.
- Watanabe, H., Yamazaki, N., Isobe, Y., XiaoWei Lu, Kobayashi, Y., Miyashita, T., Fujie, M.G. (2012). Validation of Accuracy of Liver Model with Temperature-Dependent Thermal Conductivity by Comparing the Simulation and in vitro RF Ablation Experiment. 2012 Annual International Conference of the IEEE Engineering in Medicine and Biology Society (EMBC),
- Wonnell, T., Stauffer, P., & Langberg, J. (1992). Evaluation of microwave and radio frequency catheter ablation in a myocardium-equivalent phantom model. *IEEE Transactions on Biomedical Engineering*, 39(10), 1086-1095.
- Wright, As, Lee, Ft, Johnson, Cd, & Mahvi, Dm. (2001). Comparison Of Microwave And Radiofrequency Ablation Of Hepatic Tissue In A Porcine In Vivo Model. *Radiology*. 221, Pp. 398-398. Radiological Soc North America 820 Jorie Blvd, Oak Brook, Il 60523 Usa.
- Wu, T., Rappaport, T., & Collins, C. (2015). Safe for generations to come: Considerations of safety for millimeter waves in wireless communications. *IEEE microwave magazine*, 16(2), 65-84.
- Yang, Deshan, Bertram, John M., Converse, Mark C., O'Rourke, Ann P., Webster, John G., Hagness, Susan C., Mahvi, David M. (2006). A floating sleeve antenna yields localized hepatic microwave ablation. *IEEE Transactions on Biomedical Engineering*, 53(3), 533-537.
- Yang, Deshan, Converse, Mark C, Mahvi, David M, & Webster, John G. (2007). Expanding the bioheat equation to include tissue internal water evaporation during heating. *IEEE Transactions on Biomedical Engineering*, 54(8), 1382-1388.
- Yeoh, W., & Rowe, W. (2015). An UWB conical monopole antenna for multiservice wireless applications. *IEEE Antennas and Wireless Propagation Letters*, 14, 1085-1088.
- Yeoh, W., Wong, K., & Rowe, W. (2010). Wideband miniaturized half bowtie printed dipole antenna with integrated balun for wireless applications. *IEEE Transactions on Antennas and Propagation*, 59(1), 339-342.
- Yhamyindee, P, Phasukkit, P, Tungjitkusolmon, S, & Sanpanich, Arthorn. (2012). Analysis of heat sink effect in hepatic cancer treatment near arterial for microwave ablation by using finite element method. *Biomedical Engineering International Conference (BMEiCON)*, 2012 (pp. 1-5). Ubon Ratchathani.
- Yoon, J., Cho, J., Kim, N., Kim, D.-D., Lee, E., Cheon, C., & Kwon, Y. (2011). High-frequency microwave ablation method for enhanced cancer treatment with minimized collateral damage. *International Journal of Cancer*, 129(8), 1970-1978.

References

Yu, Nam C, Lu, David SK, Raman, Steven S, Dupuy, Damian E, Simon, Caroline J, Lassman, Charles, . . . Busuttil, Ronald W. (2006). Hepatocellular Carcinoma: Microwave Ablation with Multiple Straight and Loop Antenna Clusters—Pilot Comparison with Pathologic Findings 1. *Radiology*, 239(1), 269-275.

Zhang, Huijuan, Nan, Qun, & Liu, Youjun. (2012). SAR distribution of microwave antenna for atrial fibrillation catheter ablation. *Biomedical Engineering and Informatics (BMEI), 2012 5th International Conference* (pp. 664-667). Chongqing.

Zhou, Y.-F. (2011). High intensity focused ultrasound in clinical tumor ablation. *World J Clin Oncol*, 2(1), 8-27.